Eirik Æsøy

The Effect of Hydrogen Enrichment on the Thermoacoustic Behaviour of Lean Premixed Flames

Thesis for the degree of Philosophiae Doctor

Trondheim, February 2022

Norwegian University of Science and Technology
Faculty of Engineering
Department of Energy and Process Engineering

NTNU
Norwegian University of
Science and Technology

NTNU
Norwegian University of Science and Technology

Thesis for the degree of Philosophiae Doctor

Faculty of Engineering
Department of Energy and Process Engineering

ISBN 978-82-326-6183-1 (printed ver.)
ISBN 978-82-326-6085-8 (electronic ver.)
ISSN 1503-8181 (printed ver.)
ISSN 2703-8084 (electronic ver.)

Doctoral theses at NTNU, 2022:23

PRINTED IN NORWAY
NO - 1598

NORDIC SWAN ECOLABEL
Printed matter
2041 0731

Printed by Skipnes Kommunikasjon AS

Abstract

Gas turbines (GT) burning hydrogen can help deliver large-scale zero carbon power generation and facilitate rapid decarbonisation over the short to medium term. They can also play a crucial role in increasing the penetration of renewable energy sources via power to hydrogen to power cycles where excess electricity is used to produce hydrogen which is then burned in GTs during periods of high demand for electricity. However, operating with hydrogen in lean premixed combustion regimes can lead to flashback, auto-ignition, and thermoacoustic instabilities (TIs).

This thesis puts the focus on the latter with the aim of investigating the effect of hydrogen enrichment on the thermoacoustic response of flames operated in the lean premixed regime. The work primarily consists of experimental measurements performed on single and multiple interacting flames conducted in laboratory scale can combustors. To assess thermoacoustic stability through linear stability analysis, the acoustic energy source posed by the unsteady flame was characterised through experimental measurements of flame transfer functions (FTFs). The FTF relates the coherent fluctuations in the heat release rate (HRR) to the acoustic velocity and was measured for a wide range of operating conditions and different fuels, ranging from pure methane to pure hydrogen flames.

The work can be divided into three main topics considering different aspects of TIs. In the first part, the effect of hydrogen enrichment on the linear and non linear response were investigated in single flames and multiple interacting flames. Measurements of the linear response were modeled using a distributed time lag (DTL) model where the response in HRR to acoustic velocity fluctuations was described as a superposition of delayed responses. The model was shown to successfully capture all the features of the linear response, e.g. excess gain, cut-off frequency behaviour, time delay, and gain and phase modulations caused by acoustic/convective

interference. From experimental measurements a scaling procedure was developed where these features were linked to flame and flow parameters through the DTL model constants. For sufficiently high hydrogen contents, the parameters scaled linearly with these and the procedure was shown to capture changes over a wide range of operating conditions. The predictability of hydrogen enriched flames through this scaling procedure showed a promising method to describe the stability of the combustion system when operated in a flexible manner where the thermal load and fuel composition are varied. In general the increased flame speed imposed by hydrogen leads to more compact flames which exhibit shorter time delays and larger cut-off frequencies, thereby potentially increasing the susceptibility to TIs.

When studying the effect of hydrogen enrichment, the data revealed that the increase in the cut-off frequency gave rise to significant acoustic/convective interference appearing as large modulations of the gain and phase of the FTF below the cut-off frequency. Previously this phenomena was observed in swirling flames and was attributed to swirl number fluctuations. In the second part of the work the origin of this behaviour was investigated in detail through a series of experiments designed to capture different aspects of acoustic/convective interference. It was found that the modulations arise when the vortex shedding from the upstream geometry locks onto the acoustic field. A method was proposed, where the flame response could be tailored by utilizing targeted acoustic/convective interference by tuning the time delay through careful placement of the upstream geometry. The method was shown to have potential to damp TI in GT combustors when operating in a flexible manner where the thermal load and fuel mixture are varied over wider ranges than GIs are usually operated over today.

In the third part the effect of simultaneous longitudinal and transverse acoustic oscillations on the hydrodynamic response of a turbulent jet was investigated. The aim was to simulate a simplified but similar flow condition to the one flames placed in annular combustors experience when exhibiting azimuthal TIs. It was found that the response in between the pressure and velocity nodes, where the flame exhibits both types of fluctuations simultaneously, the hydrodynamic mode of the jet resembled a superposition of the symmetric and anti-symmetric modes observed with only longitudinal or transverse forcing. The results support the method of superposition, where the combined flame response is reconstructed from individual measurements of the two modes.

Preface

This thesis was submitted to the Norwegian University of Science and Technology (NTNU) for partial fulllment of the requirements for the degree of philosophiae doctor. The doctoral work was carried out in the Thermo Fluids group at the Department of Energy and Process Engineering (EPT), from January 2018 to December 2022. The work has been supervised by Professor James R. Dawson and co-supervised by Associate Professor Jonas Moeck.

The research was supported by the NCCS FME, funded under the Norwegian research program, Centres for Environment-friendly Energy Research (FME). Grant no.: 257579/E20. NCCS seeks to develop expertise and promote innovation through focus on long-term research in selected areas of environment-friendly energy and this work is part of task 5 *'Gas turbines'*:

The thesis is made up of five chapters and six scientific articles. Chapter 1 presents an introduction to the field and a literature review. Chapter 2 provides a detailed overview of the experimental facilities and measurement diagnostics, and chapter 3 presents the processing methods used. A brief summary of the scientific articles is given in chapter 4 before chapter 5 summarises the main conclusions of the work. The articles are attached in full text at the end of the thesis and cover three main topics. The first three investigate the effect of hydrogen enrichment on single and multiple interacting flames. Articles 4 and 5 investigate the origin and effect of acoustic/convective interference on the linear flame response, and article 6 studies the hydrodynamic response of a jet submitted to simultaneous longitudinal and transverse acoustic forcing when being placed at various position in a standing wave.

A list of the articles with a summary of the authors contribution is provided.

Article 1:

Scaling and Prediction of Transfer Functions in Lean Premixed H_2/CH_4-Flames
Eirik Æsøy, José G. Aguilar, Samuel Wiseman, Mirko R. Bothien, Nicholas A. Worth, and James R. Dawson.
Combustion and Flame, Volume 215, January 2020, Pages 269–282.

Author's contributions: Eirik Æsøy and Samuel Wiseman conducted the experiments together. Eirik Æsøy analysed the data, and derived the model and wrote the manuscript together with José G. Aguilar. Mirko R. Bothien, Nicholas A. Worth, and James R. Dawson supervised the work, reviewed the manuscript, and provided technical and editorial guidance.

Article 2:

The Effect of Hydrogen Enrichment, Flame-Flame Interaction, Confinement, and Asymmetry on the Acoustic Response of Flames in a Can Combustor
Eirik Æsøy, Thomas Indlekofer, Francesco Gant, Alexis Cuquel, Mirko R. Bothien, and James R. Dawson.
Under review for Combustion and Flame.

Author's contributions: Eirik Æsøy, Thomas Indlekofer, and Francesco Gant conducted the experiments together. Eirik Æsøy analysed the data and wrote the manuscript together with Thomas Indlekofer. Francesco Gant, Alexis Cuquel, Mirko R. Bothien, and James R. Dawson reviewed the manuscript, and provided technical and editorial guidance.

Article 3:

Predicting the Influence of Hydrogen in Combustion Instabilities
José G. Aguilar, Eirik Æsøy, and James R. Dawson.
Presented at SOTIC-2021 conference and winner of the best fundamental paper award. Under review for Combustion and Flame.

Author's contributions: Eirik Æsøy conducted the experiments and José G. Aguilar and Eirik Æsøy developed the model. José G. Aguilar and Eirik Æsøy wrote the manuscript which was reviewed by James R. Dawson.

Article 4:

Acoustic-Convective Interference in Transfer Functions of Methane/Hydrogen and Pure Hydrogen Flames
Eirik Æsøy, José G. Aguilar, Mirko R. Bothien, Nicholas A. Worth, and James R. Dawson.
The Journal of Engineering for Gas Turbines and Power (2021), Paper No: GTP-21-1297

Author's contributions: Eirik Æsøy conducted the experiments. Eirik Æsøy analysed the data and wrote the manuscript which was reviewed by José G. Aguilar. Mirko R. Bothien, Nicholas A. Worth, and James R. Dawson supervised the work, reviewed the manuscript, and provided technical and editorial guidance.

Article 5:

Tailoring the Gain and Phase of the Flame Transfer Function Through Targeted Convective-Acoustic Interference
Eirik Æsøy, Håkon T. Nygård, Nicholas A. Worth, and James R. Dawson.
Combustion and Flame, Volume 236, February 2022, 111813.

Author's contributions: Eirik Æsøy and Håkon T. Nygård conducted the experiments together. Eirik Æsøy analysed the data and wrote the manuscript which was reviewed by Håkon T. Nygård. Nicholas A. Worth, and James R. Dawson supervised the work, reviewed the manuscript, and provided technical and editorial guidance.

Article 6:

The Response of an Axisymmetric Jet Placed at Various Positions in a Standing Wave
Eirik Æsøy, José G. Aguilar, Nicholas A. Worth, and James R. Dawson.
Journal of Fluid Mechanics, Volume 917, March 2021, A16.

Author's contributions: Eirik Æsøy ran the experiments, analysed the data and wrote the manuscript which was reviewed by José G. Aguilar. Nicholas A. Worth and James R. Dawson supervised the work, reviewed the manuscript, and provided technical and editorial guidance

Trondheim, September 2021
Eirik Æsøy

Acknowledgements

First of all I, would like to thank my supervisor James Dawson for giving me this opportunity and for convincing me to take on the challenge becoming a PhD student. I appreciate the guidance and discussions we have had throughout the years. I would also like to give a special thank to Nicholas Worth, Jason Hearst, and Jonas Moeck, for all the invaluable technical discussions that we have had. These have been instrumental for my progress and understanding in the various topics faced. Additionally, I would like to thank Mirko Bothien for a very fruitful collaboration and also the technical and administrative staff at EPT for their support.

I would like to thank the opponents Wolfgang Polifke and Thierry Poinsot for assessing the thesis.

I would like to thank all my co-authors and collaborators and especially Sam, Håkon, Thomas, Girish, and Srikar for the time we have shared in the lab, setting up and performing experiments. It has always been better, more productive, and more fun to work together learning from each other. A special thanks goes to José for the close collaboration through the NCCS project. You have been instrumental in most of the work, and I am proud of what we have accomplished together.

I have really enjoyed being part of the thermo fluids research group and a special thanks to Thomas and Håkon for providing a nice office environment and for keeping up with all my annoying habits. Apart from work, the group has provided a unique social environment contributing to this being amongst the best years of my life. There are too many to mention everyone, but a special thanks to Philip, Thomas, Ben, Anna, Andreas, Øyvind, and Sam.

I would also like to thank my friends and family. Finally, I would like to thank Solveig. I could not have achieved any of this without your invaluable support.

Contents

Chapter 1

Introduction

1.1 The hydrogen economy

Due to the impact of global climate change and at the same time an increasing demand for energy, there is a significant need for the energy to be supplied from sustainable sources [Conte et al., 2001]. Today, a large portion ($\sim 80\%$) of the worlds energy consumption is supplied by combustion of fossil fuels which leads to large quantities of CO_2 and other greenhouse gasses being emitted into the atmosphere [Smil, 2016]. One strategy to reduce these emissions is to transition into a '*hydrogen economy*' where fossil fuels are replaced by hydrogen, which can be used as fuel for heat, transportation, energy storage, production, etc. [Crabtree et al., 2004]. If the hydrogen is produced from renewable sources the energy cycle can be carbon neutral, and the role of hydrogen is to be an energy carrier, which needs to be stored, transported, and utilised, e.g. through combustion, during periods of high energy demand. However, today the majority of hydrogen ($> 90\%$) is still produced from natural gas through stream reforming. In order to have a truly carbon neutral cycle, large efforts are needed to either ensure CO_2 capture and storage, or to rapidly scale-up green sources, e.g. through hydrolysis [Cetinkaya et al., 2012; Dincer and Acar, 2015; Muradov and Veziroğlu, 2005].

After the hydrogen has been produced, its stored energy can be utilised by fuel cells or through combustion. In this thesis we focus on the latter, where the primary target is to investigate challenges and aspects of burning hydrogen in gas turbines (GTs) for large scale power production [ETN, 2020; Stefanizzi et al., 2021].

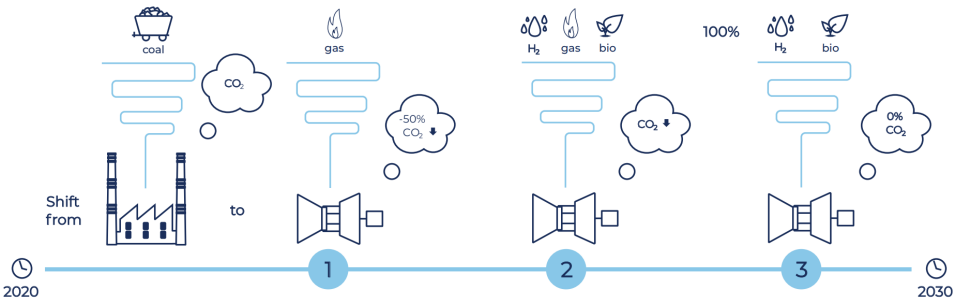

Figure 1.1: The role of gas turbines in the global energy transition adapted from [ETN, 2020]. 1. GTs fired with natural gas today emit less 50% CO_2. 2. Next step is to co-fire existing GTs with a mix of renewables and natural gas. 3. Finally to have GTs running carbon neutral.

1.1.1 The path towards a zero-carbon gas turbine

In January 2019 the GT industry committed to develop GTs running on pure hydrogen by the year 2030.

In the "Future of Hydrogen", the International Energy Agency (IEA) describes the potential of hydrogen to make a significant contribution to clean energy transition. The development of the hydrogen gas turbine can be a future carbon-neutral technology to support the society achieving the ambitious energy and climate targets. Indeed, the hydrogen gas turbines would enable deep emissions reduction for the long-term, while integrating more renewables. [ETN, 2020]

As such, GTs will fully support the transformation of the European gas grid into renewable-based through three main steps illustrated in Fig. 1.1:

1. *In combined cycle configuration, GTs are already the cleanest form of thermal power generation. Indeed, for the same amount of electricity generated, GTs running on natural gas emit* 50% *less* CO_2 *emissions than coal-fired power plants.* [ETN, 2020]

2. *Mixing renewable gas, e.g. green hydrogen, biogas, syngas, with natural gas enables further reduction in net* CO_2 *emissions. This can be achieved by direct injection in gas grids or at plant level.* [ETN, 2020]

3. *Industry is committed to enable GTs to run entirely on renewable gas fuels by 2030 and therefore achieve capabilities for* 100% *carbon neutral gasfired power generation. The ensuing objective being to implement power plants reaching* 65%+ *thermal efficiency in combined cycle configuration.* [ETN, 2020]

	ρ [kg/m^3]	E_m [MJ/kg]	E_v [MJ/m^3]	S_L [m/s]	τ_{ign} [s]	T_a [K]	I_W [MJ/Nm^3
H_2	0.09	120	10.8	2.25	$\sim 10^{-4}$	2400	40.7
CH_4	0.66	50	35.8	0.37	$\sim 10^{-1}$	2200	48.0

Table 1.1: Gas properties in terms of the density ρ, Energy per mass E_m, energy per volume E_v, laminar flame speed S_L, ignition delay time τ_{ign}, adiabatic flame temperature T_a, and Wobbe index I_W of hydrogen and methane.

.

Compared to gaseous hydrocarbons, hydrogen is a lighter fuel with significantly different properties, such as a larger flame speed [Beeckmann et al., 2017; Hu et al., 2009; Ilbas et al., 2006], shorter auto ignition delay [Brower et al., 2013], lower Wobbe index ($I_W = E_m/\sqrt{\rho/\rho_{air}}$, i.e. the lower heating value normalized by specific gravity), higher adiabatic flame temperature, etc. [ETN, 2020]. Table 1.1 shows a comparison of the gas properties of hydrogen and methane in terms of the gas density, the lower heating value giving the energy density per mass E_m and volume E_v, the laminar flame speed S_L, the ignition delay time τ_{ign}, the adiabatic flame temperature T_a, and the Wobbe index I_W. The energy density per mass is significantly larger for hydrogen, however, due to the lower density, the energy density per volume is three times lower compared to methane. This means that to maintain a similar thermal load, the volume flow rate of hydrogen needs to be increased by a factor of three.

These differences lead to challenges when introduced as fuel in GTs and below is a list of potential issues faced [Bothien et al., 2019; ETN, 2020; Lieuwen and Yang, 2006]:

- **Autoignition:** The risk of auto-ignition is higher due to the significant lower ignition delay time and ignition energy of hydrogen [Gruber et al., 2021; Ilbas et al., 2006; Lewis and Elbe, 2012]. Most combustion systems are designed such that the reactants of the fuel are converted into products at a specified location, and if the fuel spontaneously ignites elsewhere, it can lead to damage and in worst case failure of the system.

- **Flashback:** Due to the higher flame speed and lower ignition delay time, the risk of the flame propagating upstream of the fuel injection point increases [Syred et al., 2012]. For the same reasons as mentioned above this is something that needs to be avoided.

- **Increased NO_x emissions:** The increase in the adiabatic flame temperature of hydrogen will potentially lead to higher NO_x emissions. NO_x are not considered greenhouse gasses but contribute to the formation of smog, acid

rain and ground-level ozone that can damage ecosystems, animal and plant life.

- **Lower Wobbe index:** Since hydrogen has lower energy density per volume than natural gas, significantly larger flow rates are required to maintain a similar thermal load. This increase leads to higher pressure drops and larger losses within existing turbines which are currently not designed for the required flow rates [ETN, 2020]. Running GTs on pure hydrogen might require a complete redesign of existing GTs.
- **Increased thermal stress:** Hydrogen combustion leads to more moisture in the exhaust gas causing larger heat transfer to engine components which then exhibit enhanced fatigue due to thermal stresses. Therefore, hydrogen fired GTs might require a redesign of the cooling systems.
- **Modified thermoacoustic reponse:** Due to the larger flame speed and shorter auto ignition delay time, hydrogen flames may have significantly different mechanisms of stabilization leading to different flame shapes. This then leads to a significant change of the thermoacoustic response of the flame which is the coupling between combustion and the acoustic modes of the GT [Candel, 2002; Indlekofer et al., 2021; Lieuwen and Yang, 2006; Poinsot, 2017]. This challenge is the topic of this thesis.

1.1.2 Effect of H_2 on combustions properties

The main objective of this thesis is to contribute to the shift towards pure hydrogen combustion in GTs by investigating the effect of hydrogen enrichment on the thermoacoustic behaviour in lab scale combustors. The research was limited to investigating flames operated in the lean premixed combustion regime at atmospheric pressures.

The chemical reactions for methane and hydrogen combustion are given by

$$CH_4 + 2O_2 \rightarrow 2H_2O + CO_2, \tag{1.1}$$

$$2H_2 + O_2 \rightarrow 2H_2O, \tag{1.2}$$

and an important fuel parameter for premixed combustion is the equivalence ratio

$$\Phi = \frac{n_{\text{fuel}}/n_{\text{ox}}}{(n_{\text{fuel}}/n_{\text{ox}})_{\text{st}}}, \tag{1.3}$$

which gives the ratio of molecules (or volume) of fuel and oxidiser, relative to stoichiometric conditions. For methane and hydrogen, stoichiometric conditions correspond to $(n_{\text{fuel}}/n_{\text{ox}})_{\text{st}} = 0.5$ and $(n_{\text{fuel}}/n_{\text{ox}})_{\text{st}} = 2$, respectively.

To reduce emissions by reducing the flame temperature (see Fig. 1.3 a)) and increase the combustion efficiency by making sure all the fuel is burned, there is an advantage burning the fuel as a lean premixed mixture ($\Phi < 1$) with excess air. However, lean premixed flames have been shown to be considerably more prone to thermoacoustic instabilities (TIs) [Candel, 2002; Candel et al., 2014; Lieuwen and Yang, 2006].

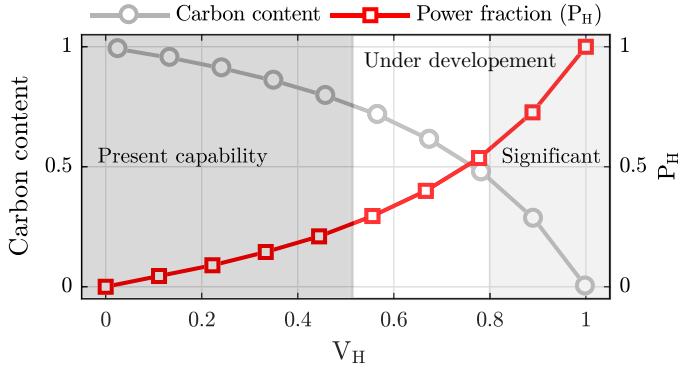

Figure 1.2: Carbon content and power fraction of hydrogen in mixtures of hydrogen/methane blends (adapted from ETN [2020]). There is not a linear decrease in the carbon content with an increase in the volume fraction of hydrogen, due to the significant difference in the gas density of hydrogen and methane.

Hydrogen enrichment enhances the challenge with TIs considerably. An important aspect is the reduction of the carbon content in the fuel as a function of hydrogen enrichment. A common metric to quantify hydrogen enrichment is the volume (or mole) fraction introduced by hydrogen in the mixture which is defined as

$$\mathrm{V_H} = \frac{\mathrm{V_{H_2}}}{\mathrm{V_{H_2}} + \mathrm{V_{CH_4}}}. \tag{1.4}$$

Here, $\mathrm{V_{H_2}}$ and $\mathrm{V_{CH_4}}$ are the volume flow rates of hydrogen and methane respectively. In Fig. 1.2 the carbon content is plotted versus $\mathrm{V_H}$. Since there is a significant difference in the energy density per mass, the carbon content does not decrease linearly with the increase in $\mathrm{V_H}$. Today, the capabilities of GTs lie around $\mathrm{V_H} = 0.5$, which only corresponds to a reduction of CO_2 by 25%. The current development lies in the range $\mathrm{V_H} > 0.5$, but $\mathrm{V_H} > 0.8$ is needed to make significant reductions in CO_2.

Therefore, to better reflect the reduction in the carbon content of the mixture, it is convenient to work with a hydrogen power fraction defined as

$$\mathrm{P_H} = \frac{\mathrm{P_{H_2}}}{\mathrm{P}} = \frac{E_{v,\mathrm{H_2}}\mathrm{V_{H_2}}}{E_{v,\mathrm{H_2}}\mathrm{V_{H_2}} + E_{v,\mathrm{CH_4}}\mathrm{V_{CH_4}}}. \tag{1.5}$$

Here, P is the total thermal power introduced by H_2 and CH_4, and P_{H_2} is the power introduced by H_2 alone. The red line in Fig. 1.2 shows the power fraction P_H versus the volume fraction V_H, and there is approximately an inverse trend of P_H and the reduction in CO_2.

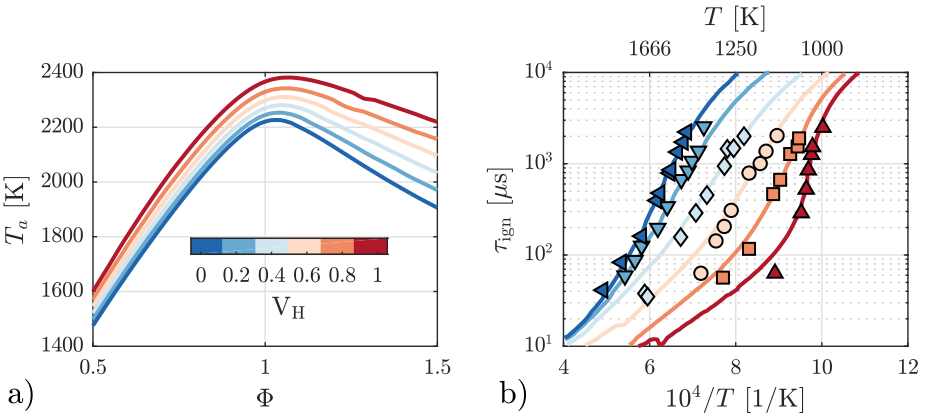

Figure 1.3: Variation in a) the adiabatic flame temperature T_a, and b) the ignition delay time τ_{ign} with the equivalence ratio Φ, and hydrogen content V_H. The profiles in a) were computed using Cantera [Goodwin et al., 2020] and in b), the data is adapted from Zhang et al. [2012] obtained from modeling and experiments and with $\Phi = 0.5$ and pressure 0.5 MPa. There is a moderate difference in T_a and a significant difference in τ_{ign} by several orders of magnitude between pure methane and pure hydrogen.

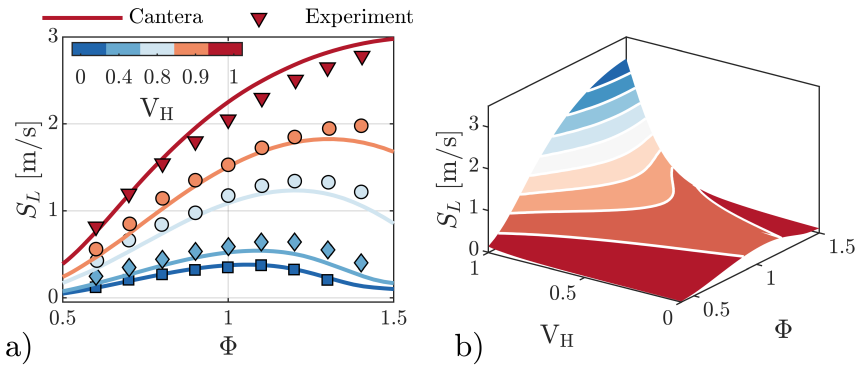

Figure 1.4: Variation in the laminar flame speed S_L, with the equivalence ratio Φ, and hydrogen content V_H. In a) the experimental data is adapted from Hu et al. [2009]. In b) S_L was computed using Cantera [Goodwin et al., 2020]. There is an increase by an order of magnitude between pure methane and pure hydrogen.

Similar to the reduction of the CO_2 content, changes in the fuel properties increase progressively with V_H. Fig. 1.3 a) shows the adiabatic flame temperature T_a for

different values of Φ and V_H. At stoichiometric conditions ($\Phi = 1$) there is an increase from $T_a = 2200\,\mathrm{K}$ to $2400\,\mathrm{K}$, a moderate increase. The largest decrease in T_a is achieved by moving towards a leaner fuel mixture, i.e. by reducing Φ.

Although the change in T_a with V_H is moderate, perhaps the most striking effect is reflected by the variation in the ignition delay time τ_{ign} and the laminar flame speed S_L, shown in Fig. 1.3 b) and Fig. 1.4 respectively. At the same temperature, pressure and equivalence ratio, the ignition delay time τ_{ign} decreases by several orders of magnitude when moving from pure CH_4 to pure H_2, posing a significant risk of spontaneous auto-ignition. The laminar flame speed is important because it provides the magnitude of how fast the flame can propagate against the flow, and the variation with hydrogen content is shown in Fig. 1.4. In a), S_L is shown for stoichiometric conditions, i.e. $\Phi = 1$, and in b), S_L is shown for a range of Φ and V_H. Compared to pure CH_4, there is an increase in S_L by an order of magnitude for pure H_2. As for the reduction in the CO_2 content, most of the increase in S_L occurs in the region $V_H > 0.8$. This is the region in which most significant changes to the flame can be expected, and the figure illustrates why the last 20% of hydrogen by volume might be particularly challenging. It should be emphasized that the flame speed also decreases with Φ, and by using blends of methane and hydrogen, there is potential for burning the fuel at even leaner conditions without blowing out the flame [Wiseman et al., 2021].

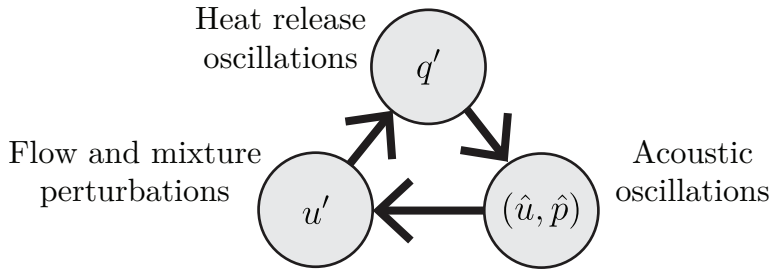

Figure 1.5: Coupling between the acoustics, flow, and HRR, with a potential of driving TI, adapted from Lieuwen and Yang [2006]. If the fluctuations in HRR are sufficiently synchronised with the acoustics close to a resonant mode of the GT, self sustained oscillations can occur.

1.2 Thermoacoustic instabilities

TIs arise when oscillations in the HRR from the combustion process couple with one or more of the acoustic modes of the combustion system. If the acoustic pressure and HRR oscillates sufficiently in phase, a feedback loop between the HRR, pressure and flow is established, as illustrated in Fig.1.5. The phenomenon of

thermoacostic oscillations has been known for more than a century and Rayleigh [1878] formulated a condition where acoustic energy is added and hence, the system is unstable, if the oscillations in HRR q', and pressure p', are in phase. This is mathematically described through the modified Rayleigh criterion

$$\int_T \int_V p'(\mathbf{x},t)q'(\mathbf{x},t)dtdV \geq \int_T \int_V \sum_i L_i(\mathbf{x},t)dtdV, \tag{1.6}$$

where the energy added has to overcome the acoustic sources of damping L_i [Lieuwen and Yang, 2006]. The driving, represented by the left hand side, is generated by the unsteady combustion process, and the damping, represented by the right hand side, arises from viscous dissipation or radiation of acoustic energy through boundaries. If the product of p' and q' is positive and larger than the damping the flame can potentially drive self sustained pressure oscillations. Therefore, the time delay between the oscillations in pressure and HRR is the most essential parameter for the onset of a TI [Lieuwen, 2012; Strutt, 1945].

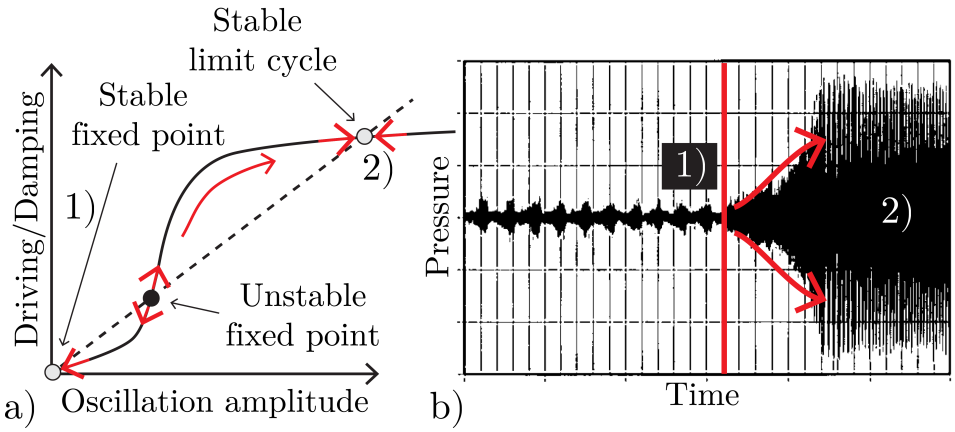

Figure 1.6: Illustration of a thermoacoustic system with a potential for limit-cycle oscillations. a) shows the driving and damping terms illustrated by the solid and dashed lines as functions of the oscillation amplitude. The points where the driving intersects with the damping correspond to fixed points. b) shows measurements of a time series where a combustor transitions into limit cycle oscillations after the noise rises above a level (adapted from [Lieuwen, 2002]).

Before a system transitions into self sustained oscillations, it is triggered and hence moves a stable operating point to an unstable one. To illustrate this process, the driving and damping are plotted against the oscillation amplitude in Fig. 1.6 a). Two stable fixed points appear, one located at the origin and the other at a finite oscillation amplitude. These are separated by an unstable fixed point, and for oscillation amplitudes below this level, the damping exceeds the driving, which

reduces the amplitude, pushing the system towards the origin. However, if the amplitude exceeds this limit, the driving overcomes the damping and the system is pushed towards the stable limit cycle. Once pushed over the edge, the system can maintain self sustained oscillations which can have serious consequences for a GT. In Fig. 1.6 b), experimental measurements of such a transition are shown [Lieuwen, 2002]. Notice, that before growing into large amplitude oscillations, the system is growing and decaying in a quasi-periodically manner. When perturbed sufficiently, the oscillations grow into large amplitude oscillations.

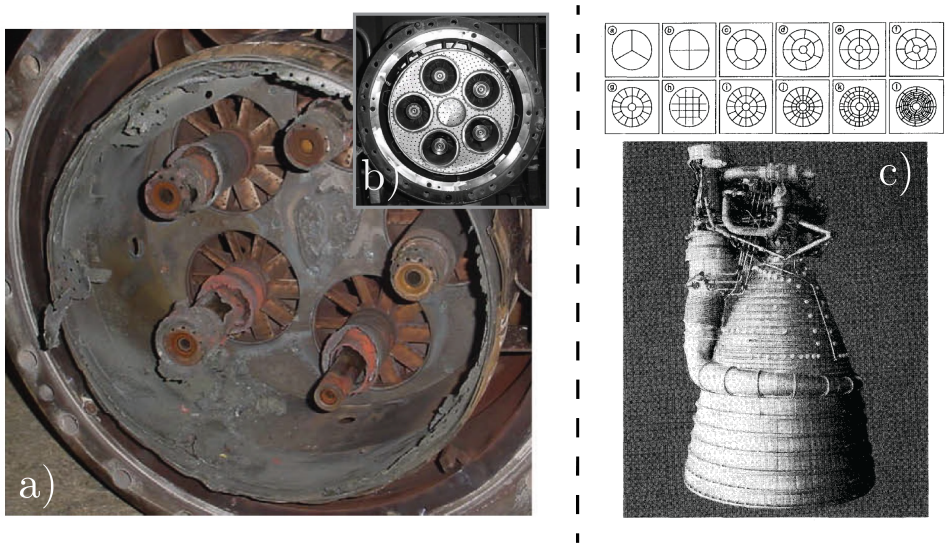

Figure 1.7: a) and b) show the fuel injection system of a GT damaged by a TI, adapted from Goy et al. [2005]. Self sustained oscillations in the pressure lead to upstream propagation of the flames which damaged parts that were not designed to tackle the conditions imposed by the flame. c) Image of key external features of the F-1 engine and the some of the baffle patterns investigated during the F-1 project first program, adapted from Oefelein and Yang [1993]. It required almost 2000 full engine tests to tame the TI and enable stable operations.

When a TI occurs, the pressure oscillations can lead to destruction of the engine components. An example is shown in Fig. 1.7 a) and b) [Goy et al., 2005], where the fuel injection system has melted due to a TI. Another famous example of a TI occurred during the development of the F-1 rocket engine used for the first stage of the Saturn-V launch. The engine featured a transverse instability, and due to a lack of fundamental knowledge of TIs, the project required almost 2000 full scale engine tests to fix the problem [Oefelein and Yang, 1993]. A solution was found by modifying the burner geometry with baffles, by trial and error, to separate the fuel injection sprays.

It is now common to analyse the onset of TIs by treating the GT as an acoustic system which can be described using the Helmholtz equation

$$\nabla \cdot (c^2 \nabla \hat{p}) + \omega^2 \hat{p} = i\omega(\gamma - 1)\hat{q}. \tag{1.7}$$

Here, c is the sound speed, and $\hat{p}$, $\hat{q}$, and ω, are the complex pressure, local HRR, and the angular frequency respectively [Poinsot and Veynante, 2005]. The acoustic/flame interaction is treated as a source term $\hat{q}$, and with a model for the source, and with prescribed boundary conditions, the solution of Eq. 1.7 provides modes (frequency and shape), and the linear stability of the system by considering the complex part of the computed eigenfrequency [Bothien et al., 2015; Buschmann et al., 2020; Dowling, 1997, 1999; Laera et al., 2017; Noiray et al., 2008].

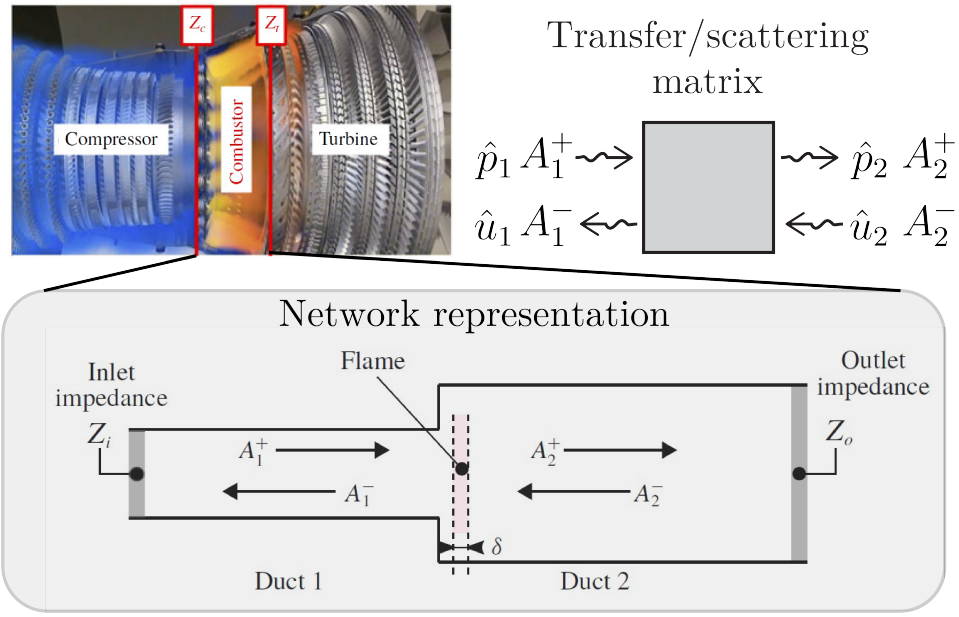

Figure 1.8: Simple network model representation of a GT gas turbine combustion chamber where compressor inlet and turbine outlet are characterised by acoustic impedances. Wave propagation is usually limited to one dimensional plane waves and described either by Riemann invariants (A^+,A^-), or the acoustic pressure and velocity ($\hat{p}$,$\hat{u}$). (images are adapted from Schuller et al. [2020])

Further simplifications are often made by considering one dimensional wave propagation through elements describing area jumps, constant area ducts, or the influence across a heat source such as a flame. The system can then be described by connecting elements which satisfy Eq. (1.7) into a network as illustrated in Fig. 1.8.

Each element is described by an acoustic transfer matrix

$$\begin{bmatrix} \hat{p}_2^- / (\rho c) \\ \hat{u}_2^+ \end{bmatrix} = \begin{bmatrix} T_{11} & T_{12} \\ T_{21} & T_{22} \end{bmatrix} \begin{bmatrix} \hat{p}_1^- / (\rho c) \\ \hat{u}_1^+ \end{bmatrix}, \tag{1.8}$$

or the equivalent acoustic scattering matrix

$$\begin{bmatrix} A_1^- \\ A_2^+ \end{bmatrix} = \begin{bmatrix} S_{11} & S_{12} \\ S_{21} & S_{22} \end{bmatrix} \begin{bmatrix} A_1^+ \\ A_2^- \end{bmatrix}. \tag{1.9}$$

The transfer matrix relates the acoustic pressure and velocity up- and downstream of the element, whereas the scattering matrix relates the in- and outgoing acoustic waves in terms of the Riemann invariant A^+ and A^-. Boundary conditions are usually described by acoustic impedances or reflection coefficients respectively given by

$$Z = \frac{\hat{p}}{\hat{u}}, \quad R = \frac{A^-}{A^+}, \tag{1.10}$$

and the network model provides a non-linear eigenvalue problem

$$\mathbf{A}(\omega)\mathbf{x} = 0, \tag{1.11}$$

where the solutions provide complex frequencies ω (eigenvalues), and corresponding mode shapes $\mathbf{x}$ (eigenvectors). If $\mathrm{Im}(\omega) > 0$, the mode is linearly unstable and hence, the amplitudes grow exponentially with time [Buschmann et al., 2020].

1.2.1 Flame as an acoustic source

The main difficulty in solving the Helmholtz equation lies in a valid description of the source term $\hat{q}$, which can only be analytically derived for simple cases [Schuller et al., 2003]. Using the linearized Rankine–Hugoniot relations through the flame yields [Poinsot and Veynante, 2005]

$$\begin{bmatrix} \hat{p}_2^- / (\rho c) \\ S_2 \hat{u}_2^+ \end{bmatrix} = \begin{bmatrix} 1 & 0 \\ 0 & 1 \end{bmatrix} \begin{bmatrix} \hat{p}_1^- / (\rho c) \\ S_2 \hat{u}_1^+ \end{bmatrix} + \begin{bmatrix} 0 \\ \frac{\gamma - 1}{\gamma \bar{p}} \end{bmatrix} \hat{Q}, \tag{1.12}$$

where the global unsteady HRR $\hat{Q} = \int_V \hat{q} \mathrm{d}V$ acts as an acoustic source. γ and $\bar{p}$ are the ratio of specific heats and mean pressure respectively and S_1 and S_2 are the cross section areas before and after the flame.

In the linear approximation the relative fluctuation $\hat{Q}/\bar{Q}$ is coupled to three main mechanisms

$$\frac{\hat{Q}}{\bar{Q}} = \mathrm{F_V} \frac{\hat{u}}{\bar{u}} + \mathrm{F_P} \frac{\hat{p}}{\bar{p}} + \mathrm{F_\Phi} \frac{\hat{\phi}}{\bar{\phi}}, \tag{1.13}$$

namely oscillations in the velocity, pressure, and equivalence ratio. F_V, F_P, and F_Φ are transfer functions relating the amplitude and phase between the fluctuations [Lieuwen, 2012]. Relating the HRR to other quantities through a transfer function was originally proposed by Merk [1957a,b], and is now a common practice.

Usually, the pressure term is neglected for low Mach number flows due to weak acoustic amplification of the pressure/density fluctuations, and for perfectly premixed combustion $\hat{\phi}$ is negligible [Polifke, 2020]. This is the case in the present study, where only premixed fuel/air mixtures are considered. However, for safety reasons the fuel injection in practical systems is done close to the combustion zone, averting perfect premixing. Therefore mixtures are often technically premixed which can lead to equivalence ratio fluctuations due to the coupling between the acoustics and the fuel injection, also one of the main drivers for TIs [Huber and Polifke, 2009; Kim and Park, 2010; Sattelmayer, 2003].

1.2.2 The flame transfer function

We consider the case where $F_P \approx 0$ and $F_\Phi \approx 0$ and hence, the global fluctuations in HRR $\hat{Q}/\bar{Q}$, are linked to the acoustic velocity $\hat{u}/\bar{u}$, through F_V, which we henceforth refer to as the Flame Transfer Function (FTF) defined as [Schuller et al., 2020]

$$\mathrm{FTF}(\omega) = \frac{\hat{Q}/\bar{Q}}{\hat{u}/\bar{u}} = G\exp(j\Theta). \tag{1.14}$$

The FTF is decomposed into a gain G, and a phase Θ, determining the amplification and delay respectively. The reference velocity is taken at a point or a plane. Theoretical models can be derived for the FTF, e.g. as in [Dowling, 1999; Fleifil et al., 1996; Hirsch et al., 2005; Schuller et al., 2003]. However, this approach is generally limited to simple cases, and usually the FTF has to be obtained either by experiments, e.g. as in [Cuquel et al., 2013; Durox et al., 2009; Kim et al., 2010; Külsheimer and Büchner, 2002; Palies et al., 2011c], or via numerical simulations [Kaufmann et al., 2002; Polifke, 2014; Tay-Wo-Chong et al., 2011], due to the complexity introduced by the unsteady turbulent combustion.

In this thesis we measured the FTF experimentally. This consists of providing controlled acoustic forcing, and simultaneous measurements of $\hat{u}$ and $\hat{Q}$. Two examples of experimental facilities used for such measurements are displayed in Fig. 1.9. To measure the global oscillations in the HRR, it is common to capture the light emissions from spontaneous radicals formed in the flame by the use of photo multiplier tubes (PMTs) equipped with suitable filters to to capture OH^* or CH^*. For measurements of the acoustic velocity, different methods have been used. One method is to measure the velocity upstream of the flame using hot wire anemo-

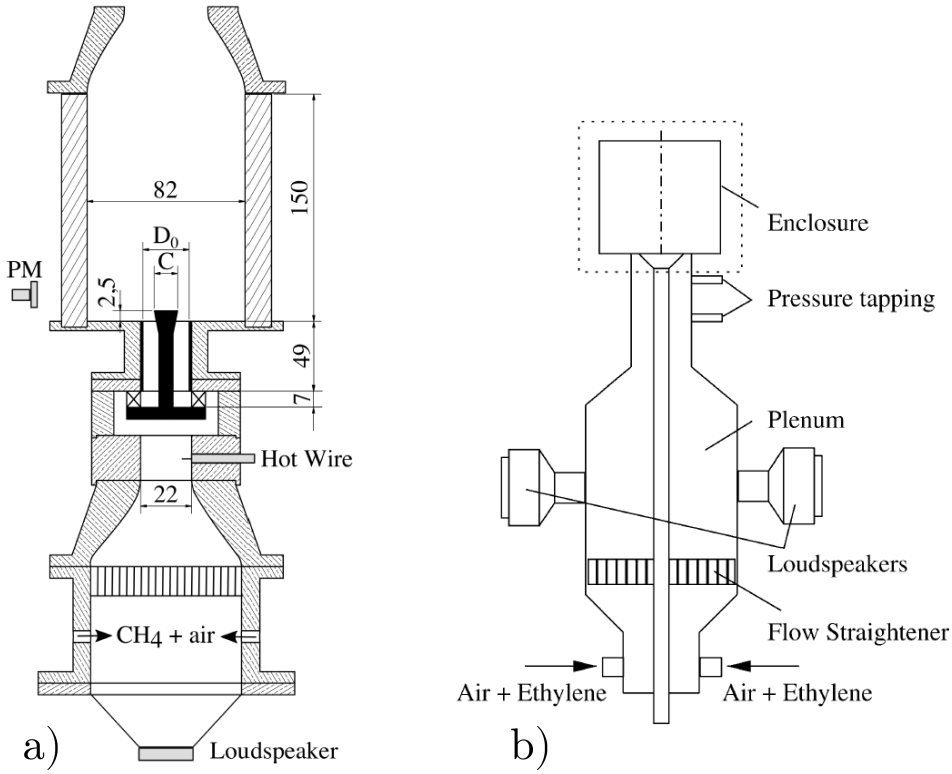

Figure 1.9: Experimental facilities to measure FTFs and FDFs in single flames stabilised using swirlers and bluff bodies. a) is adapted from Gatti et al. [2017] who used a hot wire to measure $\hat{u}$. b) is adapted from Balachandran et al. [2005] who combined measurements from multiple microphones to obtain $\hat{u}$. Both measured the global HRR fluctuations $\hat{Q}$, using PMTs.

metry, e.g. as in [Gatti et al., 2017, 2018; Komarek and Polifke, 2010; Palies et al., 2010]). Alternatively one can deploy the multiple microphone method and reconstruct the acoustic mode and thereby the velocity fluctuation at the point of interest [Balachandran et al., 2005; Kim et al., 2010; Nygård, 2021]. The former measures the absolute component of the combined acoustic and convective velocities and the latter only the acoustic part.

The principal feature of FTFs is their low-pass filter behaviour, where the gain drops exponentially towards higher frequencies. In Fig. 1.10 this drop is caused by cancellation/interference of HRR when the wavelength of convective structures propagating along the flame front become sufficiently short. A gain cut-off frequency ω_c, is often determined by the compactness of the flame, which has been

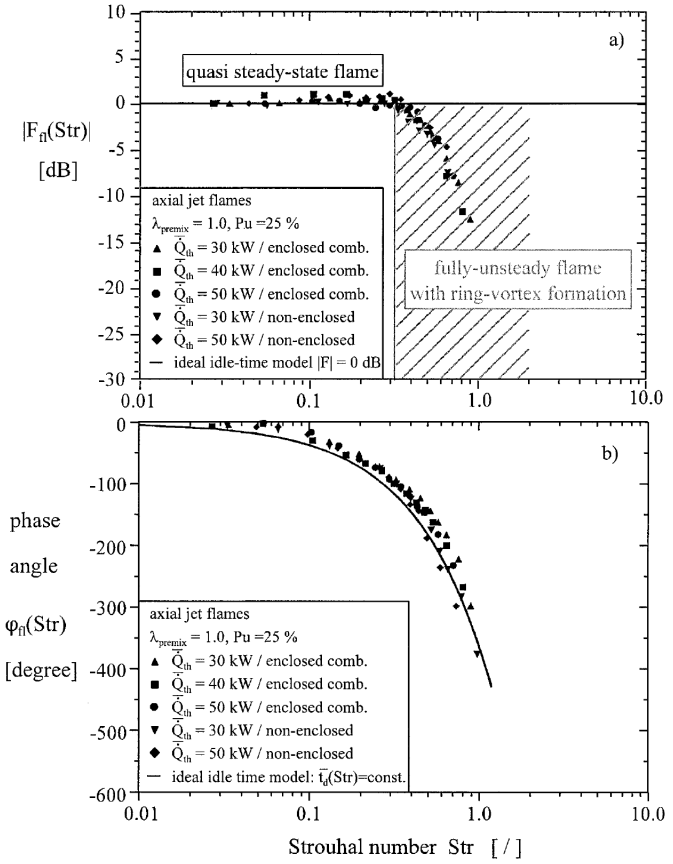

Figure 1.10: Measurements of the FTF for premixed axial jet flames adapted from Külsheimer and Büchner [2002]. a) shows the gain and b) shows the phase displaying a low-pass filter behaviour.

approximated by

$$\omega_c \propto \frac{H}{\bar{u}}, \tag{1.15}$$

where H is the flame length and $\bar{u}$ is the velocity at the flame base [Alemela et al., 2010; Fanaca et al., 2010; Kim and Santavicca, 2013a]. Usually, this ratio also provides the average slope of the phase, which is indicative of a constant convective time-delay.

A second main feature of the FTF is that the gain tends to one for in the limit of zero forcing frequency. Polifke and Lawn [2007] showed that in this limit, the gain unity occurs because the flow and flame becomes quasi steady, and can be mathematically expressed by $G = 1$ and $\Theta = 0$ for $f = 0$.

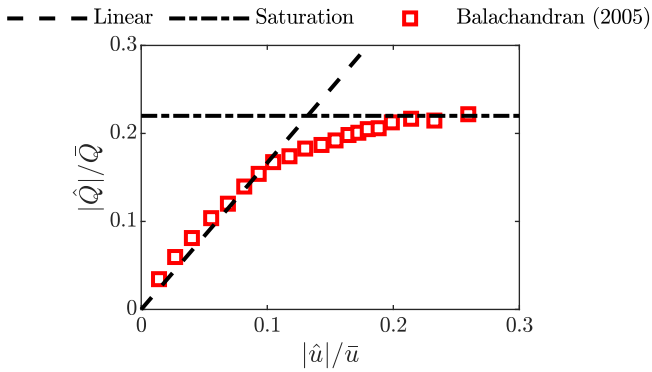

Figure 1.11: Typical non-linear flame response adapted from Balachandran et al. [2005]. For sufficiently low forcing levels, in this case $|\hat{u}|/\bar{u} < 0.1$, the relationship is linear and hence, well described by the FTF. For $|\hat{u}|/\bar{u} > 0.1$ the FDF is needed to predict the behaviour.

The FTF is implemented into low order models which are then used to predict the frequency and growth rate of modes, through a linear stability analysis. However, the FTF is only valid at sufficiently small amplitudes and can only be used to provide the initial growth rate. It is hence not sufficient to compute the amplitude of the limit cycle oscillations.

At low amplitude the relationship between $\hat{Q}$ and $\hat{u}$ is approximately linear but at larger amplitudes, the flame response tends to saturate. An example of the nonlinear response of the flame is shown in Fig. 1.11 [Balachandran et al., 2005]. In this case, $\hat{Q}/\bar{Q}$ increases linearly for $|\hat{u}/\bar{u}| < 0.1$, and for $|\hat{u}/\bar{u}| > 0.1$, the response of the flame saturates. The point where the response becomes nonlinear depends on the forcing frequency and varies with operating conditions, i.e. varies with flow conditions and flame shapes. Therefore, to predict limit cycle oscillations, the nonlinear response of the flame needs to be characterised for a range of frequencies which is not easily modeled. This is done through the flame describing function (FDF) [Noiray et al., 2008]

$$\mathrm{FDF}(\omega, |\hat{u}|/\bar{u}) = \frac{\hat{Q}/\bar{Q}}{\hat{u}/\bar{u}}, \tag{1.16}$$

which corresponds to sets of FTFs taken at different forcing amplitudes.

1.2.3 Acoustic-convective interference

A number of studies have reported various departures from the low-pass behaviour in the form of modulations in the gain and phase [Acharya and Lieuwen, 2014; Bunce et al., 2013; Di Sabatino et al., 2018; Gatti et al., 2018; Hirsch et al., 2005;

Kim and Santavicca, 2013b; Komarek and Polifke, 2010; Nygård et al., 2019; Palies et al., 2010]. These can cause significant changes to the gain and phase of the FTF, which alter the thermoacoustic behaviour of the flame, and can potentially drive TIs. Therefore, a deeper understating of the appearance and origin to potentially enable scaling and control is of great interest.

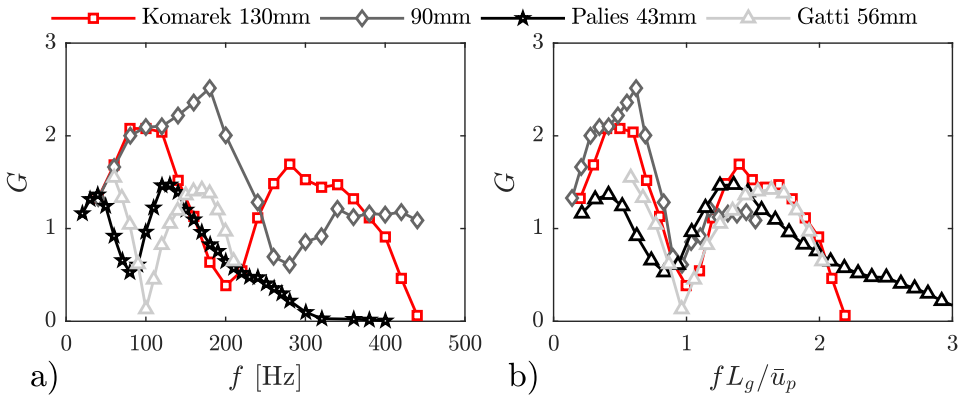

Figure 1.12: a) Gain modulations observed in the FTF due to the interaction between a swirler and the acoustic forcing. A series of maxima and minima appear below the cut-off frequency of the flame. These occur at different frequencies depending on the geometry, flow, and flame conditions. b) The FTFs plotted vs a non dimensional frequency where the locations of the dips and peaks align. The measurements are adopted from Komarek and Polifke [2010], Palies et al. [2010], and Gatti et al. [2017].

Three examples where significant modulations were caused by the interaction between a swirler and a bluff body, are shown in Fig. 1.12 a). For these flames, the effect resulted in changes in the gain by an order of magnitude. By changing the axial location of a swirler, Komarek and Polifke [2010] observed that the gain exhibited modulations where the minima and maxima changed to different frequencies and it was proposed that these may originate from fluctuations in the swirl number. In Fig. 1.12 a) the maximum and minimums shift from 100 Hz to 150 Hz and 200 Hz to 270 Hz respectively. In a separate but contemporaneous study, Palies et al. [2010] also observed modulations. The swirl number fluctuations were caused by a mode conversion process occurring when the acoustic wave impinged on the swirler, upstream of the flame, leading to modifications of the dynamics at the base and tip of the flame [Palies et al., 2011a,b].

Further insight into the origin of the modulations was recently presented in a set of papers by [Gatti, 2019; Gatti et al., 2017, 2018, 2019]. This demonstrated that specific changes to the burner geometry could generate a large dip in the gain which coincided with the suppression of vortical structures measured by PIV at

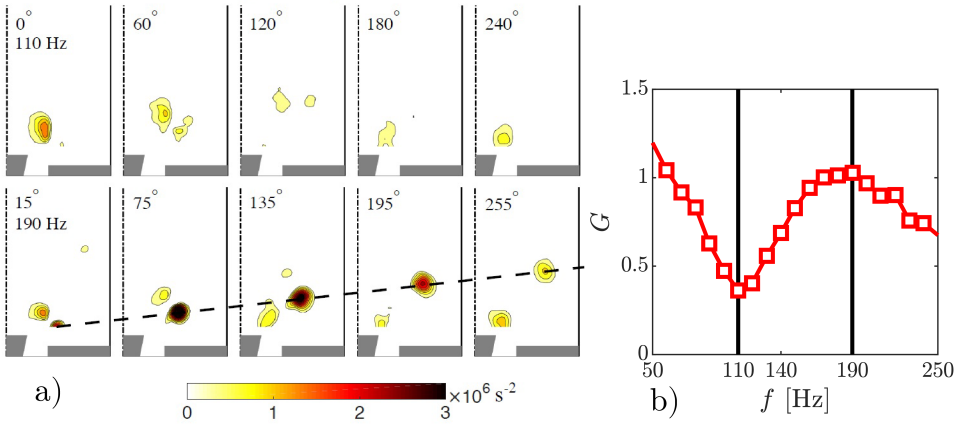

Figure 1.13: a) Suppression of the vortical structures measured in the cold flow at a frequency corresponding to a minimum in the FTF gain, viewed in b) (adapted from Gatti et al. [2018]).

frequencies where the dip occurred. The flow field and FTF, adopted from Gatti et al. [2018], are shown in Fig. 1.13. The top and bottom sets of images in a) show the phase averaged evolution of the vorticity at the frequencies indicated by the black lines in b). At $f = 110\,\text{Hz}$, the vortical structures are significantly weaker than at $f = 190\,\text{Hz}$, showing that the modulations may be driven by disturbances produced by the upstream cold flow. Gatti [2019] also suggested that both a swirler and a center rod were necessary for this interaction to take place.

A convective time delay between the swirler and the dump plane can be written as Kim and Santavicca [2013b]

$$\tau \approx L_g/\bar{u}_p, \tag{1.17}$$

where L_g is the distance between the swirler (or the cylinders) and the dump plane, and $\bar{u}_p$ is the average bulk velocity over this length. The time delay was extracted from Komarek and Polifke [2010], Palies et al. [2010], and Gatti et al. [2017], and in Fig. 1.12 b), the FTFs are plotted against a frequency normalised by $L_g/\bar{u}_p$. The maximums and minimums roughly align when the frequency is normalised by this time delay, showing that the swirler is a very likely source of the modulations.

In the present study, we further investigate modulations in gain and phase of the FTF. These features appeared as a result of hydrogen enrichment and were observed to be stronger for the pure hydrogen flames, which had a tendency to stabilise on the bluff body.

1.2.4 Time-delay models

In terms of application for GTs, it is usually sufficient to know the linear stability of a system in an effort to prevent self sustained oscillations from occurring. A common approach is to use a linear model where the FTF is implemented.

To model the time-lag nature of the FTF, it is common to use time delay models [Komarek and Polifke, 2010; Nygård and Worth, 2021; Polifke, 2014; Sattelmayer and Polifke, 2003; Schuermans et al., 2004]. Time-delay models are based on the assumption that the flame can be described as a linear time invariant (LTI) system [Polifke, 2020] . Then the acoustic flame response can be written as a convolution sum of the form

$$\frac{Q'(t)}{\bar{Q}} = \frac{(h * u')(t)}{\bar{u}}. \tag{1.18}$$

Here, h is the Impulse Response Function (IRF) which represents a distribution of delayed responses. In the frequency domain, h corresponds to the FTF

$$\frac{\hat{Q}(\omega)}{\bar{Q}} = \mathrm{FTF}(\omega)\frac{\hat{u}(\omega)}{\bar{u}}. \tag{1.19}$$

The simplest time lag model used to relate the the flame response to velocity fluctuations is the $n-\tau$ model

$$\frac{Q'(t)}{\bar{Q}} = n\frac{u'(t-\tau)}{\bar{u}}, \quad \mathrm{STL}(\omega) = n\exp\left(-j\omega\tau\right), \tag{1.20}$$

originally proposed by Crocco [1951]. Here, n is the interaction index and τ is the time-delay. This formulation with a single time-delay is only valid in the low frequency range, where the flame can be considered as compact with respect to the acoustic and convective wavelengths. The IRF h of the $n-\tau$ model is a Dirac delta function, shown in Fig. 1.14 a), and the corresponding FTF has unity gain at all frequencies.

As shown previously, flames behave as low-pass filters where the gain reduces at sufficiently large frequencies [Schuller et al., 2020]. To capture the cut-off frequency behaviour, it is not sufficient to use the STL formulation since it provides unity gain for all frequencies. Sattelmayer and Polifke [2003] proposed to use a distributed time lag (DTL) instead of STL to capture dispersion. Polifke et al. [2001] suggested to use a Gaussian probability density function (PDF) with standard deviation σ as to represent h

$$h(t) = \frac{1}{\sigma\sqrt{2\pi}}\exp\left(-\frac{(t-\tau)^2}{2\sigma^2}\right), \quad \mathrm{DTL}(\omega) = \exp\left(-\frac{1}{2}(\omega\sigma)^2 - j\tau\omega\right). \tag{1.21}$$

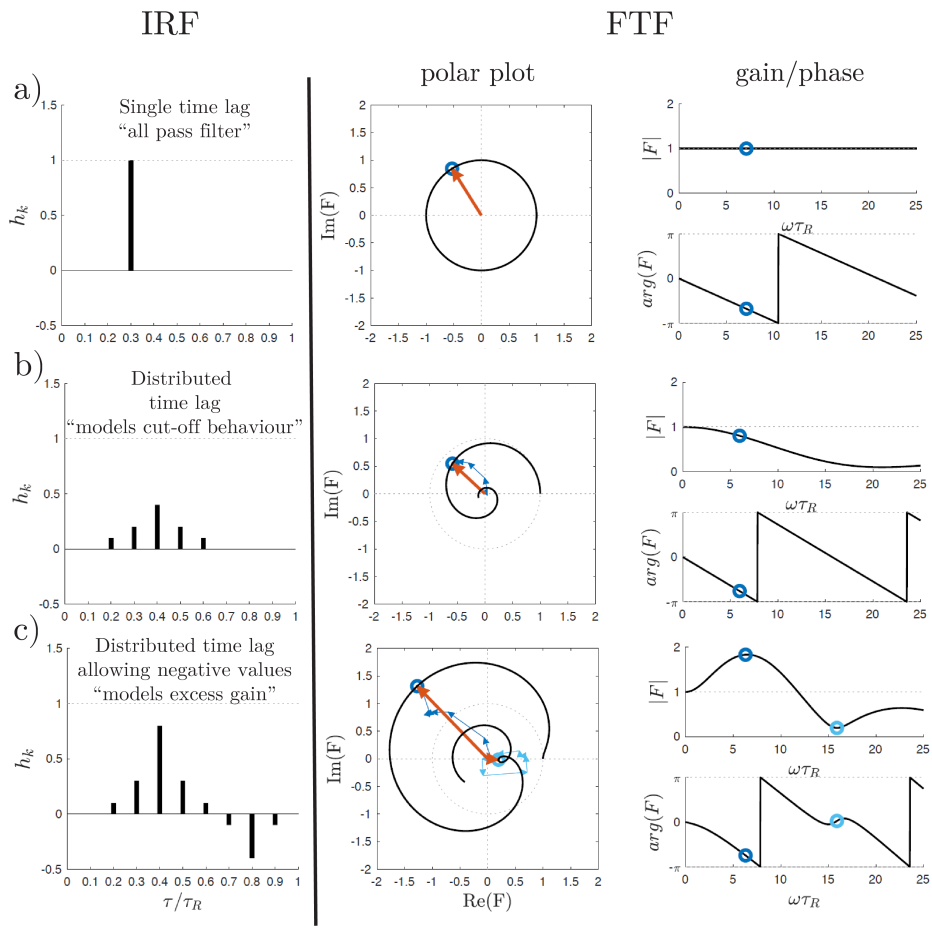

Figure 1.14: STL and DTL forumations adopted from Polifke [2020]. From left column: IRF, polar plot of the FTF, and the gain and phase of the FTF.

The corresponding IRF and FTF are shown in Fig. 1.14 b) and now the FTF gain drops exponentially at higher frequencies. However, as was discussed by Huber and Polifke [2009] and Blumenthal et al. [2013], the Gaussian PDF is not able to capture the excess gain, i.e., gain above unity ($G > 1$) at nonzero frequency ($f > 0$). This is a feature that has been observed in FTFs for a variety of flame shapes [Durox et al., 2009]. To represent excess gain, the IRF needs to contain negative values [Blumenthal et al., 2013]. Komarek and Polifke [2010] resolved this by superimposing several distributions of Eq. 1.21 with opposite signs. The corresponding IRF and FTF are shown in Fig. 1.14 c), where the negative values of h allow for $G > 1$.

If the mean time-delay of the distributions differ, the interaction can generate modulations in the gain and phase. This approach was used by Schuermans et al. [2004] do describe the effect of equivalence ratio fluctuations. Similarly, Komarek and Polifke [2010] used this method to describe the interaction between the swirler and flame, giving rise to gain and phase modulations as described in the previous section. By fitting experimental FTF data to DTL models, physical length and time scales can be extracted from the measurements. This is an approach adopted in the present work.

1.2.5 The effect of flame-flame interaction

While FTFs are quite well understood for isolated axisymmetric flames, industrial GT combustors are usually equipped with multiple injectors that are arranged around an annulus [Kunze et al., 2004; Staffelbach et al., 2009; Worth and Dawson, 2013a,b], or in multiple injectors in several cans [Lee et al., 2018, 2019; Samarasinghe et al., 2015; Szedlmayer et al., 2011], which are then arranged around the annulus. These are called annular and can-annular combustors respectivly and the acoustic flame response of such multi-flame systems has until recently received less attention. Fanaca et al. [2010] showed that the flame response measured in the annular setup and its single flame equivalent, can differ significantly. Even less attention has been given to the effect of hydrogen enrichment in such systems, which was one of the motives in the present work.

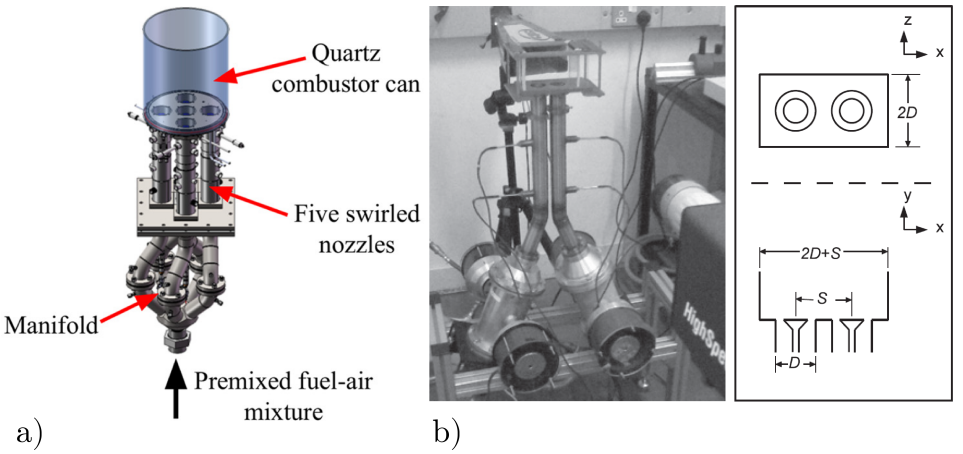

Figure 1.15: Two examples of experimental rigs used to study the effect of interaction between adjacent flames. a) is adopted from Samarasinghe et al. [2015] and b) is adopted from Worth and Dawson [2012a].

Szedlmayer et al. [2011] investigated a single can type combustor equipped with five injectors, the same configuration as shown in Fig.1.15 a). The response was

compared to a single injector, and the responses were found to be similar at moderate frequencies but differed at low and high frequencies. In a similar rig, Lee et al. [2018] investigated the effect of placing swirlers at different positions in two interacting flames. It was found that the swirler positions had a strong influence on the stability of the combustion system. A similar effect was observed when injecting mixtures with different equivalence ratios, into each of the two injectors [Kim et al., 2018]. In the same setup, Lee et al. [2019] investigated two interacting flames where the swirl direction of each injector was varied. It was shown that the FTF and the FDF differed strongly, depending on swirler orientation. The results summarised in this paragraph imply that the use of single flame data is not sufficient to predict the dynamics of the multi flame system.

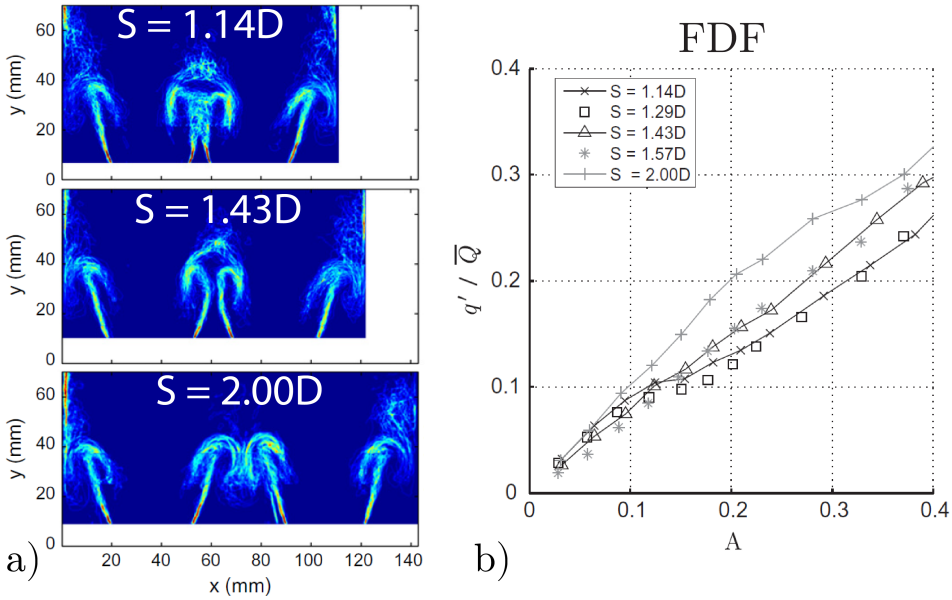

Figure 1.16: Effect of flame-flame interaction on the FDF of methane flames. In a) the phase averaged flame surface density (FSD) is shown for different separation distances S and hence, different level of flame-flame interaction. The effect on the FDF taken at $f = 160\,\text{Hz}$ is shown in b). Images were adopted from Worth and Dawson [2012a].

Studies by Worth and Dawson [2012a,b, 2019] focused on the flame dynamics in two interacting flames stabilised in the wake of bluff bodies. The setup is shown in Fig. 1.15 b), and the facility had two flames which could be moved closer or further apart and hence, change the level of flame-flame interaction. The flames were subjected to self-excited and forced acoustic oscillations and it was found that the frequency and stability of the system were dependent on the flame separation. These changes were attributed to the vortex dynamics occurring in the central

interacting region between adjacent flames, that lead to changes in the phase of the HRR and thereby the stability. Figure 1.16 a) shows the phase averaged flame surface density (FSD) taken at different separation distances S. There is a significantly higher level of flame-flame interaction in the center region for $S = 1.14D$ compared to $S = 2.00D$. This is reflected in the nonlinear response shown in b), where the FDF was shown to depend on the level of interaction.

1.2.6 Combined transverse and longitudinal oscillations

Until now, the flame response has only been discussed in the context of longitudinal forcing. That is when the acoustic waves propagate in the same direction as the flow and flame. However, in many practical systems, such as annular combustion chambers [Poinsot, 2017], the length of the circumference is in the same order of magnitude, or even longer than the longitudinal length. In such systems, the dominant acoustic mode can also propagate in the transverse direction relative to the direction of flame propagation [Bourgouin et al., 2013; Dawson and Worth, 2014, 2015; Hauser et al., 2011; Kopitz et al., 2005; O'Connor et al., 2015; Saurabh and Paschereit, 2017; Staffelbach et al., 2009; Worth and Dawson, 2013a].

Three examples of facilities capable of producing transverse forcing are shown in Fig. 1.17. In a), the annular combustor used in a series of studies [Dawson and Worth, 2014, 2015; Indlekofer et al., 2021; Mazur et al., 2019; Nygård et al., 2019; Worth and Dawson, 2013a, 2017] is displayed. Worth et al. [2017] and Nygård et al. [2019] developed a forcing method where the mode could be tuned by sets of speakers, enabling detailed studies of the flame dynamics, when submitted to spinning, standing, or mixed modes. It was shown that when submitted to spinning modes, the flame response strongly depended on the direction of the acoustic wave, relative to the swirl direction.

The facilities shown in Fig. 1.17 b) and c), adopted from O'Connor et al. [2013] and Hauser et al. [2011], correspond to unwrapped annular combustors, where the acoustic waves are confined by walls in the transverse direction. Hence, the studies were restricted to produce standing transverse wave oscillations. Similarly, Dawson and Worth [2014] investigated the flame dynamics when the flames were placed at various positions relative to the acoustic standing wave. The data was obtained during self excited TIs, where the mode type switched spontaneously between spinning and standing modes. By conditional averaging, the phase averaged flame surface density (FSD) was reconstructed at different locations, which is displayed in Fig. 1.18 a). At the pressure node, the flame features anti-symmetric dynamics (transverse flame motion), whereas at the velocity node, axisymmetric dynamics (longitudinal flame motion) are observed. In an attempt to obtain controlled forcing and a detailed view of the flow field, Worth et al. [2020] investigated

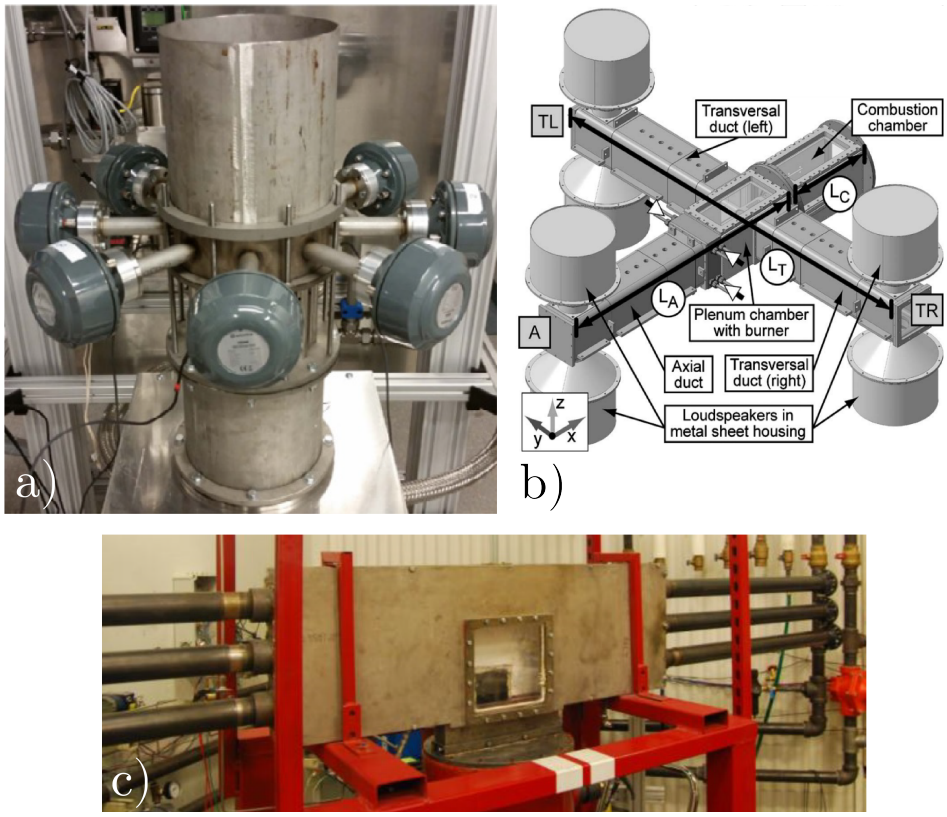

Figure 1.17: Experimental facilities designed to provide transverse forcing of flames. a) Forcing setup of the annular combustor used in a series of studies from Nygård et al. [2019]. Transverse forcing setups adopted from b) Hauser et al. [2011] and c) O'Connor et al. [2013].

a simplified case by considering the effect of transverse forcing on a turbulent jet. The setup, shown in Fig. 1.18 b), produced a simplified base flow compared to the more complex situation observed in the annular geometry [Dawson and Worth, 2014; Worth and Dawson, 2013a]. The jet discharged into a cavity forced at the transverse resonant mode, similar to the facilities displayed in Fig. 1.17 b) and c). In the near field of the jet, Worth et al. [2020] showed that pure transverse forcing corresponding to the pressure node, induced transverse motions of the jet core, leading to asymmetric vortex formation in the near field. A snapshot of the phase averaged vorticity is shown in Fig. 1.18 a), and the dynamics were similar to what was observed at the pressure node in a) [Dawson and Worth, 2014].

For the control of jets there exists an extensive amount of literature (e.g. Batchelor and Gill [1962]; Becker and Massaro [1968]; Brown and Roshko [1974]; Crow

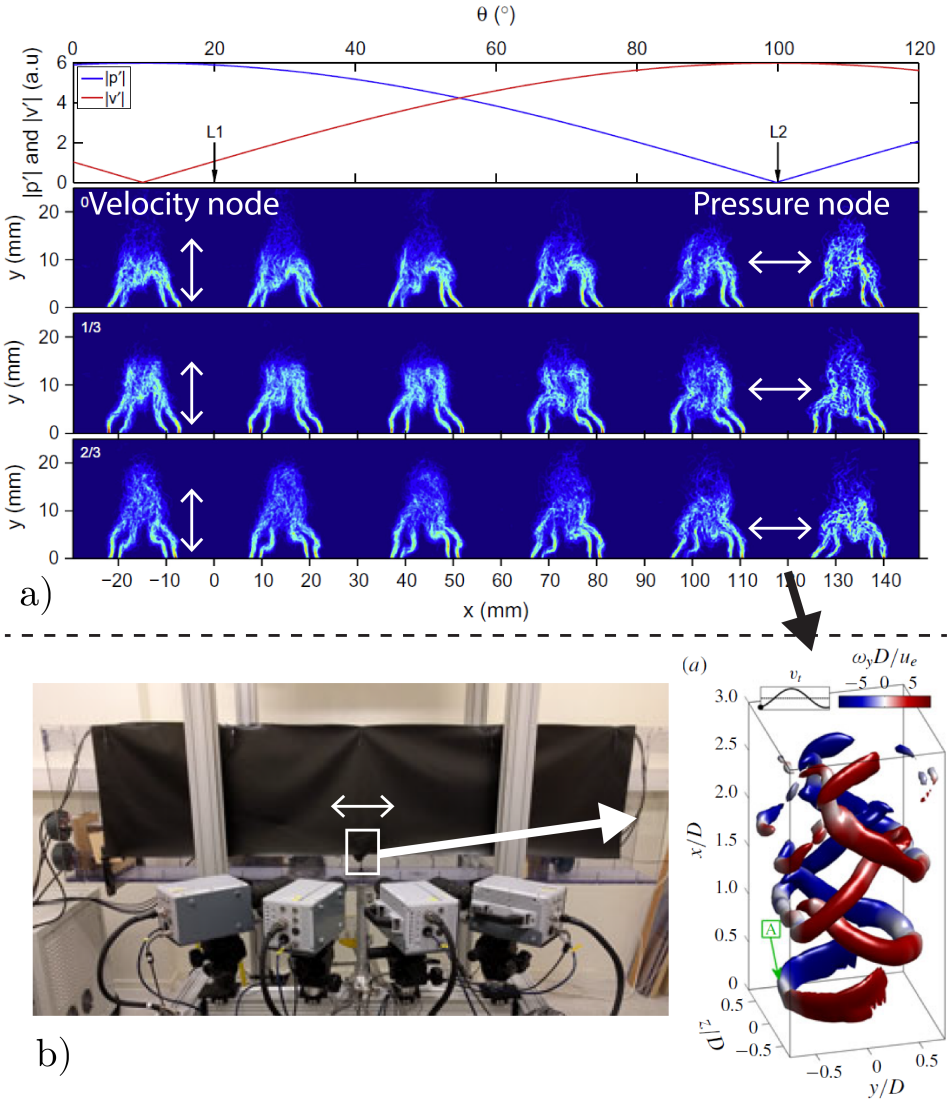

Figure 1.18: a) Flame dynamics measured at various positions in a self-excited standing wave observed in an annular combustor. (adapted from [Dawson and Worth, 2014])) b) Tomographic reconstruction of the vorticity in the near field of a turbulent jet placed at the acoustic pressure node, adapted from [Worth et al., 2020]. The transverse forcing resulted in tilted vortex rings alternating from left to right in the same plane as the acoustic wave.

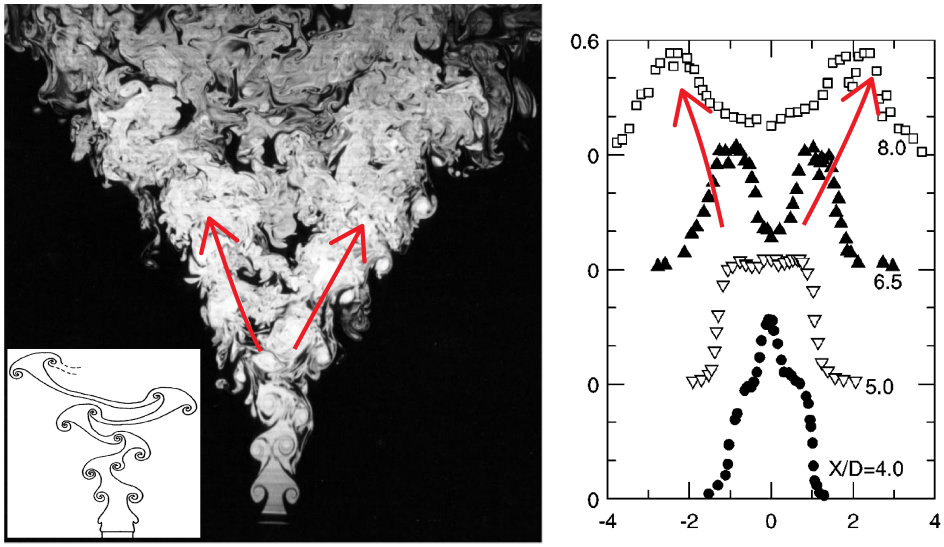

Figure 1.19: Flow visualisation of the water jet explored by Lee and Reynolds [1985]. The nozzle was rotated in an orbital motion around the jet center line simultaneously as the flow was forced longitudinally. With a frequency ratio of two, the jet splits into two individual momentum streams. The right plots shows the stream wise velocity profiles taken at various stream wise locations, showing how the jet splits into a binomial velocity distribution towards the far, indicative of a 'bifurcated' jet. The images were adapted from Reynolds et al. [2003].

and Champagne [1971]; Hussein et al. [1994]; Winant and Browand [1974] among others). However, there are not many examples of studies where jets are placed in a combined transverse and longitudinal acoustic field which is the relevant configurations for annular combustors. Some studies have focused on the combined excitation of jet modes, through active forcing or a combination of active and passive forcing (Hussain and Husain [1989]; Kusek et al. [1990]; Lee and Reynolds [1985]; Longmire and Duong [1996]; Longmire et al. [1992]; Parekh et al. [1987]; Reynolds et al. [2003]; Suzuki et al. [2004]). For specific forcing conditions, this leads to the phenomena of 'bifurcating' and 'blooming' jets that split into multiple momentum streams that can drastically increase the spreading rate Reynolds et al. [2003]. In Fig. 1.19, a flow visualisation is shown for the forced jet experiments by Lee and Reynolds [1985], where the nozzle was rotated in an orbital motion around the jet axis at a frequency twice the longitudinal forcing frequency. At this frequency ratio, the formation of structures in the near field, lead to a symmetric 'bifurcation' of the jet, which split into two individual momentum streams. The velocity profiles taken at different stream wise positions are shown in the right figure.

However, the complex jet response reported in the literature, typically requires combined forcing with different frequencies to excite multiple modes of the jet. In this thesis we investigated the effect of different levels of combined forcing when the frequency is monochromatic. As mentioned above, this flow configuration is directly relevant to the practical problem of self-excited TIs in annular combustor geometries typical of jet engines and gas turbines for power generation. We used the same facility as Worth et al. [2020], where the location of the jet relative to the pressure and velocity nodes, were varied along with the forcing frequency and amplitude.

1.3 Objectives

The main objective of this research is to contribute to a better understanding of the role hydrogen enrichment has on the thermoacoustic response of flames operated in the lean premixed regime. Although many aspects of flame dynamics, contributing to the onset of TIs, have been investigated, the role of hydrogen enrichment has received comparatively little attention. Hence, a series of experimental investigations was performed on lab scale-burners where the forced and unforced flame responses were measured for a wide variety of fuel compositions ranging from pure methane to pure hydrogen.

The work can be divided into three main research topics and the main objectives for each of these are listed below:

1. Investigate the effect of **hydrogen enrichment** on the thermoacoustic response of lean premixed flames using forced and self-excited flames. The effect of hydrogen enrichment on the level of flame-flame interaction and the thermoacoustic response of the flames is also investigated.

2. Build on the studies [Gatti, 2019; Gatti et al., 2017, 2018, 2019; Komarek and Polifke, 2010; Palies et al., 2010] and investigate the phenomena of **acoustic/convective interference** giving rise to gain and phase modulations in the FTF. Investigate the mechanisms behind how these modulations appear in non-swirling flames, and if the behaviour can be predicted such that the phenomena can be utilising to tailor/control the FTF.

3. Extend the work by Worth et al. [2020] and measure the response to simultaneous **transverse and longitudinal** acoustic fluctuations by placing a turbulent jet at various locations in a standing wave. Investigate if there is a simple relationship between the family of responses observed at intermediate positions, and the pure longitudinal and transverse forcing, observed at the pressure and velocity nodes

Chapter 2

Experimental facilities and diagnostics

2.1 Experimental set-up

All experiments were performed using different variations of a single flame test rig which is described in this section. The rig is a scaled down and modified version of the set-up used by [Ayoola et al., 2006; Balachandran et al., 2005] and is similar to the burners used in [Dawson and Worth, 2014; Nygård, 2021; Nygård et al., 2019; Worth and Dawson, 2013a]. In the present work the rig was modified and adapted to investigate the effect of hydrogen enrichment and acoustic-convective interference on single and interacting flames. More details on each set of experimental parameters can be found later in the thesis.

Plenum section

The set-up is shown in Fig. 2.1. Premixed fuel air mixture enters the plenum through two impinging jets. The bottom part of the plenum has a diameter of 32 mm and the flow then expands to another cylindrical section with a diameter of 94 mm, where it passes through a set of honeycombs for flow conditioning, before the flow is contracted to a diameter of 35 mm. Along the plenum wall, which has a length of 221 mm, two 60 mm long stand off tubes are attached, where speakers can be mounted to apply acoustic forcing.

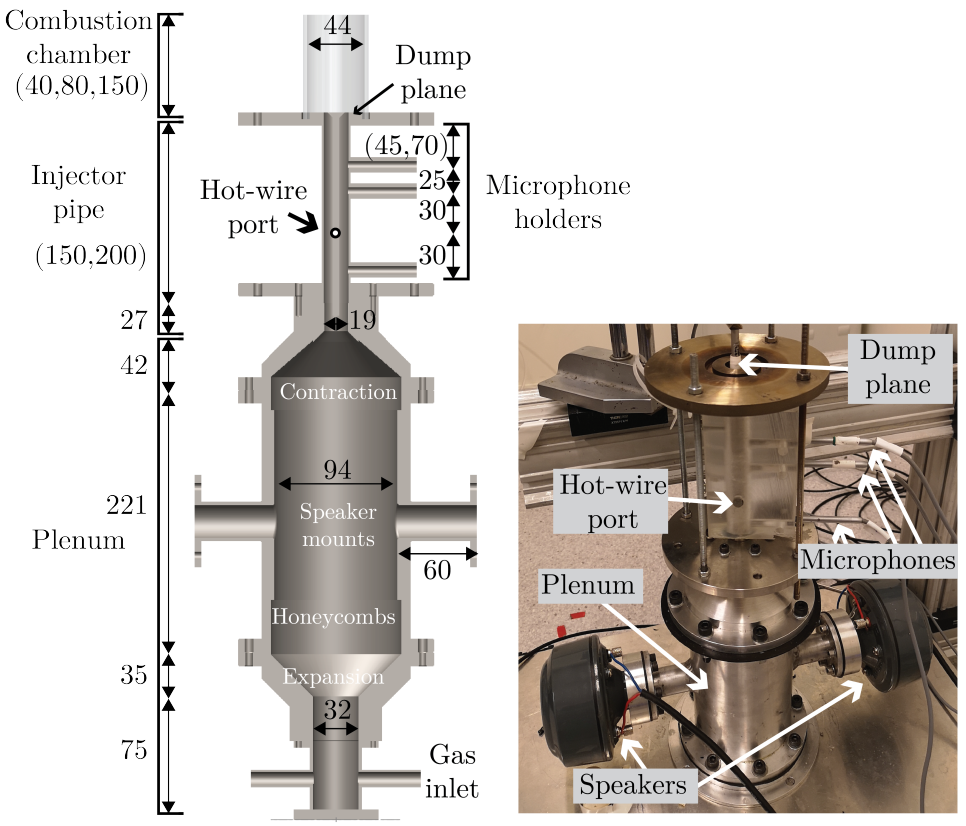

Figure 2.1: Schematic of the experimental set-up equipped with a single injector and a circular combustion chamber. The plenum section was also adapted to fit three injectors with variable spacing, and a turbulent jet which was placed in a cavity to provide transverse forcing.

2.1.1 Injector geometries

When operated with a single injector pipe, as shown in Fig. 2.1, the flow is further contracted into a tube with a diameter of 19 mm. The pipe holds a central rod with a diameter of 5 mm used to stabilise the flame. At the tube exit, defined as the burner dump plane, the flow expands, either into the room, or into a cylindrical combustion chamber. At the burner dump plane, the center diameter of the center rod was also increased linearly to a diameter of 13 mm. Detailed views are shown in Fig. 2.2, where in a), the flow accelerates before entering the chamber, due to the area change imposed by the bluff body with an inclination angle of 45°, and b) the rod diameter is held constant.

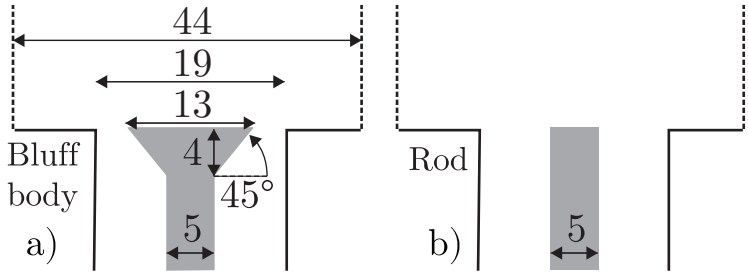

Figure 2.2: Bluff body geometries used to stabilise the flame at the burner dump plane. a) shows the 13 mm bluff body with an inclination angle of 45°, and b) shows the rod which was just extended to the dump plane. The numbers are given in mm.

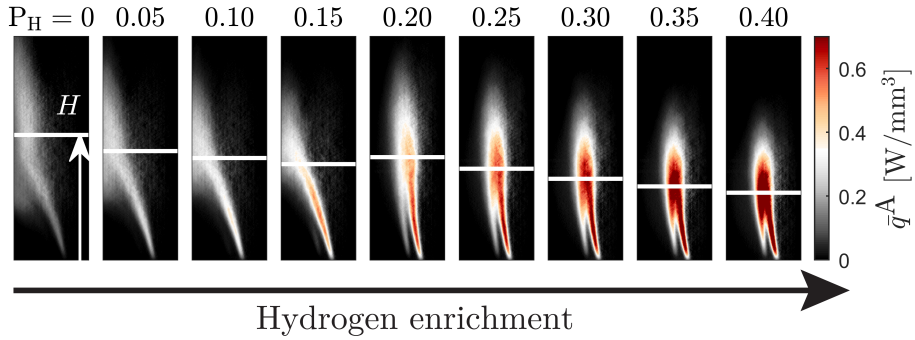

Figure 2.3: Planar distribution of HRR obtained by Abel deconvolution of the mean flame images for a range of hydrogen power fractions P_H. Increasing the hydrogen content while keeping the thermal power and equivalence ratio fixed, leads to more compact flames with a tendency to stabilise on the bluff body as an M shaped flame. $P = 7\,kW$ and $\Phi = 0.7$ and only the left half of the flame is shown.

The setup was operated with and without a combustion chamber. When operated with a combustion chamber, cylindrical quartz tubes were used giving optical access for flame measurements. Quartz tubes with a diameter of 44 mm were the most frequently used, but sizes of 90 mm and 120 mm were also used. The length was varied to stabilise or destabilise the combustor, by modifying the acoustic resonances of the set-up.

Inside the injector pipe, three microphones were mounted flush to the wall to measure the acoustic pressure fluctuations. Two pipe lengths of 150 mm and 200 mm were used, where the distance to the first microphone was 45 mm and 70 mm, respectively. The acoustic field was then estimated using the multiple microphone method described in detail in chapter 3. Additionally, the 200 mm injector pipe

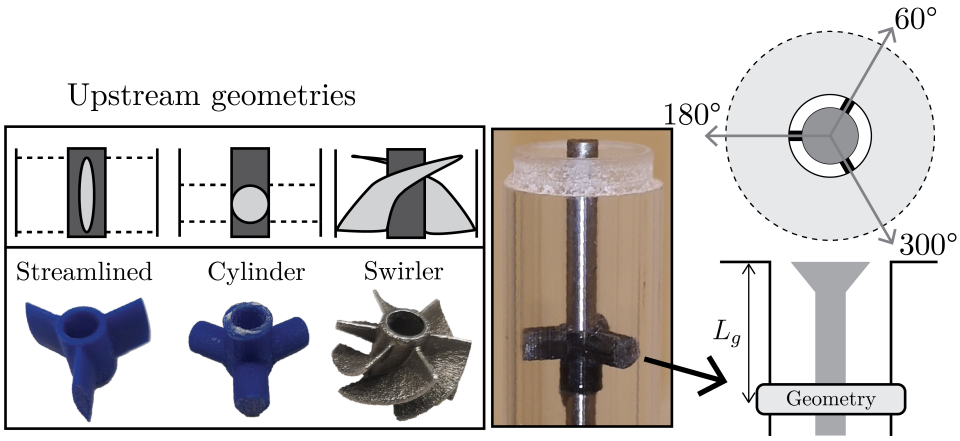

Figure 2.4: Geometrical shapes designed to generate acoustic/convective interference. From left to right, these include 10 mm long and 2.5 mm wide streamlined bodies with aspect ratio 4, circular cylinders with a diameter of 5 mm, and the six-vaned swirler with a chord length of 11 mm, used previously in [Nygård and Worth, 2021; Worth and Dawson, 2013b], and were placed at a distance L_g upstream of the bluff body.

.

was equipped with a port between the second and third microphone, as shown in Fig. 2.1. This port was used to fit a hot wire or a thermocouple to measure the flow velocity or gas temperature, respectively.

A major part of the work considered the effect of hydrogen enrichment on single flames, produced by the 13 mm bluff body displayed in Fig. 2.2 a). In Fig. 2.3 the planar distribution of HRR is shown, where the thermal power and equivalence ratio are kept fixed, while the hydrogen power fraction is increased. When more hydrogen is introduced into the fuel blend, the HRR becomes more concentrated and the flame becomes significantly more compact, with a preference for stabilising as an M shaped flame.

Upstream geometries

Originally, the centre rod was fixed by three grub screws of diameter 4 mm, placed at a distance $L_g = 45$ mm upstream of the dump plane. In articles 1 and 4, these were shown to shed vortices that lead to acoustic/convective interference having a significant influence on the FTF. To the best of our knowledge, these were the first measurements of gain and phase modulations, occurring in premixed flames without a swirler and showed that the phenomena is not necessarily a direct result of swirl. To further understand this effect, different geometrical shapes were 3D printed and placed at variable distances L_g upstream of the dump plane. These are

shown in Fig. 2.4, and include a set of 10 mm long and 2.5 mm wide streamlined bodies with aspect ratio 4, circular cylinders with a diameter of 5 mm, and the six-vaned swirler with a chord length of 11 mm, used previously in [Nygård and Worth, 2021; Worth and Dawson, 2013b]. The streamlined bodies and cylinders were placed 120° apart, as shown in the overhead schematic of Fig. 2.4. In article 5, the influence of these geometries on the FTF were investigated through a parametric study, where their distance L_g and the flow velocity were varied systematically.

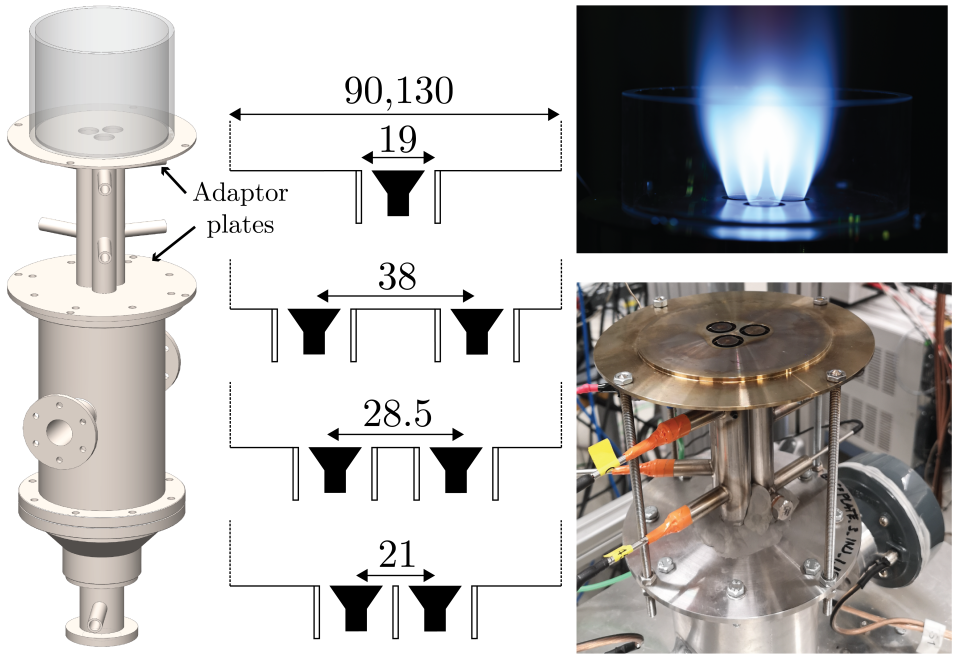

Figure 2.5: Modifications of the single burner rig shown in Fig. 2.1 to enable the study of hydrogen enrichment and flame flame interaction between multiple flames. Four plates were manufactured with different distances, 21 mm, 28.5 mm, and 38 mm, between adjacent injectors. in addition to a single injector plate for reference. The right images show three interacting flames produced by the injector pipes placed closely together.

2.1.2 Multiple injectors

To extend the study of single flames and investigate the effect of flame-flame interaction on the thermoacoustic response, the top section of the plenum was replaced by a set of plates that could fit three injectors. These were placed in a triangular pattern, shown in Fig. 2.5, with equal separation between the adjecent flames. To vary the distance, four plates were manufactured with spacing 21 mm, 28.5 mm, and 38 mm, and a plate with a single injector. These correspond to the same separa-

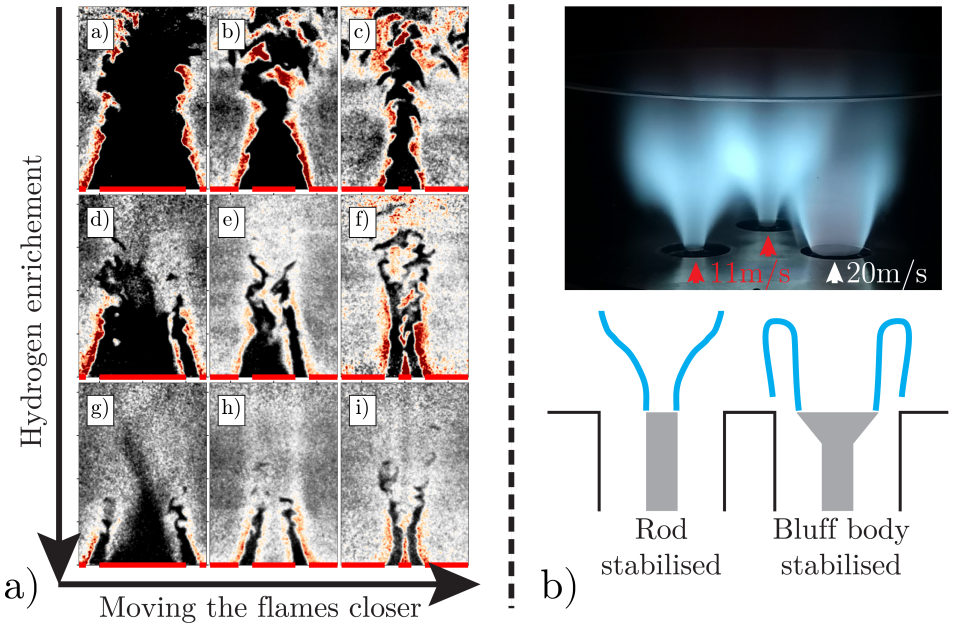

Figure 2.6: a) Snapshots of OH-PLIF images taken at different power fractions and separation distances for the interacting flames. By varying both these, the effect of hydrogen enrichment and flame-flame interaction on the FTF could be investigated in detail. b) Asymmetric collection of flames where two are stabilised on rods and one on the bluff body. In this way, the effect of asymmetric staging could be studied.

tion distances as the ones studied by Worth and Dawson [2012a], when normalised with the pipe diameter.

To enclose the flame, the diameter of the quartz tube was increased to 90 mm and 120 mm. Similar to the single flame setup, the length of the chamber was varied to stabilise/destabilise the combustor, enabling the study of forced and self excited conditions. The images on the right of Fig. 2.5 show the combustor operated with the closest spacing between adjacent flames of 21 mm, leading to significant flame-flame interaction.

When using three injectors, two were equipped with a number of two microphones to estimate the mode inside each of the injectors separately. The third injector were equipped with three, similar to the previous set up shown in Fig. 2.1.

Hydrogen enrichment and flame-flame interaction

Reducing the hydrogen content and moving the adjacent flames closer together both lead to a larger extent of flame-flame interaction. To decouple the effect

caused by hydrogen enrichment from simply moving the flames closer, both were varied systematically. In Fig. 2.6 a), snapshots of the flame fronts, obtained in the interaction zone between two adjacent injectors, are shown. By moving the injectors and changing the fuel composition, the level of flame-flame interaction could be varied systematically, enabling the effect of hydrogen enrichment and flame separation to be decoupled.

Asymmetries

When equipped with multiple injectors, the effect of having a collection of differently shaped bluff bodies was also investigated. This was achieved by combining injectors equipped either the bluff body of diameter 13 mm, or the rod with diameter 5 mm. In Fig. 2.6 b) an image of the flames operated with two rods and one bluff body is shown. Due to the difference in the blockage ratio and wake sizes, the rod stabilised flames had a different flame shape, and the bulk velocity entering the combustion chamber, was significantly lower compared to the bluff body stabilised flame. Measurements of the FTF were taken for all combinations of rod and bluff body stabilised flames, which were then compared against the single flame measurements.

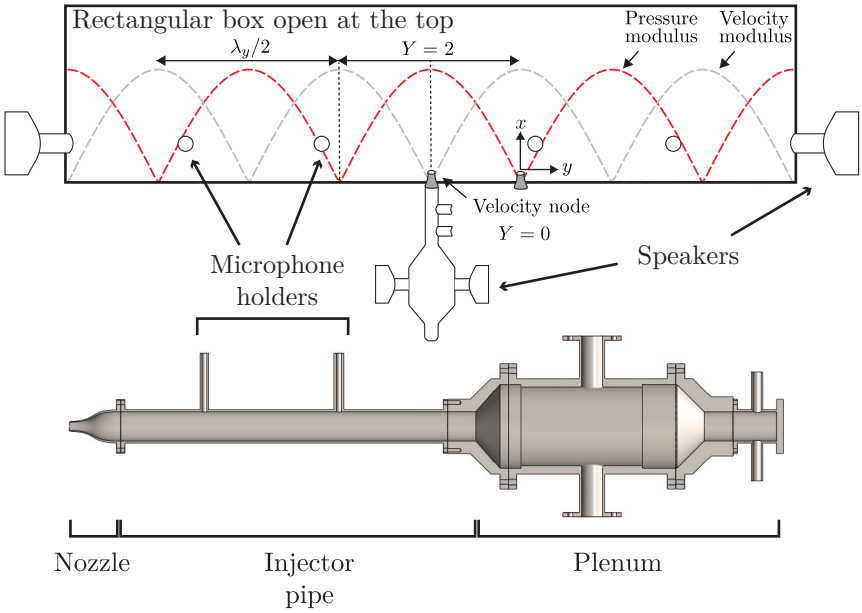

Figure 2.7: Experimental set-up capable of producing coupled longitudinal and transverse acoustic forcing by placing a turbulent jet in a resonant cavity forced at the transverse resonant modes. The plenum section was adapted to fit a longer pipe section with a converging nozzle at the end. The jet discharged into a rectangular cavity of size $[590, 1520, 220]$mm, which was forced at the transverse acoustic modes by speakers attached on the side walls. The set-up is the same as the one used by Worth et al. [2020], and here the effect of varying the nozzle position relative to the pressure and velocity nodes, indicated by Y, were investigated.

2.1.3 Transverse forcing

In combustion instabilities, the role of transverse velocity fluctuations are generally considered unimportant. However, they clearly give rise to flame dynamics Bourgouin et al. [2013]; Dawson and Worth [2014]; Hauser et al. [2011]; Nygård and Worth [2021]; O'Connor et al. [2013, 2015]; Saurabh and Paschereit [2017]; Staffelbach et al. [2009]; Worth and Dawson [2013a]. In an effort to understand the response on a more fundamental level, an axisymmetric jet was subjected to transverse forcing and its response measured at a number of locations between the pressure node and anti-node in a standing wave.

To study the effect of simultaneous transverse and longitudinal oscillations, the same setup as in Worth et al. [2020] was used and is shown in Fig. 2.7. Here, the plenum was adapted to fit a 400 mm long injector pipe of diameter 35 mm, equipped with a circular converging nozzle with an exit diameter of $D = 10$ mm.

The nozzle had a contraction ratio of 12.25 producing a top hat velocity profile at the nozzle exit. The jet flow discharged into a rectangular cavity with height, width and depth dimensions of $[590, 1520, 220]$mm, which was open to atmospheric conditions at the top.

Each side of the box was equipped with speakers used to produce an acoustic standing wave oriented transverse to the jet nodal line. The transverse length of 1520 mm was chosen so that $f = 476$ Hz and 696 Hz correspond to the second and third transverse modes of the box. The exit velocity were chosen so that $f = 476$ Hz matched the preferred mode of the jet occurring at $\mathrm{St} = fD/\bar{u} \approx 0.3$ [Crow and Champagne, 1971]. The side wall could be moved such that the position of the jet relative to the acoustic pressure and velocity nodes, could be varied.

Inside the injector pipe, two microphones were mounted flush to the pipe wall and used to characterise the longitudinal velocity fluctuations using the MMM. Similarly, four microphones were placed in the box along the transverse direction, to characterise the transverse acoustic wave. To tune the forcing level of the acoustic wave, the MMM was used.

2.2 Flow control and data acquisition

2.2.1 Flow control and low-speed acquisition

The gas flow rates entering the bottom of the plenum through the impinging jets, were controlled by Alicat MCR mass flow controllers. For reacting experiments, three MFCs were installed and a schematic of the lines is shown in Fig. 2.8. The gasses were provided from main supply lines and the pressure were regulated down to around 4 bar before they were connected to the MFCs. Downstream of the MFCs, solenoid valves were installed and both the MFCs and solenoids were controlled from a computer with a LabVIEW routine. In this way, the operating conditions could easily be varied without the need of re-ignition. This feature was useful, since it also reduced the time needed to reach thermal equilibrium, when changing the operating condition before acquiring data. For safety, a tank filled with nitrogen was installed which was used to purge the burner in case of emergency, e.g if the flame flashed back into the plenum section.

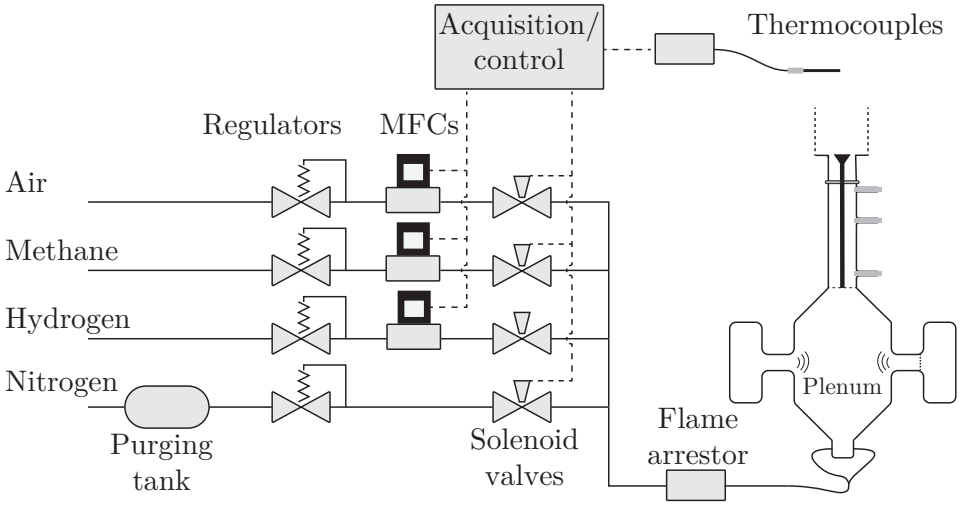

Figure 2.8: Schematic of the gas lines and the low speed acquisition system. The gasses were supplied from the main lines, regulated down to suitable pressure, and the mass flows were controlled by individual MFCs before mixing in the lines.

The MFCs used delivered a variety of mass-flow ranges between [0-10] and [0-2000] standard litre per minute. The fluctuations of the mass flow are less than 2% of the full range and hence, to reduce uncertainties, appropriate ranges were chosen based on the requirement of the total flow rate in each of the lines.

The pressure, temperature, and flow rates were obtained from each MFC and sampled at a rate of 5 Hz throughout each experiment. Additionally, temperatures were sampled using a set of k-type thermocouples, which were installed at various locations in the set-up, e.g. inside the injector pipe.

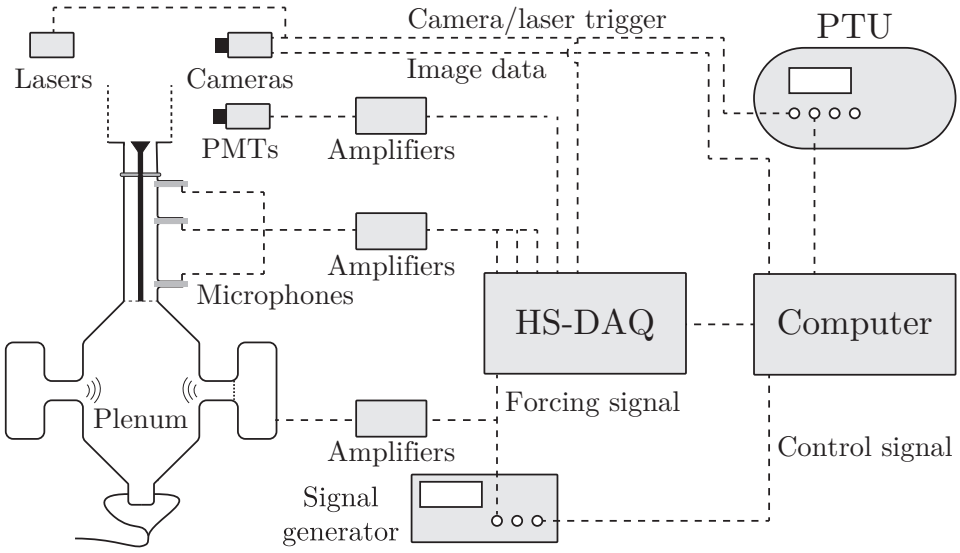

Figure 2.9: Schematic of the high-speed acquisition system. The different diagnostics (microphones, PMTs, etc.) were connected to signal amplifiers before being digitised and sampled at a rate of 51.2 kHz. Signals from the imaging system and signal generator were also sampled and used to synchronise the two measurement systems.

2.2.2 High-speed acquisition

The acoustic signals required sampling at a significantly higher rate than to the flow-rates and temperatures, described in the previous section. These signals, e.g. microphones, PMTs, hot-wires, forcing and trigger signals, etc., were connected to the measurement chain illustrated in Fig. 2.9. Four NI-9234 24-bit DAQs cards providing 16 channels, were used and the signals were sampled at a rate of 51.2 kHz. The sensors, which are described later, were usually connected to amplifiers and signal conditioning units, e.g. filters, before being digitised and sampled. The time-series data were stored as either .TDMS or .mat files, and were used for further processing. The length of acquisition varied and were chosen to obtain converged statistics. For the acoustically forced signals, where the frequency was known, a minimum of 200 forcing cycles were usually sampled. High-speed imaging system was synchronised to the times series obtained from the high-speed acquisition system by sampling of the camera triggers.

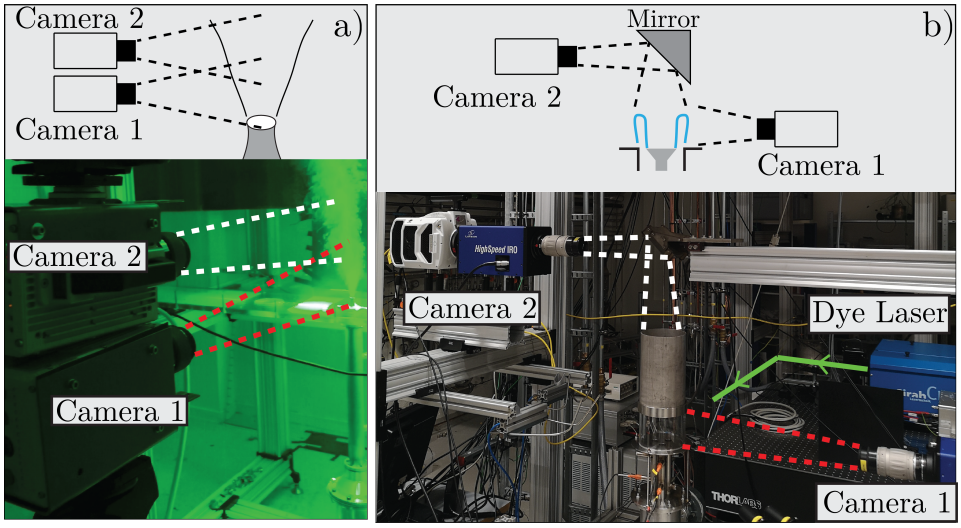

Figure 2.10: Two examples of high speed camera set-ups using two cameras. In a), two PIV cameras were used with overlapping fields of view to cover a larger region of the turbulent jet presented in article 6. In b), two intensified cameras were used to capture flame Chemiluminescence from the top and side. Camera 2 viewed the flame through an air cooled mirror, and camera 1 could also be synchronised with a UV-laser, to obtain OH-PLIF images.

2.2.3 High-speed imaging and optics

High-speed imaging was used to aquire 2D PIV, OH*-chemiluminescence, and OH-PLIF, which are described in more detail in the next sections. The various equipment, i.e. cameras, intensifiers, filters, lasers, etc., are summarized in Tab. 2.1, and all the data acquisition were performed through the Davis 8 software. The timing was controlled using a LaVision high-speed controller.

Two examples of camera set-ups are shown in Fig. 2.10. In Fig. 2.10 a), two cameras were used with overlapping fields of view, to capture the velocity field of the turbulent jet, described in detail in article 6. For these measurements, the cameras were synchronised with a laser which were used to illuminate particles seeded into the flow. In b), two cameras were used to measure OH*-chemiluminescence and OH*-PLIF of the interacting flames described in article 2. To measure OH*-chemiluminescence, each camera was fitted with Intensified Relay Optics (IRO), a UV-lens, and an OH-filter (310 ± 10 nm). To obtain an overhead view of the flame, camera 2 viewed the flame using an air cooled mirror. For the OH-PLIF measurements, the camera 1 was also synchronised with a UV-laser.

Camera	Phantom v2012 Photron Fastcam SA1.1
Optics	
IRO UV-lens OH Filter	LaVision Cerco 2178 310 ± 10nm
Laser	Model
HS-pump-laser HS-dye-laser HS-PIV-laser HS-PIV-laser	Edgewave IS400-2-L (532 nm) Sirah Credo-Dye-N (281 nm) Photonics DM150-532DH (532 nm) Litron LDY303HE-PIV (532 nm)
HS-controller	LaVision PTU

Table 2.1: Overview of the equipment used for high-speed image diagnostics. The table summarises the cameras, intensifiers, lasers, and optics.

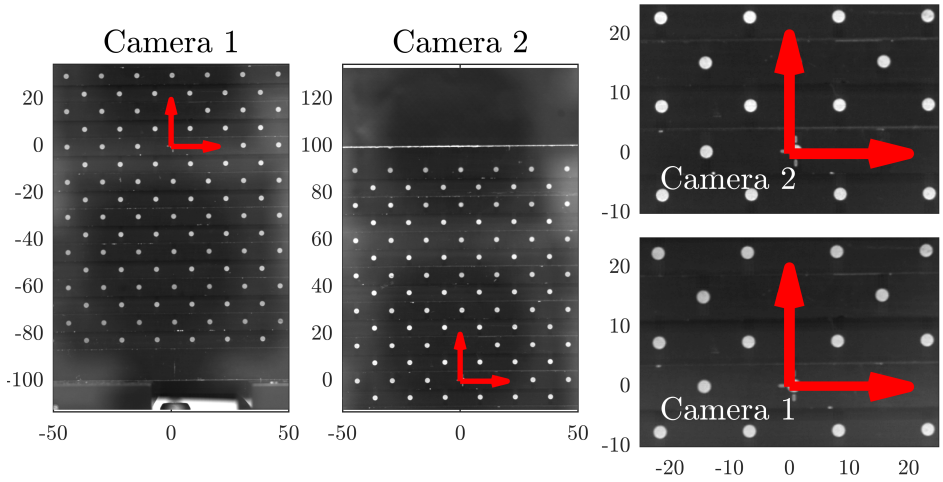

Figure 2.11: Typical set of calibration images used to map image coordinates to world coordinates. The white markers on the targets are fitted to a polynomial surface, which are then used to map from pixels to mm, where $(0,0)$ defines the origin. The example here, was taken from the two camera set-up shown in Fig. 2.10 a), where the two cameras shared a common calibration target.

Image calibration

To map the image coordinates $(\tilde{x},\tilde{y})$ to world coordinates (x,y), a camera calibration was always performed prior to any measurement campaign. This was done by imaging of a known calibration target. A typical example is shown in Fig. 2.11, where images were taken of a target placed in the field of view of the jet flow presented in article 6. The images were taken by the setup shown in Fig. 2.10 a), where the two camera views overlap. The position of the white markers, on the calibration target, were fitted to a polynomial surface $C(\tilde{x},\tilde{y})$, which is then used to map between image and world coordinates $(x,y) = C(\tilde{x},\tilde{y})$. This calibration accounts for image distortions due to the lens, imperfect alignment etc. In this example, the two cameras could obtain the same origin at $(x,y) = (0,0)$, indicated by the red arrows, since both viewed the same target. The same field of view is displayed from both camera views in the right set of images, and this enabled the velocity fields to be stitched together as described next.

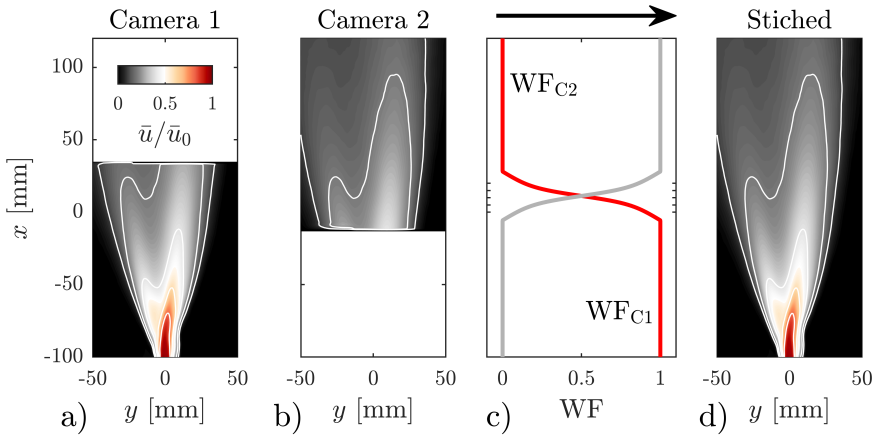

Figure 2.12: Example of image Stitching by two overlapping cameras. a) and b) show the mean velocity field obtained from camera 1 and 2 respectively and d) shows the stitched field. c) shows the two weighting functions and to obtain a smoother transition between the two fields and avoid edge effects.

Image stitching

The velocity fields obtained from the two PIV cameras, imaging the turbulent jet, were stitched together. An example of this stitching process is shown in Fig. 2.12, where a) and b) show the velocity fields obtained from camera 1 and camera 2 respectively. Since these share a common coordinate system, and the views were overlapping, the velocity field in the overlapping region $\zeta = [-1 \text{ to } 1]$, were estimated by a weighted sum of the two camera views. To obtain a smooth trans-

ition and avoid edge effects, the weights were given by functions on the form $\mathrm{WF_{c1}}(\zeta) = 0.25(2 - \tanh(\pi\zeta) - \zeta)$ and $\mathrm{WF_{c2}} = 1 - \mathrm{WF_{c1}}$, which are shown in c). The stitched velocity field is shown in d).

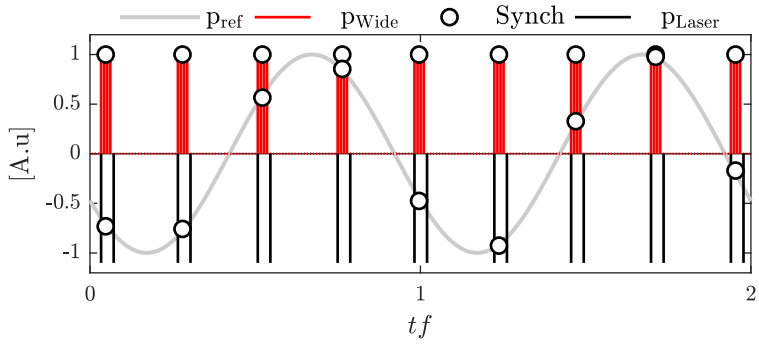

Figure 2.13: Typical time series of the signals used to synchronise the high-speed imaging system and the high-speed acquisition system. The image/laser pulses were captured and processed to identify a time stamp for the images.

Image synchronisation

To synchronize the high-speed imaging systems with analog signals from the microphones, PMTs, hot-wire, signal generator, etc., the trigger signals from the lasers/cameras were acquired simultaneously. By detecting the time stamp of these triggers, the two time series could be synchronised.

Figure. 2.13 shows a typical example, where the PIV system was synchronised to the external forcing signal $\mathrm{p_{ref}}$, from the signal generator. Since the laser triggers $\mathrm{p_{Laser}}$ are very short, the signal generator was used to output a triggered square wave with a duty cycle corresponding to the separation between the two laser pulses (PIV Δt). This signal corresponds to p_{wide}, which were used to identify the location Synch, which provide time stamps for the velocity measurement, obtained from the PIV system. A similar method was also used to synchronise the systems when acquiring images of OH-Chemiluminescence and OH-PLIF.

2.2.4 Acoustic forcing

Acoustic forcing was applied by sets of Monacor KU-516 horn drivers, which were amplified by a set of Skytec PRO1000 amplifiers. The horn drivers are mounted in the plenum, as shown in Fig. 2.1, 2.4, 2.5, and provide longitudinal forcing for FTF and FDF measurements. In a similar way, the same speakers were placed on the side walls of the rectangular cavity, shown in Fig. 2.7, to provide transverse acoustic forcing. The driver units had a frequency response in the range $f = [160 - 3500]$Hz, and were controlled using an Aim-TTi TGA1244 signal gen-

erator. The amplifiers were tuned before each experiment, and a limit was set for the amplitude, to avoid breaking the speakers.

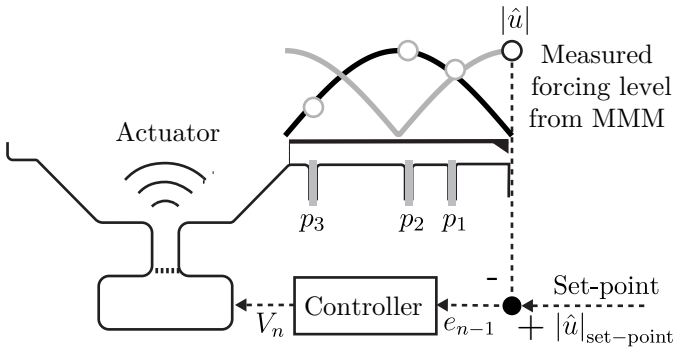

Figure 2.14: Side view of the rig showing the control strategy used to tune the acoustic forcing level. A cost function e_n, defined as the difference between the chosen set-point and the measured level was minimized by iterations, using Eq. 2.1. For FTF and FDF measurements, this difference were chosen to be an acoustic forcing level $|\hat{u}|$, measured at the burner dump plane, using the MMM.

Tuning the acoustic forcing level

Before data acquisition, it was often desired to achieve a specified forcing level from the acoustic forcing. A typical example is the acoustic forcing level for FTF and FDF measurements. For these measurements, the forcing level was chosen to be $|\hat{u}|/\bar{u} = A$ at the flame base at the dump plane. Due to the acoustic response of the rig when submitted to different frequencies, the voltage level required to achieve a constant forcing level at different frequencies had to be varied. Hence, the voltage level needed to be tuned for each frequency. To achieve this in an efficient manner, an active control strategy, utilising real time processing of the pressure measurements and iterations, was implemented.

A schematic of the control loop is shown in Fig. 2.14. Initially, for a fixed frequency, two voltage amplitudes ($V_{(1,2)} = 0.2\,\text{V}$ and $0.4\,\text{V}$) were applied to the speakers. The MMM was then used to estimate the forcing level at the reference location. Then, the next voltage amplitude was computed using the secant method

$$V_n = V_{n-1} + \frac{V_{n-1} - V_{n-2}}{e_{n-1} - e_{n-2}} e_{n-1}, \tag{2.1}$$

and this process was repeated until the cost function defined as $e_n = |\hat{u}|_{\text{set-point}} - |\hat{u}|_n$, became less than a set value.

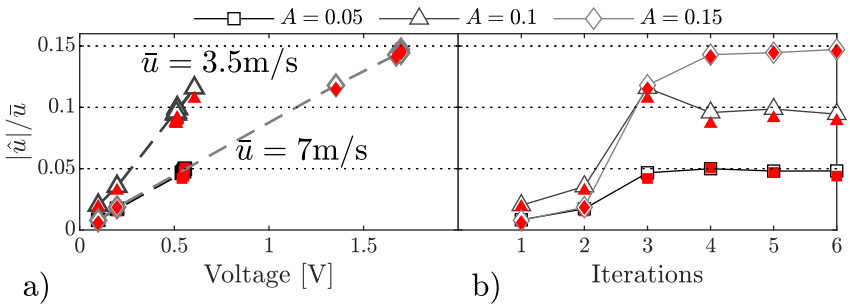

Figure 2.15: Examples of the iterative process used to tune the acoustic forcing level. a) shows the relationship between the applied voltage amplitude and the measured forcing level using the MMM (white markers △), which were verified using a hot-wire (red markers ◆) placed at the exit. b) Shows the forcing level plotted for each iteration and due to the approximately linear relationship, only a couple of iterations were usually required, making the method very efficient.

To illustrate the iterative process, Fig. 2.15 a) shows the forcing level plotted against the voltage amplitude for three cases, two taken at 5 % and 15 % for $\bar{u} = 7\mathrm{m/s}$, and one taken at 10 % for $\bar{u} = 3\mathrm{m/s}$. Additionally, the exit velocity was also measured with a hot wire placed at the dump plane to validate the method. For all measurements the MMM and hot wire were in excellent agreement. For a fixed frequency and velocity, the relationship between the voltage V and forcing level $\hat{u}$ was approximately linear. Hence, the iterative method often converged within a couple of iterations. This is shown in b), where the forcing level is plotted for the same cases, now against the number of iterations. For the three cases displayed here, 4 iterations were sufficient to reach the given forcing level.

Several studies, e.g. [Di Sabatino et al., 2018; Gatti et al., 2017, 2018, 2019; Komarek and Polifke, 2010; Palies et al., 2010], have used a hot wire placed at a distance upstream of the flame, to measure the acoustic forcing level at the dump plane. In this situation, there might be a significant discrepancy between the hot wire measurements and the acoustic fluctuations at the dump plane, at sufficiently large forcing frequencies. Figure 2.16 shows the forcing level tuned over a range of frequencies using the active control strategy described in the previous section. At the dump plane $x = 0$, the MMM provides a constant forcing level of 5 % over the range of frequencies. For these measurements, the hot wire was placed 130 mm upstream of the dump plane, i.e. between p_1 and p_2 as was shown in Fig. 2.1. The magnitude of $\hat{u}$ is also shown at the location of the hot wire $x = x_{\mathrm{hw}}$, where both measurements, i.e. from the MMM and the hot wire are in agreement. However, large discrepancies were observed between $\hat{u}(x = x_{\mathrm{hw}})/\bar{u}$ and $\hat{u}(x = 0)/\bar{u}$ for a large range of frequencies, $f = [100 \text{ to } 1000]\mathrm{Hz}$

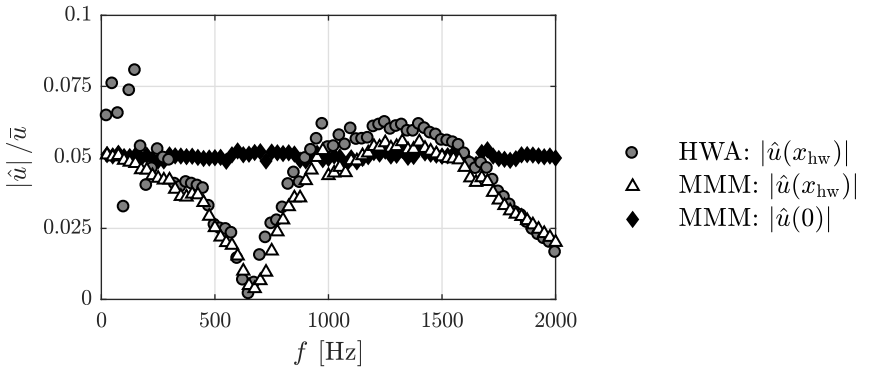

Figure 2.16: Acoustic forcing level tuned over a range of frequencies with a constant forcing amplitude, $|\bar{u}|/\bar{u} = 0.05$, at the burner exit $x = 0$ using the MMM (◆). Upstream ($x_{\mathrm{hw}} \approx 100\,\mathrm{mm}$) measurements from a hot-wire (◉) is compared against the MMM (△) and reveals that the acoustic mode shape needs to be accounted for at sufficiently large frequencies.

and for $f > 1500\mathrm{Hz}$. At $f \approx 650\,\mathrm{Hz}$ the hot wire was located at a velocity node ($f \approx c/\lambda = 340\mathrm{m/s}/(4 * 0.130\mathrm{m}) \approx 650\,\mathrm{Hz}$), although the fluctuation amplitude at the dump plane was $\hat{u}(z = 0)/\bar{u} = 0.05$. In this situation, using the hot wire to measure the reference velocity, could lead to significant errors in the FTF/FDF. Hence, several microphones, or a combination of microphones and hot-wires, e.g. as used by [Gaudron et al., 2019; Oztarlik et al., 2020], were required to accurately compute the acoustic velocity at the dump plane.

2.3 Measurement diagnostics

Type	Model	Sensitivity [mV/Pa]	Range [Pa]
Condenser Microphone	Brüel and Kjær Free-field 1/4"	4	$0 - 3.5 \times 10^3$
Amplifier	Brüel and Kjær model 2670		
piezoelectric	Kulite XCS-093-05D	4.29×10^{-3}	$0 - 3.5 \times 10^4$
piezoelectric	Kulite XCE-093-7barA	1.43×10^{-4}	$0 - 7 \times 10^5$
Amplifier	Fylde FE-579-TA		

Table 2.2: Summary of the microphones and amplifiers used to measure the acoustic pressure. Condenser microphones were used for non reacting flow measurements, and the more robust piezoelectric transducers were used for reacting flow measurements, where there was a risk of flash back.

2.3.1 Microphones

Microphones were used to measure the acoustic pressure oscillations at various locations in the set-up. Depending on the application, the two main types types listed in Table 2.2, were used. For experiments with reacting flow, piezoelectric (Kulite) transducers were chosen due to the risk of flash back, which would potentially destroy the fragile condenser microphones. The condenser microphones were significantly more sensitive, compared to the piezoelectric transducer, and when available, these were used for non reacting flow experiments, or acoustic characterisation of parts.

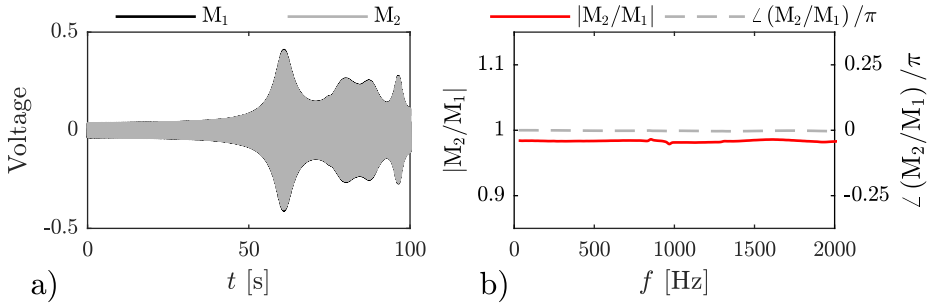

Figure 2.17: Typical procedure to obtain relative calibration for the microphones. a) show two pressure time series obtained from microphones mounted at the same location, while forcing at a range of frequencies. b) shows the transfer function between the two measurements, where there in this case was a discrepancy less than 5%.

Microphone calibration

To characterise the acoustic modes using the MMM, simultaneous measurements of the acoustic pressure at several spatial locations were required. To reduce uncertainties, the microphones were calibrated against each other before they were installed. To obtain a relative calibration, the microphones were mounted flush at the end of a closed pipe, with the speaker mounted at the other end. The speaker was then used to force at a range of frequencies while recording pressure time series from the microphones. Figure 2.17 a) show typical time series obtained from two microphones M_1 and M_2. In b), the gain and phase of the transfer function, computed between the two microphones, are shown. In this case, there is a constant offset between the two microphones which is less than 5%. If the discrepancy was less than this, a small correction factor was applied, and if larger, the microphone was either repaired or swapped with a new one.

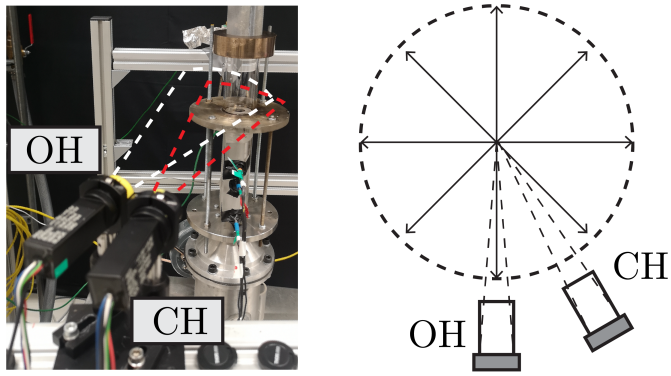

Figure 2.18: Image showing a typical PMT setup used to measure the global flame chemiluminecence. The schematic illustrates isotropic chemiluminecence from the flame, where only a sector is captured using the PMT.

2.3.2 Global heat release rate by PMTs

For premixed flames, it is a common practice to estimate the HRR by measurements of the flame chemiluminescence [Balachandran et al., 2005; Higgins et al., 2001; Schuermans et al., 2010; Schuller et al., 2003]. The global chemiluminescence was captured using a single, or a combination of two photo multiplier tubes (PMTs), as shown in Fig. 2.18. In this configuration, two Hamamatsu H11902-113 PMTs, were equipped with UV band pass filters, 310 ± 10nm for OH* and 430 ± 10nm for CH*. The PMT signals measure light in a bandwidth 185-700 nm and were amplified using Hamamatsu C7169 before being digitised and sampled. The radiation was assumed to be isotropic, and hence measuring a sector was sufficient to capture the global HRR. This was validated by comparing measurements obtained from different views, e.g. by the time series displayed in Fig. 2.19 a), where the normalised OH* and CH* intensities are shown. The corresponding energy spectra are shown in b), and the two signals were very similar.

The relationships between the light intensity and the HRR can be written for lean flames as

$$I'/\bar{I} = u'/\bar{u} + K\Phi'/\bar{\Phi}, \quad Q'/\bar{Q} = u'/\bar{u} + \Phi'/\bar{\Phi}, \tag{2.2}$$

where K is a constant of proportionality, which differs between OH* and CH* chemiluminescence and fuel type. If the mixture is perfectly premixed, $\Phi' = 0$ and the relative fluctuation of light intensity is directly a tracker for the relative fluctuation in the global HRR.

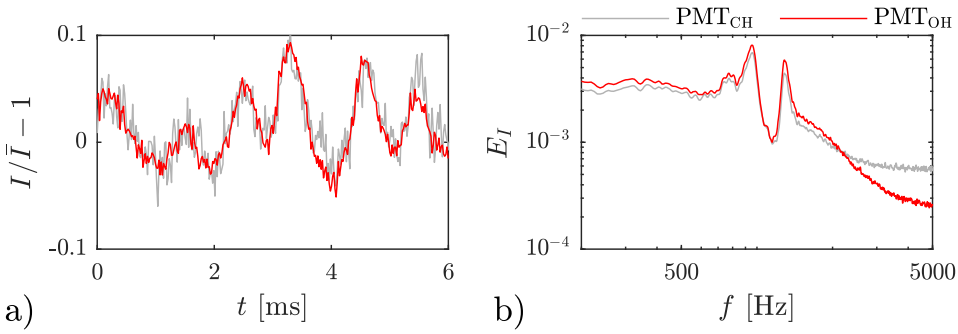

Figure 2.19: A typical time series a) and the corresponding spectra b) measured by the PMTs equipped with OH* and CH* filters.

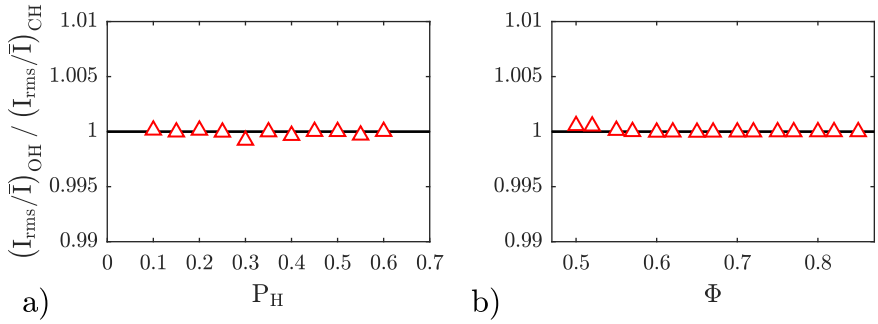

Figure 2.20: Ratio between the mean OH* and CH* chemiluminecence for a range of a) hydrogen contents (P_H) and b) equivalence ratios (Φ).

To confirm that the experiments did not exhibit equivalence ratio fluctuations, the intensity of OH* and CH* were measured for a range of Φ and P_H. In Fig. 2.20, the ratio between the two measurements is shown for a wide range of operating conditions, and the ratio differs from unity with less than 0.1%. If equivalence ratio fluctuations were present, this ratio would differ significantly from unity, and hence, the experimental set up can indeed be considered perfectly premixed. Therefore, the global HRR was estimated from either species (OH* or CH*), without the use of simultaneous calibrated PMT measurements, as described by Schuermans et al. [2010].

2.3.3 Hot wire anemometry

Hot wire anemometry was used to measure the non-reacting flow velocity, using a Dantec StreamLine pro control unit equipped with a 55P11 single wire probe of length 1.25 mm and diameter 5 nm). The probe was connected to a Wheatstone bridge and the temperature of the wire was kept constant, where the control voltage

was sampled. For isothermal flow, the control voltage is a function of the bulk fluid velocity [Tropea et al., 2007].

Calibration

There is no accurate relationship between the velocity and the heat transfer measured across the wire and hence, the system needed to be calibrated against a known velocity source regularly. To produce a well-defined velocity the hot wire was placed in the potential core of an axisymmetric jet described in article 6. To verify that the nozzle produced a top hat velocity profiles, the hot wire was also traversed across the jet close to the exit. A typical profile is shown in Fig. 2.21 c), and the exit velocity was also verified, using a pressure transducer and a Pitot probe placed at the jet exit. The relationship between the Pitot probe and the velocity estimated from the total flow rate set by the MFC is shown in Fig. 2.21 a) and were in agreement.

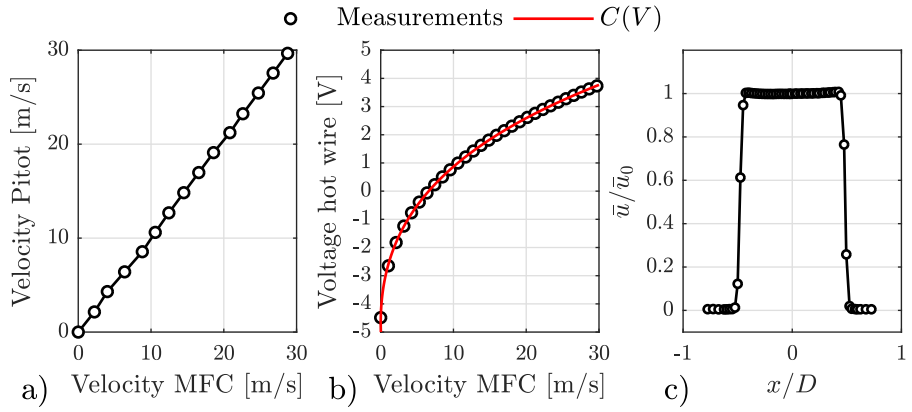

Figure 2.21: Typical calibration of the hot wire. a) shows the jet exit velocity measured by a Pitot probe against the velocity estimated from the total flow rate set by the MFC. b) shows the mean voltage measured at a range of jet exit velocities, which are fitted to a forth order polynomial. c) shows the mean velocity profile measured by traversing the hot wire across the jet exit.

To calibrate the hot-wire, time series were measured to obtain the mean voltage over a range of flow rates. These were fitted to a forth order polynomial on the form $u = C(V) = \sum_{i=0}^{4} c_i V^i$, which then were used to map the voltage to velocity. A typical example is shown in Fig. 2.21 b). Prior to the calibration, the overheat ratio was usually set to 0.8, and the offset and gain of the system, were optimized such that the full range of the DAQ $[-5,5]$V was utilized. This calibration procedure was performed daily before and repeated after the experiments to reduce uncertainties.

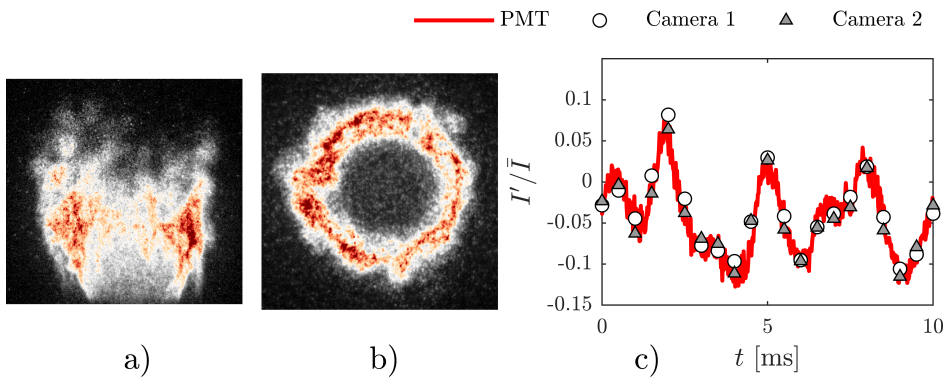

Figure 2.22: Typical images of the instantaneous OH-Chemiluminescence taken from two camera views. a) shows the front camera, and b) shows the top camera, taken using the setup shown in Fig. 2.10 b). In c), time series of the global HRR, obtained by integrating the camera fields of view, are compared against the PMT signal. The three measurements are very similar, showing that the systems were synchronised and that the flame Chemiluminescence was isotropic.

2.3.4 Imaging of OH*-chemiluminescence

The spatial distribution of the HRR was measured using intensified cameras fitted with UV-lenses and the same OH* filter as the PMT, which were described previously. The light propagates along lines of sight and the intensity measured in each camera pixel corresponds to the HRR integrated along these paths.

Figure. 2.22 shows instantaneous snap shots of the HRR taken from the front and top cameras, using the camera set up shown previously in Fig. 2.10 b). If the volumetric HRR is defined by $q(x,y,z,t)$, the front and top cameras capture q integrated along the x and z directions respectively. The global HRR, can be retrieved by integrating the spatially distributed HRR $Q'/\bar{Q} = \int_A q'/\bar{q}\ \mathrm{d}A$, over the camera field of view A. To verify that the different fields of view provide the same HRR, and that the flame chemiluminescence was isotropic, time series taken with both cameras and the PMT are shown in Fig.2.22 c). The signals are very similar and well synchronised, although the PMT signal is sampled at a higher rate. The image intensity were usually normalised such that $\bar{Q}$, obtained by integrating the mean images $\bar{q}$, provides the thermal power of the flame.

2.3.5 OH-Planar laser-induced fluorescence (OH-PLIF)

To visualise and measure the instantaneous flame front in a plane of interest, OH-Planar laser inducer fluorescence (OH-PLIF) was used, similar to [Ayoola et al., 2006; Balachandran et al., 2005; Worth and Dawson, 2012a, 2019]. More details

on the method can be found in [Donbar et al., 2000], but in short it consists of imaging the emissions from OH-radicals excited by light produced from a dye laser. When the wavelength of the laser is tuned to the absorption peak of the OH-radicals around 281 nm, the molecule emits a signal proportional to the concentration of OH. The concentration was measured by the same camera used to capture OH-chemiluminescence, described in the previous section, although with a shorter exposure time to only capture the excited chemiluminescence.

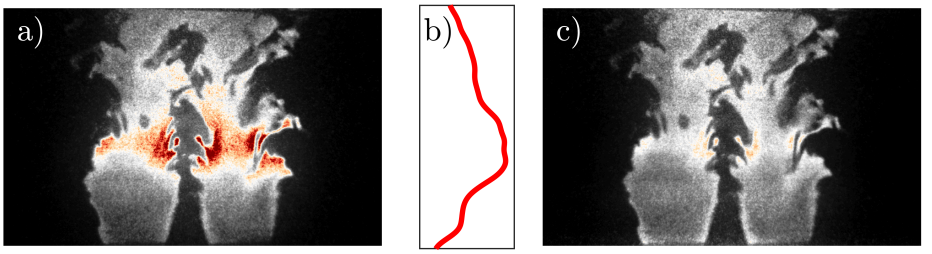

Figure 2.23: Typical OH-PLIF image captured by the high-speed camera. a) shows the raw-image, b) shows the mean laser sheet profile, and c) shows the image after laser sheet correction. The image in c) was used to visualise the flame front, but also to measure the instantaneous flame front positions using edge detection methods.

A typical raw image of two interacting flames is shown in Fig. 2.23 a), taken by the front camera shown previousl in Fig. 2.10 b). The pump laser had an power output of about 100 W and after converted to 281 nm, the power was reduced to approximately 3 W, firing at an optimal rate of 10 kHz giving a pulse intensity of 0.3 mJ/pulse. The laser sheet was not uniform, which led to local hot spots in the raw image. To correct for these variations, measurements were taken of the mean beam profile, which were then used as a correction. The laser mean sheet intensity is shown in b), and the corrected image shown in c). The image in c) was used to measure the instantaneous flame front using edge detection methods, which are described in chapter 3.

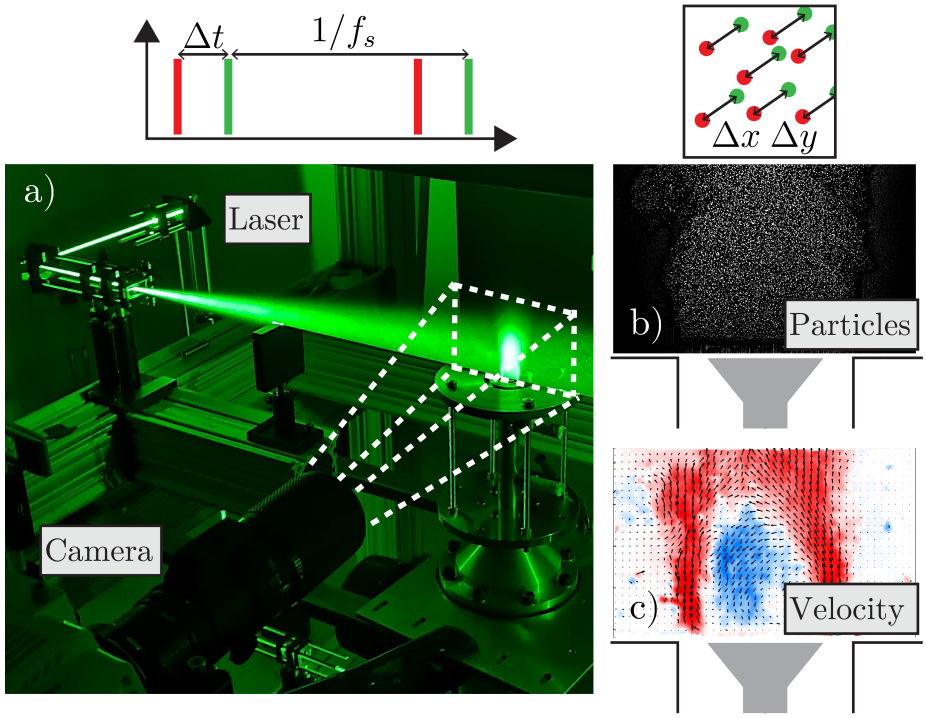

Figure 2.24: Typical set up used to obtain the planar velocity field by 2D-PIV measurements. a) shows an image of the camera and laser set up, where bluff body flow, produced by the single injector was measured. b) shows a typical Mie-scattering particle image captured by the camera, and c) Shows an instantaneous snapshot of the velocity field obtained after correlation analysis of two sequential frames.

2.3.6 Particle Image Velocimetry (PIV)

To measure the velocity in a plane, 2D-Particle Image Velocimetry (PIV) was used, which is a common technique used to track the movement of tracer particles, which are seeded into the flow. If the inertia of these particles is sufficiently small, they follow the flow, and by tracking the displacement of these, the velocity components of the flow can be estimated using correlation analysis. Only a brief overview of the method is provided in this section, and for more details, see [Adrian and Westerweel, 2011; Raffel et al., 2018; Tropea et al., 2007].

Figure 2.24 a) shows an image of the PIV set up used to measure the flow field produced by the bluff body of a single injector. The air was seeded with oil droplet using a Laskin nozzle, and the camera and laser were aligned and focused in the plane of interest shown in the image. A laser with two cavities was triggered by two pulses separated by a time delay Δt, and a high-speed camera was synchronised

with these, providing a set of images, capturing Mie-scattering from the particles. A typical example of a particle image is shown in b). These were divided into interrogation windows, where the average displacement $[\Delta x, \Delta y]$, was computed using correlation analysis. Since the two images were separated by Δt, the average velocity in each window was given by

$$[u, v] = [\Delta x, \Delta y] / \Delta t. \tag{2.3}$$

Image pairs were obtained at a sampling rate of f_s and the timing, imaging, and processing was performed through the Davis 8 software. The correlation analysis used a recursive window size technique to estimate the displacement field.

Figure 2.25 shows the time averaged velocity field, measured in the wake of the bluff body, at three different exit velocities $\bar{u} = [10, 20, 30]$ m/s. The streamlines are shown by the black arrowed lines. Behind the bluff body for $x < 15$ mm, a strong recirculation zone is present. It was in this region that the flame stabilised along the inner and outer shear layers of the jet. The velocity profiles are shown at $x = 2$ mm, which exhibited an approximately symmetric profile.

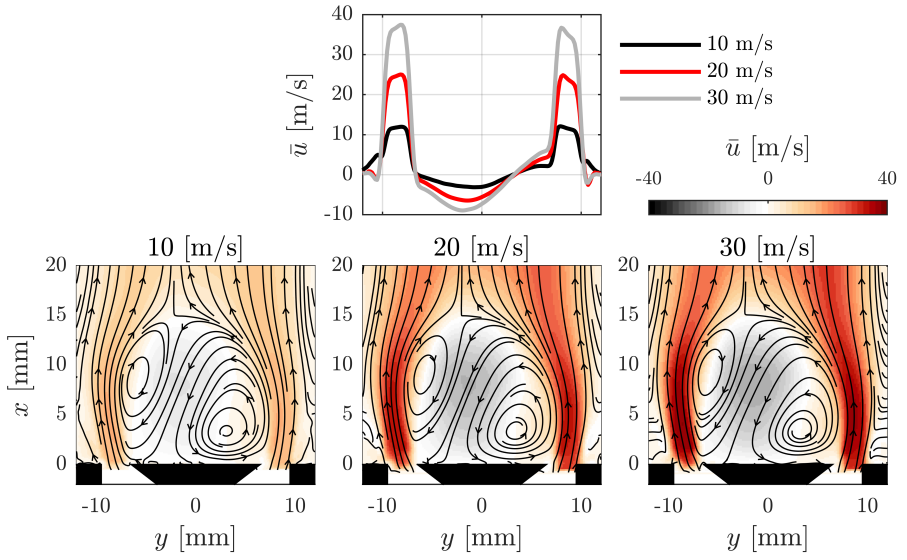

Figure 2.25: Time averaged flow fields taken of the non-reacting flow behind the bluff body for a range of exit velocities $\bar{u} = [10, 20, 30]$ m/s. The top plot shows stream wise profiles taken at $x = 2$ mm.

Optimizing the setup to reduce uncertainty

To minimize uncertainties, the camera field of view and time separation Δt were optimised so that: 1) all camera pixels were utilised and 2), an average particle dis-

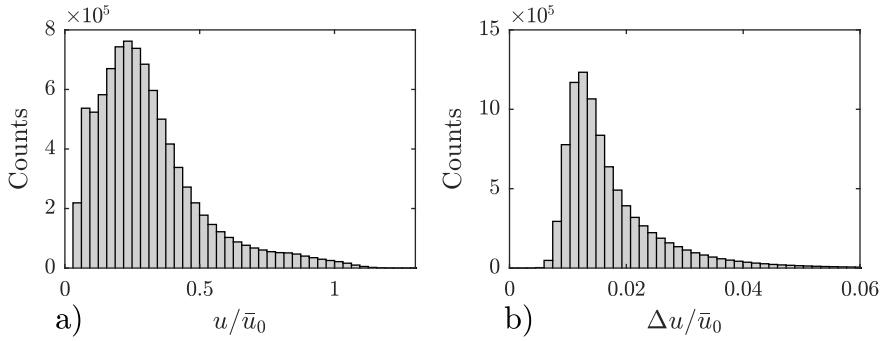

Figure 2.26: Histograms showing typical uncertainties estimated from PIV measurements of the turbulent jet presented in article 6. a) shows a histogram of the mean stream wise velocity, and b) shows a histogram of the uncertainties Δu, normalised by the jet exit velocity $\bar{u}_0$. The uncertainty was less than 5%, which is typical of these systems.

placement of $\Delta x \approx 8-14$ were obtained along the main flow direction. The DaVis 8 software uses a method outlined by Wieneke [2015] to quantify the uncertainty. There are many sources contributing to the uncertainty, but the main source is usually related to the sub pixel accuracy of the correlation analysis. Figure. 2.26 shows histograms of, a) the stream-wise velocity and, b) the uncertainty estimated for 1000 snapshots of the jet velocity for one of the cases presented in article 6. The average uncertainty, when normalized by the jet exit velocity, was around $\Delta u \approx \pm 1.8\%$, and $\Delta u \approx \pm 5\%$, when normalising by the average velocity within the field of view. This is within the expected range for these types of measurement systems.

Chapter 3

Data processing

3.1 Mode decomposition

3.1.1 Spectral analysis

The process of determining the frequency content of a time signal is known as spectral analysis. This type of analysis is very useful when analysing harmonic signals, which was often the case in this thesis. In this section, only a brief overview of the most frequently used methods are described, and for more information on spectral analysis, see [Rao and Swamy, 2018].

The discrete Fourier transform (DTF)

To transform a time-series into the frequency domain, the Discrete Fourier transform (DTF) can be computed

$$\hat{p}(f) = \frac{2}{N} \sum_{n=0}^{N-1} p(n) \exp\left(-j2\pi n \frac{f}{f_s}\right). \tag{3.1}$$

Here, f_s is the sampling frequency, and $p(n)$ is the n'th sampled data point. After transformation, $\hat{p}(f)$ represents a set of a complex numbers describing the amplitude and phase of the signal content at frequency f. As such, the DFT decomposes the signal into a linear combination of harmonic time-series. When sampled at a constant frequency f_s, the sum in Eq. (3.1) can be computed efficiently using a Fast Fourier Transform (FFT) algorithm.

The Power Spectral Density

The power spectral density (PSD) describes how the power of a signal is distributed among its decomposed frequencies. The PSD is related to the Fourier transform

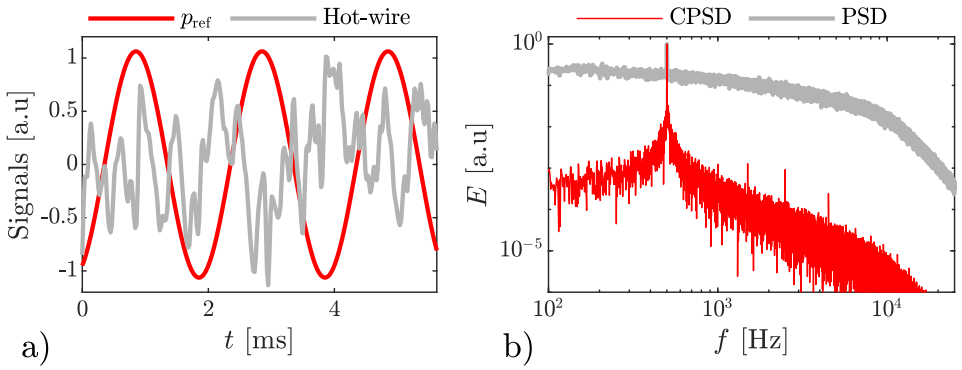

Figure 3.1: Energy spectra (PSD and CPSD) computed using the Welch method on a hot-wire signal while acoustic forcing was applied. a) shows the times series of the reference signal p_{ref} and the hot-wire signal. b) shows the energy spectra estimated using CPSD and PSD. By using the CPSD, the uncorrelated parts of the spectra is filtered out.

and is given by

$$\text{PSD}(p,p) = \hat{p}\hat{p}^*, \tag{3.2}$$

where $p^*(f)$ is the complex conjugate. Similarly, the Cross PSD between signal p and f is given by $\text{PSD}(p,f)$. Using the CPSD can be useful, e.g. if the measurements are noisy and the signal $f = p_{\text{ref}}$ represents a reference signal. Then computing the CPSD also filters out all the parts of the signal that are not coherent with the reference signal.

If we only are interested in the coherent response, i.e. the part of a signal that is synchronised with the external forcing, the amplitude spectra can be computed using

$$\hat{p} = \frac{\text{PSD}(\, p_{\text{ref}},\, p\,)}{\sqrt{\text{PSD}(\, p_{\text{ref}},\, p_{\text{ref}}\,)}}. \tag{3.3}$$

The CPSD was used when estimating the acoustic fluctuations inside the pipe for the MMM where we only were interested in the response at the forcing frequency.

The Welch method

To obtain statistically converged energy spectra or signal amplitudes with negligible influence from noise, the Welch method was applied. The method consists of binning the time series into a number of 50% overlapping windows. Each of these were then pre-multiplied by a Hanning window before the energy spectra was then computed, using Eqs. (3.1) and (3.2). The energy spectra was then given

as the average

$$E_{pp} = \frac{1}{N}\sum_{i=1}^{N} \mathrm{PSD}_i(p,p), \tag{3.4}$$

The computation of E_{pp} was normalized such that the total energy, given by the rms of the time series, was preserved, i.e. $p^2_{\mathrm{rms}} = \int_0^\infty E_{pp}(f)\mathrm{d}f$.

Figure. 3.1 shows an example where the Welch method was used on a hot-wire signal recorded while acoustic forcing at frequency $f = 500\,\mathrm{Hz}$ was applied. In a) the time series of the hot-wire signal and the reference signals are shown and in b) the energy spectra are shown using both the PSD and CPSD. The hot-wire signal contains energy among a wide range of frequencies as shown by the PSD. If we only care about the coherent part of the spectra the CPSD filters out the frequencies that are not correlated with the reference signal at 500 Hz.

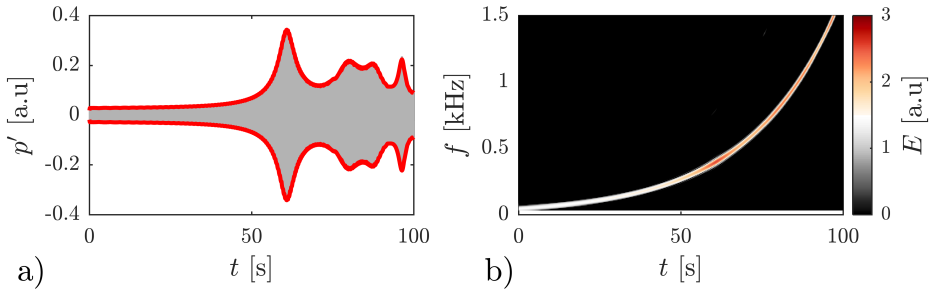

Figure 3.2: a) Time series of pressure taken while forcing with the speakers at a range of frequencies which is increased logarithmic in time. b) shows the corresponding spectrogram where the energy spectra E changes with time. The amplitude ($\pm\sqrt{E}$) at the dominant frequency is plotted as red lines in a) and give the modulus of the time series.

The spectrogram

The energy spectra provides information on how the signal energy is distributed at each frequency, but it but does not provide information of where in the time series the frequency content occurs. When analysing self-excited instabilities, it is sometimes useful to retrieve information on how the frequency content of a signal changes with time. To achieve this, the spectrogram was computed. The computation of the spectrogram is similar to the energy spectra. The only difference is that the signal is first binned into shorter time series which are then used to estimate the energy spectra locally. An example of the application is shown in Fig. 3.2, where a) shows a pressure time series recorded while acoustic forcing was applied where the frequency was changed logarithmic with time. The corresponding spectrogram, displayed in b), tracks the dominant frequency where the colour represents

the amplitude of the signal. The amplitude for the dominant frequency is shown by the red lines in a) as a function of time.

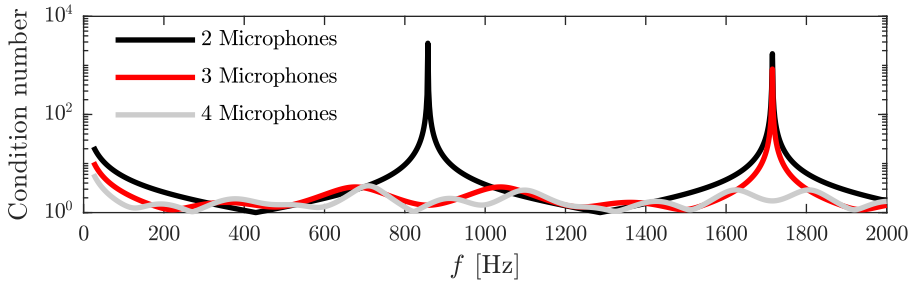

Figure 3.3: Condition number of Eq. (3.7) using 2,3, or 4 microphones. Careful placement of more microphones increases the robustness of the MMM and makes the method less sensitivity to measurement errors for a wider range of frequencies.

3.1.2 The Multiple Microphone Method (MMM)

The multiple microphone method (MMM) is a method where simultaneous measurements of the acoustic pressure are combined to reconstruct the acoustic mode. The method was used extensively to estimate the acoustic field in various parts of the experimental rigs by combining two or more microphone measurements. For a more detailed information on the method, describing the limitations, sources of error, etc., see [Seybert and Ross, 1977; Åbom, 1991; Åbom and Bodén, 1988].

Assuming 1D acoustics, low mach number, and negligible losses, the acoustic pressure and velocity propagate can be expressed by

$$\hat{p}(x) = A^+ \exp(-jk_+x) + A^- \exp(jk_-x), \tag{3.5}$$

$$\hat{u}(x) = \frac{1}{\rho c}\left(A^+ \exp(-jk_+x) - A^- \exp(jk_-x)\right). \tag{3.6}$$

Here, A^+ and A^- are the complex amplitudes (Riemann invariant) of the upstream and downstream propagating acoustic waves, ρ is the fluid density, c is the speed of sound, and k is the spatial wave-number. The wave-number is given by $k = (2\pi f)/c$, where f is the frequency and $k_\pm = k/(1+\mathrm{Ma})$ where $\mathrm{Ma} = c/\bar{u}$ is the Mach number.

By combining simultaneous measurements of the acoustic pressure at different

locations in a duct of constant area, Eq. 3.5 can written as a system of equations:

$$\begin{bmatrix} \exp(-jk_+x_1) & \exp(jk_-x_1) \\ \exp(-jk_+x_2) & \exp(jk_-x_2) \\ \vdots & \vdots \\ \exp(-jk_+x_i) & \exp(jk_-x_i) \end{bmatrix} \begin{pmatrix} A^+ \\ A^- \end{pmatrix} = \begin{pmatrix} \hat{p}(x_1) \\ \hat{p}(x_2) \\ \vdots \\ \hat{p}(x_i), \end{pmatrix} \tag{3.7}$$

By solving Eq. (3.5) for the two complex amplitudes $A^{\pm}$, the pressure and velocity can be reconstructed in the section of constant area. $\hat{p}_i$ is estimated from the microphone signals using spectral methods and a minimum number of two microphones are required. However, adding more microphones leads to an over-determined system which can be solved by the least squares method. The advantage of adding more than two microphones are: 1) the accuracy of the fit can be assessed and 2) the condition number of the equation system can be reduced over a wider range of wave numbers [Åbom and Bodén, 1988]. This is illustrated in Fig. 3.3 which shows the condition number plotted over the frequency range $f = [0, 2000]$ Hz where 2,3, and 4 microphones are placed. With 2, and 3 microphones, large condition numbers appear close to $f \approx 850$ Hz and 1700 Hz, which occur when the acoustic wavelength $\lambda = 1/k$ is equal to the distance between two microphones. If these positions correspond to pressure nodes, the method is very sensitive to measurement uncertainties. By adding more microphones, the singularities can be avoided, making the reconstruction more robust over a wider range of frequencies. Hence, a minimum number of two microphones were used (when possible).

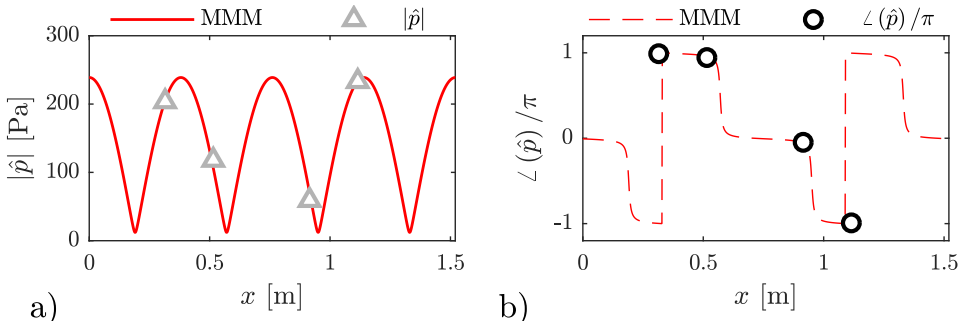

Figure 3.4: A typical mode reconstruction using the MMM in the box where transverse acoustic forcing was applied (From Article 6). a) shows the reconstructed and measured pressure amplitude and b) shows the reconstructed and measured phase. The 1D model is in excellent agreement with the pressure measurements.

Figure. 3.4 shows a typical reconstruction of the pressure field in the box used in Article 6, where 4 microphones were used. Figure. 3.4 a) shows the amplitude (modulus) and b) shows the phase, which are in excellent agreement with the mi-

crophones measurements. The method was also verified against hot-wire measurements as shown previously in Fig. 2.15 when the forcing level was tuned at the dump plane.

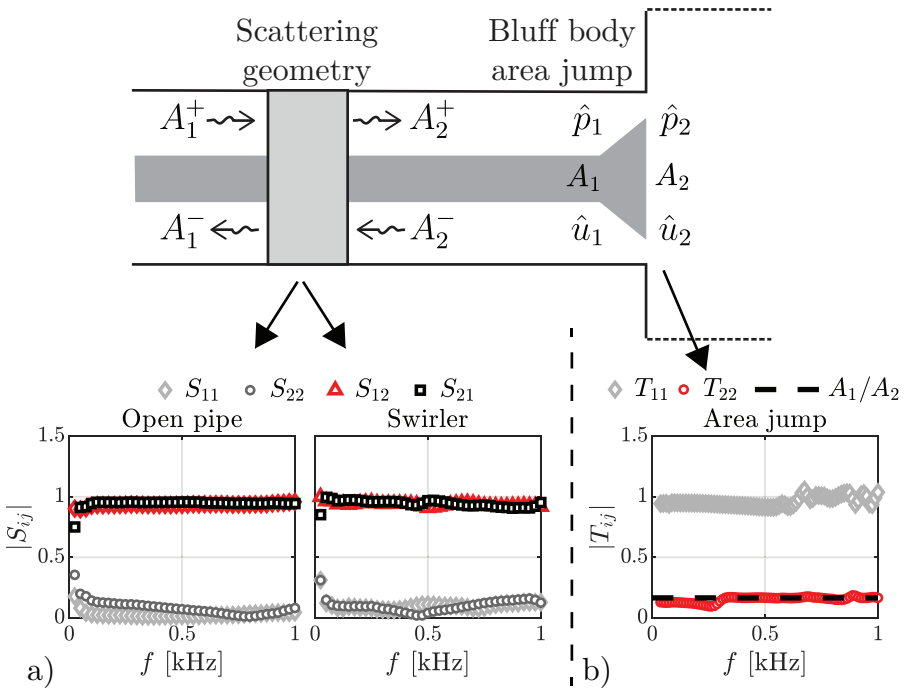

Figure 3.5: a) Acoustic scattering matrix of an open pipe section and the swirler. The influence of the swirler is similar to the influence of the open pipe where the transmission ($|S_{12}| \approx 1$ and $|S_{21}| \approx 1$) and reflection ($|S_{11}| \approx 0$ and ($|S_{22}| \approx 0$) coefficients are unity and zero respectively. Hence, the influence of the upstream geometries were neglected in the MMM when reconstructing the velocity at the dump plane. b) Acoustic transfer matrix of the area jump imposed by the bluff body and expansion into the combution chamber. The pressure is continuous ($|T_{11}| \approx 1$) and the change in velocity is equal to the area ratio ($|T_{22}| \approx A_1/A_2$). Hence, the influence of the bluff body was modeled as an area jump where a correction factor was applied to the velocity.

Transfer and scattering matrix of the upstream geometry and the bluff body

When the acoustic wave propagates through an area jump or the swirler, cylinders, or the streamlined bodies, the acoustic scattering of the element has to be characterised. This influence was characterised through an acoustic transfer matrix

$$\begin{bmatrix} \hat{p}_2^- / (\rho c) \\ \hat{u}_2^+ \end{bmatrix} = \begin{bmatrix} T_{11} & T_{12} \\ T_{21} & T_{22} \end{bmatrix} \begin{bmatrix} \hat{p}_1^- / (\rho c) \\ \hat{u}_1^+ \end{bmatrix}, \tag{3.8}$$

or the equivalent acoustic scattering matrix

$$\begin{bmatrix} A_1^- \\ A_2^+ \end{bmatrix} = \begin{bmatrix} S_{11} & S_{12} \\ S_{21} & S_{22} \end{bmatrix} \begin{bmatrix} A_1^+ \\ A_2^- \end{bmatrix}. \tag{3.9}$$

The transfer matrix relates the acoustic pressure and velocity up- and downstream of the element, whereas the scattering matrix relates the upstream and downstream acoustic waves in terms of the Riemann invariant A^+ and A^-, as indicated in Fig. 3.5.

To investigate the influence of the upstream geometry, the scattering matrix shown in Fig. 3.5 a) was measured for an open pipe section and the swirler using the method outlined in [Åbom, 1991]. Details of the set-up can be found in [Indlekofer et al., 2021]. Fig. 3.5 shows that the swirler does not significantly alter the acoustic waves where the reflection ($|S_{11}|$ and $|S_{22}|$) is approximately zero whilst the transmission ($|S_{12}|$ and $|S_{21}|$) is approximately unity, similar to the measurements of the open pipe section. These measurements were however taken without flow and the Mach number has an effect on the acoustic scattering properties. However, in this work, the effect of the swirler, cylinders, and streamlined bodies on the acoustic wave was neglected when computing the acoustic velocity using the MMM.

In a similar way, the influence of the area jump was measured and shown in b), where the coefficients now are represented by the transfer matrix elements T_{11} and T_{22}. The pressure was continuous across the area jump ($|T_{11}| \approx 1$) and the change in velocity was equal to the area ratio (($|T_{22}| \approx A_1/A_2$)). Hence, the area jump associated with the bluff body was modeled as an area jump where a simple velocity correction was applied.

3.2 Image processing

3.2.1 Planar view by Abel deconvolution

Most of the flames produced by using a single injector pipe were approximately axisymmetric. The OH-chemiluminescence image provides a line of sight integrated view of the HRR and the Abel deconvolution was used to calculate the planar distribution of the HRR from the projection by evaluating

$$q^A(r,x) = -\frac{1}{\pi}\int_r^\infty \frac{\mathrm{d}q(x,y)}{\mathrm{d}y}\frac{\mathrm{d}y}{\sqrt{y^2-r^2}}. \tag{3.10}$$

The integral in Eq. (3.10) is sensitive to noise and was evaluated using the 3 point deconvolution method described by Dasch [1992]. A typical time averaged image obtained from OH-chemiluminescence is shown in Figure. 3.6 a) and the planar distribition given by the Abel deconvolution is shown in b).

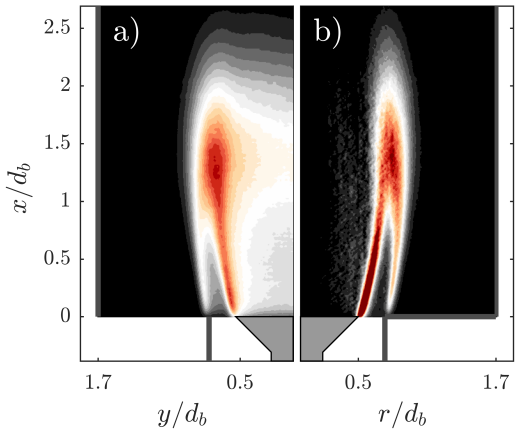

Figure 3.6: a) Typical mean flame image obtained from OH-chemiluminescence and b) the Abel deconvoluted view computed evaluating Eq. 3.10. The image intensity was normalised such that the volumetric integral gave the thermal power.

3.2.2 Flame surface and flame curvature

The OH-PLIF images were processed to obtain the instantaneous flame surface in a plane of interest. Coordinates of the flame surface was estimated using a Canny edge detection algorithm described by Rong et al. [2014], and the methodology applied was very similar to the approaches by [Balachandran et al., 2005; Worth and Dawson, 2012a, 2019].

The Canny edge detection provides a binary image $s(x,y)$, where the coordinates of the interface is given by $s(x,y) = 1$ corresponding to the coordinates of the flame surface. From the binary image the coordinates are grouped such that continuous portions $(x(l_s), y(l_s))$ are parameterized by the arc length l_s. From $x(l_s), y(l_s)$, the flame curvature κ was estimated using the method described by Mokhtarian and Abbasi [2002]. The flame curvature is related to the rate of directional change of the flame front and was used to quantify features and events such as flame pinch off and flame front wrinkling.

By convolving each coordinate by a kernel $g(l_s)$, the gradients of the smoothed coordinates (X,Y) are given by

$$X = x * g, \qquad \dot{X} = x * \dot{g}, \qquad \ddot{X} = x * \ddot{g}, \tag{3.11}$$

where the dot denotes a derivative with respect to the arc length $(\dot{:}) = \mathrm{d}/\mathrm{d}l_s$. The kernel g was chosen to be a Gaussian PDF and its derivatives ($\dot{g}$, and $\ddot{g}$) were obtained analytically and sampled with 25 equidistant points in the region $l_s =$

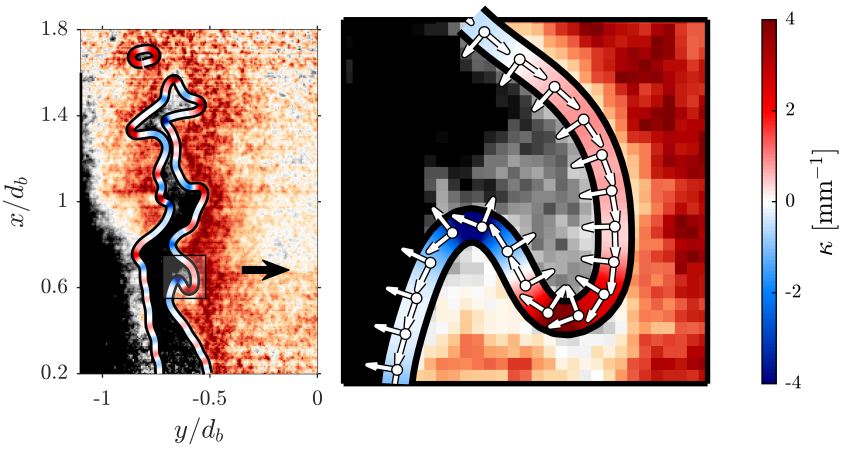

Figure 3.7: Typical example of an OH-PLIF image and the detected flame surface $(X(l_s), Y(l_s))$ which is coloured by curvature κ. In the zoomed view a typical flame wrinkling feature is characterised through an increase in the positive and negative level of curvature. The arrows indicate the direction of the parameterized where the flame normals point in towards the reactants.

$[-5\sigma_p,\ 5\sigma_p]$, where σ_p is the standard deviation. The convolution with g then acts like a smoothing kernel which was computed by circular convolution. After the various derivatives were computed, the curvature was given by

$$\kappa = \frac{\dot{X}\ddot{Y} - \dot{Y}\ddot{X}}{\left[\dot{X}^2 + \dot{Y}^2\right]^{3/2}}. \tag{3.12}$$

To make sure that the curvature of each segment had the correct sign, the average gradient of the OH-PLIF image was evaluated along the normal of (X,Y). The direction of the curve was chosen such that κ was positive when the flame normal points towards the reactants and negative when it points towards the products.

A typical OH-PLIF image and the corresponding flame surface, colored by curvature, is shown in Fig. 3.7. For closed flame curves, such as pockets, the curvature were kept for all coordinates whereas the first and last 12 points were discarded for open flame curves, to avoid end effect caused by the circular convolution.

Comparison of HRR and FSD

In premixed flames the HRR is proportional to the flame surface. To verify both methods the time averaged quantities are shown in Fig. 3.8 for a typical operating condition. In a) the mean flame surface density is shown, in b) the mean HRR is shown. Since OH-PLIF is a planar measurement, the planar distribution obtained

from Abel deconvolution is shown in b) and the HRR is normalised such that a volumetric integration gives the thermal power.

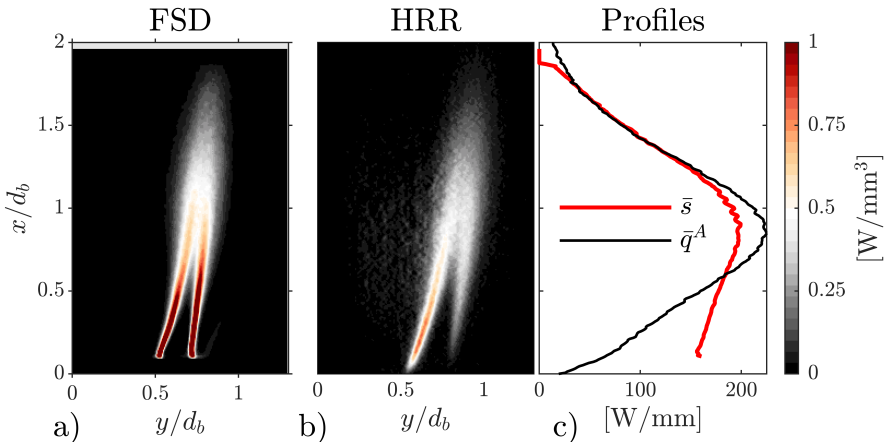

Figure 3.8: Comparison of the FSD obtained from OH-PLIF and the HRR obtained from imaging of OH-chemiluminescence. a) shows the mean FSD, b) shows the Abel deconvoluted HRR, and c) compared the stream-wise profile of both methods. There is a reasonable comparison between the two both in the flame shape and the integrated distribution.

There is a reasonably good agreement between the two methods where both are able to measure the M shaped flame. For a more quantitative comparison, the two fields are integrated to obtain the stream-wise distribution of HRR shown in c). Also here, both methods provide a reasonable agreement. However, OH-PLIF seems better in measuring the flame surface close to the bluff body.

3.2.3 Conditional averaging

When investigating the response of the flame or flow to harmonic oscillations it was useful to compute conditionally averaged quantities. For harmonic signals it is common to condition based on the phase of the external forcing signal. For a given quantity, e.g. velocity $\mathbf{u} = [u, v]$, the phase averaged components were denoted by brackets as $\langle \mathbf{u} \rangle$ and decomposed as

$$\langle \mathbf{u} \rangle = \bar{\mathbf{u}} + \langle \mathbf{u}' \rangle \,, \tag{3.13}$$

where $\langle \mathbf{u}' \rangle$ is the phase averaged fluctuation of $\mathbf{u}'$. These were approximated in two ways

1. The signal was binned according to the cycle phase t/T, where T is the cycle period. Taking the time average of each bin then provides the phase average, i.e. $\langle \mathbf{u} \rangle (t/T)$, at t/T.

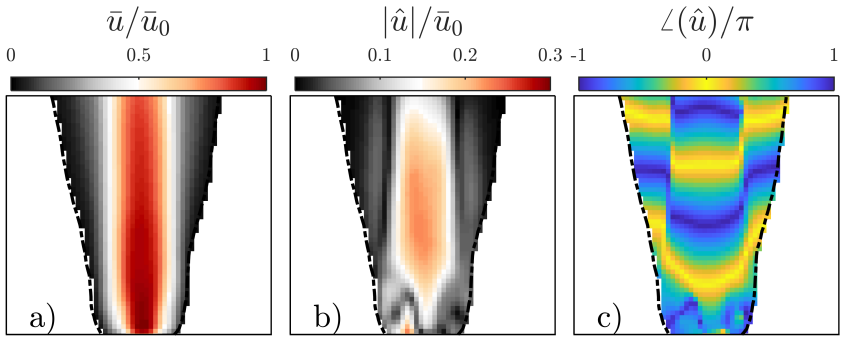

Figure 3.9: Example of conditional averaging of the velocity u. a) shows the time averaged velocity field. b) and c) show respectively the amplitude and phase of the Fourier mode. Time series of the phase averaged fluctuations was retrieved from the Fourier mode using Eq. 3.14.

2. The amplitude and phase of the signal was estimated by spectral analysis (described in 3.1.1) and the time series could be reconstructed from the Fourier mode, $\hat{\mathbf{u}}$.

Fourier mode decomposition

To obtain the phase averaged quantities by spectral analysis, each camera pixel was treated as individual time-series, similar to the method used by [Hauser et al., 2011; Worth et al., 2020]. The spatial distribution of the amplitude and phase, represented by $\hat{\mathbf{u}}$, was computed using the spectral methods (PSD or CPSD described in 3.1.1) . It should be noted that $\hat{\mathbf{u}}$ only contains information at a specific frequency, which was usually chosen to be the external excitation frequency f or any of the harmonics. When $\hat{\mathbf{u}}$ was known, $\langle \mathbf{u}' \rangle$ was given by

$$\langle \mathbf{u}' \rangle (x,y,t/T) = \Re \left(\tilde{\mathbf{u}} \exp \left(j2\pi t/T \right) \right), \tag{3.14}$$

and the time series could be reconstructed by

$$\langle \mathbf{u} \rangle (x,y,t/T) = \bar{\mathbf{u}} + \langle \mathbf{u}' \rangle. \tag{3.15}$$

An example is shown in Fig. 3.9 where the Fourier mode was computed from the stream-wise velocity $\hat{u}$. a) shows the mean velocity field $\bar{u}$, and b) and c) show the magnitude and phase of the Fourier mode respectively. An advantage of the Fourier mode is that the phase distribution $\angle(\bar{u})$, directly displays the direction of propagation and the wavelength of coherent structures. Similarly, the Fourier mode was computed for other quantities such as the HRR, Flame surface, etc.

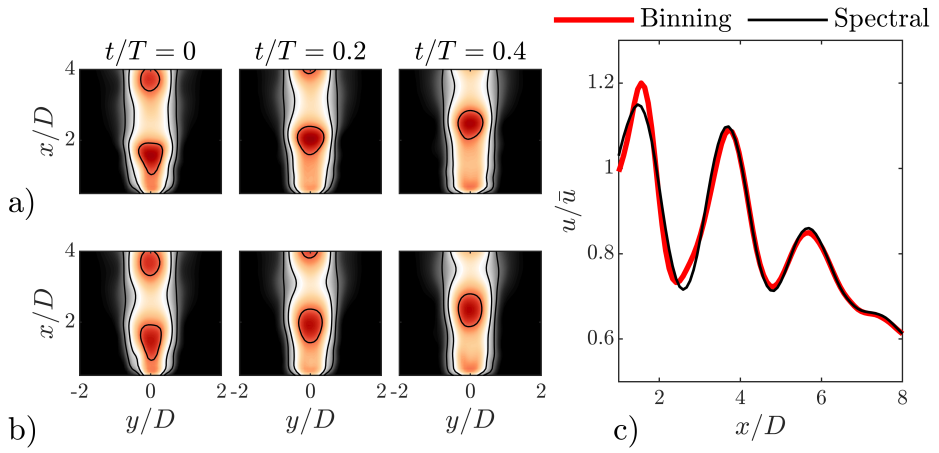

Figure 3.10: Comparison of the two methods of reconstructing the time series of the phase averaged stream-wise velocity $\langle u \rangle$. a) was reconstructed using the method of binning and b) using the Fourier mode (Eq. (3.15)). c) shows a comparison of the two methods where the center line profile at $y/D = 0$ is shown at $t/T = 0$.

Comparison of phase averaged and Fourier mode time series

For the case shown in Fig. 3.9, the two methods (binning and spectral) were used to obtain the phase average fluctuations. These are compared in Fig. 3.10. The phase averaged stream-wise velocity $\langle u \rangle$, was reconstructed through half a forcing cycle and a) shows the method of binning, and b) shows the reconstruction from the Fourier mode.

A quantitative comparison is given in c), where the profiles are compared along the jet center line $y/D = 0$, at $t/T = 0$. The two methods provide very similar dynamics and the Fourier mode was able to capture the amplitude and wavelength sufficiently.

Chapter 4

Summary of the research articles

In this chapter the six research articles are briefly summarised. The first 2 articles consider measurements and scaling of the linear behaviour of single and multiple interacting flames, where the effect of hydrogen enrichment and flame-flame interaction was investigated. In Article 3, the scaling proposed in Article 1 was utilised to model the stability of a single flame combustor as the fuel was changed from pure methane towards higher hydrogen concentration, while keeping the thermal power and equivalence ratio constant. In Articles 4 and 5 the effect of acoustic/convective interference on the FTF of single flames were investigate in detail. In Article 5 we develop and presented a control method which potentially can be used to utilise targeted acoustic/convective interference to stabilise TIs. In article 6 we investigated the response of a turbulent jet when placed at various position between the pressure and velocity nodes in an acoustic standing wave.

Article 1:
Scaling and Prediction of Transfer Functions in Lean Premixed H_2/CH_4-Flames
Eirik Æsøy, José G. Aguilar, Samuel Wiseman, Mirko R. Bothien, Nicholas A. Worth, and James R. Dawson.
Combustion and Flame, Volume 215, January 2020, Pages 269–282.
[Æsøy et al., 2020]

In *Article 1* the effect of hydrogen enrichment on the linear flame response in terms of the FTF was measured for a variety of fuel compositions. Hydrogen enrichment was shown to produce compact M shaped flames that stabilised on the bluff body and the outer rim of the injector pipe, and it was shown that the FTF shifted in a predictable way with respect to flame and flow parameters.

A modified DTL model was developed and used to extract the relevant time, length, and velocity scales from the measured FTF data. It was shown that the low pass filter characteristics in terms of the gain cut-off frequency and time delay scaled linearly with the ratio between the flame length and flow velocity at the dump plane. The main effect of hydrogen enrichment was shown to produce shorter flames with higher cut-off frequencies leading to flames that are potentially more susceptible to TIs at higher frequencies.

Furthermore, hydrogen enrichment was shown to produce a rising influence of gain and phase modulations occurring below the gain cut-off frequency. The DTL model was also used to extract the relevant scales from these features and it was shown that they originated in the cold flow, in particular due to vortex shedding from screws placed upstream to center the bluff body.

The DTL model reproduced all features of the FTF for a wide range of operating conditions and it was shown that all the model parameters scaled linearly with burner- and flame specific length and velocity scales. A generalised model was proposed where the FTF could be reproduced/extrapolated at operating conditions if these scales were known.

Article 2:

The Effect of Hydrogen Enrichment, Flame-Flame Interaction, Confinement, and Asymmetry on the Acoustic Response of Flames in a Can Combustor

Eirik Æsøy, Thomas Indlekofer, Francesco Gant, Alexis Cuquel, Mirko R. Bothien, and James R. Dawson.

Under review for Combustion and Flame.

In Article 2 the study considered in Article 1 was extended to consider three interacting flames. The main objective was to investigate the effect of hydrogen enrichment and flame/flame interaction on FTF, which were varied systematically by moving the flames closer together or changing the fuel mixture. The effects of confinement, swirl, and asymmetries were also considered. For a fixed flame spacing, hydrogen enrichment was shown to produce more compact flames with less flame interaction. It was also shown that the effect on the FTF of hydrogen enrichment was more significant than the effect of flame-flame interaction, confinement, and swirl. For the hydrogen enriched flames, the gain cut-off frequency and time delays were shown to scale linearly with the ratio between the flame length and flow velocity, similar to what was observed in Article 1 for single flames. This shows that prediction of the thermoacoustic behaviour of hydrogen flames might be less challenging compared to hydrocarbon based flames due to simpler scaling.

The nonlinear response was also measured in terms of the FDF for a selection

of cases, and it was shown that hydrogen enrichment lead to significantly higher saturation amplitude. This effect was also observed in the observed limit cycles where hydrogen enrichment lead to TIs, when the combustion chamber was made longer. Measurements were taken with different flame spacing and the effect of flame-flame interaction was shown to have a minor influence on the limit-cycle behaviour.

Article 3:

Predicting the Influence of Hydrogen in Combustion Instabilities

José G. Aguilar, Eirik Æsøy, and James R. Dawson.

Presented at SOTIC-2021 conference and winner of the best fundamental paper award. [Aguilar et al., 2021]

Under review for Combustion and Flame.

In Article 3 the generalised DTL model proposed in Article 1 was embedded into a linear network model to predict the onset of TIs in the single flame set up, when hydrogen was added to the fuel. Measurements were taken of TIs appearing when the length of the combustion chamber was increased. Hydrogen enrichment leads to a series of topological changes to the flame shape. The flame shape changed from a lifted flame attached at the wall, to a flame stabilised on the bluff body, before the flame detached from the wall forming M shaped flames. Increasing the hydrogen content more, after the flame changed to the M shape, it transitioned into a violent limit cycle. The onset of TIs was well reproduced using the network model with the scalable DTL model which provides validity to the approach.

Additionally, a bi-stable region was observed close to the point where the flame detached from the wall, where the flame had two different lengths for the same hydrogen content. When the chamber was shortened, both states were observed, indicating that the onset of instability forced the flame to detach from the wall. This was confirmed by the stability analysis run on both flame lengths, which showed that the bi-stable region coincides with the onset of linear instability.

Article 4:

Acoustic-Convective Interference in Transfer Functions of Methane/Hydrogen and Pure Hydrogen Flames

Eirik Æsøy, José G. Aguilar, Mirko R. Bothien, Nicholas A. Worth, and James R. Dawson.

The Journal of Engineering for Gas Turbines and Power (2021), Paper No: GTP-21-1297

[Æsøy et al., 2021a]

In article 1 the presence of gain and phase modulations was observed in the FTF, which were attributed to acoustic/convective interference. In article 4 these features were investigated where the cold flow was investigated in detail. Acoustically forced and unforced measurements were taken for the cold and reacting flows and screws placed upstream of the flame inside the injector pipe lead to a signature of the modulations in the hydrodynamic flow.

The modulations were shown to be centered around the natural shedding frequency of the vortex shedding in the wake of the screws. Hydrogen enrichment led to an increase in the cut-off frequency and as such the shedding frequency could appear in the FTF response that was not cut-off by the finite flame length.

A hydrodynamic transfer function (HTF) was constructed which relates the acoustic and convective velocity measured at the burner dump plane using the MMM and a hot-wire. Similar, modulations appeared in the HTF showing that the magnitude and phase of the modulations of the HRR, appearing in the FTF, were caused by an increase in the reference velocity.

Article 5:

Tailoring the Gain and Phase of the Flame Transfer Function through Targeted Convective-Acoustic Interference

Eirik Æsøy, Håkon T. Nygård, Nicholas A. Worth, and James R. Dawson.
Combustion and Flame, Volume 236, February 2022, 111813.
[Æsøy et al., 2022]

In Article 5 the effect of acoustic/convective interference, investigated in Article 4, was optimised by modifying the upstream geometry. The effect was investigated for stream lined bodies, cylinders, and a swirler placed at a variable distance relative to the dump plane. It was shown that when placed sufficiently close to the bluff body, the cylinders produced the strongest modulations in the FTF, whereas the influence of the stream lined bodies were smaller.

The influence of the cylinders followed a more predictable scaling where the time, velocity and length scales were retrieved using the DTL model introduced in Article 1. The behaviour of the modulations were shown to scale with two important groups: 1) the gain maximum and minimums were determined by the time delay from the geometry to the dump plane, and 2) the modulations were centered on the natural shedding frequency of the cylinder. These two scalable groups were utilised to propose a control strategy, where the gain and phase of the FTF could be tailored at specified frequencies by careful placement of cylinders.

In the second part of the paper the flame dynamics caused by the interference were

analysed in detail using flame front tracking methods. The changes in the gain was shown to be proportional to the amount of stream-wise interference of convective disturbances propagating along the flame front. Similarly, the change in the phase was shown to be caused by a change in the distance the convective disturbances had to propagate to reach the flame front. It was also shown that acoustic forcing was not causing a significant increase of flame wrinkling and pinch-off events, quantified through statistics of the flame curvature. However, forcing synchronised these events causing an increase or decrease in the global flame surface and HRR which significantly altered the linear flame response (FTF).

Article 6:

The Response of an Axisymmetric Jet Placed at Various Positions in a Standing Wave

Eirik Æsøy, José G. Aguilar, Nicholas A. Worth, and James R. Dawson.
Journal of Fluid Mechanics, Volume 917, March 2021, A16.
[Æsøy et al., 2021b]

In article 6 the hydrodynamic response of an axisymmetric jet place at various positions in a standing wave was investigated in detail. When placed at the velocity and pressure nodes the axisymmetric and flapping modes were excited through manipulation of the jet exit boundary conditions. At intermediate positions both these are simultaneously excited leading to aymmetric dynamics in the near field with a preferred direction induced by the phase between the transverse and longitudinal acoustic wave. The dynamics was analysed using Fourier mode analysis and it was shown that the boundary conditions at intermediate locations could be reproduced as a superposition of the symmetric and anti-symmetric modes observed at the two nodes.

Towards the far field the asymmetric forcing lead to jet bifurcation, where the momentum split into two or three individual momentum streams. The momentum in the far field were characterised through a statistical analysis, which showed that the jet spreading rate and asymmetry were proportional to the transverse forcing. Additionally, a model was proposed and used to decompose the bifurcated jets into the individual momentum streams, by superimposing self-similar profiles. It was shown that the individual streams behaved in a self-similar manner, with the classical decay and spreading rates of unforced turbulent jets.

Chapter 5

Conclusions

Due to the challenge of climate change, hydrogen fired GTs can potentially accelerate the green transition by providing large-scale power generation with negligible CO_2 emissions. In this work the main objective was to investigate the effect of hydrogen enrichment on the thermoacoustic response of premixed flames and hence contribute towards a better fundamental understanding to aid the transition towards hydrogen fired GTs. Initially, experimental investigations were performed on laboratory scale flames produced by single and multi flame combustors. These resulted in data published in Articles 1, 2, and 3 and the main conclusions with respect to the initial research goals defined in Chapter 1 are summarised below.

- Compared to operations with pure methane, **hydrogen enrichment** led to more convectively compact flames. This resulted in significant changes to the thermoacoustic response, where an increase in the gain cut-off frequency and a shorter time delay were observed. In terms of TIs, the flame became more responsive over a wider range of frequencies, leading to higher probability of being unstable.

- For the bluff body stabilised flames, **hydrogen enrichment** led to M shaped flames, which stabilised on the inner and outer lips of the pipe and bluff body respectively, at the dump plane. The thermoacoustic response of these flames scaled linearly with the flame and flow parameters, and the most important parameters were the exit velocity and the flame length, given by the distance to the centre of HRR. The changes in the FTF of these flames were well captured using a DTL model, whose model parameters followed a predictable scaling. This approach allowed to extrapolate the FTF and investigate the linear stability in parts of the operational map where experimental

measurements were not used.

- When several interacting flames were introduced **hydrogen enrichment** again led to shorter and more compact flames, which exhibited less flame-flame interaction. The reduced level of flame-flame interaction was observed to make the difference from single flame FTF measurements less significant. For the flames with larger contents of hydrogen the cut-off frequency and time delay scaled linearly with the velocity and flame length. This shows that the effect of flame-flame interaction plays a less crucial role for hydrogen flames.

  The nonlinear response of interacting flames were investigated and it was observed that **hydrogen enrichment** lead to a significant increase in the saturation of the FDF. Furthermore, the combustor was shown to be more prone to instabilities at higher hydrogen contents. The influence of flame-flame interaction was shown to play a minor role on the frequency and amplitude of the limit-cycle oscillations.

While investigating the first main objective, **hydrogen enrichment** also lead to FTFs with significant gain and phase modulations caused by acoustic-convective interference. These had previously only been observed in flames stabilised using both a swirler in combination with a bluff body ([Gatti et al., 2019; Komarek and Polifke, 2010; Palies et al., 2010]). In Articles 4 and 5 we investigated the nature and influence of acoustic-convective interference in detail. The main conclusions are summarised below

- Cylindrical screws placed upstream of the bluff body lead to convective disturbances that synchronised to the acoustic forcing, generating acoustic-convective interference similar to what has been observed in swirling flames (e.g. [Komarek and Polifke, 2010; Palies et al., 2010]). These results show that the phenomenon is not only restricted to swirling flows, and that any upstream geometry, that generates vortex shedding in its wake, can lead to significant influence on the flame response if synchronised with the acoustics.

- The influence of convective disturbances was shown to be well captured using DTL models. Scaling of the model parameters revealed that the modulations appeared in the proximity of the natural shedding frequency of the upstream geometry. For the cylinders, it was shown to be very similar to the scaling of the well known Kármán vortex street. Hence, the influence of acoustic-convective interference could be amplified by utilising the Kármán scaling for cylinders in a free stream.

The peaks and troughs of the gain and phase modulations were shown to be determined by the time delay for the convective disturbances to propagate from the cylinders to the dump plane. By matching the cylinder diameter such that the natural shedding frequency coincides with the acoustic mode of the combustor, and then carefully placing the cylinder to generate destructive interference at a specified frequency, the effect could be used to tailor the gain and phase of the FTF. This could potentially be used to stabilise the combustor when exhibiting TIs.

- The low pass filter behaviour of the flame effectively filters out the influence of natural shedding frequencies occurring at frequencies larger than the gain cut-off frequency. As **hydrogen enrichment** lead to more compact flames with higher cut-off frequencies, these flames were shown to be significantly more prone to the influence of acoustic-convective interference. This feature suggests that hydrogen flames are more susceptible to controlled disturbances, hence making them excellent candidates to control using targeted acoustic-convective interference.

In Article 6 we investigated the influence of simultaneous transverse and longitudinal acoustic forcing on the response of a turbulent jet by placing it at various location in an acoustic standing wave. The setup was aimed to simulate a simple base flow in a situation occurring often in annular combustion chambers studied in [Dawson and Worth, 2014; Nygård et al., 2019; Worth and Dawson, 2013a] and was a more general case than the jet studied at the pressure node by [Worth et al., 2020]. The main conclusions are summarised below.

- The flow dynamics in the near field of the jet was shown to change significantly when moved relative to the nodes of the acoustic standing wave. At the velocity node, symmetric roll up of vortices was observed, whereas at the pressure node, anti-symmetric vortex pattern was observed. The response observed at intermediate positions, where both fluctuations were present, resembled a superposition of the responses observed at the two nodes. This was verified where the jet exit boundary conditions could be reproduced using a superposition of the Fourier modes observed at the pressure and velocity nodes.

  These observations support the validity of the strategy, commonly used to model the influence of longitudinal and transverse acoustic oscillations of flames, where the flame response is obtained from experiments on single flame combustors. The transverse forcing is however usually neglected, or not measured, except from some recent studies ([Nygård, 2021; Nygård

et al., 2019; O'Connor et al., 2013; Saurabh and Paschereit, 2017]). If the global behaviour can be reproduced as a superposition of the response obtained at the nodes, the response to pure symmetric and anti-symmetric forcing might be sufficient to capture the combined effect at intermediate locations by superposition.

- Towards the far field of the jet, transverse forcing caused the jet to split into separate branches and form bifurcated and trifurcated jets. At positions between the two nodes, the jet tilted towards the nearest pressure node and were shown to have a preferred direction, where the branch were shown to contain most of the momentum. A model was proposed to separate the far field into its individual branches, which then were shown to behave in a self-similar manner.

Bibliography

V. S. Acharya and T. C. Lieuwen. Role of azimuthal flow fluctuations on flow dynamics and global flame response of axisymmetric swirling flames. In *52nd aerospace sciences meeting*, page 0654, 2014.

R. J. Adrian and J. Westerweel. *Particle Image Velocimetry*. Cambridge University Press, 2011.

J. G. Aguilar, E. Æsøy, and Dawson J. R. Predicting the influence of hydrogen in combustion instabilities. in:Symposium on Thermoacoustics in Combustion: Industry Meets Academia (SoTiC), Munich, Germany, 2021. ,p. 9.

P. R. Alemela, D. Fanaca, C. Hirsch, T. Sattelmayer, and B. Schuermans. Determination and Scaling of Thermo Acoustic Characteristics of Premixed Flames. *Int. J. Spray Combust. Dyn.*, 2(2):169–198, June 2010. doi: 10.1260/1756-8277.2.2.169.

B. O. Ayoola, R. Balachandran, J. H. Frank, E. Mastorakos, and C. F. Kaminski. Spatially resolved heat release rate measurements in turbulent premixed flames. *Combust. Flame*, 144(1):1–16, January 2006. doi: 10.1016/j.combustflame.2005.06.005.

R. Balachandran, B. O. Ayoola, C. F. Kaminski, A. P. Dowling, and E. Mastorakos. Experimental investigation of the nonlinear response of turbulent premixed flames to imposed inlet velocity oscillations. *Combust. Flame*, 143(1):37–55, October 2005. doi: 10.1016/j.combustflame.2005.04.009.

G. K. Batchelor and A. E. Gill. Analysis of the stability of axisymmetric jets. *J. Fluid Mech.*, 14(04):529, December 1962. doi: 10.1017/S0022112062001421.

H. A. Becker and T. A. Massaro. Vortex evolution in a round jet. *J. Fluid Mech.*, 31(3):435–448, February 1968. doi: 10.1017/S0022112068000248.

J. Beeckmann, R. Hesse, S. Kruse, A. Berens, N. Peters, H. Pitsch, and M. Matalon. Propagation speed and stability of spherically expanding hydrogen/air flames: Experimental study and asymptotics. *Proc. Combust. Inst.*, 36 (1):1531–1538, January 2017. doi: 10.1016/j.proci.2016.06.194.

R. S. Blumenthal, P. Subramanian, R. I. Sujith, and W. Polifke. Novel perspectives on the dynamics of premixed flames. *Combust. Flame*, 160(7):1215–1224, July 2013. doi: 10.1016/j.combustflame.2013.02.005.

M. R. Bothien, N. Noiray, and B. Schuermans. Analysis of Azimuthal Thermoacoustic Modes in Annular Gas Turbine Combustion Chambers. *J. Eng. Gas Turbines Power*, 137(6), June 2015. doi: 10.1115/1.4028718.

M. R. Bothien, A. Ciani, J. P. Wood, and G. Fruechtel. Toward Decarbonized Power Generation With Gas Turbines by Using Sequential Combustion for Burning Hydrogen. *J. Eng. Gas Turbines Power*, 141(12), December 2019. doi: 10.1115/1.4045256.

J. F. Bourgouin, D. Durox, J. P. Moeck, T. Schuller, and S. Candel. Self-Sustained Instabilities in an Annular Combustor Coupled by Azimuthal and Longitudinal Acoustic Modes. American Society of Mechanical Engineers Digital Collection, November 2013. doi: 10.1115/GT2013-95010.

M. Brower, E. L. Petersen, W. Metcalfe, H. J. Curran, M. Füri, G. Bourque, N. Aluri, and F. Güthe. Ignition Delay Time and Laminar Flame Speed Calculations for Natural Gas/Hydrogen Blends at Elevated Pressures. *J. Eng. Gas Turbines Power*, 135(2), February 2013. doi: 10.1115/1.4007763.

G. L. Brown and A. Roshko. On density effects and large structure in turbulent mixing layers. *J. Fluid Mech.*, 64(4):775–816, July 1974. doi: 10.1017/S002211207400190X.

N. A. Bunce, B. D. Quay, and D. A. Santavicca. Interaction Between Swirl Number Fluctuations and Vortex Shedding in a Single-Nozzle Turbulent Swirling Fully-Premixed Combustor. *J. Eng. Gas Turbines Power*, 136(2), October 2013. doi: 10.1115/1.4025361.

P. E. Buschmann, G. A. Mensah, F. Nicoud, and J. P. Moeck. Solution of Thermoacoustic Eigenvalue Problems With a Noniterative Method. *J. Eng. Gas Turbines Power*, 142(031022), February 2020. doi: 10.1115/1.4045076.

S. Candel. Combustion dynamics and control: Progress and challenges. *Proc. Combust. Inst.*, 29(1):1–28, January 2002. doi: 10.1016/S1540-7489(02)80007-4.

S. Candel, D. Durox, T. Schuller, J. F. Bourgouin, and Jonas P. Moeck. Dynamics of Swirling Flames. *Annual Review of Fluid Mechanics*, 46(1):147–173, 2014. doi: 10.1146/annurev-fluid-010313-141300.

E. Cetinkaya, I. Dincer, and G. F. Naterer. Life cycle assessment of various hydrogen production methods. *Int. J. Hydrog.*, 37(3):2071–2080, February 2012. doi: 10.1016/j.ijhydene.2011.10.064.

M. Conte, A. Iacobazzi, M. Ronchetti, and R. Vellone. Hydrogen economy for a sustainable development: state-of-the-art and technological perspectives. *Journal of Power Sources*, 100(1):171–187, November 2001. doi: 10.1016/S0378-7753(01)00893-X.

G. W. Crabtree, M. S. Dresselhaus, and M. V. Buchanan. The hydrogen economy. *Physics today*, 57(12):39–44, 2004. Publisher: American Institute of Physics.

L. Crocco. Aspects of Combustion Stability in Liquid Propellant Rocket Motors Part I: Fundamentals. Low Frequency Instability With Monopropellants. *Journal of the American Rocket Society*, 21(6):163–178, 1951. doi: 10.2514/8.4393.

S. C. Crow and F. H. Champagne. Orderly structure in jet turbulence. *J. Fluid Mech.*, 48(03):547, August 1971. doi: 10.1017/S0022112071001745.

A. Cuquel, D. Durox, and T. Schuller. Impact of flame base dynamics on the nonlinear frequency response of conical flames. *Comptes Rendus Mécanique*, 341(1):171–180, January 2013. doi: 10.1016/j.crme.2012.11.004.

C. J. Dasch. One-dimensional tomography: a comparison of Abel, onion-peeling, and filtered backprojection methods. *Applied Optics*, 31(8):1146, March 1992. doi: 10.1364/AO.31.001146.

J. R. Dawson and N. A. Worth. Flame dynamics and unsteady heat release rate of self-excited azimuthal modes in an annular combustor. *Combust. Flame*, 161(10):2565–2578, October 2014. doi: 10.1016/j.combustflame.2014.03.021.

J. R. Dawson and N. A. Worth. The effect of baffles on self-excited azimuthal modes in an annular combustor. *Proc. Combust. Inst.*, 35(3):3283–3290, January 2015. doi: 10.1016/j.proci.2014.07.011.

F. Di Sabatino, Thibault F. Guiberti, W. R. Boyette, W. L. Roberts, J. P. Moeck, and D. A. Lacoste. Effect of pressure on the transfer functions of premixed methane and propane swirl flames. *Combust. Flame*, 193:272–282, July 2018. doi: 10.1016/j.combustflame.2018.03.011.

I. Dincer and C. Acar. Review and evaluation of hydrogen production methods for better sustainability. *Int. J. Hydrog.*, 40(34):11094–11111, September 2015. doi: 10.1016/j.ijhydene.2014.12.035.

J. M. Donbar, J. F. Driscoll, and C. D. Carter. Reaction zone structure in turbulent nonpremixed jet flames—from CH-OH PLIF images. *Combust. Flame*, 122(1): 1–19, July 2000. doi: 10.1016/S0010-2180(00)00098-5.

A. P. Dowling. Nonlinear self-excited oscillations of a ducted flame. *J. Fluid Mech.*, 346:271–290, September 1997. doi: 10.1017/S0022112097006484.

A. P. Dowling. A kinematic model of a ducted flame. *J. Fluid Mech.*, 394:51–72, September 1999. doi: 10.1017/S0022112099005686.

D. Durox, T. Schuller, N. Noiray, and S. Candel. Experimental analysis of nonlinear flame transfer functions for different flame geometries. *Proc. Combust. Inst.*, 32(1):1391–1398, 2009. doi: 10.1016/j.proci.2008.06.204.

Hydrogen Gas Turbines ETN. The path towards a zero-carbon gas turbine, 2020. https://etn.global/wp-content/uploads/2020/02/ETN-Hydrogen-Gas-Turbines-report.pdf.

D. Fanaca, P. R. Alemela, C. Hirsch, and T. Sattelmayer. Comparison of the Flow Field of a Swirl Stabilized Premixed Burner in an Annular and a Single Burner Combustion Chamber. *J. Eng. Gas Turbines Power*, 132(7), April 2010. doi: 10.1115/1.4000120.

M. Fleifil, A. M. Annaswamy, Z. A. Ghoneim, and A. F. Ghoniem. Response of a laminar premixed flame to flow oscillations: A kinematic model and thermoacoustic instability results. *Combust. Flame*, 106(4):487–510, September 1996. doi: 10.1016/0010-2180(96)00049-1.

M. Gatti. *Combustion dynamics of premixed swirling flames with different injectors*. PhD Thesis, Université Paris-Saclay; Technische Universität (Darmstadt, Allemagne), 2019.

M. Gatti, R. Gaudron, C. Mirat, and T. Schuller. Effects of the Injector Design on the Transfer Function of Premixed Swirling Flames. American Society of Mechanical Engineers, June 2017. doi: 10.1115/GT2017-63874.

M. Gatti, R. Gaudron, C. Mirat, L. Zimmer, and T. Schuller. A Comparison of the Transfer Functions and Flow Fields of Flames With Increasing Swirl Number. pages V04BT04A003–V04BT04A003. American Society of Mechanical Engineers, June 2018. doi: 10.1115/GT2018-76105.

M. Gatti, R. Gaudron, C. Mirat, L. Zimmer, and T. Schuller. Impact of swirl and bluff-body on the transfer function of premixed flames. *Proc. Combust. Inst.*, 37(4):5197–5204, January 2019. doi: 10.1016/j.proci.2018.06.148.

R. Gaudron, M. Gatti, C. Mirat, and T. Schuller. Flame Describing Functions of a Confined Premixed Swirled Combustor With Upstream and Downstream Forcing. *J. Eng. Gas Turbines Power*, 141(5), May 2019. doi: 10.1115/1.4041000.

D. G. Goodwin, R. L. Speth, H. K. Moffat, and B. W. Weber. *Cantera: An Object-oriented Software Toolkit for Chemical Kinetics, Thermodynamics, and Transport Processes*. 2020. doi: 10.5281/zenodo.1174508.

C. J. Goy, S. R James, S. Rea, T. Lieuwen, and V. Yang. Monitoring combustion instabilities: E. ON UK's experience. *Combustion Instabilities in Gas Turbine Engines: Operational Experience, Fundamental Mechanisms, and Modeling*, 210:163–175, 2005. Publisher: AIAA (American Institute of Aeronautics & Astronautics).

A. Gruber, M. R. Bothien, A. Ciani, K. Aditya, J. H. Chen, and F. A. Williams. Direct Numerical Simulation of hydrogen combustion at auto-ignitive conditions: Ignition, stability and turbulent reaction-front velocity. *Combust. Flame*, 229: 111385, July 2021. doi: 10.1016/j.combustflame.2021.02.031.

M. Hauser, M. Lorenz, and T. Sattelmayer. Influence of Transversal Acoustic Excitation of the Burner Approach Flow on the Flame Structure. *J. Eng. Gas Turbines Power*, 133(4), April 2011. doi: 10.1115/1.4002175.

B. Higgins, M. Q. McQuay, F. Lacas, J. C. Rolon, N. Darabiha, and S. Candel. Systematic measurements of OH chemiluminescence for fuel-lean, high-pressure, premixed, laminar flames. *Fuel*, 80(1):67–74, January 2001. doi: 10.1016/S0016-2361(00)00069-7.

C. Hirsch, D. Fanaca, P. Reddy, W. Polifke, and T. Sattelmayer. Influence of the swirler design on the flame transfer function of premixed flames. volume Volume 2: Turbo Expo 2005 of *Turbo Expo: Power for Land, Sea, and Air*, pages 151–160, 06 2005. doi: 10.1115/GT2005-68195.

E. Hu, Z. Huang, J. He, C. Jin, and J. Zheng. Experimental and numerical study on laminar burning characteristics of premixed methane–hydrogen–air flames. *Int. J. Hydrog.*, 34(11):4876–4888, June 2009. doi: 10.1016/j.ijhydene.2009.03.058.

A. Huber and W. Polifke. Dynamics of Practical Premixed Flames, Part II: Identification and Interpretation of CFD Data. *Int. J. Spray Combust. Dyn.*, 1(2): 229–249, June 2009. doi: 10.1260/175682709788707440.

F. Hussain and H. S. Husain. Elliptic jets. Part 1. Characteristics of unexcited and excited jets. *J. Fluid Mech.*, 208(-1):257, November 1989. doi: 10.1017/S0022112089002843.

H. J. Hussein, S. P. Capp, and W. K. George. Velocity measurements in a high-Reynolds-number, momentum-conserving, axisymmetric, turbulent jet. *J. Fluid Mech.*, 258:31–75, January 1994. doi: 10.1017/S002211209400323X.

M. Ilbas, A. P. Crayford, İ. Yılmaz, P. J. Bowen, and N. Syred. Laminar-burning velocities of hydrogen–air and hydrogen–methane–air mixtures: An experimental study. *Int. J. Hydrog.*, 31(12):1768–1779, September 2006. doi: 10.1016/j.ijhydene.2005.12.007.

T. Indlekofer, A. Faure-Beaulieu, N. Noiray, and J. R. Dawson. The effect of dynamic operating conditions on the thermoacoustic response of hydrogen rich flames in an annular combustor. *Combust. Flame*, 223:284–294, January 2021. doi: 10.1016/j.combustflame.2020.10.013.

A. Kaufmann, F. Nicoud, and T. Poinsot. Flow forcing techniques for numerical simulation of combustion instabilities. *Combust. Flame*, 131(4):371–385, December 2002. doi: 10.1016/S0010-2180(02)00419-4.

D. Kim and S. W. Park. Effects of hydrogen addition on flame structure and forced flame response to velocity modulation in a turbulent lean premixed combustor. *Fuel*, 89(11):3475–3481, November 2010. doi: 10.1016/j.fuel.2010.06.021.

D. Kim, J. Park, D. Han, and K. T. Kim. Symmetry-breaking for the control of combustion instabilities of two interacting swirl-stabilized flames. *Combust. Flame*, 194:180–194, August 2018. doi: 10.1016/j.combustflame.2018.04.035.

K. T. Kim and D. A. Santavicca. Generalization of Turbulent Swirl Flame Transfer Functions in Gas Turbine Combustors. *Combust. Sci. Technol.*, 185(7):999–1015, July 2013a. doi: 10.1080/00102202.2012.752734.

K. T. Kim and D. A. Santavicca. Interference mechanisms of acoustic/convective disturbances in a swirl-stabilized lean-premixed combustor. *Combust. Flame*, 160(8):1441–1457, August 2013b. doi: 10.1016/j.combustflame.2013.02.022.

K. T. Kim, J. G. Lee, B. D. Quay, and D. A. Santavicca. Response of partially premixed flames to acoustic velocity and equivalence ratio perturbations. *Combust. Flame*, 157(9):1731–1744, September 2010. doi: 10.1016/j.combustflame.2010.04.006.

T. Komarek and W. Polifke. Impact of Swirl Fluctuations on the Flame Response of a Perfectly Premixed Swirl Burner. *J. Eng. Gas Turbines Power*, 132(6), June 2010. doi: 10.1115/1.4000127.

J. Kopitz, A. Huber, T. Sattelmayer, and W. Polifke. Thermoacoustic Stability Analysis of an Annular Combustion Chamber With Acoustic Low Order Modeling and Validation Against Experiment. volume Volume 2: Turbo Expo 2005 of *Turbo Expo: Power for Land, Sea, and Air*, pages 583–593, 06 2005. doi: 10.1115/GT2005-68797.

K. Kunze, C. Hirsch, and T. Sattelmayer. Transfer function measurements on a swirl stabilized premix burner in an annular combustion chamber. volume Volume 1: Turbo Expo 2004 of *Turbo Expo: Power for Land, Sea, and Air*, pages 21–29, 06 2004. doi: 10.1115/GT2004-53106.

S. M. Kusek, T. C. Corke, and P. Reisenthel. Seeding of helical modes in the initial region of an axisymmetric jet. *Experiments in Fluids*, 10(2):116–124, December 1990. doi: 10.1007/BF00215019.

C. Külsheimer and H. Büchner. Combustion dynamics of turbulent swirling flames. *Combust. Flame*, 131(1):70–84, October 2002. doi: 10.1016/S0010-2180(02)00394-2.

D. Laera, T. Schuller, K. Prieur, D. Durox, S. M. Camporeale, and S. Candel. Flame Describing Function analysis of spinning and standing modes in an annular combustor and comparison with experiments. *Combust. Flame*, 184:136–152, October 2017. doi: 10.1016/j.combustflame.2017.05.021.

M. Lee and W. C. Reynolds. Bifurcating and blooming jets. report tf-22, thermosciences division, department of mechanical engineering, 1985.

T. Lee, J. Lee, J. Park, D. Han, and K. T. Kim. Staggered swirler arrangement in two self-excited interacting swirl flames. *Combust. Flame*, 198:363–375, December 2018. doi: 10.1016/j.combustflame.2018.10.001.

T. Lee, J. Park, D. Han, and K. T. Kim. The dynamics of multiple interacting swirl-stabilized flames in a lean-premixed gas turbine combustor. *Proc. Combust. Inst.*, 37(4):5137–5145, January 2019. doi: 10.1016/j.proci.2018.05.110.

B. Lewis and G. Elbe. *Combustion, Flames and Explosions of Gases*. Elsevier, December 2012.

T. Lieuwen. Experimental Investigation of Limit-Cycle Oscillations in an Unstable Gas Turbine Combustor. *J. Propuls. Power*, 18(1):61–67, 2002. doi: 10.2514/2.5898.

T. Lieuwen. *Unsteady Combustor Physics*. Cambridge University Press, Cambridge, 2012. doi: 10.1017/CBO9781139059961.

T. Lieuwen and Vigor Yang. *Combustion Instabilities In Gas Turbine Engines: Operational Experience, Fundamental Mechanisms, and Modeling*. American Institute of Aeronautics and Astronautics, Reston ,VA, 2006. doi: 10.2514/4.866807.

E. K. Longmire and L. H. Duong. Bifurcating jets generated with stepped and sawtooth nozzles. *Physics of Fluids*, 8(4):978–992, April 1996. doi: 10.1063/1.868876.

E. K. Longmire, J. K. Eaton, and C. J. Elkins. Control of jet structure by crown-shaped nozzles. *AIAA Journal*, 30(2):505–512, February 1992. doi: 10.2514/3.10945.

M. Mazur, H. T. Nygård, J. R. Dawson, and N. A. Worth. Characteristics of self-excited spinning azimuthal modes in an annular combustor with turbulent premixed bluff-body flames. *Proc. Combust. Inst.*, 37(4):5129–5136, January 2019. doi: 10.1016/j.proci.2018.07.080.

H. J. Merk. An analysis of unstable combustion of premixed gases. *Symposium (International) on Combustion*, 6(1):500–512, January 1957a. doi: 10.1016/S0082-0784(57)80067-8.

H. J. Merk. Analysis of heat-driven oscillations of gas flows. *Applied Scientific Research, Section A*, 6(4):317–336, July 1957b. doi: 10.1007/BF03184653.

F. Mokhtarian and S. Abbasi. Shape similarity retrieval under affine transforms. *Pattern Recognition*, 35(1):31–41, January 2002. doi: 10.1016/S0031-3203(01)00040-1.

N. Z. Muradov and T. N. Veziroğlu. From hydrocarbon to hydrogen–carbon to hydrogen economy. *Int. J. Hydrog.*, 30(3):225–237, March 2005. doi: 10.1016/j.ijhydene.2004.03.033.

N. Noiray, D. Durox, T. Schuller, and S. Candel. A novel strategy for passive control of combustion instabilities through modification of flame dynamics. volume Volume 3: Combustion, Fuels and Emissions, Parts A and B of *Turbo Expo: Power for Land, Sea, and Air*, pages 1133–1144, 06 2008. doi: 10.1115/GT2008-51520.

H. T. Nygård. *Experimental Measurement of Flame Describing Functions in an Azimuthally Forced Annular Combustor*. NTNU, 2021.

H. T. Nygård and N. A. Worth. Flame Transfer Functions and Dynamics of a Closely Confined Premixed Body Stabilised Flame with Swirl. *J. Eng. Gas Turbines Power*, January 2021. doi: 10.1115/1.4049513.

H. T. Nygård, M. Mazur, J. R. Dawson, and N. A. Worth. Flame dynamics of azimuthal forced spinning and standing modes in an annular combustor. *Proc. Combust. Inst.*, 37(4):5113–5120, January 2019. doi: 10.1016/j.proci.2018.08.034.

J. C. Oefelein and V. Yang. Comprehensive review of liquid-propellant combustion instabilities in F-1 engines. *J. Propuls. Power*, 9(5):657–677, September 1993. doi: 10.2514/3.23674.

G. Oztarlik, L. Selle, T. Poinsot, and T. Schuller. Suppression of instabilities of swirled premixed flames with minimal secondary hydrogen injection. *Combust. Flame*, 214:266–276, April 2020. doi: 10.1016/j.combustflame.2019.12.032.

J. O'Connor, N. A. Worth, and J. R. Dawson. Flame and Flow Dynamics of a Self-Excited, Standing Wave Circumferential Instability in a Model Annular Gas Turbine Combustor. American Society of Mechanical Engineers Digital Collection, November 2013. doi: 10.1115/GT2013-95897.

J. O'Connor, V. Acharya, and T. Lieuwen. Transverse combustion instabilities: Acoustic, fluid mechanic, and flame processes. *Prog. Energy Combust. Sci.*, 49:1–39, August 2015. doi: 10.1016/j.pecs.2015.01.001.

P. Palies, D. Durox, T. Schuller, and S. Candel. The combined dynamics of swirler and turbulent premixed swirling flames. *Combust. Flame*, 157:1698–1717, September 2010. doi: 10.1016/j.combustflame.2010.02.011.

P. Palies, D. Durox, T. Schuller, and S. Candel. Acoustic–convective mode conversion in an aerofoil cascade. *J. Fluid Mech.*, 672:545–569, April 2011a. doi: 10.1017/S0022112010006142.

P. Palies, D. Durox, T. Schuller, and S. Candel. Experimental Study on the Effect of Swirler Geometry and Swirl Number on Flame Describing Functions. *Combust. Sci. Technol.*, 183(7):704–717, April 2011b. doi: 10.1080/00102202.2010.538103.

P. Palies, D. Durox, T. Schuller, and S. Candel. Nonlinear combustion instability analysis based on the flame describing function applied to turbulent premixed swirling flames. *Combust. Flame*, 158(10):1980–1991, October 2011c. doi: 10.1016/j.combustflame.2011.02.012.

D. Parekh, W. Reynolds, and M. Mungal. Bifurcation of round air jets by dual-mode acoustic excitation. In *25th AIAA Aerospace Sciences Meeting*, Aerospace Sciences Meetings. American Institute of Aeronautics and Astronautics, March 1987. doi: 10.2514/6.1987-164.

T. Poinsot. Prediction and control of combustion instabilities in real engines. *Proc. Combust. Inst.*, 36(1):1–28, January 2017. doi: 10.1016/j.proci.2016.05.007.

T. Poinsot and D. Veynante. *Theoretical and numerical combustion*. RT Edwards, Inc., 2005.

W. Polifke. Black-box system identification for reduced order model construction. *Annals of Nuclear Energy*, 67:109–128, May 2014. doi: 10.1016/j.anucene.2013.10.037.

W. Polifke. Modeling and analysis of premixed flame dynamics by means of distributed time delays. *Prog. Energy Combust. Sci.*, 79:100845, July 2020. doi: 10.1016/j.pecs.2020.100845.

W. Polifke and C. Lawn. On the low-frequency limit of flame transfer functions. *Combust. Flame*, 151(3):437–451, November 2007. doi: 10.1016/j.combustflame.2007.07.005.

W. Polifke, J. Kopitz, and A. Serbanoviv. Impact of the fuel time lag distribution in elliptical premix nozzles on combustion stability. In *7th AIAA/CEAS Aeroacoustics Conference and Exhibit*, pages 1–11, Reston, Virigina, May 2001. American Institute of Aeronautics and Astronautics. doi: 10.2514/6.2001-2104.

M. Raffel, C. E. Willert, F. Scarano, C. J. Kähler, S. T. Wereley, and J. Kompenhans. *Particle Image Velocimetry: A Practical Guide*. Springer, April 2018.

K. Deergha Rao and M. N. S. Swamy. *Digital Signal Processing: Theory and Practice*. Springer Singapore, 2018. doi: 10.1007/978-981-10-8081-4.

L. Rayleigh. The explanation of certain acoustical phenomena. *Roy. Inst. Proc.*, 8: 536–542, 1878.

W. C. Reynolds, D. E. Parekh, P. J. D. Juvet, and M. J. D. Lee. Bifurcating and Blooming Jets. *Annual Review of Fluid Mechanics*, 35(1):295–315, 2003. doi: 10.1146/annurev.fluid.35.101101.161128.

W. Rong, Z. Li, W. Zhang, and L. Sun. An improved Canny edge detection algorithm. In *2014 IEEE International Conference on Mechatronics and Automation*, pages 577–582, August 2014. doi: 10.1109/ICMA.2014.6885761.

J. Samarasinghe, S. J. Peluso, B. D. Quay, and D. A. Santavicca. The Three-Dimensional Structure of Swirl-Stabilized Flames in a Lean Premixed Multinozzle Can Combustor. *J. Eng. Gas Turbines Power*, 138, September 2015. doi: 10.1115/1.4031439.

T. Sattelmayer. Influence of the Combustor Aerodynamics on Combustion Instabilities From Equivalence Ratio Fluctuations. *J. Eng. Gas Turbines Power*, 125(1):11–19, January 2003. doi: 10.1115/1.1365159.

T. Sattelmayer and W. Polifke. Assessment of methods for the computation of the linear stability of combustors. *Combust. Sci. Technol.*, 175(3):453–476, March 2003. doi: 10.1080/00102200302382.

A. Saurabh and C. O. Paschereit. Dynamics of premixed swirl flames under the influence of transverse acoustic fluctuations. *Combust. Flame*, 182:298–312, August 2017. doi: 10.1016/j.combustflame.2017.04.014.

B. Schuermans, V. Bellucci, F. Guethe, F.and Meili, P. Flohr, and C. O. Paschereit. A Detailed Analysis of Thermoacoustic Interaction Mechanisms in a Turbulent Premixed Flame. In *GT2004*, pages 539–551, Volume 1: Turbo Expo 2004, June 2004. doi: 10.1115/GT2004-53831.

B. Schuermans, F. Guethe, D. Pennell, D. Guyot, and C. O. Paschereit. Thermoacoustic Modeling of a Gas Turbine Using Transfer Functions Measured Under Full Engine Pressure. *J. Eng. Gas Turbines Power*, 132(11):111503, 2010. doi: 10.1115/1.4000854.

T. Schuller, D. Durox, and S. Candel. A unified model for the prediction of laminar flame transfer functions: comparisons between conical and V-flame dynamics. *Combust. Flame*, 134(1):21–34, July 2003. doi: 10.1016/S0010-2180(03)00042-7.

T. Schuller, T. Poinsot, and S. Candel. Dynamics and control of premixed combustion systems based on flame transfer and describing functions. *J. Fluid Mech.*, 894, July 2020. doi: 10.1017/jfm.2020.239.

A. F. Seybert and D. F. Ross. Experimental determination of acoustic properties using a two-microphone random-excitation technique. *The Journal of the Acoustical Society of America*, 61(5):1362–1370, May 1977. doi: 10.1121/1.381403.

V. Smil. *Energy transitions: global and national perspectives*. ABC-CLIO, 2016.

G. Staffelbach, L. Y. M. Gicquel, G. Boudier, and T. Poinsot. Large Eddy Simulation of self excited azimuthal modes in annular combustors. *Proc. Combust. Inst.*, 32(2):2909–2916, January 2009. doi: 10.1016/j.proci.2008.05.033.

M. Stefanizzi, T. Capurso, G. Filomeno, M. Torresi, and G. Pascazio. Recent Combustion Strategies in Gas Turbines for Propulsion and Power Generation toward a Zero-Emissions Future: Fuels, Burners, and Combustion Techniques. *Energies*, 14(20):6694, January 2021. doi: 10.3390/en14206694.

J. W. Strutt. *The theory of sound*. Dover, New York, NY, 2nd ed edition, 1945.

H. Suzuki, N. Kasagi, and Y. Suzuki. Active control of an axisymmetric jet with distributed electromagnetic flap actuators. *Experiments in Fluids*, 36(3):498–509, March 2004. doi: 10.1007/s00348-003-0756-0.

N. Syred, M. Abdulsada, T. Griffiths, A.and O'Doherty, and P. Bowen. The effect of hydrogen containing fuel blends upon flashback in swirl burners. *Applied Energy*, 89(1):106–110, January 2012. doi: 10.1016/j.apenergy.2011.01.057.

M. T. Szedlmayer, B. D. Quay, J. Samarasinghe, A. De Rosa, J. G. Lee, and D. A. Santavicca. Forced Flame Response of a Lean Premixed Multi-Nozzle Can Combustor. volume Volume 2: Combustion, Fuels and Emissions, Parts A and B of *Turbo Expo: Power for Land, Sea, and Air*, pages 883–891, 06 2011. doi: 10.1115/GT2011-46080.

L. Tay-Wo-Chong, S. Bomberg, A. Ulhaq, T. Komarek, and W. Polifke. Comparative Validation Study on Identification of Premixed Flame Transfer Function. *J. Eng. Gas Turbines Power*, 134(2), December 2011. doi: 10.1115/1.4004183.

C. Tropea, A. Yarin, and J. Foss. *Springer Handbook of Experimental Fluid Mechanics*. January 2007. doi: 10.1007/978-3-540-30299-5.

B. Wieneke. PIV uncertainty quantification from correlation statistics. *Measurement Science and Technology*, 26(7):074002, June 2015. doi: 10.1088/0957-0233/26/7/074002. Publisher: IOP Publishing.

C. D. Winant and F. K. Browand. Vortex pairing : the mechanism of turbulent mixing-layer growth at moderate Reynolds number. *J. Fluid Mech.*, 63(2):237–255, April 1974. doi: 10.1017/S0022112074001121.

S. Wiseman, Ma. Rieth, A. Gruber, J. R. Dawson, and J. H. Chen. A comparison of the blow-out behavior of turbulent premixed ammonia/hydrogen/nitrogen-air and methane–air flames. *Proc. Combust. Inst.*, 38(2):2869–2876, January 2021. doi: 10.1016/j.proci.2020.07.011.

N. A. Worth and J. R. Dawson. Cinematographic OH-PLIF measurements of two interacting turbulent premixed flames with and without acoustic forcing. *Combust. Flame*, 159(3):1109–1126, March 2012a. doi: 10.1016/j.combustflame.2011.09.006.

N. A. Worth and J. R. Dawson. Tomographic reconstruction of OH* chemiluminescence in two interacting turbulent flames. *Measurement Science and Technology*, 24(2):024013, December 2012b. doi: 10.1088/0957-0233/24/2/024013.

N. A. Worth and J. R. Dawson. Modal dynamics of self-excited azimuthal instabilities in an annular combustion chamber. *Combust. Flame*, 160(11):2476–2489, November 2013a. doi: 10.1016/j.combustflame.2013.04.031.

N. A. Worth and J. R. Dawson. Self-excited circumferential instabilities in a model annular gas turbine combustor: Global flame dynamics. *Proc. Combust. Inst.*, 34(2):3127–3134, January 2013b. doi: 10.1016/j.proci.2012.05.061.

N. A. Worth and J. R. Dawson. Effect of equivalence ratio on the modal dynamics of azimuthal combustion instabilities. *Proc. Combust. Inst.*, 36(3):3743–3751, 2017. doi: 10.1016/j.proci.2016.06.115.

N. A. Worth and J. R. Dawson. Characterisation of flame surface annihilation events in self excited interacting flames. *Combust. Flame*, 199:338–351, January 2019. doi: 10.1016/j.combustflame.2018.10.032.

N. A. Worth, J. R. Dawson, J. AM Sidey, and E. Mastorakos. Azimuthally forced flames in an annular combustor. *Proc. Combust. Inst.*, 36(3):3783–3790, January 2017. doi: 10.1016/j.proci.2016.06.107.

N. A. Worth, D. Mistry, T. Berk, and J. R. Dawson. Vortex dynamics of a jet at the pressure node in a standing wave. *J. Fluid Mech.*, 882, January 2020. doi: 10.1017/jfm.2019.821.

Y. Zhang, Z. Huang, L. Wei, J. Zhang, and C. K. Law. Experimental and modeling study on ignition delays of lean mixtures of methane, hydrogen, oxygen, and

argon at elevated pressures. *Combust. Flame*, 159(3):918–931, March 2012. doi: 10.1016/j.combustflame.2011.09.010.

M. Åbom. Measurement of the scattering-matrix of acoustical two-ports. *Mechanical Systems and Signal Processing*, 5(2):89–104, March 1991. doi: 10.1016/0888-3270(91)90017-Y.

M. Åbom and H. Bodén. Error analysis of two-microphone measurements in ducts with flow. *The Journal of the Acoustical Society of America*, 83(6):2429–2438, June 1988. doi: 10.1121/1.396322.

E. Æsøy, J. G. Aguilar, S. Wiseman, M. R. Bothien, N. A. Worth, and J. R. Dawson. Scaling and prediction of transfer functions in lean premixed H2/CH4-flames. *Combust. Flame*, 215:269–282, May 2020. doi: 10.1016/j.combustflame.2020.01.045.

E. Æsøy, J. G. Aguilar, M. R. Bothien, N. A. Worth, and J. R. Dawson. Acoustic-Convective Interference in Transfer Functions of Methane/Hydrogen and Pure Hydrogen Flames. *J. Eng. Gas Turbines Power*, 143(12), October 2021a. doi: 10.1115/1.4051960.

E. Æsøy, J. G. Aguilar, N. A. Worth, and J. R. Dawson. The response of an axisymmetric jet placed at various positions in a standing wave. *J. Fluid Mech.*, 917, June 2021b. doi: 10.1017/jfm.2021.246.

E. Æsøy, H. T. Nygård, N. A. Worth, and J. R. Dawson. Tailoring the gain and phase of the flame transfer function through targeted convective-acoustic interference. *Combust. Flame*, 236:111813, February 2022. doi: 10.1016/j.combustflame.2021.111813.

Article 1

Scaling and Prediction of Transfer Functions in Lean Premixed H_2/CH_4-Flames

Eirik Æsøy, José G. Aguilar, Samuel Wiseman, Mirko R. Bothien, Nicholas A. Worth and James R. Dawson

Published in the Journal of Combustion and Flame

Combustion and Flame 215 (2020) 269–282

Contents lists available at ScienceDirect

Combustion and Flame

journal homepage: www.elsevier.com/locate/combustflame

Scaling and prediction of transfer functions in lean premixed H_2/CH_4-flames

Eirik Æsøy[a,*], José G. Aguilar[a], Samuel Wiseman[a], Mirko R. Bothien[b], Nicholas A. Worth[a], James R. Dawson[a]

[a] Department of Energy and Process Engineering, Norwegian University of Science and Technology, Trondheim N-7491, Norway
[b] Ansaldo Energia Switzerland, Haselstrasse 18, 5400 Baden, Switzerland

ARTICLE INFO

Article history:
Received 14 September 2019
Revised 18 October 2019
Accepted 31 January 2020

Keywords:
Thermoacoustics
Flame transfer function
Distributed time lag model
Turbulent premixed flame
Hydrogen

ABSTRACT

Features of the flame transfer function (FTF) are characterized for turbulent, non-swirled, bluff body stabilized "M" flames for different hydrogen and methane blends including pure hydrogen flames. An increase in the cut-off frequency of the FTF is observed for increasing hydrogen concentration. Modulations in the form of peaks and troughs in the gain and the phase were also observed and are shown to be caused by the interaction of two different flow disturbances, acoustic and convective, originating upstream of the flame. The first mechanism is due to the acoustic velocity fluctuations imposed at the base of the flame. A Strouhal number scaling based on the flame height and bulk velocity is shown to collapse the phase slopes and the cut-off frequencies. The second mechanism is shown to be due to vortex shedding from the grub screws used to align the bluff body in the inlet pipe. The associated convective time-delay is used to define a second Strouhal number which collapses the modulations in the gain and phase.

A model is developed that separately considers the impulse response of each mechanism and is interpreted as a distribution of time lags between velocity fluctuations and the unsteady heat release rate. The distributed time lag (DTL) model consists of two distributions that are shown to capture all the features of the FTFs. The distributions show that the acoustic and convective mechanisms behave as a low pass filter and band pass filter, respectively. This results in a band of frequencies where they interact through superposition driving fluctuations of heat release rate. Similar interactions are shown to exist in the forced cold flow revealing that they are of hydrodynamic origin. Further, the band of frequencies are shown to be centered around the natural shedding frequency of the grub screws appearing as peaks in the unforced energy spectra of the velocity at the dump plane.

Finally, a generalized model which takes as an input the bulk velocity, flame height and a geometric parameter is derived assuming a linear dependency of the DTL parameters. The model is shown to predict the behavior of the FTFs relatively well and can potentially be used to analyse regions in the operating conditions map which have not been experimentally tested.

1. Introduction

Hydrogen fired gas turbines for power generation can potentially play a crucial role in large-scale decarbonization. This is because hydrogen can be produced using excess energy from renewable energy sources or from reforming from natural gas combined with capture and storage of carbon dioxide. However, the higher flame speeds of hydrogen mixtures introduces new flame dynamics that may lead to thermoacoustic oscillations in addition to other flame stability issues such as flashback.

Thermoacoustic instabilities can arise whenever there is feedback from the unsteady heat release into the acoustic field of the surrounding geometry [1]. In order to predict and control these instabilities, a model of the combustion system is required. Typically, these models are built considering the acoustic characterization of the chamber, boundary conditions and a transfer function that relates the acoustic excitation to the unsteady heat release. The latter occurs because heat sources, such as flames, are volume sources which act as acoustic monopoles.

* Corresponding author.
E-mail address: eirik.asoy@ntnu.no (E. Æsøy).

https://doi.org/10.1016/j.combustflame.2020.01.045
0010-2180/

As it provides closure to the thermoacoustic feedback loop, flame transfer function (FTF) analysis is a core subject of research in thermoacoustics. FTFs can be obtained experimentally [2–5], via high fidelity numerical simulations [6], or using theoretical models [7–10]. Owing to the weak acoustic amplification of the pressure and/or density fluctuations across a flame, the FTF is usually assumed to be proportional to the velocity fluctuations only and is by definition independent of the forcing level. This corresponds to the case where there is a linear relationship between the normalized heat release fluctuations and the normalized velocity fluctuations.

The time-lag nature of thermoacoustic instabilities is commonly expressed using single time-lag (STL) models as FTFs, such as the $n-\tau$ model introduced by Crocco [11]. These models have an impulse response function (IRF), where the local response is both: amplified by a factor of n, and delayed τ seconds. However, this representation is only valid at low frequencies where the flame is considered compact with respect to the acoustic and convective wavelengths. At moderate frequencies, STL formulation has been shown incapable of capturing the spatial dispersion that arises due to the presence of convective phenomena [7]. In other words STL formulation cannot capture cut-off frequency behavior. To circumvent this limitation Sattelmayer [12] introduced the distributed time lag (DTL) formulation. In this formalism, the FTF is computed from the IRF obtained from the probability density function (PDF) of time-delays. This analysis was extended in Polifke et al. [13] to handle arbitrary shapes of the PDF enabling the FTF to capture cut-off frequency behavior. Furthermore, there are some premixed flames, whose FTFs also display excess gain (Gain >1) at non zero frequencies ($f>0$) [14]. Huber and Polifke [15] discussed that for the FTF to display excess gain the IRF must allow for negative values. This was shown by Blumenthal et al. [16] to be the case in some laminar flames. In most of the aforementioned studies, the FTF is due the mechanisms that occur around one dominant time scale. In these cases the FTFs can be well represented by a single DTL model. However, there are situations in which there are two mechanisms with very different time scales responsible for the fluctuations in the heat release rate. In such cases it is convenient to use the sum of two DTL models to approximate the IRF. For instance, Schuermans et al. [17] used this approach to model the mechanisms due to equivalence ratio fluctuations and vorticity fluctuations in a full scale gas turbine burner mounted in an atmospheric test rig.

The most common feature of a FTF is that the flame behaves as a low-pass filter [7] however other features can appear strongly influenced by the shape of the flame [3]. In the case of so-called "M" flames, particular features include the presence of peaks and troughs (also referred to as modulations), such as those appearing in the studies of swirl stabilized flames [5,18–20]. Using premixed flames Komarek and Polifke [19] demonstrated that the peaks and troughs shift in frequency when the position of the swirler is changed. The same effect was achieved by Polifke [18] by changing the location of the fuel injection point when equivalence ratio oscillations are present. On a different configuration Palies et al. [21] identified the peaks and troughs to be the interaction between two different unsteady heat release mechanisms: swirl number fluctuations and vortices shed from the bluff-body. In a series of more recent experiments [22–24] it was demonstrated that the levels of swirl number fluctuations observed at both the peaks and the troughs of the FTF were the result of the axial and angular velocity fluctuations being in or out of phase. Gatti et al. [23] further showed that the FTF of a non-swirling flame, and a swirling flame without a center rod, did not exhibit peaks or troughs.

In the present paper FTFs are measured for a variety of non-swirling flames stabilized on a bluff-body over a wide range of hydrogen/methane mixtures with "M" flame shape. The experimental FTFs show that the modulations can also occur under these conditions. Scaling laws, similar to those used by Alemela et al. [25], are deduced to collapse the cut-off frequency and the modulations in the gain and the phase of the measurements. The time scales derived are similar to those identified in [26] where the flame was subject to interference between vortical and acoustic disturbances. The data is compared against a double DTL model, which includes a modulating term that allows for excess gain to be modelled. It is shown that the modulations in the FTF are caused by the constructive and destructive interference between the acoustic velocity and vortex shedding originating from the geometry upstream. Each of these mechanisms are also shown to act on the flame with different mean time-delays. Using these considerations a generalized FTF model is derived which takes as an input the bulk velocity, flame length and a geometric parameter.

2. Experimental set-up and methods

2.1. Experimental set-up

Figure 1 shows a schematic of the experimental set-up. The burner used in these experiments consists of a single sector rig. The injector geometry is identical to the injectors used in the annular combustor of [27,28] but without swirlers. The burner has a circular quartz combustion chamber of inner diameter $d_q = 44$ mm, that enables optical access and it is open to atmospheric conditions. The length of the quartz tube can be changed to avoid self excited instabilities during FTF measurements. Two lengths $L_q = 80$ mm and 55 mm are used for these measurements. The combustor is operated with different mixtures of hydrogen, methane and air. The flow rates are controlled by Alicat mass flow controllers (MFC's) and the fluid bulk velocity $\bar{u}$ at the burner dump plane and in the pipe $\bar{u}_p$ are computed from the volume flow rate. The air and fuels are mixed in the feeding lines approximately a meter before entering the bottom of the plenum section to ensure that the mixture is fully premixed. In the plenum section, the gas expands, and flows through a set of honeycombs and perforated plates before it contracts and passes through a pipe of diameter $d_p = 19$ mm. The flame anchors on a bluff body ($d_b = 13$ mm) with blockage ratio of 47%, supported by a center rod ($d_r = 5$ mm) located at the pipe exit. The rod is held in place by three grub screws ($d_g = 4$ mm) at a distance of $L_g = 45$ mm from the dump plane. On the side wall of the plenum, two Monacor KU-516 (75 W, 16 Ω) horn drivers are attached at the end of two stand off tubes for longitudinal acoustic forcing. The speakers are powered by QTX Sound PRO1000 power amplifiers and controlled by an Aim-TTi TGA1244 40 MHz signal generator (SG). The signal from the SG p_{ref} is sampled as a common reference for cross spectral analysis of pressure, heat release, and velocity oscillations. To characterize the cold flow a Hot Wire Anemometer (HWA) is used at six locations L_{1-6} in the pipe. The velocity magnitude u_{hw} across a single wire (55P11) of diameter 5 μm and length 1.25 mm is measured using a StreamLine pro. Throughout the paper a cylindrical coordinate system (x, r, θ) is used with the origin placed at the center of the bluff body.

2.2. Operating conditions

Measurements were carried out for a range of thermal powers P, bulk velocities $\bar{u}$, equivalence ratios Φ, and hydrogen contents in terms of power fraction P_{H} (or the equivalent volume fraction V_H) computed as:

$$P_{\text{H}} = \frac{P_{\text{H}_2}}{P_{\text{H}_2} + P_{\text{CH}_4}}, \qquad V_{\text{H}} = \frac{V_{\text{H}_2}}{V_{\text{H}_2} + V_{\text{CH}_4}}, \tag{1}$$

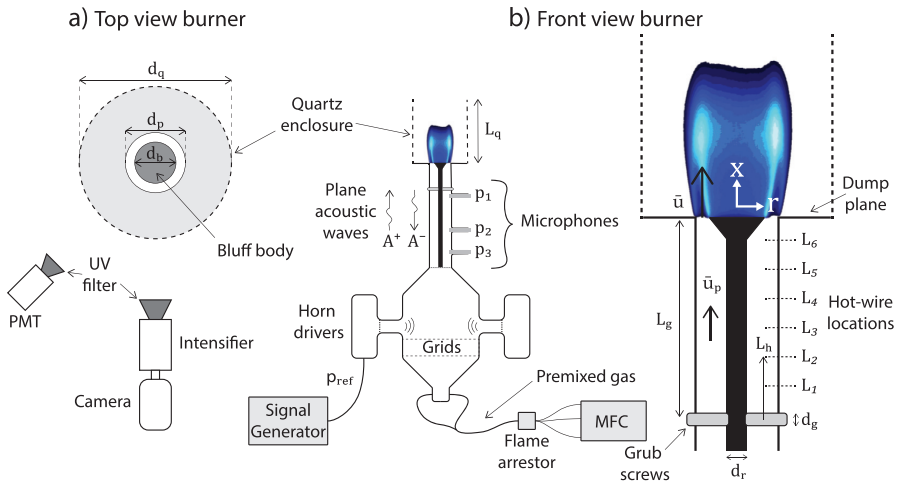

Fig. 1. Schematic of the experimental set-up. (a) Top view of the burner showing the optical arrangement with the photo multiplier tube and camera. (b) Front view of the set-up showing MFCs, signal generator, plenum, horn drivers, microphones, combustion chamber, and a zoomed view of the burner showing the pipe, bluff body, grub screws, combustion chamber, and the locations of the hot-wire used for the cold flow measurements.

Table 1
Operating conditions in terms of thermal powers P, bulk velocities $\bar{u}$, equivalence ratios Φ, hydrogen power fraction P_H, and hydrogen volume fraction V_H for FTF measurements of "M"-flames.

P_H	V_H	$\bar{u}$ [m/s]	P [kW]	Φ	Case
1.0	1.0	12.8–51.3	3–12	0.4	1–9
1.0	1.0	30	7–9.8	0.4–0.6	10–12
1.0	1.0	23.4–19.4	5.47	0.4–0.5	13–14
0.3	0.57	8.6–31.7	3–11	0.7	15–19
0.3	0.57	17.9	7	0.8	20
0.3–0.4	0.57–0.67	20	7	0.7	21–23
0.8–1.0	0.92–1.0	30	7	0.4	24–25

where P_{H_2} and P_{CH_4} are the thermal powers from hydrogen and methane, and V_{H_2} and V_{CH_4} are the volume flow rates of hydrogen and methane. The 25 cases are summarized in Table 1. All these operating points correspond to "M"-flames (similar to the flame shown in Fig. 3), where the flame is stabilized both on the inner and outer shear layers near the burner lip. The operating conditions are divided into seven groups which correspond to cases where two parameters are held constant while the rest are changed. These operating conditions are chosen to show the difference in flame dynamics for a similar flame shape.

2.3. Flame response from global chemiluminescence

The flame response is measured by the spatially integrated heat release rate Q. This is tracked by measuring radiation emitted from OH* radicals, using a photo multiplier tube (PMT) equipped with a UV band pass filter with 310 nm center wave length and a half width of 10 nm. Since we are only considering fully premixed flames, the PMT signal $I(t)$ is assumed to be proportional to the global heat release rate following the example of numerous previous studies [7,29–31]. Hence, relative fluctuations, $Q'/\bar{Q}$, are evaluated from the time-series of $I(t)$ from the PMT.

The velocity fluctuations at the burner exit are computed using the multiple microphone method (MMM) [32]. For this purpose three (Kulite XCS-093-05D) microphones located at different axial locations in the inlet pipe are used to measure time-series of pressure (p_1, p_2, and p_3). A cross power spectral analysis is used to estimate the amplitude and phase of each signal p'_{1-3} and Q', correlated with the excitation signal p_{ref}, i.e., the phase is computed relative to p_{ref}. The amplitude and phase of each signal, e.g., Q', is expressed as a complex number and is computed by:

$$\hat{Q}(f_e) = \left.\frac{\Gamma(\, p_{\text{ref}},\ Q'\,)}{\sqrt{\Gamma(\, p_{\text{ref}},\ p_{\text{ref}}\,)}}\right|_{f_e}, \qquad (2)$$

$$\Gamma(\, p_{\text{ref}},\ Q'\,) = \mathcal{F}(\, p_{\text{ref}}\,)\mathcal{F}(\, Q'\,)^*,$$

where the cross power spectral density (CPSD), Γ, is computed as the product of the Fourier transforms $\mathcal{F}$ of each signal, respectively. Hatted quantities ($\hat{}$) denote a fluctuation in frequency space. The excitation signals are harmonic, hence the signal response is estimated as the complex value at the excitation frequency f_e. Segments of the time-series of $p'_1(t)$, $Q'(t)$, and p_{ref} are plotted in Fig. 2(b). Figure 2(a) shows the spectra of the heat release rate computed by Eq. (2) at $f_e = 950$ Hz.

Assuming 1D acoustics and a low mach number, the acoustic pressure and velocity propagate only in the axial direction and are expressed by:

$$\hat{p}(x) = A^+ \exp(-jkx) + A^- \exp(jkx), \qquad (3)$$

$$\hat{u}(x) = \frac{1}{\bar{\rho}\bar{c}}\left(A^+ \exp(-jkx) - A^- \exp(jkx)\right), \qquad (4)$$

where A^+ and A^- are the amplitude and phase (Riemann invariants) of the upstream and downstream propagating acoustic waves, $\bar{\rho}$ is the fluid density, $\bar{c}$ is the speed of sound, and k is the spatial wave-number. The wave-number is given by $k = \omega/\bar{c}$, where $\omega = 2\pi f$ is the angular frequency. The amplitude and phase of the microphone signals ($\hat{p}_{1-3}$), are used to compute A^+ and A^- which then are used to reconstruct the acoustic pressure and velocity fields in the tube. Hence, $\hat{u}$ can be evaluated at the burner exit, relating the heat release fluctuations to the acoustic velocity fluctuations at the burner dump plane.

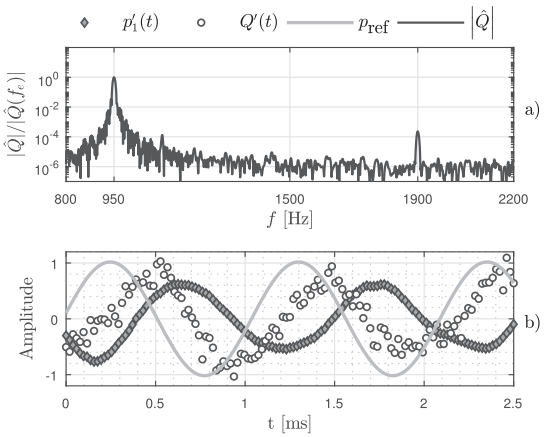

Fig. 2. Amplitude spectra of $\hat{Q}$ and corresponding time-series $p'_1(t)$, $Q'(t)$, and p_{ref} at excitation frequency $f_e = 950$ Hz. The time series in (b) are normalized by the amplitudes estimated by Eq. (2).

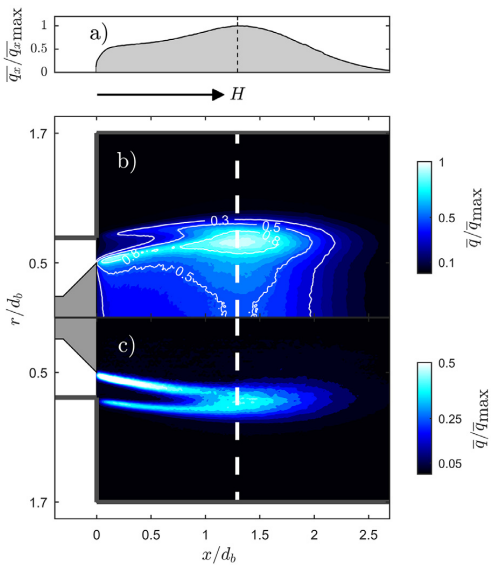

Fig. 3. Images of the mean flame for case 5 ($P = 7$ kW, $P_{\text{H}} = 1$, and $\Phi = 0.4$). (a) Stream-wise distribution of heat release rate. (b) Line of sight integrated heat release rate. (c) Planar heat release rate computed by a 3 point Abel deconvolution algorithm. All images are normalized by the maximum intensity.

The relationship between $\hat{u}$ and $\hat{Q}$ is described by the flame transfer function (FTF) expressed by:

$$\text{FTF}(\omega) = \frac{\hat{Q}/\bar{Q}}{\hat{u}/\bar{u}}. \tag{5}$$

At low forcing amplitudes the FTF is independent of the forcing level $|\hat{u}|/\bar{u}$ [33]. Discrete points of the FTF are measured using $|\hat{u}|/\bar{u} = 0.04$ at a range of frequencies $f_e = [200\text{–}2200]$ Hz. At each frequency time-series of pressure and chemiluminescence are recorded in 10 s intervals at a sampling rate of $f_s = 51.2$ kHz. This corresponds to 5.12×10^5 samples which are binned into 40 separate time-series. Each of the time series has a length of 250 ms which correspond to more than 50 cycles at the lowest frequency.

2.4. High-speed imaging and flame shape

The spatial distribution of normalized heat release rate, $q'(x, r, t)/\bar{q}(x, r)$, is measured by high-speed imaging of the flame. The measurement is line of sight integrated (similar to the PMT), and $q'/\bar{q}$ is obtained in the same way as $Q'/\bar{Q}$. The total heat release rate is retrieved by integrating the spatially distributed heat release: $Q'/\bar{Q} = \int_A q'/\bar{q}\, dA$ over the camera field of view, A.

The equipment used is a Phantom V2012 high-speed camera equipped with a LaVision IRO high-speed two-stage intensifier, fitted with a Cerco 2178 UV lens 100F/2.8 and a UV band pass filter with 310 nm center wave length and a half width of 10 nm. The mean spatial distribution of heat release rate $\bar{q}$ is used to compute the mean flame shape and corresponding flame height H. Figure 3(b) shows the upper half of $\bar{q}$ in the x–r plane, obtained from averaging 2000 chemiluminescence images of the unforced flame. Figure 3(c), is computed by a three point Abel deconvolution algorithm [34] and shows the radial profile of the heat release rate. The image intensity is normalized by the maximum intensity ($\bar{q}_{\max}$). Figure 3(a) shows the stream wise intensity profiles of $\bar{q}$, integrated in the radial direction:

$$\bar{q}_x(x) = \int_0^\infty \bar{q}\, dr. \tag{6}$$

The location where $\bar{q}_x$ is maximum indicates the flame length H. The flame length is shown with a dashed line. From Fig. 3(c), one can see that the flame anchors on both the inner and outer burner lips forming the characteristic “M” shape.

3. Results

Figure 4 shows FTFs measurements of two fuel mixtures. The first mixture is an H_2/CH_4 blend at $P_{\text{H}} = 0.3$, with equivalence ratio, $\Phi = 0.7$, at a range of thermal powers $P = [3 - 7]$ kW. The second mixture is pure H_2, $P_{\text{H}} = 1$, with equivalence ratio, $\Phi = 0.4$, at a range of thermal powers $P = [4\text{–}12]$ kW. The FTF is plotted using $\text{FTF} = G\exp(j\theta)$, where G is the gain and θ is the phase. Log–log plots of the gain are shown on the left, and the phase is plotted on the right of the figure. The gain plots highlight the low-pass filter behavior where an exponentially decaying gain appears as a line with negative slope at high frequencies. The phase is plotted in a linear scale to highlight the time-delayed response of the flame as indicated by the approximately constant slope. It is evident that the cut-off frequency increases and the time-delay decreases with thermal power. The pure hydrogen mixture exhibits a significantly higher cut-off frequency and a slower time delay when compared to the H_2/CH_4 mixture at similar thermal powers. Furthermore, one can see that before the cut-off frequency, the gain modulates around unity and the phase is deviating from a straight line by the same type of oscillations (see Fig. 11(b) for individual plots of some of the cases). The planar flame images in Fig. 5, correspond to each of the FTFs in Fig. 4(a), and show that hydrogen flames are stabilized as an “M” flame for a large range of thermal powers. The flame height is denoted by the dashed line. By increasing the thermal power and thus the bulk velocity, the turbulent flame speed also increases, albeit less than the bulk velocity. This results in longer flames as the flame height is primarily controlled by the balance between turbulent flame speed and bulk velocity.

3.1. FTF measurements for pure hydrogen “M”-flames

Some features of the FTF collapse when scaled by appropriate Strouhal numbers. Figure 4(b) shows that when the frequency in the FTFs of Fig. 4(a) is non-dimensionalized by a time-scale based on the flame height and the bulk velocity, $\tau_1 = H/\bar{u}$, such that $\text{St}_1 = f\tau_1$ the cut-off characteristics in the gain and the phase

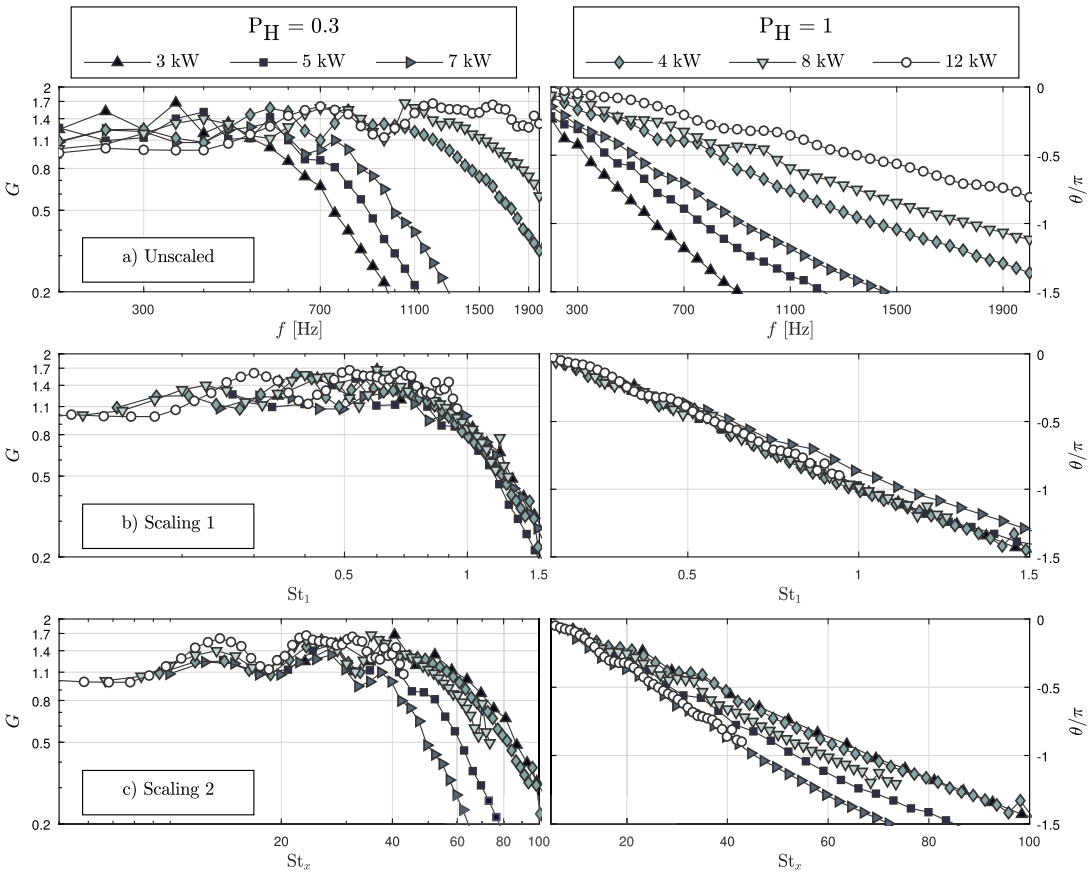

Fig. 4. Experimental FTFs for "M" -flames at different thermal powers: $P = [3 - 7]$ kW for $P_H = 0.3$ at $\Phi = 0.7$, and $P = [4 - 12]$ kW for $P_H = 1$ at $\Phi = 0.4$. (a) Gain and phase plotted against frequency. (b) Plotted against reduced frequency St_1. (c) Plotted against reduced frequency St_x.

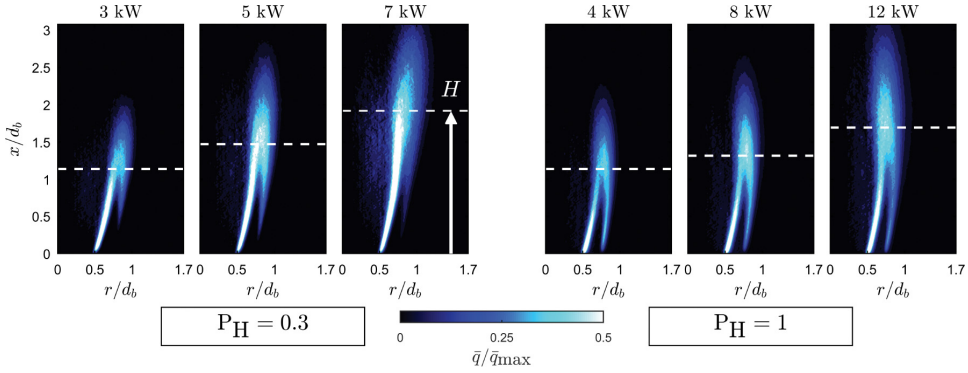

Fig. 5. Planar flame images of the unforced flame at different thermal powers: $P = [3 - 7]$ kW for $P_H = 0.3$ at $\Phi = 0.7$, and $P = [4 - 12]$ kW for $P_H = 1$ at $\Phi = 0.4$. The flames correspond to the FTFs shown in Fig. 4. All flames have a characteristic "M"-shape and the intensity is normalized by the maximum intensity $\bar{q}_{max}$.

slopes collapse. The periodic nature of the peaks and troughs in the low frequency gain and phase curves suggests that there is another Strouhal number, say St_x, which collapses the modulations as shown in Fig. 4(c). The nature of the second time-delay is analysed in Section 3.4. Given that different features of the FTF scale with different Strouhal numbers, one can conclude that the system is governed by two distinct time scales. Similar observations were made in swirling flames [21–24] where it was shown that two different time-scales affected the FTF, one corresponding to the acoustic velocity disturbances at the burner exit and the other to vorticity waves produced by the swirler vanes.

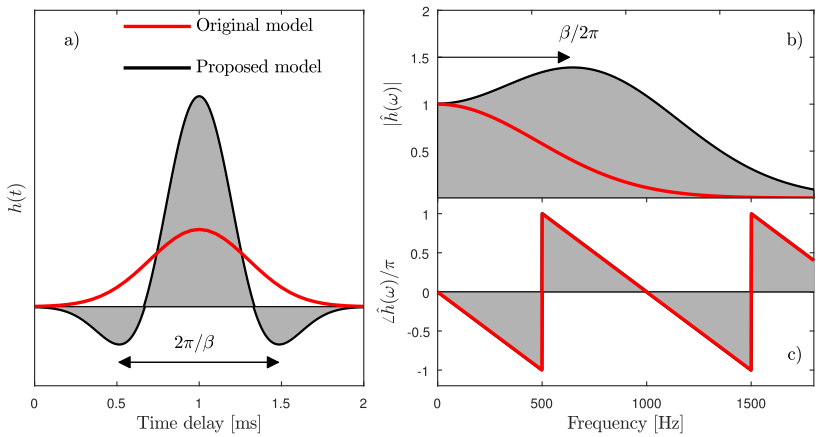

Fig. 6. (a) Impulse response function $h(t)$, with mean time-delay $\tau = 1$ ms and a modulation frequency of $\beta/(2\pi) = 700$ Hz. This corresponds to a modulation wavelength of 1 ms. (b) Transfer function $\hat{h}(\omega)$ displaying excess gain at $f = \beta/(2\pi)$.

In the following sections an in depth characterization of the time-delays is performed. First by adopting a distributed time lag model to extract the actual time-delays and then analysing the corresponding nature of the disturbances.

3.2. Distributed time-lag model

The simplest time lag model used to relate the velocity fluctuations with the flame response is the $n-\tau$ model, originally proposed by Crocco [11]:

$$\frac{Q'(t)}{\bar{Q}} = n\frac{u'(t-\tau)}{\bar{u}}. \tag{7}$$

Here n is the interaction index, and τ is the time-delay. This representation is only valid in the low frequency range, where the flame can be treated as a compact element with respect to the acoustic and convective wavelengths.

This is not the case for the flames and frequencies considered in this paper. At moderate frequencies, disturbances that convect with the mean flow velocity can have a significant effect on the flame. In this case, the flame response is better represented by a distributed time-lag model. Using CFD Polifke et al. [13] computed the probability density function of time delays, also interpreted as the impulse response function $h(t)$ and then approximated it analytically using a Gaussian distribution with standard deviation σ:

$$h(t) = \frac{1}{\sigma\sqrt{2\pi}}\exp\left(-\frac{(t-\tau)^2}{2\sigma^2}\right). \tag{8}$$

In order to capture excess gain, i.e., gain above unity ($G > 1$) at nonzero frequency ($f > 0$) Komarek and Polifke [19] used several distributions with opposite signs. In order to achieve the same effect we extend the model to include an amplitude g and a modulating term with frequency β. The advantages of using the modulating term are twofold:

1. It allows the impulse response function h to become negative and therefore it is useful to model excess gain in the FTF (see Fig. 6).
2. If such a distribution is used to model a phenomenon with a preferred frequency, β represents this explicitly (as will be shown in Section 3.5).

Under these considerations the impulse response for a single time lagged distribution is given by:

$$h(t) = \frac{g}{\sigma\sqrt{2\pi}}\exp\left(-\frac{(t-\tau)^2}{2\sigma^2}\right)\cos\left(\beta(t-\tau)\right). \tag{9}$$

The relationship between the unsteady heat release fluctuations and the velocity fluctuations is given by the convolution of the latter with the impulse response function:

$$\frac{Q'(t)}{\bar{Q}} = \frac{(h * u')(t)}{\bar{u}}, \tag{10}$$

$$= \int_{-\infty}^{\infty} h(\tau)\frac{u'(t-\tau)}{\bar{u}}\,\mathrm{d}\tau. \tag{11}$$

In the frequency domain this can be rewritten as:

$$\frac{\hat{Q}(\omega)/\bar{Q}}{\hat{u}(\omega)/\bar{u}} = \hat{h}(\omega), \tag{12}$$

where $\hat{h}(\omega)$ is the associated transfer function given by:

$$\hat{h}(\omega) = \frac{g}{2}\left(\exp\left(-\frac{1}{2}(\omega-\beta)^2\sigma^2\right) + \exp\left(-\frac{1}{2}(\omega+\beta)^2\sigma^2\right)\right)\mathrm{e}^{-j\omega\tau}. \tag{13}$$

This formulation can be used to describe the mechanisms responsible for the unsteady heat release fluctuations that occur around a single time scale (τ). When there are two different time scales, as the analysis in Section 3.1 suggests, it is convenient to use two distributed time lag models [17]. Therefore the full FTF expressed as $\mathrm{DTL_T}(\omega)$ is given by:

$$\mathrm{DTL_T}(\omega) = \mathrm{DTL_1} + \mathrm{DTL_2}, \tag{14}$$

where

$$\mathrm{DTL}_i = E_i^+ + E_i^-, \tag{15}$$

$$E_i^{\pm} = \frac{g_i}{2}\exp\left(-\frac{1}{2}(\omega\pm\beta_i)^2\sigma_i^2 - j\omega\tau_i\right). \tag{16}$$

3.3. Estimation of the DTL model parameters

Having developed the DTL model, the next step is to compute the model parameters (g_i, β_i, σ_i and τ_i) that best fit the experimental FTFs. This is performed using a nonlinear least squares

(NLS) optimization routine which minimizes the difference between the DTL model and the experimental measurements. The procedure is as follows:

1. The measurements are fitted to a DTL model consisting of one distribution. Hence, the model parameters g_1, σ_1, β_1, and τ_1 are computed while g_2, σ_2, β_2, and τ_2 are set to zero.
2. The measurements are fitted to a DTL model consisting of two distributions. The first distribution takes the values computed in the previous step, and only the model parameters g_2, σ_2, β_2, and τ_2 are computed.
3. The measurements are fitted to a DTL model consisting of two distributions, where all the model parameters are fitted simultaneously and physical constraints are imposed.

The main challenge associated with the NLS approximation is that it easily gets trapped in local minima which may not necessarily be the global minima. This is important for steps 1 and 2 (step 3 takes as initial guesses the values computed in steps 1 and 2). Therefore one may prefer to use a global minimization approach as applied by genetic algorithms. However, the NLS algorithm is favored in this paper because, as will be shown in the following sections, a careful analysis of the features of the FTFs can provide good initial estimates of the model parameters.

3.3.1. Parameter estimation for the first distribution

When dealing with a single distribution, one can divide the model parameters into gain (g_1, σ_1, β_1) and phase (τ_1) parameters. Good estimations for the gain parameters can be obtained by inspection of the FTF, by considering $G_m = \max(G)$:

$$g_1 \approx 2G_m, \qquad \beta_1 \approx \omega\Big|_{G=G_m}, \qquad \sigma_1 \approx \frac{3}{\omega\big|_{G=G_m/100} - \beta_1}.$$

Figure 4(b) shows that using a Strouhal number based on the time-delay $\tau_1 = H/\bar{u}$ collapses the cut off frequency characteristics and the phase slopes of 5 curves. However, instead of taking this as granted, the initial guess for the time-delay is given as the slope of the phase computed using linear regression.[1] The same figure also shows that the phase at the origin is not zero (which is a feature of the DTL model). This can be caused by systematic measurement errors. In order to get a better estimate of the phase slopes a small phase offset (θ_0) is added to the model such that $\exp(-j\omega\tau_i) \rightarrow \exp(-j(\omega\tau_i + \theta_0))$. Note that the offset needs to be the same for both distributions. The initial estimation for this offset is taken to be zero.

3.3.2. Parameter estimation for the second distribution

In Fig. 4(c) it is shown that the modulations collapse with a, yet unknown, Strouhal number. This suggests that a detailed analysis of the modulations can provide accurate estimations for the model parameters of the second distribution. Having computed the model parameters of the first distribution, the modulations in the gain[2] are extracted by taking the difference between the gain of the experimental data (G_{exp}) and the gain of the DTL model with a single distribution (G_{DTL_1}):

$$\Delta G = G_{\text{exp}} - G_{\text{DTL}_1}. \tag{17}$$

The modulations appear only in a band of frequencies, thus the part of the signal out of this band is discarded. This gives an estimate for β_2 which is approximately the center of the band. The width of the band is roughly $6/\sigma_2$ and the amplitude of the modulations are twice g_2. The resulting signal (shown later in Fig. 8) closely resembles a sinusoidal curve where the peaks and troughs can be interpreted as the frequencies at which the mechanisms of different time scales have constructive and destructive interference, respectively.

The periodicity of this curve is linked to the second time-delay. Recall that the magnitude of the addition of two complex numbers $z_1 = r_1 e^{j\phi_1}$ and $z_2 = r_2 e^{j\phi_2}$ is given by:

$$|z_1 + z_2| = \sqrt{r_1^2 + r_2^2 + 2r_1 r_2 \cos(\phi_1 - \phi_2)}. \tag{18}$$

The peaks of the signal will appear whenever $\phi_1 - \phi_2 = 2\pi n$, with $n \in \mathbb{Z}$. Considering that $\phi_2 = -\omega\tau_2 - \theta_0$ and $\phi_1 = -\omega\tau_1 - \theta_0$ then it is possible to find the frequency of the nth peak:

$$\omega_n = \frac{2\pi n}{\tau_2 - \tau_1}. \tag{19}$$

Using the wavelength between two consecutive peaks $\lambda = \omega_{n+1} - \omega_n$ one finds an estimate for the second time-delay:

$$\begin{aligned}\tau_2 &= \tau_1 + \frac{2\pi}{\lambda} \\ &= \tau_1 + \tau_3.\end{aligned} \tag{20}$$

3.3.3. Physical constraints for the final DTL model

Using mass and energy conservation laws Polifke and Lawn [8] show that in the low frequency limit, $\omega \rightarrow 0$, the FTF approaches unity for perfectly premixed flames. This translates to:

$$1 = g_1 \exp\left(-\frac{1}{2}\beta_1^2\sigma_1^2\right) + g_2 \exp\left(-\frac{1}{2}\beta_2^2\sigma_2^2\right). \tag{21}$$

For numerical reasons it is convenient to define the gain of the first distribution as a function of the second one:

$$g_1 = \exp\left(\frac{1}{2}\beta_1^2\sigma_1^2\right)\left(1 - g_2 \exp\left(-\frac{1}{2}\beta_2^2\sigma_2^2\right)\right). \tag{22}$$

This constraint is ensured only in the third step of the fitting process, effectively eliminating one of the variables (g_1) from the fitting procedure.

3.4. Analysis of DTL model parameters

After obtaining the model parameters from the fitting procedure for the 25 cases, we proceed to analyse the nature of the time-delays.

Consider first the time-delay associated with the first distribution of the model (DTL_1). Figure 7 shows that the phase slopes and cut-off frequency characteristics of the 25 sets of experimental data collapse when scaled using the Strouhal number $\text{St}_1 = fH/\bar{u}$. Therefore by plotting τ_1 vs $H/\bar{u}$ one would expect a linear relationship with unit proportionality constant. Figure 9(a) shows that this is exactly the case. Given that the markers closely follow the trend, one can conclude that the time-delay is given by:

$$\tau_1 = \frac{H}{\bar{u}}. \tag{23}$$

The small deviations may be associated with the way the flame height is computed.

On the other hand, Eq. (20) states that the time-delay associated with the second distribution is composed of two time-delays: τ_1 (given in Eq. (23)) and τ_3. A key characteristic with respect to τ_3 is that when the bulk velocity is kept constant (e.g., cases 10–12) while other operating conditions are varied, its value remains constant. This implies that the time-delay is associated with a fixed length scale. After inspection of the combustor, it is found that this length (L_g) corresponds to the distance between the grub screws and the dump plane (see Fig. 10). Therefore:

$$\tau_3 = \frac{L_g}{\bar{u}_p}, \tag{24}$$

[1] It will be shown later in the paper that the slope of the first distribution is exactly τ_1.

[2] This analysis is carried out with the modulations in the gain, the same analysis giving similar results can be done with the phase modulations but is not shown here for brevity.

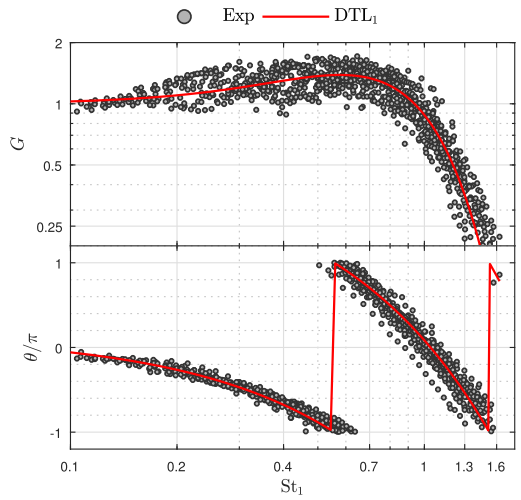

Fig. 7. Experimental FTFs of cases 1-25 scaled by St_1. The solid line is the DTL model using a single distribution. Notice that the phase slopes and the cut off frequency characteristics collapse. The phase offset of the red curve is $\theta_0/(2\pi) = 0.075$.

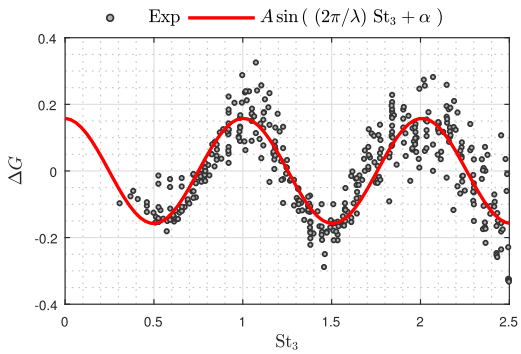

Fig. 8. Low frequency modulations scaled by St_3. The solid line is a sinusoidal curve fitted to the data. Since the data is already scaled by the appropriate Strouhal number $\lambda \approx 1$, otherwise it can be used to compute the wavelength and thus extract the value of τ_3. Note that the peaks occur at $St_3 = n$ with $n \in \mathbb{Z}$.

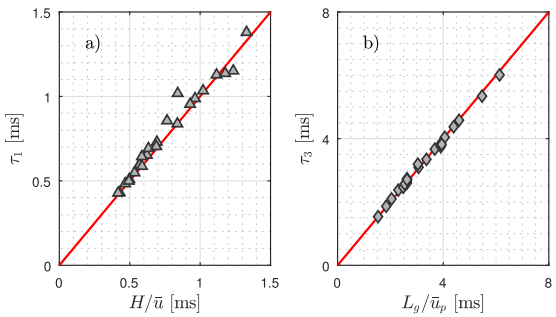

Fig. 9. Time-delays vs scaling parameters. The markers are the values of the time-delays obtained from the fitting procedure. The solid line is a straight line with unit slope.

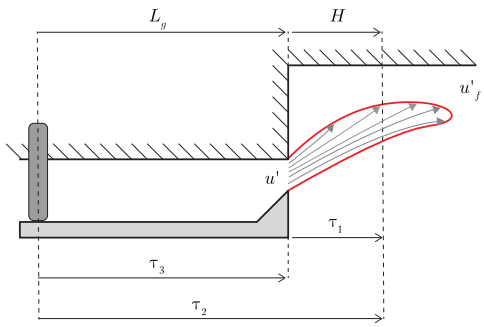

Fig. 10. Schematic of an M flame. The solid line denotes the flame front and the gray arrows represent the different paths that the velocity perturbations take to reach the flame front. Each path represents a different time-delay. Mean time-delays τ_1 and τ_2 and associated length scales L_g, and H are indicated on the schematic.

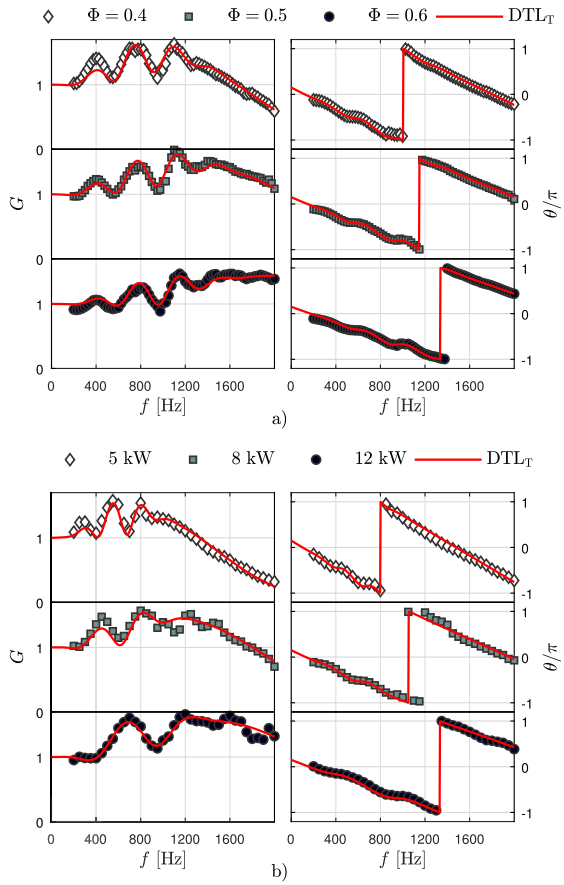

Fig. 11. FTFs of pure hydrogen $P_H = 1$, at different equivalence ratios and thermal powers. (a) Case 10, case 11 and case 12 corresponding to an increase equivalence ratio at $\bar{u} = 30$ m/s and $P_H = 1$. (b) Case 3, case 6, and case 9 corresponding to an increase in thermal power for $P_H = 1$ and $\Phi = 0.4$.

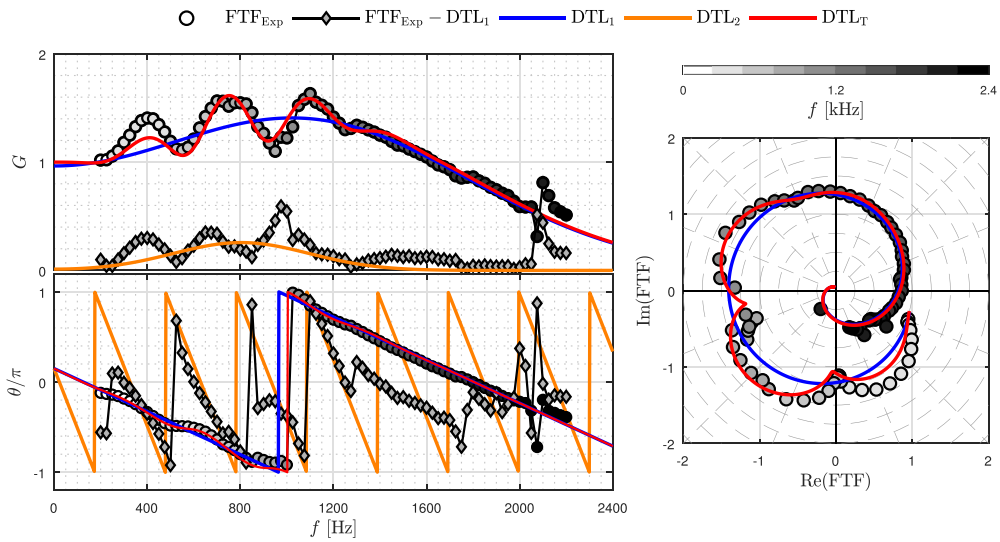

Fig. 12. DTL model and its components corresponding to the FTF of case 5, $P_H = 1$, $\Phi = 0.4$, and $P = 7$ kW.

where $\bar{u}_p$ is the bulk velocity in the pipe, which is approximately $\bar{u}_p = 4/7\bar{u}$. As with the first time-delay, Fig. 9(b) confirms that for all the cases τ_3 is given by Eq. (24). Associated with τ_3 a Strouhal number is defined such that $\mathrm{St}_3 = f\tau_3$ which scales the low frequency modulations and is independent of the flame height. This is shown in Fig. 8, where the gain difference (defined in Eq. (17)) of the 25 cases is plotted against St_3. Using Eqs. (24) and (20) one can relate the wavelength of the modulations to physical quantities: $\lambda = 2\pi\bar{u}_p/L_g$. This implies that the location of the modulations is given by the bulk velocity and the distance of the grub screws from the dump plane.

To portray the difference between the two time-delays (and to demonstrate the accuracy of the model to capture these FTFs) the attention is placed on two different sets of experimental data where pure hydrogen is used ($P_H = 1$). The first set shown in Fig. 11(a) corresponds to three FTFs where the equivalence ratio is increased while the bulk velocity is kept constant ($\bar{u} = 30$ m/s). Under these circumstances the flame length shortens because the flame speed increases. This implies that τ_1 gets smaller but τ_3 remains constant. Notice that the cut off frequency increases but that the periodicity and location of the modulations remain approximately constant. The second set shown in Fig. 11(b) corresponds to three FTFs where the thermal power is increased at a constant equivalence ratio. Under these conditions both the flame length and bulk velocity increase. This causes τ_1 to become smaller because the bulk velocity grows faster than the flame length. τ_3 also becomes smaller. As before the cut-off frequency increases but to a lesser degree. Nonetheless, the modulations shift and stretch out in the frequency axis.

Having characterized each of the time-delays allows one to associate each of the distributions with the corresponding physical mechanisms. Take as an example case 5 plotted in Fig. 12. The first distribution (DTL$_1$) corresponds to the heat release fluctuations caused by the velocity fluctuations as they propagate from the dump plane until they reach the flame front. It presents a low pass filter behavior and a short time-delay. The second distribution (DTL$_2$) corresponds to heat release fluctuations caused by the velocity fluctuations generated by vortex shedding at the grub screws. It has a band pass filter behavior and a long time-delay. This behavior is similar to that observed in swirl stabilized flames

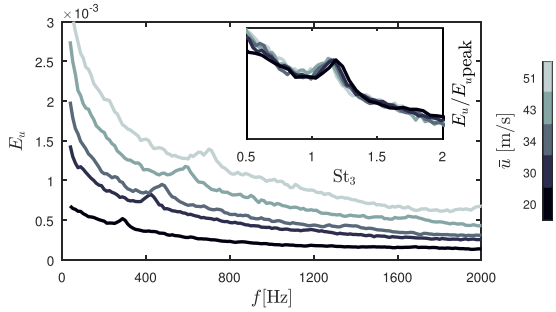

Fig. 13. Energy spectra of the unforced flow at a range of bulk velocities. Peaks appear at $\mathrm{St}_3 \approx 1.2$ due to vortex shedding from the grub screws. This corresponds to $\mathrm{St}_{d_g} = fd_g/\bar{u}_p \approx 0.12$.

[21], where a trough in the gain appeared due to the destructive interference between a vorticity wave generated at the swirler and the acoustic velocity disturbances. For this case a similar conclusion is obtained: vortices shed from the grub screws generate large flame surface area fluctuations.

In general, this suggests that any type of upstream flow disturbances induced by geometry, can introduce modulations in the FTF. As long as the disturbances have a low pass or band pass filter behavior they can be accurately represented by the distributed time lag model. In the following section a detailed cold flow analysis is performed to support the assumption that the second mechanism, DTL$_2$, is driven by vortex shedding from the grub screws.

3.5. Characterization of the second mechanism via cold flow measurements

Two sets of cold flow measurements are conducted. One measures the velocity at the burner exit and the second measures the velocity at different positions between the grub screws and the dump plane. For the first set of experiments a HWA is placed at the burner exit above one of the grub screws. The HWA is used to sample time series of unforced flow velocity u_{hw} in 5 min in-

tervals, at 5 different bulk velocities. The time series are used to estimate the energy spectra $E_u = \int \left(u'_{\mathrm{hw}} * u'_{\mathrm{hw}}\right) \exp(j\omega t)\, dt$ plotted in Fig. 13. We observe that there is a peak in the spectra at all bulk velocities. The frequency at which the peaks are located increases with bulk velocity. In the inset of Fig. 13 each spectra is normalized by the peak value and plotted against St_3. The collapse of this data with St_3, is an indication that the second mechanism is driven by vortex shedding. The corresponding Strouhal number based on the grub screw diameter (d_g) is $\mathrm{St}_{d_g} = 0.12$ and the range of Reynolds numbers is $\mathrm{Re}_{d_b} = [1200–7500]$.

For the second set of experiments the bluff body is removed in order to fit the HWA inside the pipe. However, the center rod and the grub screws are left in, such that the forced flow experiences the same conditions as when measuring FTFs. For this set of experiments the forcing level and the bulk velocity in the pipe are kept constant. The velocities measured by the MMM (u) and the HWA (u_{hw}) are sampled simultaneously at different downstream locations $L_h = \tilde{L}\, d_g$ with respect to the grub screws (see Fig. 1 for an schematic). Figure 14 shows the magnitude and phase of the ratio $\hat{u}/\hat{u}_{hw}$ vs frequency at three different locations. Both quantities are computed in the same way as for the FTFs (Eq. (2)). Notice the presence of similar modulations that decay with the distance from the grub screw. These modulations are caused by the interference between the acoustic velocity and the velocity disturbances induced by vortex shedding from the grub screws. The time delay, being inversely proportional to the wavelength of the modulations, increases when the measurement point is further away from the grub screw. These measurements show that changing the position of the grub screws (varying L_g) has the same effect in the time delay as increasing the bulk velocity (as done above for the FTFs).

To obtain more information from the measurements we fit two distributions $\mathrm{DTL_H} = \mathrm{DTL}_a + \mathrm{DTL_h}$. The first distribution $\mathrm{DTL}_a \approx 1$ is used to represent the fraction of velocities containing only the acoustic component. A small time delay is added to correct for the small phase deviation caused by uncertainty between the two measurements. The second distribution DTL_h represents the fraction of velocities between the acoustic and induced velocities due to vortex shedding. Thus, the coefficients τ_h, g_h, β_h, and σ_h, describe the nature of the interfering mechanism, i.e., the frequency response of vortex shedding.

The fits ($\mathrm{DTL_H}$) are indicated by the red lines in Fig. 14. The coefficients τ_h, g_h, σ_h, and β_h are shown in Fig. 15. As expected, the time delay τ_h increases with L_h. The amplitude g_h decays exponentially with L_h. The frequency response given by σ_h and β_h remains constant. This indicates that the acoustic forcing locks on the natural shedding frequency of the grub screws [35]. These characteristics are taken into account when a generalized DTL model is developed later in the paper. The Strouhal number based on the grub screw diameter $\mathrm{St}_{d_g} = \beta_h d_g/(2\pi \bar{u}_p) = 0.13$ is close to the value obtained from the peaks of the spectra in Fig. 13.

The analysis performed in this section provides further evidence that any type flow disturbances induced by the geometry upstream of the flame can introduce modulations in the FTF. Furthermore, the DTL model is able to capture the band pass filter characteristics of the second mechanism which in this case is centered at the shedding frequency given explicitly by $\beta_h/(2\pi)$ (a model parameter). Hence, the model used in this paper (Eq. (15)) gives an advantage compared to previous formulations of the DTL model [19].

In the following section we take advantage of the trends observed in both mechanisms in order to obtain a generalized DTL model for the measured FTFs.

4. Generalized distributed time lag model

Having analysed the two different mechanisms that constitute the distributed time lag model, we proceed to generalize the model. This enables the prediction of FTFs for a given flame height H, bulk velocity $\bar{u}$ and distance from the grub screws L_g. The challenge is to find a general expression for the gain parameters of the distributions (g_i, β_i, and σ_i) in terms of these inputs. General expressions for the phase parameters, i.e., time-delays, have already been deduced as seen in Fig. 9.

In Fig. 7 it is shown that the cut off characteristics collapse under the frequency scaling $H/\bar{u}$. Therefore it is convenient to define a cut-off frequency ω_c that scales with this reduced frequency. The value of ω_c is based on the following gain value of a single distribution:

$$|\mathrm{DTL}_1(\omega_c)| = \frac{1}{\sqrt{2}} \frac{g_1}{2}. \tag{25}$$

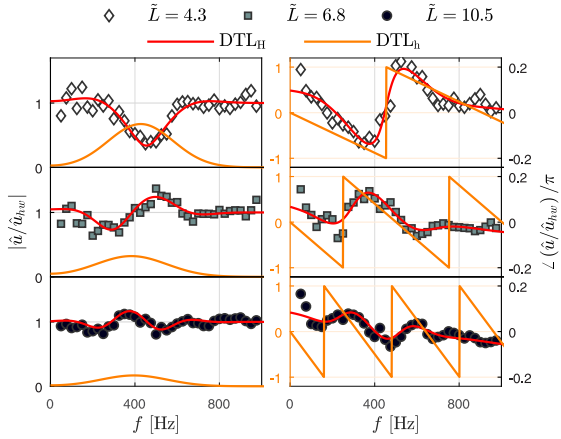

Fig. 14. Magnitude and phase difference of the ratio $\hat{u}/\hat{u}_{\mathrm{hw}}$ at $\bar{u}_p = 13.7$ m/s. $\mathrm{DTL_H}$ (red lines) is used to capture the cold flow modulations between the velocity measured by the MMM and the velocity measured by HWA. This data set presents similar interference patterns as those observed in the FTFs. (For interpretation of the references to color in this figure legend, the reader is referred to the web version of this article.)

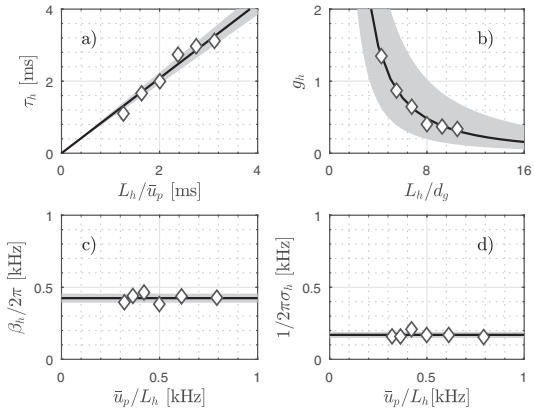

Fig. 15. Parameters from $\mathrm{DTL_H}$ fitted to $\hat{u}/\hat{u}_{\mathrm{hw}}$ (red lines in Fig. 14). The cold flow exhibits modulations with band-pass characteristics similar to those observed for the FTFs. $\tau_h \approx L_g/\bar{u}_p$. σ_h and β_h are approximately constant while g_h decays exponentially as indicated by the fitted solid lines. Shaded regions indicate 95% confidence intervals.

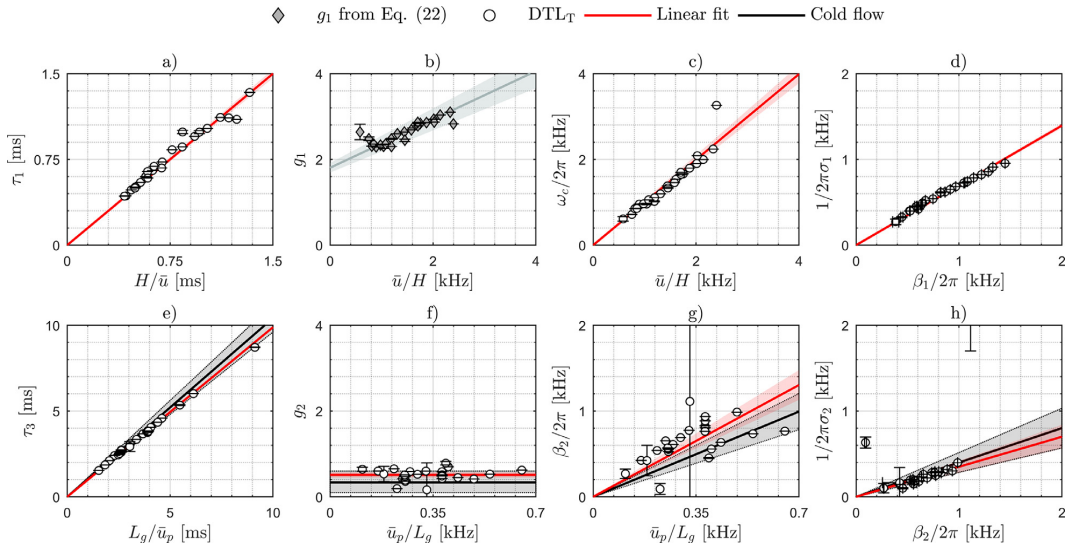

Fig. 16. Dependence of the DTL model parameters with the flame and burner parameters H, $\bar{u}$ and L_g. Each marker corresponds to one of the 25 cases. The error bounds correspond to 3 standard deviations. The red lines correspond to linear fits of the data. Plot (b) is only displayed for completeness, the actual value of g_1 is given by Eq. (22). No linear regression is required for this variable. The black lines are estimates from the cold flow analysis. All shaded regions correspond to 95% confidence intervals. (For interpretation of the references to color in this figure legend, the reader is referred to the web version of this article.)

Using this definition, combining it with Eq. (15) and reorganizing the terms gives an implicit expression for the cut off frequency:

$$\omega_c = \beta_1 + \frac{1}{\sigma_1}\sqrt{2\ln\left(\sqrt{2}\left(1+\exp\left(-2\sigma_1^2\beta_1\omega_c\right)\right)\right)}. \tag{26}$$

For all cases considered in this paper, $\exp(-2\sigma_1^2\beta_1\omega_c) \ll 1$, hence the previous equation can be approximated as:

$$\omega_c = \beta_1 + \frac{\sqrt{\ln(2)}}{\sigma_1}. \tag{27}$$

Since the cut off frequency depends on two parameters, another equation is required in order to generalize the model. The scaling used in Section 3.3.1 and the results from Section 3.5 suggest the following relationship between σ_i and β_i:

$$\frac{1}{\sigma_i} \propto \beta_i. \tag{28}$$

From the cold flow measurements we obtain that since L_g is constant $g_2 \approx$ constant and that the shedding frequency $\beta_2/(2\pi)$ increases linearly with bulk velocity:

$$\frac{\beta_2}{2\pi} \propto \frac{\bar{u}_p}{L_g}. \tag{29}$$

With all these definitions one can propose linear scalings for each of the distributions as shown in Fig. 16 with their corresponding linear regression curve. The shaded regions indicate 95% confidence intervals on the fits. To generate this figure recall that each FTF corresponds to the mean of 40 different samples (see Section 2.3). Therefore, in order to obtain the values of the model parameters instead of fitting them to the mean FTF values, they are fitted to each of the 40 samples. This enables the visualization of the experimental scatter given by the error bounds in the figure.

The first row in Fig. 16 corresponds to the parameters of the first distribution all of which display a linear dependency as denoted by the fitted red line. The parameters of the second distribution are shown in the second row. For comparison, a black line and a gray shaded region have been added to represent the mean and scatter of the cold flow measurements. The parameters of the second distribution also display linear trends except for the gain g_2 which is shown to be constant with respect to $\bar{u}_p/L_g$. The shedding frequency $\beta_2/(2\pi)$ presents the most scatter. These data points seem to cluster along two lines corresponding to $\mathrm{St}_{d_g} \approx 0.11$ and $\mathrm{St}_{d_g} \approx 0.22$. A possible explanation is that both these lines correspond to the shedding frequency and the corresponding subharmonic. However, for consistency the linear fit (red line) is used to represent the trend for the generalized model.

By knowing the coefficients of the linear fits (red lines in Fig. 16) one can predict the FTF at different operating points which have not been tested. At least two points are required in order to compute the regression curves. In order to increase accuracy it is desirable to choose operating points with a large separation between the values of $H/\bar{u}$ and similarly for the values of $L_g/\bar{u}_p$.

4.1. Performance of generalized DTL

As a matter of example, the generalized model is computed using two operating conditions. Then its performance in terms of precision and accuracy is studied in detail.

For the computation of the generalized DTL model case 7 ($P_H = 1$, $\Phi = 0.4$, $P = 9$ kW) and case 15 ($P_H = 0.3$, $\Phi = 0.7$, $P = 3$ kW) are used. Case 7 has values $H/\bar{u} = 0.50$ ms and $L_g/\bar{u}_p = 2.00$ ms, while case 15 has $H/\bar{u} = 1.72$ ms and $L_g/\bar{u}_p = 9.1$ ms. This ensures that the points used to obtain the regression curves are far apart from each other.

To quantify the performance of the generalized model it is useful to start by defining the different transfer functions:

- FTF$_{Sin}$ corresponds to a single sample of the experimental FTF.
- FTF$_{Exp}$ corresponds to the FTF obtained by averaging the 40 samples of experimental data.
- DTL$_T$ corresponds to the FTF obtained by fitting a single sample of the experimental data.
- DTL$_G$ corresponds to the FTF obtained from the generalized model by interpolation.

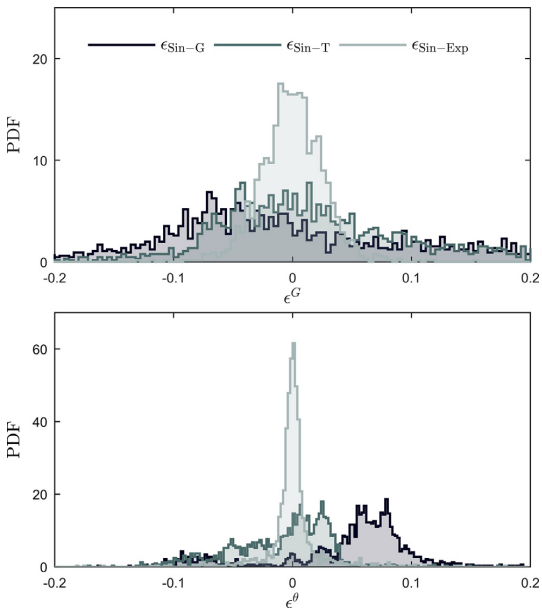

Fig. 17. Histogram of relative errors in the gain ϵ^G and in the phase ϵ^θ for case 5 ($P_H = 1$, $\Phi = 0.4$, $P = 7$ kW)

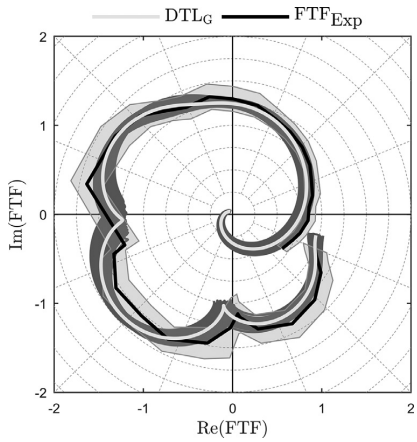

Fig. 18. DTL_G and FTF_{Exp} for case 5 ($P_H = 1$, $\Phi = 0.4$, $P = 7$ kW) plotted as complex numbers. The dark gray shaded region shows a normally distributed uncertainty of 3% imposed on all input parameters of DTL_G. The light gray shaded region corresponds to the error bounds given by 3 standard deviations of the experimental measurements.

Then the relative error between the gain of two transfer functions, say FTF_A and DTL_B is defined by:

$$\epsilon^G_{A-B} = 1 - \frac{|FTF_A|}{|DTL_B|} \tag{30}$$

A similar definition is given for the relative error between the phases (ϵ^θ_{A-B}). The three relevant relative errors used to study the accuracy and precision are:

1. $\epsilon_{Sin-Exp}$, measures error due to experimental scatter.
2. ϵ_{Sin-T}, measures the error due to the fitting procedure.
3. ϵ_{Sin-G}, measures the error due to interpolation (regression model), the fitting procedure, the computation of flame height and experimental scatter.

The errors are computed for each of the 40 samples at all measured frequencies. The resulting arrays of relative error are shown as histograms in Fig. 17 for case 5 ($P_H = 1$, $\Phi = 0.4$, $P = 7$ kW). The errors take approximately the shape of a Gaussian probability density function (PDF) with S as the standard deviation and μ as the mean value. The metrics S and μ represent precision and accuracy, respectively, and are computed directly from the errors listed above for both the gain and the phase. The errors of DTL_G and FTF_{Exp} can be visualized in Fig. 18. The dark gray shaded region corresponds to a normally distributed scatter of 3% in each of the parameters around the curve given by DTL_G. The light gray shaded region corresponds to 3 times the standard deviation of the 40 samples. As it can be seen the generalized model predicts the FTF well within the uncertainty bounds of the experimental scatter.

To get an idea about the order of magnitude that each source of error (experimental scatter, fitting procedure, interpolation) contributes to the generalized model, S and μ are compared between the three computed errors ($\epsilon_{Sin-Exp}$, ϵ_{Sin-T}, and ϵ_{Sin-G}). First the relative errors in the prediction of the gain are considered. The experimental scatter has a precision of $\mu = 0.00$ and an accuracy of $S = 0.02$. The fitting procedure DTL_T has a precision of $\mu = 0.01$ and an accuracy of $S = 0.07$. The generalized model DTL_G predicts the gain with a precision of $\mu = 0.04$ and an accuracy of $S = 0.09$. Notice that the errors due to the fitting procedure and the experimental scatter are included in DTL_G, therefore it is expected that the values of μ and S from the generalized model to be higher. Furthermore, one can notice that in terms of accuracy all estimates are of same order of magnitude and if one adds S computed from $\epsilon_{Sin-Exp}$ and ϵ_{Sin-T}, one gets roughly the same value as computed from ϵ_{Sin-G}. This indicates that the generalized model predicts the gain to a similar degree of precision as the fitting procedure and the experimental scatter. A similar conclusion can be made by considering the errors from the phase. An estimation of the magnitude of the error for this case is $|\mu| < 0.1$ and $|S| < 0.1$ for the gain and $|\mu| < 0.05$ and $|S| < 0.05$ for the phase.

This procedure is repeated for all 25 cases where μ and S are computed for both the gain and the phase. The results are summarized in Fig. 19 which shows ϵ^G and ϵ^θ for the three errors. The error bars correspond to a projection of the histograms displayed in Fig. 17. The markers indicate the mean μ and the error bounds are computed as $\pm$ 1.3S which correspond to 80% confidence intervals given that the error is Gaussian distributed. The shaded regions also correspond to 80% confidence intervals of the experimental scatter with $\mu = 0$ by definition. One can see that the accuracy of the fitting procedure is better than the accuracy of the generalized model as one would expect. However, the precision is in the same order of magnitude for both DTL_T and DTL_G and for most cases the value of 1.3S is less than 20%. The prediction of the phase is better than for the gain, mainly due to the lower values of the experimental scatter.

To get a better visual representation of the performance (Fig. 19) DTL_G and FTF_{Exp} are presented for six cases as shown in Fig. 20. The cases correspond to the same FTFs fitted in Fig. 11. One can see that using only two cases to get the regression lines for the generalized model provides a good estimation of both the gain and the phase. The cut-off frequency varies significantly in Fig. 20(a) and both the cut-off frequency and the periodicity of the modulations change significantly in Fig. 20(b). This shows that the generalized model is able to predict a great variety of cases provided that the scaling is approximately linear, as shown before. It is important to stress that the generalization of the method still

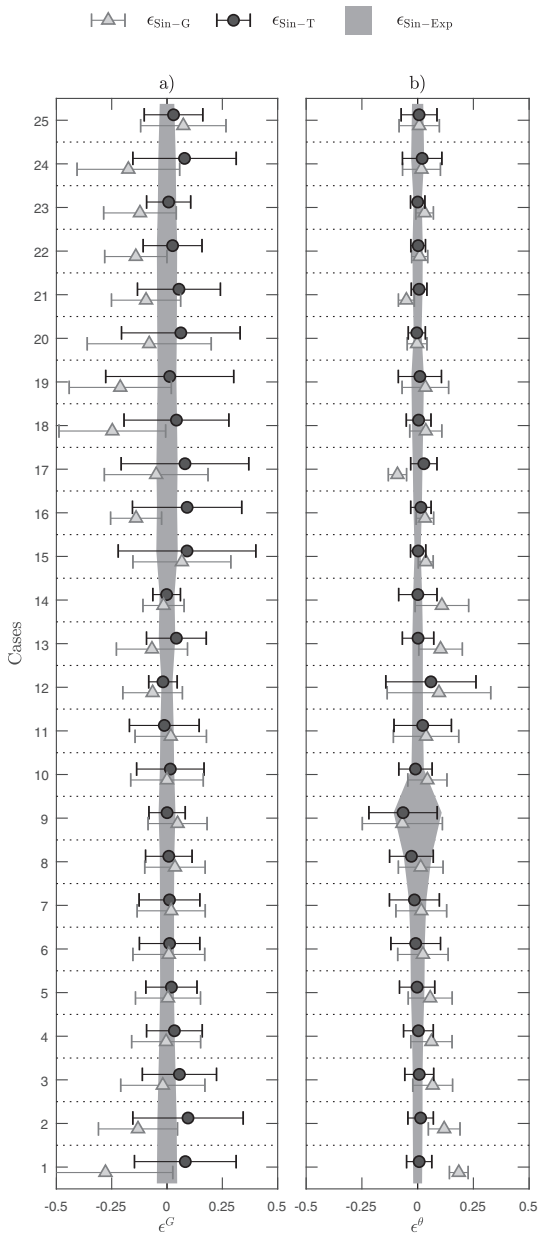

Fig. 19. Summary of the performance of the generalized DTL model. Accuracy (μ) and precision (S) computed for the gain (a) and phase (b) for all three errors ($\epsilon_{\text{Sin-Exp}}$, $\epsilon_{\text{Sin-T}}$, and $\epsilon_{\text{Sin-G}}$). Error bounds are $\pm$ 1.3S.

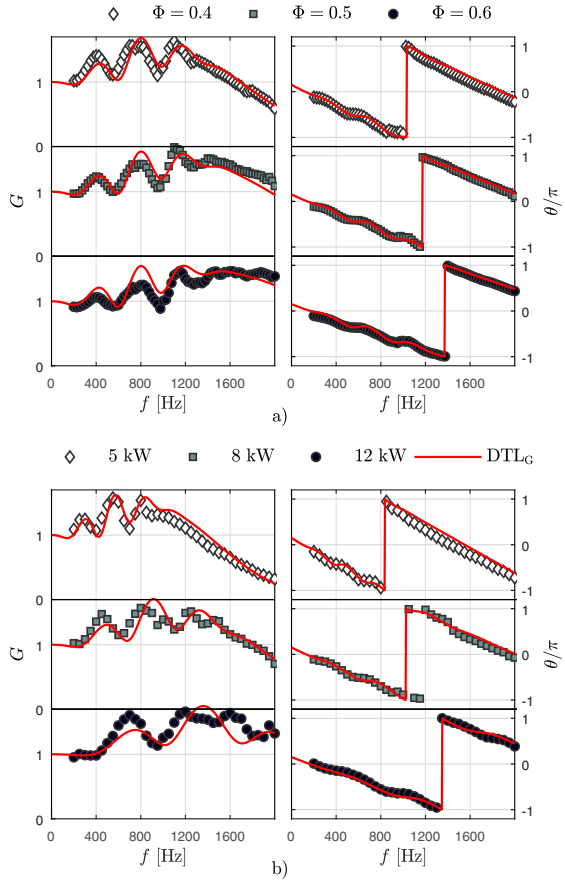

Fig. 20. FTF_{Exp} and predicted FTFs by DTL_G. (a) Case 10, case 11 and case 12 corresponding to an increase equivalence ratio at $\bar{u} = 30$ m/s and $P_\text{H} = 1$. (b) Case 3, case 6, and case 9 corresponding to an increase in thermal power for $P_\text{H} = 1$ and $\Phi = 0.4$. All cases correspond to the same fitted cases shown in Fig. 11.

needs to be tested for different flames shapes and conditions such as swirling flames.

5. Conclusions

Flame transfer function measurements of perfectly premixed, hydrogen-methane, bluff body stabilized, "M" flames are presented. The FTFs display peaks and troughs in both the gain and the phase which are shown to be a manifestation of the interaction of two velocity fluctuation mechanisms. The first mechanism corresponds to the velocity perturbations generated at the base of the flame as they propagate downstream to the flame front. It has a time-delay given by the flame height and the bulk velocity, i.e., $\tau_1 = H/\bar{u}$. The second mechanism corresponds to the vortices shed from the grub screws as they propagate downstream to the flame front as evidenced by the forced and unforced cold flow measurements. It has a time-delay given by the position of the grub screws, the bulk velocity in the pipe and the first time-delay, i.e., $\tau_2 = \tau_1 + L_g/\bar{u}_p$. It is shown that a Strouhal number based on τ_1 collapses the cut off frequency characteristics of the 25 measured cases. On the other hand a Strouhal number based on the time-delay $\tau_3 = \tau_2 - \tau_1$ is shown to collapse all the peaks and troughs of the FTF.

A distributed time lag model based on the impulse response of each of the mechanisms is developed. It builds from previous models found in literature which consider two normal distributions of time-delays. The new model introduces a modulating term which shifts the peak of the distribution in the frequency space. This allows a single distribution to capture excess gain and allows the second mechanism to behave as a band pass filter centered around the modulating frequency. The benefit of this is that mech-

anisms exhibiting a preferred frequency, such as vortex shedding can easily be identified by analysing the model parameters. The new model is able to capture all the characteristics of the FTFs and the cold flow in detail.

Finally a generalized form of the distributed time lagged model is developed. This model takes as an input the bulk velocity and the flame height and predicts the corresponding FTF based on interpolation of the model parameters. The performance of the model is tested showing good predicting capabilities in terms of precision and accuracy. However, the model has only been used in M flames. The behavior is expected to be different for V flames, conical flames or swirled flames, which may require the model to be extended.

Declaration of Competing Interest

The authors declare that they have no known competing financial interests or personal relationships that could have appeared to influence the work reported in this paper.

Acknowledgments

The authors acknowledge support from the NCCS Centre, funded under the Norwegian research program, Centres for Environment-friendly Energy Research (FME). Grant no.: 257579/E20. The authors would also like to thank Prof. W. Polifke for valuable comments on an early draft of the paper.

References

[1] T.C. Lieuwen, V. Yang, Combustion Instabilities In Gas Turbine Engines: Operational Experience, Fundamental Mechanisms, and Modeling, American Institute of Aeronautics and Astronautics, Reston, VA, 2006, doi:10.2514/4.866807.
[2] C. Klsheimer, H. Bchner, Combustion dynamics of turbulent swirling flames, Combust. Flame 131 (1) (2002) 70–84, doi:10.1016/S0010-2180(02)00394-2.
[3] D. Durox, T. Schuller, N. Noiray, S. Candel, Experimental analysis of nonlinear flame transfer functions for different flame geometries, Proc. Combust. Inst. 32 (1) (2009) 1391–1398, doi:10.1016/j.proci.2008.06.204.
[4] K.T. Kim, J.G. Lee, B.D. Quay, D.A. Santavicca, Response of partially premixed flames to acoustic velocity and equivalence ratio perturbations, Combust. Flame 157 (9) (2010) 1731–1744, doi:10.1016/j.combustflame.2010.04.006.
[5] P. Palies, D. Durox, T. Schuller, S. Candel, Nonlinear combustion instability analysis based on the flame describing function applied to turbulent premixed swirling flames, Combust. Flame 158 (10) (2011) 1980–1991, doi:10.1016/j.combustflame.2011.02.012.
[6] A. Kaufmann, F. Nicoud, T. Poinsot, Flow forcing techniques for numerical simulation of combustion instabilities, Combust. Flame 131 (4) (2002) 371–385, doi:10.1016/S0010-2180(02)00419-4.
[7] T. Schuller, D. Durox, S. Candel, A unified model for the prediction of laminar flame transfer functions: comparisons between conical and V-flame dynamics, Combust. Flame 134 (1) (2003) 21–34, doi:10.1016/S0010-2180(03)00042-7.
[8] W. Polifke, C. Lawn, On the low-frequency limit of flame transfer functions, Combust. Flame 151 (3) (2007) 437–451, doi:10.1016/j.combustflame.2007.07.005.
[9] A.P. Dowling, A kinematic model of a ducted flame, J. Fluid Mech. 394 (1999) 51–72, doi:10.1017/S0022112099005686.
[10] M. Fleifil, A.M. Annaswamy, Z.A. Ghoneim, A.F. Ghoniem, Response of a laminar premixed flame to flow oscillations: A kinematic model and thermoacoustic instability results, Combust. Flame 106 (4) (1996) 487–510, doi:10.1016/0010-2180(96)00049-1.
[11] L. Crocco, Aspects of combustion stability in liquid propellant rocket motors Part I: fundamentals. low frequency instability with monopropellants, J. Am. Rocket Soc. 21 (6) (1951) 163–178, doi:10.2514/8.4393.
[12] T. Sattelmayer, Influence of the combustor aerodynamics on combustion instabilities from equivalence ratio fluctuations, J. Eng. Gas Turb. Power 125 (1) (2003) 11–19, doi:10.1115/1.1365159.
[13] W. Polifke, J. Kopitz, A. Serbanoviv, Impact of the fuel time lag distribution in elliptical premix nozzles on combustion stability, 7th AIAA/CEAS Aeroacoustics Conference and Exhibit, American Institute of Aeronautics and Astronautics, Reston, Virigina (2001), pp. 1–11, doi:10.2514/6.2001-2104.
[14] P. Preetham, S. Hemchandra, T. Lieuwen, Forced response of premixed flames: effect of flow non-uniformity, 46th AIAA Aerospace Sciences Meeting and Exhibit, American Institute of Aeronautics and Astronautics (2008), doi:10.2514/6.2008-978.
[15] A. Huber, W. Polifke, Dynamics of practical premixed flames, Part ii: identification and interpretation of CFD data, Int. J. Spray Combust. Dyn. 1 (2) (2009) 229–249, doi:10.1260/175682709788707440.
[16] R.S. Blumenthal, P. Subramanian, R.I. Sujith, W. Polifke, Novel perspectives on the dynamics of premixed flames, Combust. Flame 160 (7) (2013) 1215–1224, doi:10.1016/j.combustflame.2013.02.005.
[17] B. Schuermans, V. Bellucci, F. Guethe, F. Meili, P. Flohr, C.O. Paschereit, A detailed analysis of thermoacoustic interaction mechanisms in a turbulent premixed flame, Volume 1: Turbo Expo 2004, ASME, Vienna, Austria (2004), pp. 539–551, doi:10.1115/GT2004-53831.
[18] W. Polifke, Black-box system identification for reduced order model construction, Ann. Nucl. Energy 67 (2014) 109–128, doi:10.1016/j.anucene.2013.10.037.
[19] T. Komarek, W. Polifke, Impact of swirl fluctuations on the flame response of a perfectly premixed swirl burner, J. Eng. Gas Turb. Power 132 (6) (2010), doi:10.1115/1.4000127.
[20] M.T. Szedlmayer, B.D. Quay, J. Samarasinghe, A. De Rosa, J.G. Lee, D.A. Santavicca, Forced flame response of a lean premixed multi-nozzle can combustor, Volume 2: Combustion, Fuels and Emissions, Parts A and B, ASME, Vancouver, British Columbia, Canada (2011), pp. 883–891, doi:10.1115/GT2011-46080.
[21] P. Palies, D. Durox, T. Schuller, S. Candel, The combined dynamics of swirler and turbulent premixed swirling flames, Combust. Flame 157 (9) (2010) 1698–1717, doi:10.1016/j.combustflame.2010.02.011.
[22] M. Gatti, R. Gaudron, C. Mirat, T. Schuller, Effects of the Injector Design on the Transfer Function of Premixed Swirling Flames, American Society of Mechanical Engineers (2017), doi:10.1115/GT2017-63874. V04AT04A054–V04AT04A054
[23] M. Gatti, R. Gaudron, C. Mirat, L. Zimmer, T. Schuller, A Comparison of the Transfer Functions and Flow Fields of Flames With Increasing Swirl Number, American Society of Mechanical Engineers (2018), doi:10.1115/GT2018-76105. V04BT04A003–V04BT04A003
[24] M. Gatti, R. Gaudron, C. Mirat, L. Zimmer, T. Schuller, Impact of swirl and bluff-body on the transfer function of premixed flames, Proc. Combust. Inst. 37 (4) (2019) 5197–5204, doi:10.1016/j.proci.2018.06.148.
[25] P.R. Alemela, D. Fanaca, C. Hirsch, T. Sattelmayer, B. Schuermans, Determination and scaling of thermo acoustic characteristics of premixed flames, Int. J. Spray Combust. Dyn. 2 (2) (2010) 169–198, doi:10.1260/1756-8277.2.2.169.
[26] K.T. Kim, D.A. Santavicca, Generalization of turbulent swirl flame transfer functions in gas turbine combustors, Combust. Sci. Technol. 185 (7) (2013) 999–1015, doi:10.1080/00102202.2012.752734.
[27] J.R. Dawson, N.A. Worth, Flame dynamics and unsteady heat release rate of self-excited azimuthal modes in an annular combustor, Combust. Flame 161 (10) (2014) 2565–2578, doi:10.1016/j.combustflame.2014.03.021.
[28] N.A. Worth, J.R. Dawson, Self-excited circumferential instabilities in a model annular gas turbine combustor: Global flame dynamics, Proc. Combust. Inst. 34 (2) (2013) 3127–3134, doi:10.1016/j.proci.2012.05.061.
[29] B. Higgins, M.Q. McQuay, F. Lacas, J.C. Rolon, N. Darabiha, S. Candel, Systematic measurements of OH chemiluminescence for fuel-lean, high-pressure, premixed, laminar flames, Fuel 80 (1) (2001) 67–74, doi:10.1016/S0016-2361(00)00069-7.
[30] R. Balachandran, B.O. Ayoola, C.F. Kaminski, A.P. Dowling, E. Mastorakos, Experimental investigation of the nonlinear response of turbulent premixed flames to imposed inlet velocity oscillations, Combust. Flame 143 (1) (2005) 37–55, doi:10.1016/j.combustflame.2005.04.009.
[31] B. Schuermans, F. Guethe, D. Pennell, D. Guyot, C.O. Paschereit, Thermoacoustic modeling of a gas turbine using transfer functions measured under full engine pressure, J. Eng. Gas Turb. Power 132 (11) (2010) 111503, doi:10.1115/1.4000854.
[32] A.F. Seybert, D.F. Ross, Experimental determination of acoustic properties using a two-microphone random-excitation technique, J. Acoust. Soc. Am. 61 (5) (1977) 1362–1370, doi:10.1121/1.381403.
[33] B.D. Bellows, M.K. Bobba, J.M. Seitzman, T. Lieuwen, Nonlinear flame transfer function characteristics in a swirl-stabilized combustor, J. Eng. Gas Turb. Power 129 (4) (2007) 954–961, doi:10.1115/1.2720545.
[34] C.J. Dasch, One-dimensional tomography: a comparison of Abel, onion-peeling, and filtered backprojection methods, Appl. Opt. 31 (8) (1992) 1146, doi:10.1364/AO.31.001146.
[35] O.M. Griffin, M.S. Hall, Review vortex shedding lock-on and flow control in bluff body wakes, J. Fluids Eng. 113 (4) (1991) 526–537, doi:10.1115/1.2926511.

Article 2

The effect of hydrogen enrichment, flame-flame interaction, confinement, and asymmetry on the acoustic response of flames in a can combustor

Eirik Æsøy, Thomas Indlekofer, Francesco Gant, Alexis Cuquel, Mirko R. Bothien, and James R. Dawson

Considered for the Journal of Combustion and Flame

This paper is awaiting publication and is therefore not included.

Article 3

Predicting the influence of Hydrogen in Combustion Instabilities

José G. Aguilar, Eirik Æsøy, and James R. Dawson

Considered for the Journal of Combustion and Flame

This paper is awaiting publication and is therefore not included.

Article 4

Acoustic-Convective Interference in Transfer Functions of Methane/Hydrogen and Pure Hydrogen Flames

Eirik Æsøy, José G. Aguilar, Mirko R. Bothien, Nicholas A. Worth and James R. Dawson

Published in the Journal of Engineering for Gas Turbines and Power

Article 5

Tailoring the gain and phase of the flame transfer function through targeted convective-acoustic interference

Eirik Æsøy, Håkon T. Nygård, Nicholas A. Worth and James R. Dawson

Published in the Journal of Combustion and Flame

Combustion and Flame 236 (2022) 111813

Contents lists available at ScienceDirect

Combustion and Flame

journal homepage: www.elsevier.com/locate/combustflame

Tailoring the gain and phase of the flame transfer function through targeted convective-acoustic interference

Eirik Æsøy*, Håkon T. Nygård, Nicholas A. Worth, James R. Dawson

Department of Energy and Process Engineering, Norwegian University of Science and Technology, Trondheim N-7491, Norway

ARTICLE INFO

Article history:
Received 29 June 2021
Revised 10 October 2021
Accepted 11 October 2021

Keywords:
Hydrogen
Thermoacoustic instability
Flame transfer function
Flame dynamics

ABSTRACT

This paper investigates how targeted interference between two well characterized sources of hydrodynamic disturbances can modify the response of premixed bluff body stabilised H_2/CH_4 flames with and without swirl. We introduce modulations into the Flame Transfer Function (FTF) through hydrodynamic interference between the shedding of vortices/wakes from different shaped bodies upstream of the flame and the vortex roll-up at the flame base caused by acoustic forcing. By placing a set of small diameter cylinders, a streamlined body, or a swirler upstream of the bluff body and varying the distance from the dump plane, the gain and phase of the FTFs could be modulated at targeted frequencies providing a method to suppress thermoacoustic instabilities. We further investigate the flame response which shows that modulations in the fluctuating global heat release rate are caused by linear superposition along the flame front. At frequencies leading to destructive interference, large-scale wrinkling of the flame front occurs which increases the flame surface area but is offset by the simultaneous pinch-off of the flame tip which decreases flame surface area. Their combined effect reduces the amplitude of the fluctuating global heat release rate. At frequencies of constructive interference, large-scale wrinkling of the flame occurs before the flame tip pinches off, leading to an overall increase in the flame surface and amplitude of the fluctuating global heat release rate.

1. Introduction

Gas turbines burning hydrogen can potentially help deliver large-scale zero carbon power generation and facilitate rapid decarbonisation over the short to medium term. They can also play a crucial role in increasing the penetration of renewable energy sources via power to hydrogen to power cycles where excess electricity is used to produce hydrogen. This marks a shift away from their traditional role of providing a constant base load to dynamic operation. Using hydrogen as primary fuel in lean premixed combustion regimes poses certain challenges such as flashback, autoignition, and thermoacoustic instabilities [1–3]. In this paper we focus on the latter.

Thermoacoustic instabilities occur when fluctuations in the heat release rate respond to fluctuations in the flow that are coupled to combustor acoustics in a feedback loop and are a major challenge in the development of gas turbines. Low-order acoustic network models, which are used to predict thermoacoustic instabilities, require information about the relationship between the acoustically driven velocity fluctuations and the fluctuations in the heat release rate as the flame acts as a source of acoustic energy. A standard approach is to construct a Flame Transfer Function (FTF) which aims to capture how the fluctuations of the global heat release rate (HRR) respond to fluctuations in the flow velocity over a range of frequencies [4]. It has been known for a long time that the time delay between the pressure and HRR fluctuations is a key parameter that often determines the stability of a combustor [5]. Normally FTFs are empirically derived and therefore obtained from experiments as they encode burner specific information [6–9] but they can also be extracted from numerical simulations [10], or theoretically derived [11–14].

The FTF is expected to behave as a low-pass filter with a cut-off frequency determined by the flame length and an approximately linear development of the phase for a constant convective time-delay [11,15]. A number of studies have reported various departures from the low-pass behaviour in the form of modulations in the gain and phase [16–20]. By changing the axial location of a swirler Komarek and Polifke [16] observed that the gain exhibited modulations at different frequencies. Similar

* Corresponding author.
E-mail address: eirik.asoy@ntnu.no (E. Æsøy).

https://doi.org/10.1016/j.combustflame.2021.111813

modulations were also produced by changing the location of fuel injection in a technically premixed configuration [21]. In separate but contemporaneous studies, Palies et al. [17] also observed modulations in the gain in swirling premixed flames leading to the hypothesis that the modulations may originate from fluctuations in the swirl number due to convective-acoustic interactions between vorticity waves shed from the swirler and acoustic waves [22,23].

Further insight into the origin of the modulations was recently presented in a set of papers by Gatti et al. [18,24]. They demonstrated that specific changes to the burner geometry could generate a large dip in the gain which coincided with the suppression of vortical structures (measured by PIV) at frequencies where the dips occurred showing that the modulations may be driven by disturbances produced by the upstream cold flow. However, it was also suggested that both a swirler and a center rod were still important components in the generation of modulations in the gain.

Æsøy et al. [15] also observed the presence of modulations in hydrogen/methane and pure hydrogen flames. However, there were two important differences. Firstly, hydrogen enriched and pure hydrogen flames result in very short compact flames which significantly increases the cut-off frequency of the FTF compared with methane flames increasing the range over which modulations could form and secondly, the flames did not employ swirl. The modulations were shown to emanate from convective-acoustic interference from vortex shedding upstream but more importantly showed that swirl itself was not an important mechanism but rather that geometries that produce small but sufficiently phased convective disturbances lead to convective-acoustic interference. In a continuing study [25] the cold flow was investigated in detail and it was shown that similar modulations appeared in a hydrodynamic transfer function relating the acoustic and total velocity oscillations measured at the burner exit. The study showed that the modulations of the total velocity were proportional to the modulations of the HRR indicating that the effect is hydrodynamic and that the response is linear.

In this paper, we investigate the effect of flow disturbances generated upstream by three different geometries; a set of small diameter cylinders, a streamlined body, and a swirler. Their upstream location is varied to adjust the relative time-delay between the acoustic forcing and when the flow disturbances reach the flame base and elucidate how they govern acoustic-convective interference. We furthermore demonstrate how the acoustic forcing and flow disturbances can be tuned to modify the gain and phase of FTFs without significant changes to the stabilisation or the mean structure of the flame. The tuning approach is based on the concept of distributed time lags (see [15,26]) which are used to identify the optimal location for the upstream geometry needed to produce convective disturbances that result in large amplitude modulations in the gain and phase over a narrow band frequency range in the FTF. We also present high-speed imaging of OH*-chemiluminescence and Planar Laser Induced Fluoresecence (OH-PLIF) to better understand the link between the modulations and the flame dynamics.

The paper layout is as follows: Section 2 describes the experimental set-up, measurement and analysis methods used, in Section 3, measurements of the FTF for three different upstream geometries (streamlined bodies, a swirler and circular cylinders) are presented. In addition, a method to tailor the acoustic/convective interference and control the FTF gain and phase is presented and analysed. In Section 4 we consider how the flame responds to convective-acoustic interference using flame-front tracking methods to link the acoustic/convective interference to the flame sheet kinematics. Section 5 summarizes the main conclusions.

2. Experimental set-up and methods

2.1. The burner set-up

A schematic of the burner geometry is shown in Fig. 1 and is similar to the set-up used in [15]. The cylindrical quartz combustion chamber had a diameter of 44mm and a length of 50mm which was sufficiently short to avoid self-excited instabilities but long enough to enclose the flame. The bluff body had a diameter $d_b = 13$mm with a 45° inclination angle and was mounted to a rod of diameter $d_r = 5$mm.

A Cartesian coordinate system (x, y) in the streamwise and radial directions respectively is used with the origin placed at the center of the bluff body as shown in Fig. 1 b). Polar coordinates (r, θ), when used, denote the location of the relative blockage locations on each of the geometries. Three different geometric shapes were placed upstream at $L_g = 30$mm and 50mm from the bluff body as shown in Fig. 1 a). They include a set of $d_g = 10$mm long and 2.5mm wide streamlined bodies with aspect ratio 4, circular cylinders of diameter $d_g = 5$mm, and a six-vaned swirler with a chord length of $d_g = 11$mm used previously [20,27]. The subscript d_g denotes the characteristic length of the upstream geometry (chord length, diameter of the cylinders and swirler vane length).

Each produces flow disturbances (vortex/wake shedding) of varying degree locked into the forcing frequency at Strouhal number, $\mathrm{St}_{d_g} = f d_g/\bar{u}_p$, that constructively or destructively interferes with the acoustic fluctuations at the burner exit. Premixed flames using different blends of hydrogen, methane and air were investigated at a constant equivalence ratio $\Phi = 0.7$. The fraction of hydrogen by power is $\mathrm{P_H} = 0.4$ for the non-swirled and $\mathrm{P_H} = 0.2$ for the swirled cases to avoid flashback. This corresponds to volume fractions of $\mathrm{V_H} = 0.67$ and $\mathrm{V_H} = 0.43$, respectively. $\mathrm{P_H} = \frac{\mathrm{P_{H_2}}}{\mathrm{P_{H_2}+P_{CH_4}}}$ and $\mathrm{V_H} = \frac{\mathrm{V_{H_2}}}{\mathrm{V_{H_2}+V_{CH_4}}}$, where $\mathrm{P_{H_2}}$ and $\mathrm{P_{CH_4}}$ are the thermal powers from hydrogen and methane, and $\mathrm{V_{H_2}}$ and $\mathrm{V_{CH_4}}$ are the volume flow rates of hydrogen and methane. Fuel and air flows were controlled by individual Alicat mass flow controllers (MFCs) which were combined together approximately 1m upstream before entering the plenum for premixing.

Several exit velocities $\bar{u} = [10, 20, 30, 40]$ m/s measured at the bluff body were investigated. This corresponds to inlet velocities $\bar{u}_p = [5.7, 11.4, 17.1, 22.9]$ m/s which are the relevant velocity scale for the vortex shedding from upstream geometries. Acoustic forcing was provided by two Monacor KU-516 horn drivers mounted in the plenum in combination with an Aim-TTi TGA1244 signal generator and a QTX Sound PRO1000 power amplifier. The operating conditions are summarized for all cases in Table 1.

2.2. Pressure measurements

The reference acoustic velocity fluctuations $\hat{u}(x)$, were obtained at the burner dump plane using the multiple microphone method (MMM) [28]. The acoustic pressure and velocity fluctuations are given by $p'(x,t) = \mathrm{Re}\{\hat{p}(x)e^{\mathrm{j}\omega t}\}$ and $u'(x,t) = \mathrm{Re}\{\hat{u}(x)e^{\mathrm{j}\omega t}\}$ respectively. Here, $\omega = 2\pi f$ is the angular frequency, and $\hat{p}(x)$ and $\hat{u}(x)$ are given by:

$$\hat{p}(x) = A^+ \exp\left(-\mathrm{j}k_x^+ x\right) + A^- \exp\left(\mathrm{j}k_x^- x\right), \tag{1a}$$

$$\hat{u}(x) = \frac{1}{\bar{\rho}\bar{c}}\left(A^+ \exp\left(-\mathrm{j}k_x^+ x\right) - A^- \exp\left(\mathrm{j}k_x^- x\right)\right). \tag{1b}$$

In Eq. (1) the complex valued A^+ and A^- are the amplitude and phase (Riemann invariants) of upstream and downstream propagating 1D acoustic waves. The quantities $\bar{\rho}$, $\bar{c}$ and $k_x^\pm = k_x/(1 \pm \bar{u}/\bar{c})$

Table 1
Summary of operating conditions in terms of the upstream geometry, distance from the upstream geometry to the dump plane L_g, hydrogen power fraction P_H, hydrogen volume fraction V_H, equivalence ratio Φ, thermal power P, and bulk velocities $\bar{u}_p$ and $\bar{u}$ inside the pipe and at the dump plane respectively..

Geometry	L_g [mm]	P_H	V_H	Φ	P [kW]	$\bar{u}_p$ [m/s]	$\bar{u}$ [m/s]
Streamlined	50	0.4	0.67	0.7	3.5	5.7	10
Streamlined	50	0.4	0.67	0.7	7.0	11.4	20
Streamlined	50	0.4	0.67	0.7	10.5	17.1	30
Streamlined	50	0.4	0.67	0.7	14.0	22.9	40
Cylinder	50	0.4	0.67	0.7	3.5	5.7	10
Cylinder	50	0.4	0.67	0.7	7.0	11.4	20
Cylinder	50	0.4	0.67	0.7	10.5	17.1	30
Cylinder	50	0.4	0.67	0.7	14.0	22.9	40
Swirler	50	0.2	0.43	0.7	3.4	5.7	10
Swirler	50	0.2	0.43	0.7	6.9	11.4	20
Swirler	50	0.2	0.43	0.7	10.3	17.1	30
Swirler	50	0.2	0.43	0.7	13.8	22.9	40
Cylinder	30	0.4	0.67	0.7	3.5	5.7	10
Cylinder	30	0.4	0.67	0.7	7.0	11.4	20
Cylinder	30	0.4	0.67	0.7	10.5	17.1	30
Cylinder	30	0.4	0.67	0.7	14.0	22.9	40
Swirler	30	0.2	0.43	0.7	3.4	5.7	10
Swirler	30	0.2	0.43	0.7	6.9	11.4	20
Swirler	30	0.2	0.43	0.7	10.3	17.1	30
Swirler	30	0.2	0.43	0.7	13.8	22.9	40

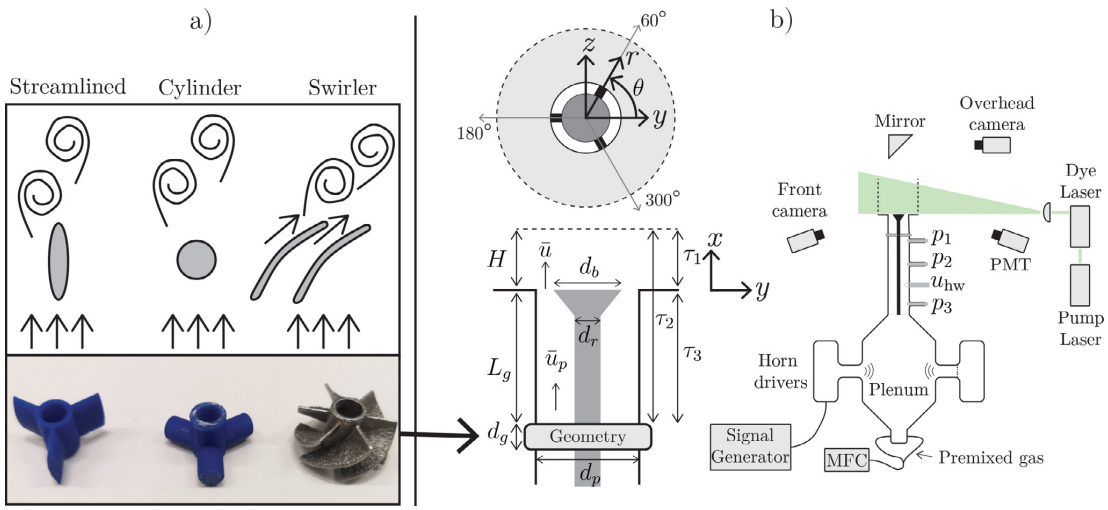

Fig. 1. Schematic of the experimental set-up and different upstream geometries investigated. a) shows images of the three geometries investigated and a schematic of the vortex shedding behind each of these. b) shows a schematic of the experimental set-up, including the injector pipe geometry with the bluff body and the location of the upstream geometries where the important time delays are indicated, a top view showing their angular location, and a front view showing the diagnostics and instrumentation.

are the density, the speed of sound and the stream-wise wave number respectively. Note that $k_x^{\pm}$ is modified by the mean flow, where $k_x = 2\pi f/c$. Eq. (1) is valid inside the pipe and the influence of the upstream geometries are negligible, which was verified experimentally. The influence of the bluff body was modeled as an acoustically compact area jump. The dynamic pressure was measured using Kulite XCS-093-0.35D pressure transducers at three locations denoted p_i for $i = 1, 2, 3$ shown in Fig. 1 b). The signals were sampled at a rate of 51.2kHz for 10s and digitized using a 24-bit NI-9234 DAQ. Spectral analysis was used to obtain $\hat{p}(x_i)$ and $A^{\pm}$ by solving for the two unknowns in Eq. (1a).

The measured values of $\hat{p}_i$, in Eq. (1a), were evaluated by:

$$\hat{p}_i = \hat{p}(x_i) = \frac{\mathrm{PSD}\left(p'_{\mathrm{ref}}, p'_i\right)}{\sqrt{\mathrm{PSD}\left(p'_{\mathrm{ref}}, p'_{\mathrm{ref}}\right)}}, \tag{2}$$

where $\mathrm{PSD}\left(p'_{\mathrm{ref}}, p'_i\right)$ is the cross power spectra between the reference signal p'_{ref} from the signal generator and the measured pressure fluctuations p'_i. Each spectrum was obtained using the Welch method by averaging 50% overlapping segments of the signal multiplied by a Hanning window.

2.3. FTF measurements

FTFs were measured at a constant forcing level $|\hat{u}|/\bar{u} = 0.05$ at the dump plane over the frequency range $f = 25 - 2000$Hz. Normalised fluctuations of the heat release rate were obtained using a Hamamatsu H11902-113 photomultiplier tube (PMT) equipped with a UV band pass filter ($310 \pm (10)$nm). It has been well established that in premixed flames the measured intensity is approximately proportional to the global HRR $Q(t) = \bar{Q} + Q'(t)$ [11,29–32].

FTFs were then calculated using [7,11]:

$$\mathrm{FTF}(\omega) = \frac{\hat{Q}/\bar{Q}}{\hat{u}/\bar{u}} = G\exp\left(j\Theta\right). \tag{3}$$

The acoustic velocity $\hat{u}$ was obtained from Eq. (1b), while the complex valued HRR $\hat{Q}$, was obtained using Eq. (2) but substituting for various HRR terms. The FTF was decomposed into a gain G and a phase Θ, which describe the relative magnitude and phase between the two quantities, $\hat{Q}$ and $\hat{u}$ respectively.

2.4. High-speed imaging: Chemiluminescence and PLIF

To characterize the flame dynamics high speed imaging of OH*-chemiluminescence from both the side ($x-y$ plane) and top ($y-z$ plane) views of the flame were obtained. OH-PLIF was also acquired in the $x-y$ plane for selected frequencies. Two high speed cameras each equipped with LaVision Intensified Relay Optics (IRO) unit, a Cerco 2178 UV lens (100F/2.8), and a notch filter $310\pm(10)$nm were used. Top views of the flame were obtained using a cooled mirror mounted at 45° approximately 1.5m above the flame. The spatial resolution of the side and top images is 11.7pixel/mm and 8.8pixel/mm.

The OH-PLIF system was comprised of a 100W green (532nm wavelength) Edgewave laser used to pump a Sirah Credo-Dye-N laser beam collimated to an approximately 1mm thick laser sheet in the $x-y$ plane. The output wavelength of the dye laser was tuned to the OH absorption peak near 281nm and the power output was approximately 3W at 10kHz. A gate time of 80nm was used to ensure that only the OH radicals excited by the laser pulse were captured. To extract the flame surface the following post-processing steps were followed: 1) a laser sheet intensity correction, 2) Gaussian smoothing, and 3) a Canny edge detection algorithm [33], similar to the approach used in [30,34,35]. The edge detection provides a binary image where $s=1$ for the pixels where the flame front is located providing a set of flame surface coordinates (x_s, y_s).

2.5. FTF described by the DTL model

To identify general trends and scalings of the flame response related to the cut-off frequency, phase development, as well as low frequency gain and phase modulations, measurements were fitted to a distributed time lag (DTL) model [26]. The general form of the model is given by:

$$\mathrm{DTL_T} = \mathrm{DTL_1} + \mathrm{DTL_2} = \left(E_1^+ + E_1^-\right) + \left(E_2^+ + E_2^-\right), \tag{4a}$$

$$E_i^{\pm} = \frac{g_i}{2}\exp\left(-\frac{1}{2}(\omega\pm\beta_i)^2\sigma_i^2 - j\omega\tau_i\right), \tag{4b}$$

where Eqs. (4a) and (4b) are a linear combination of two normally distributed time lags in the frequency domain, $\mathrm{DTL_1}$ and $\mathrm{DTL_2}$, that describe the global HRR response to velocity fluctuations. The modulation frequency β_i corresponds to the preferred frequency where the maximum response of each distribution occurs and g_i, σ_i^2, and τ_i are the gain, variance, and mean time delay respectively. The model and fitting procedure were described in detail in [15].

To illustrate the physics of the problem being modeled, we show a sketch of the relevant time-scales and dimensions in Fig. 1 b). The time lags that are represented within the DTL model parameters are solved relative to the centre of heat release $H = \max_x\left(\bar{q}_{yz}\right)$ obtained from the mean flame image. As shown in Fig. 1 b), $\tau_1 \approx H/\bar{u}$ and is the time taken for acoustic velocity fluctuations to travel from the dump plane to H whereas $\tau_2 \approx H/\bar{u} + L_g/\bar{u}_p$ is the time taken by a vortex shed from the upstream geometry (locked into the forcing frequency) to reach H. At a fixed operating condition, the interaction between $\mathrm{DTL_1}$ and $\mathrm{DTL_2}$ is therefore controlled by the relative time-delay $\tau_3 = \tau_2 - \tau_1$ which only depends on the distance L_g and $\bar{u}_p$. Due to the increase of $\bar{u}_p$ over the contraction of the bluff body a correction is added to L_g which is reduced by 1.55mm when computing τ_3.

To characterise the interference between these time delays it is convenient to rewrite Eq. (4) as:

$$\mathrm{DTL_T} = \mathrm{DTL_1}\left(1 + \frac{|\mathrm{DTL_2}|}{|\mathrm{DTL_1}|}\exp\left(j2\pi f\tau_3\right)\right), \tag{5a}$$

$$f\tau_3 \approx \frac{fL_g}{\bar{u}_p}, \tag{5b}$$

where $f\tau_3$ is the non-dimensional time-delay which determines the phase between the two sources. Under the condition that $|\mathrm{DTL_2}| < |\mathrm{DTL_1}|$, the second term in Eq. (5a), can be considered a modulation term. Whenever $f\tau_3$ is integer valued, i.e. $f\tau_3 = N$ where $N\in\mathbb{N}$, the two contributions are in phase, resulting in peaks in the gain of the FTF. Therefore the wavelength of the modulations in the gain is inversely proportional to $1/\tau_3$. Similarly, a minimum in the gain occurs when $f\tau_3 = N\pm 1/2$. When $f\tau_3 = N\pm 1/4$, the two contributions are 90° out-of-phase, resulting in a relatively large shift in the phase but a comparatively small modulation in the gain. We show how to use these features to tailor the gain and phase of the FTF in the next section.

3. Tailoring the Flame Transfer Function

3.1. FTFs for different upstream geometries

A set of FTFs were measured with each set of geometries placed at $L_g = 30$mm and 50mm upstream of the dump plane for a range of $\bar{u}$. These are shown in Fig. 2 a), b), and c) for the streamlined bodies, cylinders, and the swirler respectively. The corresponding mean flame shapes are also plotted in Fig. 3 for selected operating conditions. Particular care was taken to align the image plane with one of the cylinders and streamlined goemetries shown in Fig. 1 to capture their effect on mean flame shape. Panel d) shows the presence of a small asymmetry of the mean flame shape which exhibit weaker modulations in the FTF gain whereas the strongest modulations occur in flames a), b), f) and g) which appear approximately axisymmetric. As small deviations in axisymmetry are often observed in flames, this serves to demonstrate how the mean flame shape is not a reliable indicator of the presence of non-uniformities in the base flow that may affect the transfer function.

Figure 2 shows that the cut-off frequencies collapse when scaling with a Strouhal number based on the centre of heat release H, $\mathrm{St}_H = fH/\bar{u}$. We can also express St_H as an equivalent non-dimensional time-delay: $\mathrm{St}_H = f\tau_1$. Figure 2 shows that streamlined body and cylinders show good collapse of the cut-off frequency whereas the swirler shows a reasonable but less effective degree of collapse. This is due to the reference velocity scale being ill defined as $\bar{u}$ does not take the tangential velocity component into account.

When the upstream geometries are placed at $L_g = 50$mm, weak modulations in the gain are observed for the streamlined bodies, become more pronounced with the cylinders, and are strongest in swirling flames [16,17,20,24]. The wavelengths and relative phase of the modulations do not scale with St_H exemplified by the swirler case in Fig. 2 c). This demonstrates that an additional non-dimensional group is needed to scale both the cut-off frequency behaviour and the modulations of the FTF.

Figure 4 plots the modulations in the gain in the low-frequency range for the cyclinder and swirler geometries at $L_g = 30$mm and 50mm scaled by $fL_g/\bar{u}_p$ and $fd_g/\bar{u}_p$ for comparison. The figure shows that positioning the upstream geometries closer to the burner exit increases the amplitude of the modulations (the disturbances have less time to decay) and that scaling by L_g best aligns

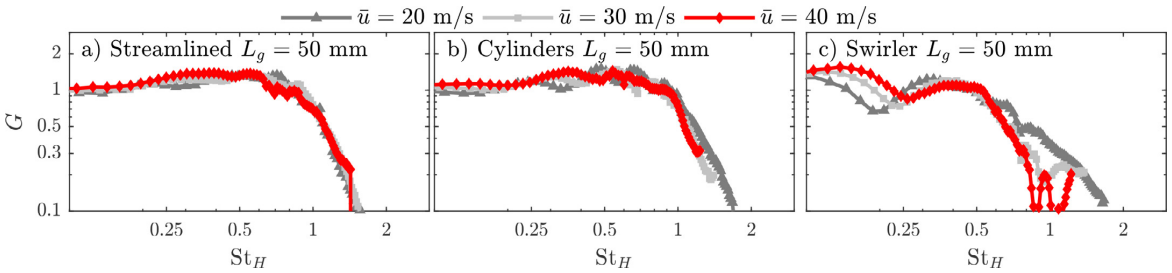

Fig. 2. Gain G of measured FTFs for the different upstream geometries (streamlined body, cylinder, and swirler) at different velocities. The gain cut-off is collapsed well for the cases with streamlined bodies and cylinders, and reasonably well for the cases with the swirler by scaling the FTFs by the time delay $\mathrm{St}_H \approx fH/\bar{u} \approx f\tau_1$.

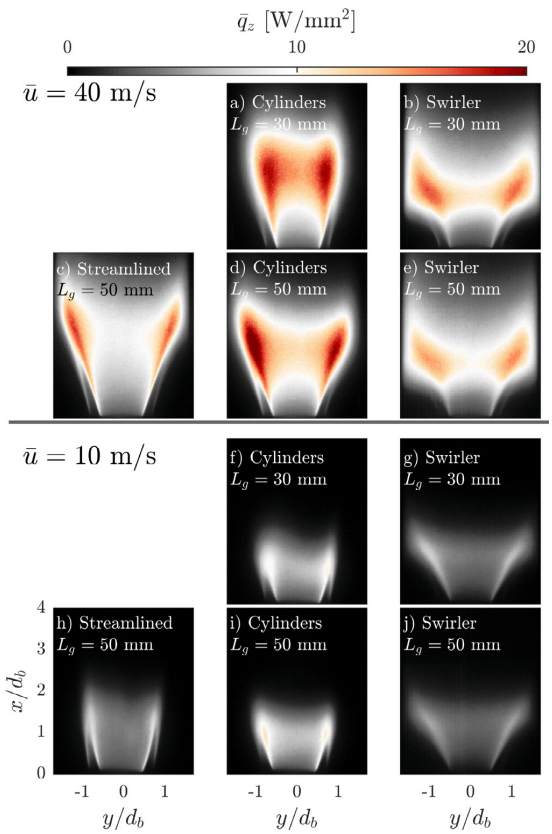

Fig. 3. Time-averaged flame shapes viewed from the side $\bar{q}_z$. The top set of images are taken at $\bar{u} = 40$m/s and the bottom set at $\bar{u} = 10$m/s. The different position L_g and type of geometry are annotated in each panel.

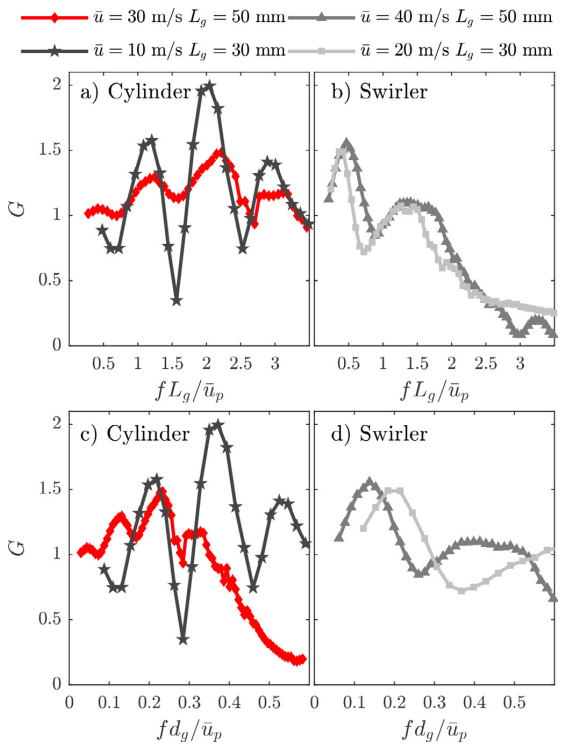

Fig. 4. Scaling of the gain modulations of the FTFs. In a) and b) the acoustic/convective interference is collapsed by scaling the frequency by $fL_g/\bar{u}_p$, aligning the modulations. In c) and d) the acoustic/convective interference is collapsed by scaling the frequency by $fd_g/\bar{u}_p$, showing that the band of the interference centers on a natural shedding frequency close to $fd_g/\bar{u}_p \approx [0.2 \text{ to } 0.4]$.

the wavelengths of the modulations. This shows that the wavelength and hence characteristic time-scale of the modulations are governed by τ_3 but the physical origin of the modulations is the vortex shedding which scales with St_{d_g}, where large modulations appear close to $\mathrm{St}_{d_g} \approx [0.2 \text{ to } 0.3]$ consistent with scaling of the Kármán vortex street [36]. Again, in the case of the swirling flames the azimuthal component will alter the velocity scale and time-delay associated with convective disturbances downstream of the swirler, which has been shown to propagate as inertial waves at a different velocity than the axial bulk flow velocity [37].

3.2. Generating strong modulations in the FTF gain

We now demonstrate how strong modulations can be produced by the upstream geometry. Figure 5 shows the FTF of the cylinders when placed upstream at $L_g = 30$mm for $\bar{u} = 10$m/s, corresponding to the black line with stars in Fig. 4, which results in strong low-frequency modulations. The corresponding DTL model of the FTF is shown by the solid line. At non-dimensional time delays $f\tau_3 \approx 1.5$ and 2.5 the gain is suppressed to minimum values whereas integer values $f\tau_3 \approx 1$ and 2 show regions of large amplification. These changes to the gain are also accompanied by abrupt changes in the phase. The underlying physical mecha-

Table 2
Fitted constants of the DTL model and comparison with physical time delays shown in Fig. 1b) for $\bar{u} = 10$m/s at $L_g = 50$mm and 30mm.

L_g [mm]	g_1 [-]	$1/\sigma_1$ [kHz]	β_1 [kHz]	τ_1 [ms]	g_2 [-]	$1/\sigma_2$ [kHz]	β_2 [kHz]	τ_2 [ms]	$\mathrm{St}_{d_g} = \beta_2 d_g/\bar{u}_p$ [-]	$\tau_1\bar{u}/H$ [-]	$\tau_3\bar{u}_p/L_g$ [-]
50	1.49	0.54	0.35	1.3	0.18	0.15	0.29	8.9	0.25	0.94	0.92
30	1.22	0.51	0.37	1.13	0.84	0.14	0.37	5.8	0.32	1.01	0.98

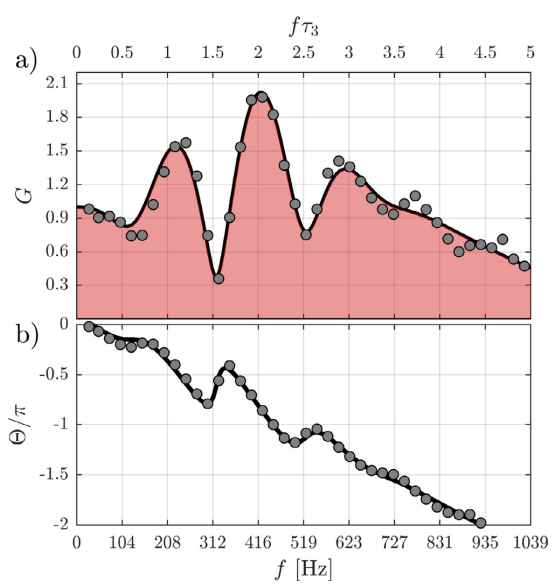

Fig. 5. Gain a) and phase b) of the FTF with strong modulations with the cylinder placed at $L_g = 30$mm at $\bar{u} = 10$m/s. (∘) and (——) show the measurements and fitted model $\mathrm{DTL_T}$ respectively, which are in excellent agreement.

nisms appear in the model constants summarized for $L_g = 30$mm and 50mm in Tab. 2. All the model constants are very similar for both L_g except for g_2 and τ_2. This shows that the acoustic response of the flame τ_1 is not strongly dependent on L_g. The main effect of moving L_g is the adjustment of the time delay τ_2 which, in turn, causes a large increase in the magnitude of the gain modulations g_2 from 0.18 to 0.85. This drastic increase in g_2 is due to the decay of the vortex shedding which has been shown to decrease exponentially for $L_g/d_g > 5$ in cylinder wakes [38]. In other words, if L_g is chosen sufficiently short ($L_g/d_g < 7$) increasing or decreasing L_g affects the combined time-delay τ_3 which can be tuned to suppress the gain over a given range of frequencies.

We can use the DTL model to identify the modulation frequency β_2 and the non-dimensional vortex shedding frequency from the cylinders $\mathrm{St}_{d_g} = \beta_2 d_g/\bar{u}_p$. We find $\mathrm{St}_{d_g} = 0.32$ and 0.25, which are in good agreement with the optimal range of non-dimensional shedding frequencies of flow around a cylinder over a wide range of Reynolds numbers [36]. From the DTL model we find a range of $\mathrm{St}_{d_g}(1 \pm 3\beta_2\sigma_2)$ which exhibits a band pass filter structure centered on $f = \beta_2$ where the maximum modulation of the amplitudes in the gain and phase occur. This envelope is plotted in red in Fig. 7 and can be used to effect large changes in the gain and phase response over a specific frequency range as discussed in the next sections. This envelope results from lock-on of the non-dimensional optimal vortex shedding frequency to the acoustic forcing frequency [39].

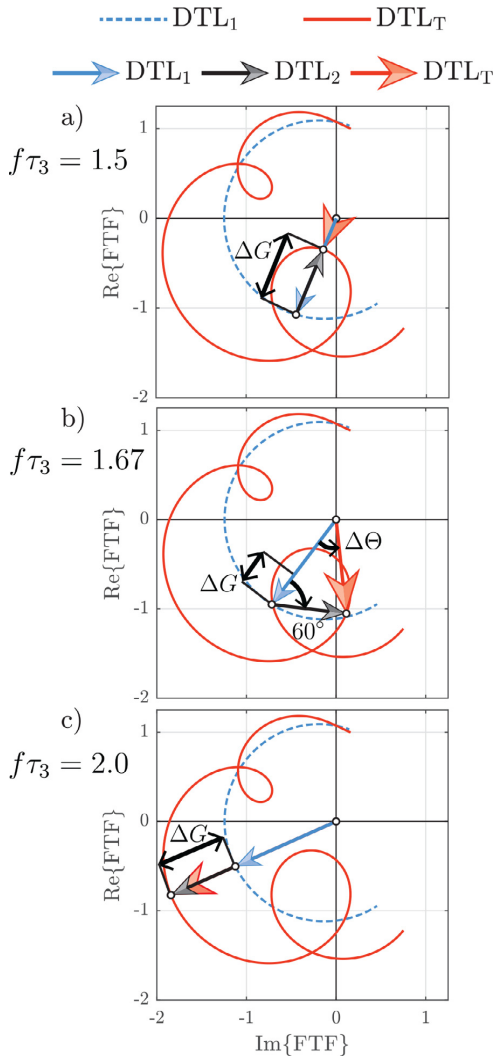

Fig. 6. The FTF shown in the complex plane as phasors for $L_g = 30$mm in the range $f\tau_3 = [1 \text{ to } 3.5]$, corresponding to large gain and phase modulations. The arrows show the two vectors $\mathrm{DTL_1}$, $\mathrm{DTL_2}$ and their sum $\mathrm{DTL_T}$ at a) destructive gain interference at $f\tau_3 = 1.5$, b) large phase modulation at $f\tau_3 = 1.67$, and c) constructive gain interference at $f\tau_3 = 2.0$. The second source (vortex shedding) of convective perturbations, described by $\mathrm{DTL_2}$, modulates the gain and phase of $\mathrm{DTL_1}$.

3.3. Controlling the gain and phase modulations

How the convective and acoustic sources interfere can be illustrated using the phasor diagrams plotted in Fig. 6 for $L_g = 30$mm. Equation (5a) expresses the total response of the FTF as an interaction between $\mathrm{DTL_1}$ and $\mathrm{DTL_2}$ where $f\tau_3$ determines their relative

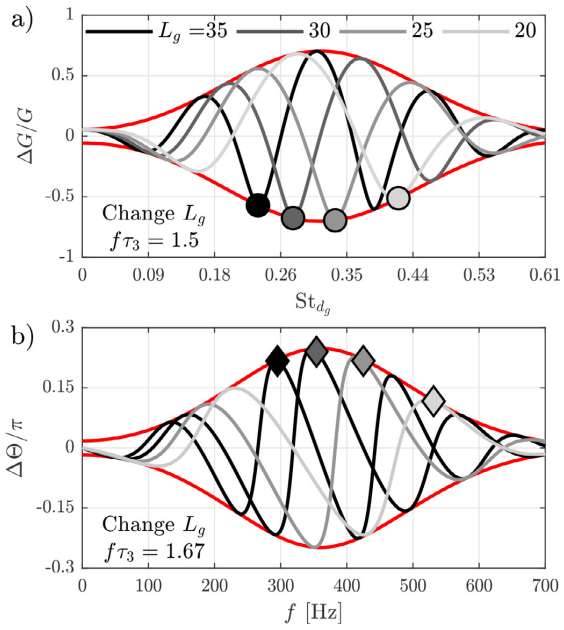

Fig. 7. Tuning of a) the gain $\Delta G/G$ and b) the phase $\Delta\Theta/\pi$ by controlling the cylinder location L_g. The line (—) shows the envelope of potential modulations and the gray lines show the modulations at the different cylinder positions where $L_g = 35$mm (—), 30mm (—), 25mm (—), and 20mm (—). Markers are added at $f\tau_3 = 1.5$(●) in a) and at $f\tau_3 = 1.67$(◆) in b) to show how matching $f\tau_3$ leads to large modulations at frequencies of interest. (For interpretation of the references to colour in their figure legend, the reader is referred to the web version of this article.)

phase, and thus the superposition between the acoustic and convective sources. The arrows indicate the direction of the vectors DTL_1, DTL_2, and their sum DTL_T in the complex plane of the FTF. The length, $|\mathrm{DTL}_\mathrm{T}| = G$, and the angle, $\angle(\mathrm{DTL}_\mathrm{T}) = \Theta$, correspond to the gain and phase respectively.

When $f\tau_3 = 1.5$ and 2.0, as shown in a) and c), the vectors are parallel leading to a minimum and maximum in the gain respectively. Parallel vectors lead to a negligible shift in Θ but a large shift in G denoted by ΔG in the figure. When $f\tau_3 = 1.5$ the two sources are a half-cycle out-of-phase resulting in a reduction in ΔG, whereas when $f\tau_3 = 2.0$ the two sources are in phase and ΔG increases (by roughly a factor of 4). When the two vectors approach orthogonality, a large shift of the phase $\Delta\Theta$ occurs with a relatively small ΔG. Although not quite orthogonal, this is observed by the large shift in the phase in Fig. 6 b). This also corresponds to the phase jump observed in Fig. 5 for $f\tau_3 = 1.67$.

The expression in Eq. (5a) provides an explicit way to predict and control the frequencies of constructive and destructive interference as a function of $f\tau_3$. We now have the parameters/scalings needed to control the gain and phase of the modulations. Through careful selection of the upstream geometry and its location L_g, the gain and phase of the FTF can be modified over a range of selected frequencies and passively suppress self-excited instabilities.

To illustrate the procedure we use the cylinders as the upstream geometry to take advantage of the Strouhal number scaling. To modify the gain or phase at a given operating condition (a fixed flowrate) requires the following procedure:

1. Identify the target frequency or centre of the frequency range where modifications to the gain or phase are required. For example, a resonant mode that requires suppression. Select the diameter of the cylinders, d_g, so that the non-dimensional shedding frequency lies in the range $\mathrm{St}_{d_g} = [0.2 \text{ to } 0.4]$, where f is set to the target acoustic frequency. Matching the non-dimensional shedding frequency St_{d_g} with the acoustic frequency is required to ensure lock-on.
2. Next, the cylinder location L_g should be chosen to provide the desired range of non-dimensional time delays, $f\tau_3$, which controls the level of interference between the convective and acoustic disturbances. This can be chosen to either modify the gain or the phase over a range of frequencies centred on the target frequency. To achieve a large suppression in the gain, $f\tau_3 = N \pm 1/2$ should be matched, and for a large shift of the phase, $f\tau_3 \approx 0.33 + N$ or $f\tau_3 \approx 0.67 + N$ should be matched. The cylinder location must also be sufficiently close to the flame base such that g_1 and g_2 are in the same order of magnitude. If the cylinders are too far upstream, the coherent structures will decay limiting their effect on the flame response.

These two steps can be thought of as firstly, exploiting the Strouhal number scaling to generate optimal convective-acoustic disturbances over a targeted frequency range and secondly, using their relative time-delay to amplify or damp the gain or phase as required. The method is illustrated in Fig. 7 which shows the effect of different cylinder positions L_g on the relative change in the gain $\Delta G/G$ and phase $\Delta\Theta/\pi$. Note that a) and b) show the non-dimensional and equivalent dimensional frequencies respectively to ease interpretation.

Figure 7 a) shows how the gain can be tuned by adjusting L_g. The line for $L_g = 30$mm corresponds to DTL_T fitted to the measurements. Lines for the other values of L_g were obtained using the DTL model by varying the time-delay τ_2. The other model parameters are all approximately constant except for the gain g_2 which changes with L_g. The large markers denote when the non-dimensional time-delay $f\tau_3 = 1.5$, which corresponds to the largest reduction in the gain for each L_g (see Fig. 5 when $L_g = 30$ mm). As L_g changes, the frequencies where minimum (and maximum) values of $\Delta G/G$ occur are shifted.

Figure 7 b) shows how the phase can also be tuned by adjusting L_g. The large markers denote when the non-dimensional time-delay $f\tau_3 = 1.67$, which corresponds to the largest positive change in the the phase $\Delta\Theta$. As is the case for the gain, the frequencies where the maximum $\Delta\Theta$ occur shift depending on L_g. At these frequencies large modulations in the gain or shifts in the phase can be achieved and shows how time delays can be used to tailor the gain and phase at specific frequencies.

However, by decreasing the gain at a selected range of frequencies we also increase the gain at other frequencies. This might be a limitation of the method that leads to mode switching instead of suppression of the instability. Hence, testing the strategy on a configuration undergoing self excited oscillations remains a task for future studies.

4. Flame dynamics and analysis of interference

4.1. Phase averaged heat release rate

We now investigate the dynamics associated with the global interference. The global and spatial signals of the HRR Q and q were obtained in the range $f\tau_3 = [1.1 \text{ to } 3.6]$ which correspond to the large gain modulations presented in Fig. 5.

Figure 8 plots the rms fluctuations and the magnitude of the coherent fluctuations obtained from the Fourier modes (see Appendix A) $\hat{q}_x$ and $\hat{q}_z$ in a) and b) respectively. Both top and side views are presented. The rms fluctuations are similar for all frequencies despite the large gain increase from $G = 0.4$ to 2.0 be-

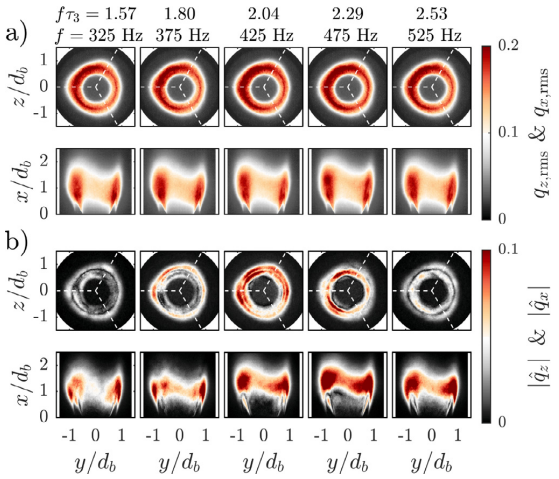

Fig. 8. Magnitude of HRR fluctuations in the range $f\tau_3 = [1.57 \text{ to } 2.53]$, corresponding to large gain and phase modulations in the FTF. a) shows rms fluctuations $q_{x,\mathrm{rms}}$ (top view) and $q_{z,\mathrm{rms}}$ (side view). b) shows magnitude of the Fourier modes $|\hat{q}_x|$ and $|\hat{q}_z|$. All images are normalized by the maximum HRR obtained from the mean flame image $\bar{q}_{z,\max}$ and $\bar{q}_{x,\max}$.

tween $f\tau_3 = 1.57$ to $f\tau_3 = 2.04$ and then decrease from $G = 2.0$ to 0.7 between $f\tau_3 = 2.04$ to $f\tau_3 = 2.53$.

However, the Fourier modes in Fig. 8 b) shows a distinct response that follows the gain modulations in both top and side views. At the gain minimum, $f\tau_3 = 1.57$ the top view shows $\hat{q}_z$ reaches a minimum and increases to peak values at $f\tau_3 = 2.04$ which corresponds to the maximum gain in Fig. 5.

To understand the effect of the modulations on the flame response in more detail, Fig. 9 plots zoomed in views of the left side of the flame for the gain minimum when $f\tau_3 = 1.57$ (*a-c*) and the gain maximum when $f\tau_3 = 2.04$ (*d-f*). The images show the mean HRR $\bar{q}_z$ (*left column*), as well as the magnitude and phase of the Fourier mode $\hat{q}_z$ (*middle and right columns*). The mean flame is very similar for both frequencies and most of the HRR occur at the center of the flame brush at $x/d_b \approx 1$. Most of the HRR oscillations displayed in b) and e) occur at the tip of the flame at $x/d_b \approx 1.4$. The phase in Figs. 9 c) and f) shows an approximately linear development downstream ($x-$direction) and is approximately constant along the radius indicative of convective propagation where the convective wavelength can be estimated as $\lambda^{-1} \approx \partial(\angle\tilde{q}_z/2\pi)/\partial x$. However, the phase at the base and the rate of development are noteably different. If the disturbance originated from a single source, the convective wavelength would be expected to be $\lambda \approx \bar{u}/f$. In the case of $f\tau_3 = 2.04$, $\partial(\angle\tilde{q}_z/2\pi)/\partial x$ is significantly smaller resulting in a longer convective wavelength compared to when $f\tau_3 = 1.57$. Changes in the convective wavelength result from superposition of the convective and acoustic sources resulting in a significantly different level of stream-wise interference along the flame front. As shown by the Nyquist plots in Fig. 6, the two sources act in phase at $f\tau_3 = 2.04$, leading to more regular fluctuations in the HRR and a longer convective wavelength. At $f\tau_3 = 1.57$, the two sources are half-a-cycle out of phase along the flame front, leading to destructive interference and a shorter convective wavelength.

4.2. Characterization of stream-wise interference

Given that Fig. 9 showed that the phase mainly develops linearly in the stream-wise direction, we can therefore analyse the

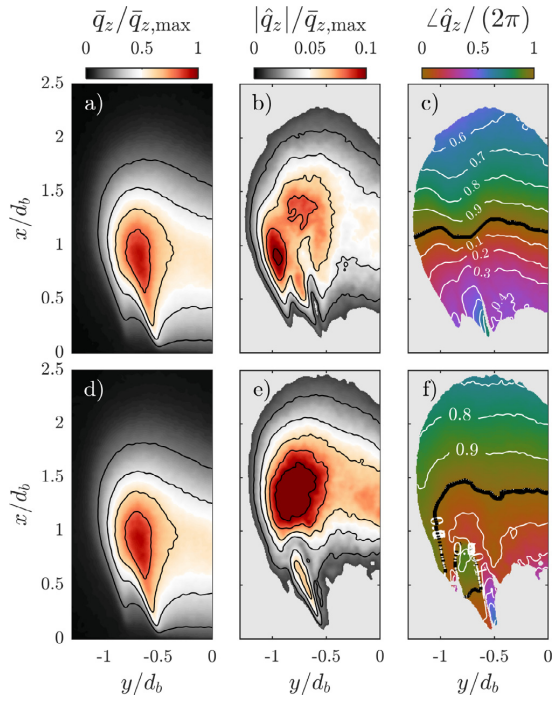

Fig. 9. Structure of: (*left column*) mean HRR $\bar{q}_z$, (*middle column*) the magnitude and (*right column*) phase of the Fourier mode $\hat{q}_z$, at $f\tau_3 = 1.57$ a-c) and $f\tau_3 = 2.04$ d-f). Despite an increase in the forcing frequency, a decrease in the convective wavelength is observed.

interference using line-averaged quantities evaluated in the x-direction only. We can show the effect of $f\tau_3$ on the level of stream-wise interference, following a similar approach to Palies et al. [17] and Wang et al. [40] who divided the flame image into different regions to analyse phase variations in the fluctuating HRR between the different flame regions. We also did the same analysis using the flame surface from the OH-PLIF measurements which yielded a very similar result (not shown for brevity).

Figure 10 plots the line averaged fluctuations in the HRR $\langle q'_{yz}\rangle$ over the oscillation cycle where the vertical axis is the non-dimensional cycle time t/T and the horizontal axis the stream-wise position. Maximum destructive interference resulting in a gain minimum occurs when $f\tau_3 = 1.57$ is shown by the multiple transitions from red-blue-red or vice-versa along a constant t/T. Maximum constructive interference leading to a maximum in gain, occurs when only a single colour is present along a constant t/T as found when $f\tau_3 = 1.8 - 2.04$.

We can further elucidate the nature of the convective-acoustic interference by calculating a stream-wise interference index R which evaluates how the fluctuations in HRR are in phase with itself when integrated over space in a similar way to Wang et al. [40]. To construct R, two scalars $\mathscr{Q}_1$ and $\langle Q'\rangle_{\max}$, are defined as follows:

$$\mathscr{Q}_1 = \int_0^\infty \left|\hat{q}_{yz}\right| \, \mathrm{d}x\,, \tag{6a}$$

$$\langle Q'\rangle_{\max} = \max_{t/T}\left(\int_0^\infty \langle q'_{yz}\rangle \, \mathrm{d}x\right). \tag{6b}$$

$\mathscr{Q}_1$ is the area under the envelope of $\langle q'_{yz}\rangle$ (which are shown by dashed lines in Fig. 11). This provides a measure of the maximum

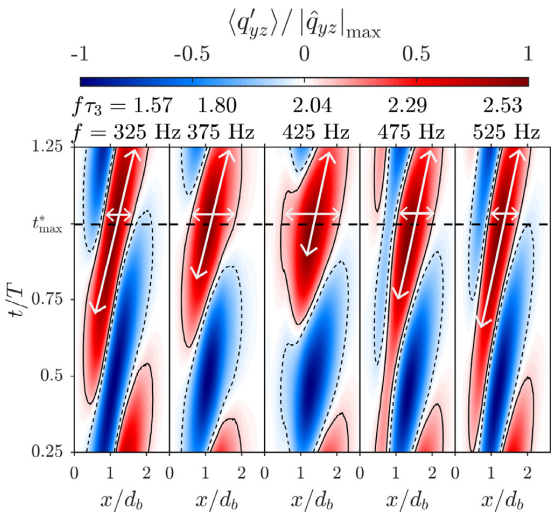

Fig. 10. Evolution of the phase averaged fluctuations of stream-wise HRR $\langle q'_{yz}\rangle$ at different $f\tau_3$. Each panel shows how the fluctuations are distributed in time and space simultaneously. The white arrows indicate the orientation and the convective wavelength of the regions of positive fluctuations, as they change with the forcing frequency. (For interpretation of the references to colour in their figure legend, the reader is referred to the web version of this article.)

amplitude of the integrated fluctuations, in the absence of spatial interference, i.e. neglecting the effect of a non-uniform phase. The second scalar $\langle Q'\rangle_{\max}$, is a measure of the phase-averaged integrated response $\langle Q'\rangle$, when the effect of the non-uniform phase is considered. We condition at $t/T = 1 = t^*_{\max}$ to investigate the interference when the cycle is at maximum HRR at $t^*_{\max}$ as shown in Fig. 10.

Figure 11 a) shows a graphical representation of the two scalars $\mathscr{Q}_1$ and $\langle Q'\rangle_{\max}$ at $f\tau_3 = 1.57$. The area under the dashed black curve A + C, represents the measure $\mathscr{Q}_1$. The area under the dash-dotted red curve A − B, represents the measure $\langle Q'\rangle_{\max}$. Since $\langle Q'\rangle_{\max} \leq \mathscr{Q}_1$ we can define an interference index as:

$$R = \frac{\langle Q'\rangle_{\max}}{\mathscr{Q}_1} \leq 1 \tag{7}$$

which quantifies the effect of the spatial variation of the phase on the integrated amplitude. With $R \approx 0$, the effect of spatial interference is large and in the limit $R = 1$ the effect is negligible.

Figure 11 a) shows regions of positive ($0.7 < x/d_b < 1.5$) and negative ($0 < x/d_b < 0.7$ and $1.5 < x/d_b < 2.3$) fluctuations leading to destructive stream-wise interference and a gain minimum for $f\tau_3$. When $f\tau_3$ is increased, the amount of interference reduces before increasing again. At $f\tau_3 = 2.04$, there is minimal interference and cancellation. However, as $f\tau_3 > 2.04$ regions of negative fluctuations appear again leading to some global cancellation. In Fig. 10 these trends are indicated by the white arrows whose lengths indicate a change of the convective wavelength. The horizontal arrow gets longer from $f\tau_3 = 1.57$ to $f\tau_3 = 2.04$, while the vertical arrow gets shorter. The stream-wise alignment at $f\tau_3 = 2.04$, represented by longer horizontal arrows, results in more constructive interference, and shows a spatial localization of the positive fluctuations. The opposite is observed at $f\tau_3 = 1.57$ and $f\tau_3 = 2.53$, where the fluctuations are more vertically aligned, represented by longer vertical arrows.

We can compare the interference index R to the gain modulations in the FTF by considering the relative change of the different

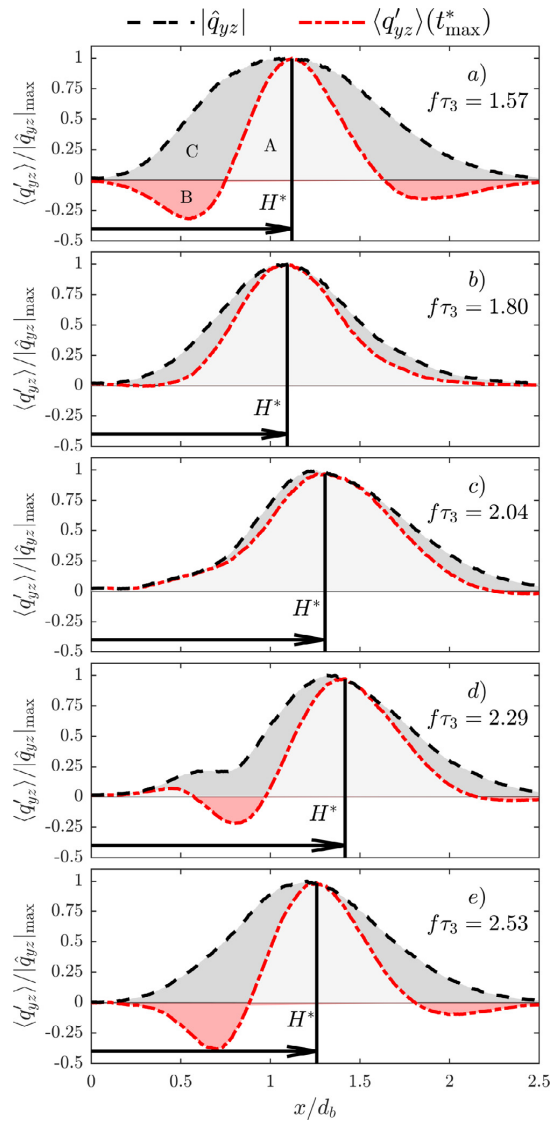

Fig. 11. Phase averaged fluctuations $\langle q'_{yz}\rangle$ shown at $t^*_{\max}$ (along horizontal lines in Fig. 10) and the corresponding envelope $|\hat{q}_{yz}|$ illustrating the metric for stream-wise interference. The area under $|\hat{q}_{yz}|$ corresponds to the first scalar, $\mathscr{Q}_1 = A + C$. The area under $\langle q'_{yz}\rangle$ corresponds to the second scalar, $\langle Q'\rangle_{\max} = A - B$, which gives the global fluctuation in HRR. The modified flame length is estimated as $H^* = \max_x(\langle q'_{yz}\rangle)$.

quantities. The relative change of interference is given by:

$$\frac{\Delta R}{R} = \frac{R}{\bar{R}} - 1. \tag{8}$$

For the FTF the relative change of gain due to the modulations is given for the DTL model and measurements by:

$$\frac{\Delta G_{\mathrm{DTL}}}{G} = \left|\frac{\mathrm{DTL_T}}{\mathrm{DTL_1}}\right| - 1, \quad \frac{\Delta G_{\mathrm{Exp}}}{G} = \left|\frac{\mathrm{FTF_{Exp}}}{\mathrm{DTL_1}}\right| - 1. \tag{9}$$

The two quantities, $\Delta R/R$ and $\Delta G/G$, are shown in Fig. 12 a). Both quantities form a very similar interference pattern showing

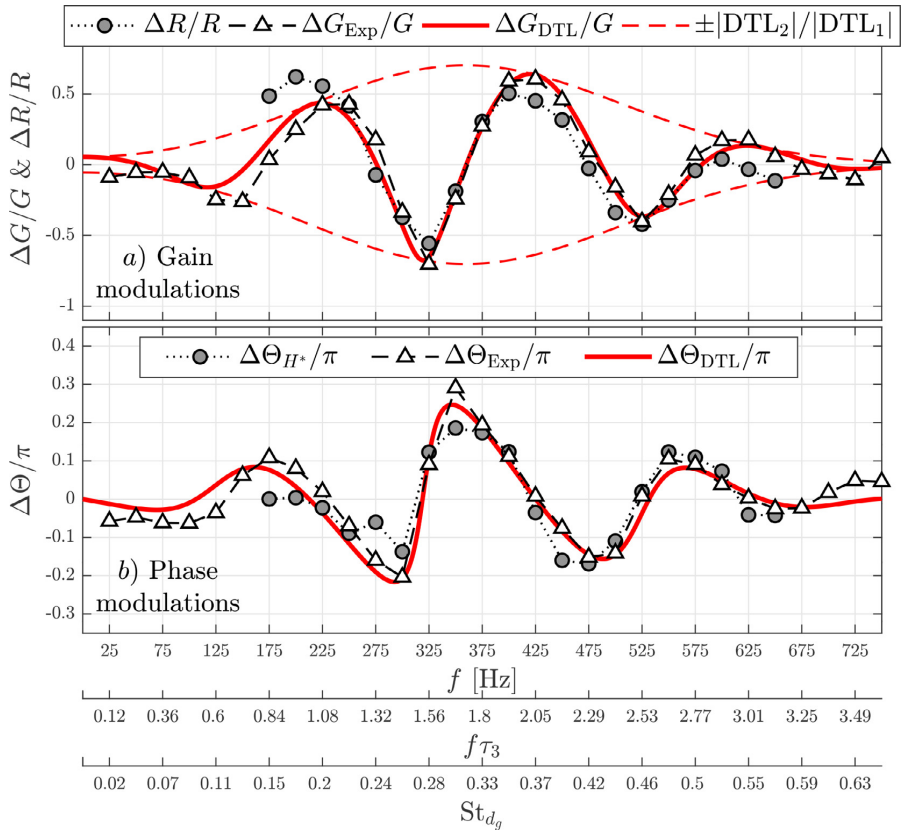

Fig. 12. a) Comparison between the modulations of gain $\Delta G/G$ and the change of the stream-wise interference index $\Delta R/\bar{R}$. The close comparison shows that the modulations in the FTF gain are caused by an equal change in the level of spatial interference, caused by acoustic/convective interference along the flame front. b) Comparison of the relative change of the phase $\Delta\Theta/\pi$, estimated from the FTF and from the characteristic length H^*.

good collapse demonstrating that the change of global HRR which appear as modulations in the FTF gain G are driven by stream-wise interference. It further emphasises the linear interaction in the form of superposition of the convective-acoustic sources along the flame front which determines the global response in HRR. The range of frequencies (or time delays $f\tau_3$) where the band pass filter is active is given by the envelope, $|\mathrm{DTL}_2|/|\mathrm{DTL}_1|$, indicated by the red dashed line in Fig. 12 a) which is centered on the natural shedding frequency of the cylinders at $\mathrm{St}_{d_g} = 0.3$.

In Fig. 11 we can define a distance H^* from the dump plane to the peak HRR in the stream-wise direction, $\max_x\left(\langle q'_{yz}\rangle\right)$. The distance H^* varies with the forcing frequency and differs from H used as the characteristic length in the Strouhal number scaling for the cut-off frequency which was based on the mean flame images ($\max_x\left(\bar{q}_{yz}\right)$) not the Fourier quantities. The change in H^* leads to a change in the phase $\Delta\Theta$ and can be estimated by:

$$\Delta\Theta_{H^*} = \frac{-2\pi\left(H^* - \bar{H}^*\right)f}{\bar{u}}, \tag{10}$$

where $\bar{H}^*/\bar{u}$ represents the average time-delay. From the DTL model and FTF measurements, the change of the phase is given by:

$$\Delta\Theta_{\mathrm{DTL}} = \angle\left(\frac{\mathrm{DTL_T}}{\mathrm{DTL_1}}\right), \quad \Delta\Theta_{\mathrm{Exp}} = \angle\left(\frac{\mathrm{FTF_{Exp}}}{\mathrm{DTL_1}}\right). \tag{11}$$

The various ways to calculate $\Delta\Theta$ are plotted in Figure 12 b) showing a good collapse and that the phase is modulated within the same band of frequencies as the gain modulations in a). It also demonstrates that:

1. The characteristic length H^* obtained from fluctuating quantities provides a good estimate of the total time delay/phase from the global measurements. Usually this length is taken to be H from the mean flame images which has been shown to only provide a good estimate for the mean time delay [15].
2. The interference is a linear phenomenon. The DTL model assumes a linear superposition of convective and acoustic sources by construction and it provides an excellent representation of the global behaviour. As the relative time-delay between the two sources represented by $f\tau_3$ changes, the characteristic length H^* also shifts accordingly, which leads to a change of the global time-delay observed in the phase of the FTF.

4.3. Flame sheet kinematics

In this section we draw a link between the constructive and destructive interference observed in the global HRR response to the local flame statistics and dynamics. To do this we compute the flame curvature from the flame surface coordinates $(x_s(l_s), y_s(l_s))$ which are parameterized by the arc length l_s. The flame curvature gives the local rate of change of direction of the flame front

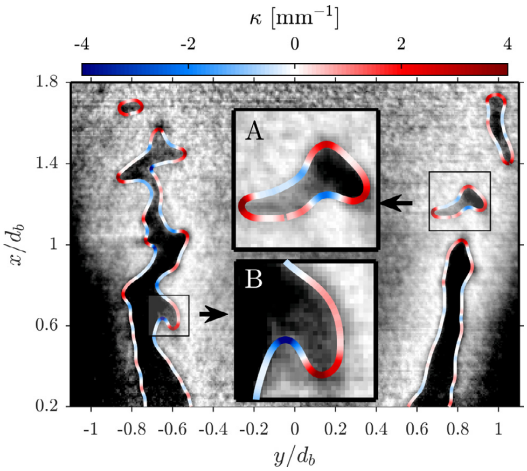

Fig. 13. Snapshot of an OH*-PLIF image and the flame surface (X_s, Y_s) for the unforced flame. The flame surface is coloured by curvature κ. The two boxes labeled A and B indicate two features along the flame front. A) shows flame pinch-off which has a preference for positive curvature. B) shows flame front wrinkling which has a preference for both positive and negative curvature.

but can also be used to quantify dynamic features along the flame front, such as vortex roll-up and flame pinch off. Curvature is computed using the approach of [41] and is briefly explained here. By convolving each coordinate along an open or closed flame curve by a kernel, $h(l_s)$, the gradients of the smoothed coordinates (X_s, Y_s) are (for x_s only for brevity):

$$X_s = x_s * h, \qquad \dot{X}_s = x_s * \dot{h}, \qquad \ddot{X}_s = x_s * \ddot{h}, \tag{12}$$

where the dot denotes a derivative with respect to the arc length, $\dot{X}_s = \partial X_s / \partial l_s$. The kernel $h(l_s)$ was chosen to be a Gaussian PDF which is sampled with $n_p = 25$ equidistant points in the region $l_s = [-5\sigma_p,\ 5\sigma_p]$, where σ_p is the standard deviation. In this way h is a weighting function whose sum equals to unity, and thus Eq. (12) can be considered a weighted average operator over n_p neighbouring points. The quantities in Eq. (12) are computed and the curvature κ for the smoothed curve (X_s, Y_s) is given by:

$$\kappa = \frac{\dot{X}_s \ddot{Y}_s - \dot{Y}_s \ddot{X}_s}{\left[\dot{X}_s^2 + \dot{Y}_s^2\right]^{3/2}}, \tag{13}$$

where κ is positive when the flame concave towards the unburnt reactants and negative when it convex towards the unburnt reactants.

Figure 13 shows a snapshot of an instantaneous PLIF image where the flame surface (X_s, Y_s) is shown colored by curvature κ. The insets in the figure labeled A and B show zoomed areas of two characteristic features tracked by curvature. Inset A shows a pocket of unburned gas that has pinched-off from the main flame and curves in towards the reactants. This increases the amount of positive curvature. Inset B shows a typical wrinkle along the flame front typical of vortex roll-up, which leads to an increase of both positive and negative curvature.

We first consider the statistics of the local flame curvature to identify any effect of acoustic forcing. The Probability Density Function (PDF) of κ is shown in Fig. 14 a) for the unforced flame and two different $f\tau_3$. A non-Gaussian distribution is observed with longer tails for positive κ for the forced and unforced flames. Overall, the forced flames exhibit longer tails for both positive and negative κ compared to the unforced flame. This indicates that forced flames exhibit an increase curvature over all length-scales

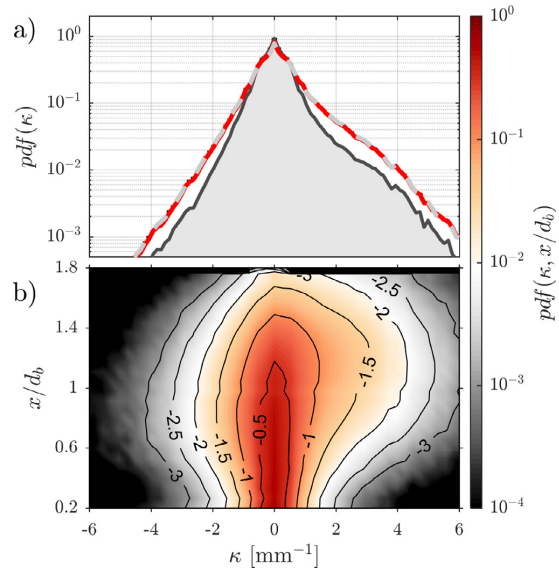

Fig. 14. a) PDFs ($pdf(\kappa)$) of curvature for $f\tau_3 = 1.57$ (——), $f\tau_3 = 2.04$ (——), and the unforced flame (——). Acoustic forcing increases the total magnitude of curvature but is very similar for both frequencies. b) Joint PDFs ($pdf(\kappa, x/d_b)$) of curvature and stream-wise position shown for $f\tau_3 = 2.04$.

leading to more contorted flames. The PDFs for the two frequencies are also very similar, suggesting that the overall increase in curvature of the forced flames may only weakly depend on frequency.

Figure 14 b) plots the joint PDF of κ with stream-wise position x/d_b for $f\tau_3 = 2.04$ showing the spatial evolution of the curvature probability. Both frequencies displayed very similar distributions, hence only a single case is presented. Close to the flame base the PDF is reasonably symmetric reflecting the low level of flame wrinkling near the flame base. The PDF becomes increasingly skewed downstream as the variance of the PDF becomes wider for positive κ. The increased probability in positive κ is expected to result from the effect of vortex roll-up from acoustic forcing. The maximum positive κ occurs near the tip of the flame, i.e. $x/d_b > 0.8$, which indicates that consumption of pockets due to flame pinch-off, as shown in A of Fig. 13, is dominant in this region as shown previously [35,42–44].

More insight in the flame dynamics can be obtained by considering the phase-averaged curvature. Figure 15 compares phase-averaged curvature $\langle |\kappa|_{xy} \rangle$, flame surface $\langle s_{xy} \rangle$, and HRR $\langle Q \rangle$ plotted over two cycles. The global fluctuations of HRR and flame surface are in phase with each other for both frequencies as expected. Due to the different convective-acoustic interference, the amplitude of $\langle Q \rangle$ for $f\tau_3 = 1.57$ in a) is significantly lower than $f\tau_3 = 2.04$ shown in b). However, the opposite trend is found for the amplitude of curvature $\langle |\kappa|_{xy} \rangle$ which is larger for $f\tau_3 = 1.57$. Furthermore, there is also a difference in the phase with $\langle Q \rangle$ and $\langle |\kappa|_{xy} \rangle$ by half a cycle for $f\tau_3 = 1.57$ and under a quarter of a cycle for $f\tau_3 = 2.04$.

To further elucidate differences in the flame response between the two frequencies, the spatial response of the phase-averaged fluctuation of curvature in the form of joint PDFs of the phase-averaged fluctuations of curvature $\langle \kappa' \rangle$ and stream-wise position x/d_b, $pdf(\langle \kappa' \rangle, x/d_b)$ are plotted in Fig. 16. The figure shows half of a forcing cycle with the top and bottom rows corresponding to $f\tau_3 = 1.57$ and 2.04 respectively. The figure shows the probability

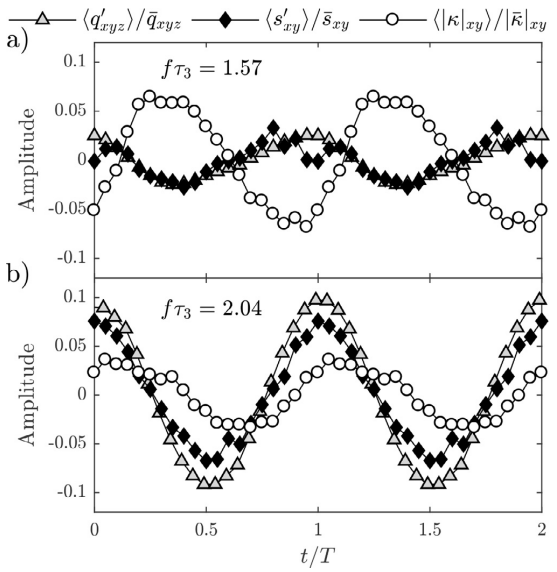

Fig. 15. Phase averaged fluctuations of global HRR $\langle Q\rangle$ (●) flame surface $\langle s_{xy}\rangle$ (●) and curvature $\langle|\kappa|_{xy}\rangle$ (○) shown at a) $f\tau_3 = 1.57$, and b) $f\tau_3 = 2.04$. At $f\tau_3 = 1.57$, the fluctuations of curvature is half a cycle out of phase with the HRR and flame surface. At $f\tau_3 = 2.04$, the fluctuations of curvature are more in phase with the HRR and flame surface.

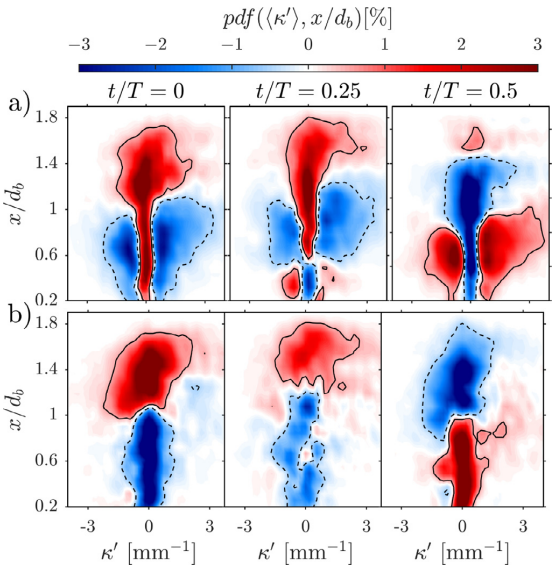

Fig. 16. joint PDF of the phase averaged fluctuations of curvature and stream-wise position $pdf(\langle\kappa'\rangle, x/d_b)$ shown through half a cycle for a) $f\tau_3 = 1.57$ and b) $f\tau_3 = 2.04$.

of the fluctuations in curvature above and below the mean curvature. Therefore zero (white) values of the colour bar is the mean curvature and the positive (red) and negative (blue) values represent variations about the mean.

Both frequencies show a relatively sharp change in the distributions upstream and downstream of $x/d_b = 1$. Beginning with $f\tau_3 = 1.57$ at $t/T = 0$, upstream the probability of curvature fluc-

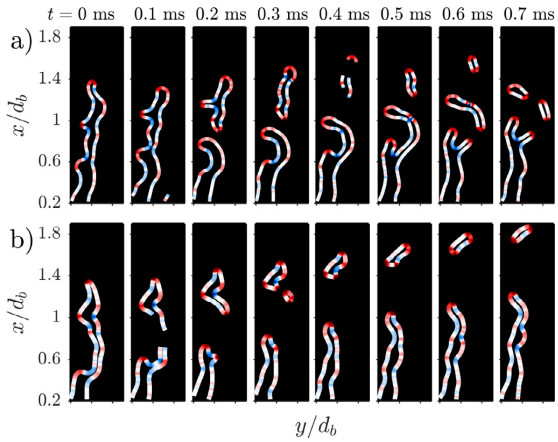

Fig. 17. Time-series of the instantaneous flame surface (X_s, Y_s) colored by curvature κ for a) $f\tau_3 = 1.57$ and b) $f\tau_3 = 2.04$.

tuations is very low illustrated by both the narrow red band of high probability centred on $\kappa' \approx 0$ surrounded by blue regions of low probability. Downstream beyond $x/d_b > 1$, a high probability of curvature fluctuations (both positive and negative) is observed by the large red area which corresponds to the flame tip region which shortly pinches-off. This corresponds to minimum curvature and maximum HRR as shown in Fig. 15. A similar distribution is found at $t/T = 0.25$ except below $x/d_b < 0.5$ where the probability distribution has reversed: the probability has decreased along $\kappa' = 0$ but increased for $|\kappa'| > 0$ shown by the blue and red bands. This corresponds to the start of the periodic vortex-flame roll-up whereas the high probability of region downstream $x/d_b > 1$ is due to the large-scale pinch-off of the flame front that leads to pocket formation. When $t/T = 0.5$, the probability distribution is almost the inverse of $t/T = 0$ with upstream flame now strongly wrinkled due to vortex-flame interaction but having low probability (blue) of curvature fluctuations downstream as the flame pockets have advected and burned out.

The corresponding flame dynamics leading to these PDFs are shown in Fig. 17 a). At $t = 0$ms the overall curvature along the flame front is increasing resulting in pinch-off of the flame front at $x/d_b \approx 1$ and large-scale hook-shaped deformation of the flame. As the pocket advects downstream and burns out, a second pocket is formed leaving a highly contorted forked flame tip. The second pocked then divides into two. Overall, the process shows that although the flame dynamics lead to high levels of curvature/deformation where the destruction of flame surface area by multiple pocket burnout downstream is counteracted by the simultaneous increase in the flame surface due to wrinkling upstream. These out-of-phase contributions lead to the reduction in the amplitude in the HRR observed in Figure 15.

The curvature of the flame is comparatively reduced when $f\tau_3 = 2.04$ in Fig. 16 b). As observed in a) there is a sharp change in the probability distribution upstream and downstream of $x/d_b = 1$. However, the upstream region now shows a much lower probability of κ' as shown by the narrower blue and red regions centred along $\kappa' = 0$. At $t/T = 0$ a narrow low probability of $\kappa' = 0$ indicates the flame experiences a relatively low level of wrinkling upstream but a high level of wrinkling downstream in the region of the flame tip which is about to pinch off. Similar distributions are observed at $t/T = 0.25$ but with lower values. At $t/T = 0.5$, again the probability distribution is almost the inverse of $t/T = 0$ with upstream having high probability centred $\kappa' = 0$ and a low prob-

ability (blue) of curvature fluctuations downstream as the flame pockets have advected and/or burned out. The PDFs show lower overall probability of curvature fluctuations than a).

The lower overall curvature can be observed in the corresponding flame dynamics in Fig. 17 b). Once pinch-off occurs around $t = 0.1$ms and forms a pocket which advects and burns out downstream, the flame upstream increases in surface area but is significantly less contorted than the flame in sequence a). The main difference with the flame dynamics $f\tau_3 = 1.57$ is that there is only one pinch-off event and pocket burnout, compared with multiple pocket formations and burnout in a), and therefore a larger relative production in flame surface occurs via the wrinkling of the flame front upstream.

5. Conclusions

This paper presented a method which can be used to passively modulate the gain and phase of FTFs of bluff-body stabilized CH_4/H_2 flames by controlling the interference between convective and acoustic disturbances through careful scaling of relative time delays. Convective disturbances were produced by several different upstream geometries: a set of three small diameter cylinders, three streamlined bodies (Rankine ovals) and a six-vaned swirler which were placed upstream at two different locations. Modulations in the gain were produced for all geometries demonstrating that their physical origin is the vortex/wake shedding (locked on to the forcing frequency) which scales with $\mathrm{St}_{d_g} = fd_g/\bar{u}_p$ where d_g is the characteristic length of the upstream geometry (e.g. the diameter of the cyclinder) and $\bar{u}_p$ the approach velocity. The different upstream geometries produce different modulation wavelengths which scale with the time-delay, $\tau_3 = L_g/\bar{u}_p$ where L_g is distance from the upstream geometry to the flame base. The global flame response was shown to result from a linear superposition of convective-acoustic disturbances which can be controlled by the relative time-delay, τ_3. The underlying scalings and time delays of the convective-acoustic interference are shown to be well modelled using a distributed time-lag (DTL) model which can also be used to tune and optimise the convective-acoustic interference. Using the DTL model to control the convective-acoustic interference the following steps are required (for cylinders):

1. The diameter of the cylinders, d_g, should be chosen such that $\mathrm{St}_{d_g} = [0.2 \text{ to } 0.4]$ for a target mass flow and frequency range. This ensures the frequency range to be controlled is close to the natural shedding frequency of the cylinders to ensure lock-on.
2. The relative time-delay is then changed by placing the upstream geometry at an upstream distance L_g from the flame such that the gain parameters g_1 and g_2 are of a similar order of magnitude.
3. To obtain large phase modulations at a given frequency L_g should be chosen in intervals of $\pi/2$ such that $f\tau_3 = fL_g/\bar{u}_p = [0.75, 1.25, 1.75]$.
4. To obtain large gain suppression at a given frequency L_g should be chosen in intervals of π such that $f\tau_3 = [0.5, 1.5, 2.5]$.

The second part of the paper show how the convective-acoustic interference affects the flame dynamics. The modulations in the gain are accompanied by stream-wise interference of HRR and flame surface fluctuations which change the integrated magnitude and the characteristic length of the flame. At frequencies of destructive interference, an increase of flame surface due to flame vortex roll-up occurs simultaneously as flame surface is annihilated at the tip of the flame due to multiple pinch off events. At frequencies of constructive interference the increase of flame surface due to the two mechanisms, i.e. flame vortex roll-up and flame pinch off, occur in phase, leading to an increase in the global HRR. Despite the small magnitude of these coherent oscillations on a turbulent flame, the role of the forcing is not to result in larger scale pinch off or significantly stronger wrinkling, but to synchronise the occurrence of wrinkling, pinch off, pocket formation and burnout resulting in the global flame response observed as modulations in the FTF.

Declaration of Competing Interest

The authors declare that they have no known competing financial interests or personal relationships that could have appeared to influence the work reported in this paper.

Acknowledgments

The authors acknowledge support from the NCCS Centre, funded under the Norwegian research program, Centres for Environment-friendly Energy Research (FME). Grant no.: 257579/E20. This work was also supported by the European Research Council (ERC) under the European Union's Horizon 2020 research and innovation programme (grant agreement no 677931 TAIAC).

Appendix A. Phase average and Fourier mode analysis

When investigating the response of the flame to harmonic oscillations it is useful to compute phase averaged quantities. For a given quantity, e.g. q_z, the phase averaged is denoted by brackets as $\langle q_z \rangle$ and is decomposed as:

$$\langle q_z \rangle = \bar{q}_z + \langle q'_z \rangle \,, \tag{A.1}$$

where $\langle q'_z \rangle$ is the phase averaged fluctuation of q'_z obtained by conditional averaging on the cycle phase.

The amplitude and phase of the fluctuations are also estimated from the Fourier modes which are obtained from spectral analysis similar to [45,46]. For the images each camera pixel is treated as individual time-series. Then, the spatial distribution of the amplitude and phase, represented by $\hat{q}_z$, is computed similar to the method outlined in Eq. (2) by computing the PSD. $\hat{q}_z$ only contains information at a specific frequency, which is chosen to be the external excitation frequency f. Hence, harmonics of f are discarded. When $\hat{q}_z$ is known, $\langle q'_z \rangle$ is given by:

$$\langle q'_z \rangle (x, y, t) = \mathrm{Re}\left\{ \hat{q}_z(x, y) \exp\left(2\pi j \frac{t}{T} \right) \right\}. \tag{A.2}$$

Similarly, Eq. (A.1) and Eq. (A.2) are used to obtain the other quantities, e.g. the phase averaged flame surface $\hat{s}$. The phase reference of all hatted quantities ($\hat{\cdot}$) is chosen so that $t/T = 0$ occurs at peak HRR, i.e. at $\max_t(\langle q'_{xyz} \rangle)$. This phase instance is denoted as $t^*_{\max}$.

References

[1] T.C. Lieuwen, V. Yang, Combustion instabilities in gas turbine engines: Operational experience, fundamental mechanisms, and modeling, AIAA, Reston,VA, 2006.
[2] A. Gruber, M.R. Bothien, A. Ciani, K. Aditya, J.H. Chen, F.A. Williams, Direct Numerical Simulation of hydrogen combustion at auto-ignitive conditions: Ignition, stability and turbulent reaction-front velocity, Combust. Flame 229 (2021) 111385, doi:10.1016/j.combustflame.2021.02.031.
[3] M.R. Bothien, A. Ciani, J.P. Wood, G. Fruechtel, Toward decarbonized power generation with gas turbines by using sequential combustion for burning Hydrogen, J. Eng. Gas Turb. Power 141 (12) (2019), doi:10.1115/1.4045256.
[4] T. Schuller, T. Poinsot, S. Candel, Dynamics and control of premixed combustion systems based on flame transfer and describing functions, J. Fluid Mech. 894 (2020) P1, doi:10.1017/jfm.2020.239.
[5] J.W. Strutt, The theory of sound, 2nd ed, Dover, New York, NY, 1945.
[6] C. Külsheimer, H. Büchner, Combustion dynamics of turbulent swirling flames, Combust. Flame 131 (1) (2002) 70–84, doi:10.1016/S0010-2180(02)00394-2.
[7] D. Durox, T. Schuller, N. Noiray, S. Candel, Experimental analysis of nonlinear flame transfer functions for different flame geometries, Proc. Combust. Inst. 32 (1) (2009) 1391–1398, doi:10.1016/j.proci.2008.06.204.

[8] K.T. Kim, J.G. Lee, B.D. Quay, D.A. Santavicca, Response of partially premixed flames to acoustic velocity and equivalence ratio perturbations, Combust. Flame 157 (9) (2010) 1731–1744, doi:10.1016/j.combustflame.2010.04.006.
[9] P. Palies, D. Durox, T. Schuller, S. Candel, Nonlinear combustion instability analysis based on the flame describing function applied to turbulent premixed swirling flames, Combust. Flame 158 (10) (2011) 1980–1991, doi:10.1016/j.combustflame.2011.02.012.
[10] A. Kaufmann, F. Nicoud, T. Poinsot, Flow forcing techniques for numerical simulation of combustion instabilities, Combust. Flame 131 (4) (2002) 371–385, doi:10.1016/S0010-2180(02)00419-4.
[11] T. Schuller, D. Durox, S. Candel, A unified model for the prediction of laminar flame transfer functions: comparisons between conical and V-flame dynamics, Combust. Flame 134 (1) (2003) 21–34, doi:10.1016/S0010-2180(03)00042-7.
[12] W. Polifke, C. Lawn, On the low-frequency limit of flame transfer functions, Combust. Flame 151 (3) (2007) 437–451, doi:10.1016/j.combustflame.2007.07.005.
[13] A.P. Dowling, A kinematic model of a ducted flame, J. Fluid Mech. 394 (1999) 51–72, doi:10.1017/S0022112099005686.
[14] M. Fleifil, A.M. Annaswamy, Z.A. Ghoneim, A.F. Ghoniem, Response of a laminar premixed flame to flow oscillations: A kinematic model and thermoacoustic instability results, Combust. Flame 106 (4) (1996) 487–510, doi:10.1016/0010-2180(96)00049-1.
[15] E. Æsøy, J.G. Aguilar, S. Wiseman, M.R. Bothien, N.A. Worth, J.R. Dawson, Scaling and prediction of transfer functions in lean premixed H2/CH4-flames, Combust. Flame 215 (2020) 269–282, doi:10.1016/j.combustflame.2020.01.045.
[16] T. Komarek, W. Polifke, Impact of swirl fluctuations on the flame response of a perfectly premixed swirl burner, J. Eng. Gas Turb. Power 132 (6) (2010), doi:10.1115/1.4000127.
[17] P. Palies, D. Durox, T. Schuller, S. Candel, The combined dynamics of swirler and turbulent premixed swirling flames, Combust. Flame 157 (9) (2010) 1698–1717, doi:10.1016/j.combustflame.2010.02.011.
[18] M. Gatti, R. Gaudron, C. Mirat, L. Zimmer, T. Schuller, A comparison of the transfer functions and flow fields of flames with increasing swirl number, ASME, 2018.
[19] F. Di Sabatino, T.F. Guiberti, W.R. Boyette, W.L. Roberts, J.P. Moeck, D.A. Lacoste, Effect of pressure on the transfer functions of premixed methane and propane swirl flames, Combust. Flame 193 (2018) 272–282, doi:10.1016/j.combustflame.2018.03.011.
[20] H.T. Nygård, N. Worth, Flame transfer functions and dynamics of a closely confined premixed body stabilised flame with swirl, J. Eng. Gas Turb. Power (2021), doi:10.1115/1.4049513.
[21] W. Polifke, Black-box system identification for reduced order model construction, Ann. Nucl. Energy 67 (2014) 109–128, doi:10.1016/j.anucene.2013.10.037.
[22] P. Palies, D. Durox, T. Schuller, S. Candel, Experimental Study on the Effect of Swirler Geometry and Swirl Number on Flame Describing Functions, Combust. Sci. Technol. 183 (7) (2011) 704–717, doi:10.1080/00102202.2010.538103.
[23] P. Palies, D. Durox, T. Schuller, S. Candel, Acoustic-convective mode conversion in an aerofoil cascade, J. Fluid Mech. 672 (2011) 545–569, doi:10.1017/S0022112010006142. Publisher: Cambridge University Press
[24] M. Gatti, R. Gaudron, C. Mirat, L. Zimmer, T. Schuller, Impact of swirl and bluff-body on the transfer function of premixed flames, Proceedings of the Combustion Institute 37 (4) (2019) 5197–5204, doi:10.1016/j.proci.2018.06.148.
[25] E. Æsøy, J.G. Aguilar, M.R. Bothien, N. Worth, J. Dawson, Acoustic-Convective interference in transfer functions of Methane/Hydrogen and Pure Hydrogen flames, J. Eng. Gas Turb. Power (2021), doi:10.1115/1.4051960.
[26] W. Polifke, Modeling and analysis of premixed flame dynamics by means of distributed time delays, Prog. Energy Combust. Sci. 79 (2020) 100845, doi:10.1016/j.pecs.2020.100845.
[27] N.A. Worth, J.R. Dawson, Self-excited circumferential instabilities in a model annular gas turbine combustor: Global flame dynamics, Proc Combust Inst. 34 (2) (2013) 3127–3134, doi:10.1016/j.proci.2012.05.061.
[28] A.F. Seybert, D.F. Ross, Experimental determination of acoustic properties using a two-microphone random-excitation technique, The Journal of the Acoustical Society of America 61 (5) (1977) 1362–1370, doi:10.1121/1.381403.
[29] B. Higgins, M.Q. McQuay, F. Lacas, J.C. Rolon, N. Darabiha, S. Candel, Systematic measurements of OH chemiluminescence for fuel-lean, high-pressure, premixed, laminar flames, Fuel 80 (1) (2001) 67–74, doi:10.1016/S0016-2361(00)00069-7.
[30] R. Balachandran, B.O. Ayoola, C.F. Kaminski, A.P. Dowling, E. Mastorakos, Experimental investigation of the nonlinear response of turbulent premixed flames to imposed inlet velocity oscillations, Combust. Flame 143 (1) (2005) 37–55, doi:10.1016/j.combustflame.2005.04.009.
[31] B. Schuermans, F. Guethe, D. Pennell, D. Guyot, C.O. Paschereit, Thermoacoustic modeling of a gas turbine using transfer functions measured under full engine pressure, J. Eng. Gas Turb. Power 132 (11) (2010) 111503, doi:10.1115/1.4000854.
[32] M. Reyes, F.V. Tinaut, B. Giménez, J.V. Pastor, Effect of hydrogen addition on the OH* and CH* chemiluminescence emissions of premixed combustion of methane-air mixtures, Int. J. Hydrog 43 (42) (2018) 19778–19791, doi:10.1016/j.ijhydene.2018.09.005.
[33] W. Rong, Z. Li, W. Zhang, L. Sun, An improved canny edge detection algorithm, 2014 IEEE international conference on mechatronics and automation, IEEE (2014), pp. 577–582.
[34] N.A. Worth, J.R. Dawson, Cinematographic OH-PLIF measurements of two interacting turbulent premixed flames with and without acoustic forcing, Combust. Flame 159 (3) (2012) 1109–1126, doi:10.1016/j.combustflame.2011.09.006.
[35] N.A. Worth, J.R. Dawson, Characterisation of flame surface annihilation events in self excited interacting flames, Combust. Flame 199 (2019) 338–351, doi:10.1016/j.combustflame.2018.10.032.
[36] A. Roshko, On the Development of Turbulent Wakes from Vortex Streets (1954). http://ntrs.nasa.gov/search.jsp?R=19930092207.
[37] A. Albayrak, M.P. Juniper, W. Polifke, Propagation speed of inertial waves in cylindrical swirling flows, J. Fluid Mech. 879 (2019) 85–120, doi:10.1017/jfm.2019.641.
[38] S.B. Pope, Turbulent Flows, Measurement Science and Technology 12 (11) (2001) 2020–2021, doi:10.1088/0957-0233/12/11/705. Publisher: IOP Publishing
[39] O.M. Griffin, M.S. Hall, Review-Vortex shedding lock-on and flow control in bluff body wakes, J. Fluids Eng. 113 (4) (1991) 526–537, doi:10.1115/1.2926511.
[40] G. Wang, T.F. Guiberti, X. Xia, L. Li, X. Liu, W.L. Roberts, F. Qi, Decomposition of swirling flame transfer function in the complex space, Combust. Flame 228 (2021) 29–41, doi:10.1016/j.combustflame.2021.01.032.
[41] F. Mokhtarian, S. Abbasi, Shape similarity retrieval under affine transforms, Pattern Recognition 35 (1) (2002) 31–41, doi:10.1016/S0031-3203(01)00040-1.
[42] A. Tyagi, I. Boxx, S. Peluso, J. O'Connor, The role of flow interaction in flame-flame interaction events in a dual burner experiment, Proc. Combust. Inst. 37 (2) (2019) 2485–2491, doi:10.1016/j.proci.2018.07.036.
[43] A. Tyagi, I. Boxx, S. Peluso, J. O'Connor, Pocket formation and behavior in turbulent premixed flames, Combust. Flame 211 (2020) 312–324, doi:10.1016/j.combustflame.2019.09.033.
[44] A. Tyagi, J. O'Connor, Towards a method of estimating out-of-plane effects on measurements of turbulent flame dynamics, Combust. Flame 216 (2020) 206–222, doi:10.1016/j.combustflame.2020.02.010.
[45] J. O'Connor, V. Acharya, T. Lieuwen, Transverse combustion instabilities: Acoustic, fluid mechanic, and flame processes, Prog. Energy Combust. Sci. 49 (2015) 1–39, doi:10.1016/j.pecs.2015.01.001.
[46] E. Æsøy, J.G. Aguilar, N.A. Worth, J.R. Dawson, The response of an axisymmetric jet placed at various positions in a standing wave, J. Fluid Mech. 917 (2021), doi:10.1017/jfm.2021.246.

Article 6

The Response of an Axisymmetric Jet Placed at Various Positions in a Standing Wave

Eirik Æsøy, José G. Aguilar, Nicholas A. Worth and James R. Dawson

Published in the Journal of Fluid Mechanics

J. Fluid Mech. (2021), *vol*. 917, A16, doi:10.1017/jfm.2021.246

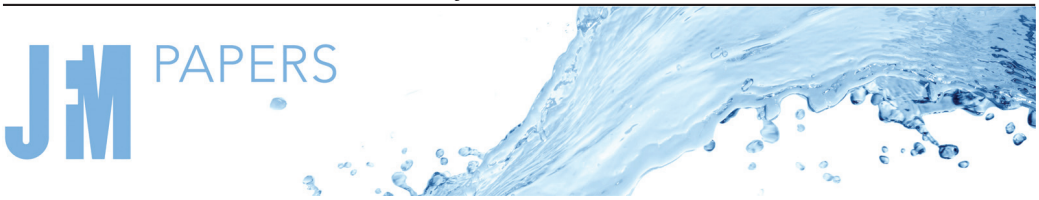

The response of an axisymmetric jet placed at various positions in a standing wave

Eirik Æsøy[1],†, **José G. Aguilar**[1], **Nicholas A. Worth**[1] **and James R. Dawson**[1]

[1]Department of Energy and Process Engineering, Norwegian University of Science and Technology, N-7491 Trondheim, Norway

(Received 24 September 2020; revised 15 January 2021; accepted 15 March 2021)

The hydrodynamic response of an axisymmetric jet placed at various positions in a standing wave oriented normally to the jet is investigated. At the velocity and pressure nodes the axisymmetric ($m = 0$) and first azimuthal ($m = \pm 1$) modes are excited, respectively, through manipulation of the jet exit boundary conditions. At positions between the nodes, both the $m = 0$ and $m = \pm 1$ modes are simultaneously excited resulting in asymmetric forcing due to the phase difference between the transverse and longitudinal acoustic fluctuations. This leads to the asymmetric formation of vortices in the near field and bifurcation into two or more momentum streams further downstream. The dominant momentum stream is deflected in the direction of the velocity node. It is shown that the asymmetric response can be well approximated by a superposition of the boundary conditions at the pressure and velocity nodes where the contributions from each mode are proportional to the acoustic pressure and velocity. A method is proposed to characterize the bifurcation behaviour statistically via moments of the probability density functions constructed from profiles of streamwise momentum. The jet symmetry and momentum spreading are shown to be proportional to the magnitude of the transverse acoustic velocity. Finally, the streamwise velocity is reconstructed as a superposition of Gaussian profiles providing a robust method to characterize the number of individual momentum streams which also shows that each of the streams behave self-similarly.

Key words: jets, vortex dynamics

1. Introduction

Over the years there has been an extensive scientific effort to understand and control the behaviour of turbulent jets (e.g. Batchelor & Gill 1962; Becker & Massaro 1968; Crow &

† Email address for correspondence: Eirik.asoy@ntnu.no

Champagne 1971; Brown & Roshko 1974; Winant & Browand 1974; Hussein, Capp & George 1994 among others). In a free axisymmetric jet, characteristics such as mixing, spreading and decay rates are uniquely described by the momentum flux at the jet exit (Wygnanski & Fiedler 1969; Panchapakesan & Lumley 1993; Hussein *et al.* 1994; Pope 2001). However, altering the boundary conditions through control methods can be used to significantly alter the behaviour of the jet (Reynolds *et al.* 2003).

Early studies focused on the preferred mode of jets identified through axial perturbations of the mean flow typically generated by loudspeakers far upstream of the nozzle. Crow & Champagne (1971) showed that axisymmetric coherent structures are formed along the developing shear layer in the near field at a preferred normalized frequency giving a Strouhal number of $St = fD/\bar{u}_0 \approx 0.3$, where f, D and $\bar{u}_0$ are the forcing frequency, nozzle diameter and mean jet exit velocity, respectively. Other studies have found that the frequency of the preferred mode lies in the range $St \approx [0.24 \text{ to } 0.64]$ (Bechert & Pfizenmaier 1975; Moore 1977; Hussain & Zaman 1981; Gutmark & Ho 1983). The preferred mode normally refers to excitation of the axisymmetric mode ($m = 0$) (Crow & Champagne 1971), which together with the first azimuthal modes ($m = \pm 1$), corresponds to the most dominant linear modes originally derived by Batchelor & Gill (1962) and Michalke & Hermann (1982) and later confirmed experimentally by Cohen & Wygnanski (1987) and Corke & Kusek (1993). Other observed modes can be interpreted as a superposition of the $m = 0$ and $m = \pm 1$ modes. For example, the flapping mode caused by transverse forcing in the numerical simulations of Danaila & Boersma (2000) and Gohil & Saha (2019) and the experimental studies of Corke & Kusek (1993) and Worth *et al.* (2020) is a combination of two counter-rotating azimuthal modes, $m = \pm 1$, that induce transverse motions along a plane leading to asymmetric vortex formation in the near field followed by bifurcation of the far field. These studies have shown that the jet response is most amplified when forced at or near the preferred mode.

Fewer studies have focused on the combined excitation of these modes through active forcing or a combination of active and passive forcing (Lee & Reynolds 1985; Parekh, Reynolds & Mungal 1987; Hussain & Husain 1989; Kusek, Corke & Reisenthel 1990; Longmire, Eaton & Elkins 1992; Longmire & Duong 1996; Reynolds *et al.* 2003; Suzuki, Kasagi & Suzuki 2004). For specific forcing conditions, this leads to the phenomena of 'bifurcating' and 'blooming' jets that split into multiple momentum streams that increase the spreading rate (see the review by Reynolds *et al.* (2003)). A 'bifurcation' of the jet into two streams has also been observed in elliptical (Hussain & Husain 1989) and sawtooth (Longmire & Duong 1996) shaped nozzles combined with symmetric forcing. Others have used different combinations of active forcing to excite combinations of modes in both experiments (Lee & Reynolds 1985; Parekh *et al.* 1987; Suzuki *et al.* 2004; Kasagi 2006; Worth *et al.* 2020) and numerical simulations (Urbin & Métais 1997; Danaila & Boersma 2000; da Silva & Métais 2002; Tyliszczak & Geurts 2014; Gohil, Saha & Muralidhar 2015; Tyliszczak 2015; Gohil & Saha 2019).

These complex forcing methods usually combine two or more frequencies to excite multiple modes. For example, Lee & Reynolds (1985) applied axisymmetric forcing at a frequency f_l simultaneously with azimuthal forcing at a frequency f_h and explored different forcing ratios $r_f = f_h/f_l$. It was found that forcing with $r_f = 2$ led to a 'bifurcated' jet whereas non-integer values, e.g. $r_f = 1.6$ and $r_f = 3.2$, led to a 'blooming' jet. The blooming jet is characterized by a so-called shower of vortex rings which propagate in all angular directions normal to the nozzle centreline. Tyliszczak (2015) showed numerically that 'bifurcated', 'trifurcated' and 'multi-armed' jets occur when r_f is chosen such that the two fluctuations (symmetric and azimuthal) act in phase at an integer number of angles

corresponding to the directions of the momentum streams. This gives rise to a 'blooming' jet with the formation of vortex rings along a fixed number of preferred directions.

As mentioned earlier, the complex jet response observed typically requires combined forcing $r_f \neq 1$ to excite multiple modes of the jet. To the best of the authors' knowledge, the effect of different levels of combined forcing when $r_f = 1$ has not been investigated. Yet, this case is directly relevant to the practical problem of self-excited thermoacoustic instabilities in annular combustor geometries typical of jet engines and gas turbines for power generation (Staffelbach *et al.* 2009; Worth & Dawson 2013; Bourgouin *et al.* 2013; Dawson & Worth 2014; O'Connor, Acharya & Lieuwen 2015). We consider the general case of an annular combustor that has a rotationally symmetric geometry with a number of equally spaced burners/jets immersed in a self-excited thermoacoustic resonance in the form of a standing wave at the first azimuthal acoustic mode of the annulus. A jet located at a pressure anti-node will be subjected to axisymmetric forcing resulting in the $m = 0$ mode, whereas a jet located at the pressure node will be subjected to anti-symmetric (transverse) forcing resulting in the $m = \pm 1$ mode. Both modes are excited at the same resonant frequency corresponding to the azimuthal mode of the geometry. However, at all locations in between each jet is subjected to combined forcing from both $m = 0$ and $m = \pm 1$ modes simultaneously but with a frequency ratio of $r_f = 1$.

This paper presents the results of a parametric study where different combinations of symmetric and anti-symmetric forcing are applied to an axisymmetric turbulent jet where $r_f = 1$ by placing the jet at different locations in a standing wave. A second aspect addressed in the paper is how to characterize these jets. Normally, forced jets are characterized as 'bifurcated', 'trifurcated', 'Ψ'-shaped, 'Y'-shaped, 'blooming' or 'multi-armed' based on two criteria first suggested by Parekh, Leonard & Reynolds (1988) which are as follows:

(i) The jet should be considered 'bifurcated' by visual inspection.
(ii) The velocity profile should contain several 'peaks' persisting towards the far field.

Although useful, this definition is somewhat subjective.

Based on the many results presented herein, we propose a statistical method based on probability density functions (p.d.f.s) constructed from profiles of streamwise momentum. Statistical moments of the p.d.f.s characterize the centre of momentum, spreading rate and symmetry which are used to provide a more quantitative measure of bifurcation. We also address the unanswered question of whether the different momentum streams resulting from bifurcation are self-similar. In the last section of this paper, a method is proposed to decompose the streamwise velocity field into separate momentum streams. Each stream of the forced jet is then analysed separately and compared with the unforced jet indicating that they are self-similar. The method also introduces for the first time a quantitative way to determine the number of individual momentum streams.

The paper layout is as follows. In § 2 we describe the experimental set-up detailing the acoustic forcing and measurement methods followed by a thorough characterization of the unforced jet in § 3 which serves as a reference for the forced cases presented afterwards. A characterization of the acoustic forcing system is described in § 4. Flow visualizations of the forced jet at various locations in the standing wave are then presented in § 5 to illustrate the jet response. This is followed by the dynamics of coherent structures formed in the jet near field by the various combinations of symmetric and anti-symmetric forcing in § 6. Section 7 provides an analysis of the Fourier modes and the modification of the base flow by the forcing conditions. Then §§ 8–10 present the time-averaged effects of forcing towards the jet far field, a statistical analysis of the streamwise momentum and

a simple method which can be used to empirically identify the individual momentum streams. Finally, we present the conclusions in § 11.

2. Experiments and methods

2.1. *Experimental set-up*

A schematic of the experimental set-up is shown in figure 1 and is similar to the set-up reported in Worth *et al.* (2020). An axisymmetric jet of exit diameter $D = 10$ mm was placed at the base of a long rectangular box with side-mounted speakers designed to produce approximately one-dimensional plane waves which propagate normally to the streamwise flow direction of the jet. For all cases, the jet can be considered acoustically compact such that $D \ll \lambda_y$, where λ_y is the wavelength of the transverse acoustic wave. The box dimensions were $[L_x, L_y, L_z] = [590, 1520, 220]$ mm with the top open and exposed to atmospheric conditions. A large ratio of box width to jet diameter, $L_z/D = 22$, was employed to minimize confinement effects in the near field and developing region of the jet. The air flow rate for the jet was controlled by an Alicat MCR 500SLPM D mass flow controller (MFC) which ensures less than 2 % variation of the flow rate throughout the experiments. The flow enters the bottom of a plenum where it is expanded passing through a set of grids and honeycomb. The flow then enters a 35 mm diameter tube before entering the nozzle which has a contraction ratio of 12.25 which ensures <0.3 % fluctuations of the velocity at the centre of the jet exit. The jet exit was knife-edged. The Reynolds number, $Re_D = \bar{u}_0 D/\nu = 9500 \sim 10^4$, was held constant and corresponds to a mean jet exit velocity of $\bar{u}_0 = 14.8\ \mathrm{m\,s^{-1}}$, where ν is the kinematic viscosity. Throughout the paper, a Cartesian coordinate system (x, y, z) is used with the origin placed at the nozzle exit with mean and fluctuating velocities (u, v, w) corresponding to the streamwise x-direction of the jet, the y-direction parallel with the base of the box and the z-direction along the depth axis of the box.

Each side of the box is equipped with a Monacor KU-516 (75 W, 16 Ω) horn driver powered by PRO1000 power amplifiers and controlled by an Aim-TTi TGA1244 40 MHz signal generator for transverse acoustic forcing. To characterize the acoustic fluctuations pressure time series are measured in the box (p_{1-4}) and the injector pipe (p_{5-6}) using six Brüel and Kjær free-field 1/4″ condenser microphones flush-mounted to the pipe and box walls. During the forced jet experiments the two speakers in the box are driven in phase. Two frequencies: $f = 476$ Hz and $f = 696$ Hz, were investigated corresponding to the frequencies of the fourth and sixth transverse half-modes of the box computed using $f = c\sqrt{(n_x/L_x)^2 + (n_y/L_y)^2 + (n_z/L_z)^2}$, where c is the speed of sound. Here, $n_x = 1/4$, $n_y = 4/2$, $n_z = 0$ give $f = 476$ Hz and $n_x = 1/4$, $n_y = 6/2$, $n_z = 0$ give $f = 696$ Hz. These produce standing acoustic waves with transverse wavelength $\lambda_y = L_y/n_y$. In figure 1 the acoustic mode at $f = 476$ Hz is indicated schematically by the dashed lines showing the pressure in red and the velocity in grey. This mode has four pressure nodes and four velocity nodes along the transverse direction of the box. The two frequencies correspond to jet Strouhal numbers $St = 0.32$ and $St = 0.47$ which are in the range of the 'preferred mode' of the jet (Crow & Champagne 1971; Bechert & Pfizenmaier 1975; Moore 1977; Hussain & Zaman 1981; Gutmark & Ho 1983). The relative position between the nozzle and centre of the box is changed by moving both side walls of the box. A non-dimensional distance, $Y = (L_n - L_y/2)/(\lambda_y/4)$, describes the position of the nozzle relative to the velocity node at the centre, normalized by a quarter of the acoustic wavelength in the transverse direction. Hence, $Y = 0$ and $Y = \pm 1$ correspond to the velocity and pressure

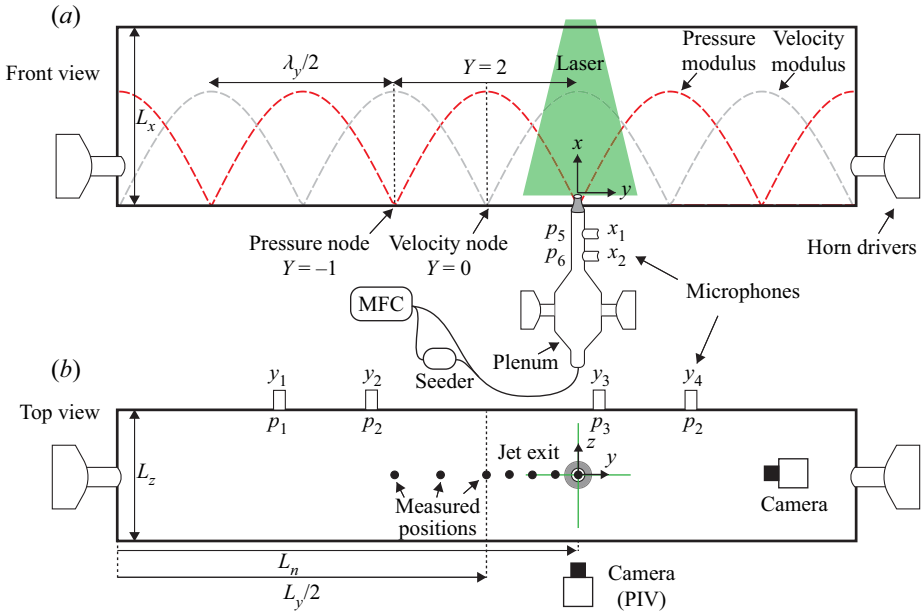

Figure 1. Schematic of the experimental set-up showing the horn drivers used for forcing, the camera set-up and the nozzle position relative to the acoustic standing wave. (*a*) Front view and (*b*) top view.

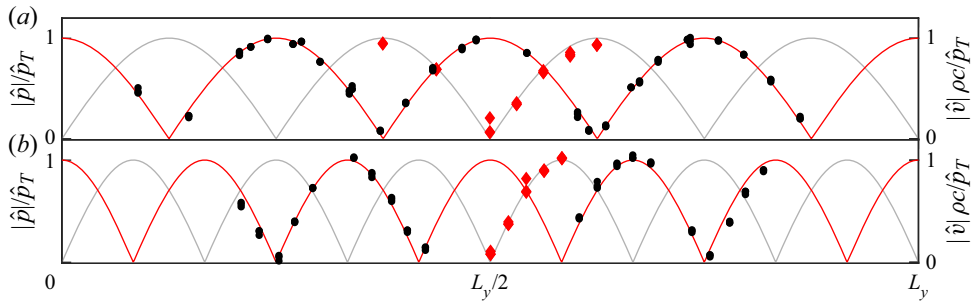

Figure 2. Pressure (microphones (black bullet)) and velocity (PIV (red lozenge)) measurements in the box for (*a*) $f = 476$ Hz and (*b*) $f = 696$ Hz corresponding to the fourth ($n_y = 4/2$) and sixth ($n_y = 6/2$) transverse half-modes of the box indicated by the solid lines $|\cos(2\pi(n_y/L_y)y)|$ (red solid line) and $|\sin(2\pi(n_y/L_y)y)|$ (grey solid line). All the measurements are normalized by the corresponding maximum pressure in the box $\hat{p}_T$.

nodes, respectively. Measurements of the velocity fields are carried out at seven positions in the range $Y = [-1 \text{ to } 1]$ for $St = 0.32$ and five positions in the range $Y = [0 \text{ to } 1]$ for $St = 0.47$. In this way the jet is subject to different combinations of transverse and longitudinal acoustic velocity fluctuations, from the symmetric and anti-symmetric modes. Figure 2 shows the pressure modulus $|\hat{p}|$ measured by the four microphones (p_{1-4}) in the box and velocity modulus $|\hat{u}|$ measured by particle image velocimetry (PIV) at the nozzle centreline at $x/D = 10$ for all operating points, normalized by the maximum pressure in the box $\hat{p}_T$. The data collapse on the lines, showing that the mode is approximately one-dimensional in the transverse direction. The acoustic measurements are described in detail in § 4.

2.2. *Velocity measurements*

The effect of the transverse forcing on the jet was investigated using high-speed planar PIV carried out in the x–y plane. A time-series of 5000 images were obtained at a fixed sampling rate of 2 kHz. During the forced experiments the images are sampled simultaneously with the acoustic pressure measurements and the excitation signal p_{sig}. The pressure and reference signals are sampled at 51.2 kHz for 2.5 s. The signal p_{sig} was used to synchronize the acoustic and PIV measurements. Two Photron SA1.1 1024 pixel^2 cameras equipped with 50 mm lenses with roughly 30 % overlapping fields of view cover a total area corresponding to $y/D = [-8 \text{ to } 8]$ and $x/D = [0 \text{ to } 24]$. A Litron LDY303HE-PIV dual-cavity green laser was collimated to a 1 mm thick light sheet illuminating oil droplets generated by a Laskin nozzle seeder. All velocity vectors were calculated using a recursive window size algorithm with a final size of 24 pixel^2 with 75 % overlap. This corresponds to a spatial resolution of 0.70 mm. An average uncertainty $\Delta \boldsymbol{u}$, due to various sources, such as measurement uncertainties for all experimental and processing parameters, seeding density, out-of-plane-motion, interrogation window size, etc., was estimated from 1000 vector fields using the method outlined by Wieneke (2015). Within the field of view, an average value $\Delta \boldsymbol{u} \approx \pm 0.27 \text{ m s}^{-1}$ is obtained. This corresponds to an uncertainty of 1.8 % relative to $\bar{u}_0$, and 5.7 % relative to an average velocity within the jet field of view.

The velocity fields were decomposed into mean $(\bar{u}, \bar{v})$ and fluctuating (u', v') components noting that the fluctuations contain both the turbulent fluctuations and harmonic components from the acoustic forcing. The harmonic components are recovered by conditional averaging, via phase averaging and Fourier analysis. Phase-averaged velocity fields were obtained by sorting the vector fields into $b = 20$ bins synchronized with the phase ϕ_b of the external forcing signal p_{sig} and are denoted $\langle \boldsymbol{u} \rangle_b(x, y, \phi_b) = 1/N \sum_{n=1}^{N} \boldsymbol{u}_n$, where $\boldsymbol{u}_n$ are the binned velocity fields at phase ϕ_b.

The jet modes excited by the acoustic forcing conditions were identified using spectral analysis. Fourier modes denoted by a tilde ($\tilde{}$) were computed using the discrete Fourier transform as follows:

$$\tilde{\boldsymbol{u}}(x, y) = \frac{2}{N} \sum_{n=0}^{N-1} \boldsymbol{u}'(x, y) \exp\left(-j2\pi n \frac{f}{f_s}\right), \tag{2.1}$$

where f_s is the sampling frequency and f is the forcing frequency. Each pixel of $\tilde{\boldsymbol{u}}$ provides the magnitude and phase of the Fourier mode of the velocity components represented as complex numbers. To estimate an uncertainty related to spectral convergence of the modes, an additional computation using 90 % of the samples produces differences of less than 2 %. The harmonic time evolution of the flow field is then given by the addition of the mean fields and the real value of the Fourier mode:

$$\langle \boldsymbol{u} \rangle_F(x, y, \phi) = \bar{\boldsymbol{u}} + \text{Re}\left(\tilde{\boldsymbol{u}} \exp\left(j2\pi\phi\right)\right), \tag{2.2}$$

which are used in § 7 to examine the modal response of the base flow and near field.

3. Characterization of the unforced jet

To identify the preferred mode of the unforced jet, hot wire anemometer (HWA) measurements are taken along the jet centreline, $y/D = 0$ from $x/D = [0 \text{ to } 20]$. Figure 3(a) shows contours of the power spectral density (PSD) of the magnitude of velocity compensated by f, plotted against St. Figure 3(b) shows the spectra at $x/D = 7$, after the end of the potential core corresponding to the dashed line in figure 3(a).

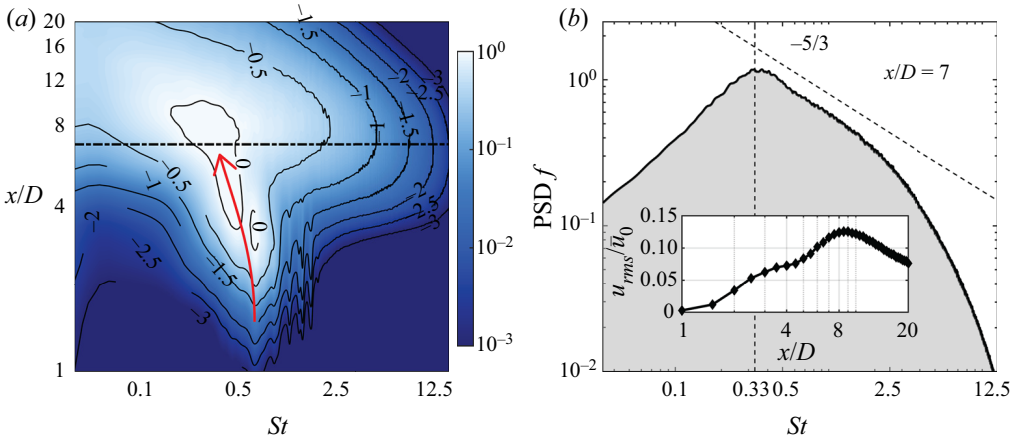

Figure 3. Compensated energy spectra (PSD) of u' measured along the jet centreline by the HWA. (*a*) Contours of streamwise development of the energy spectra and corresponding frequencies/scales. (*b*) A cut through (*a*) at $x/D = 7$ and $y/D = 0$. The inset shows u_{rms} and is obtained by taking the square root of the integrated spectra.

Close to the nozzle exit the energy is contained in a band of frequencies being $St =$ [0.4 to 0.6] due to the growth of instability modes in the developing shear layer through the Kelvin–Helmholtz instability (Ho & Huerre 1984). Figure 3(*b*) shows the expected energy spectra at $x/D = 7$ similar to previous measurements of the preferred mode of the jet found to be in the range $St =$ [0.24 to 0.64] (Crow & Champagne 1971; Bechert & Pfizenmaier 1975; Moore 1977; Hussain & Zaman 1981; Gutmark & Ho 1983). The inset in figure 3(*b*) shows the development of u_{rms} obtained by taking the square root of the total energy, which, in turn, is obtained by integrating the energy spectra ($u_{rms}^2 = \int \text{PSD}\, \mathrm{d}St$). As the shear layer develops, the total energy increases due to the growth of the coherent structures and peaks at $x/D \approx 8$. After this location, most of the coherent structures break down into turbulence and for $x/D > 8$ the total energy decays exponentially. It can be seen that the preferred mode varies along the potential core ranging from $St \approx$ [0.3 to 0.5].

The velocity exit profile at $x/D \approx 0$ is shown in figure 4(*a*). The HWA was traversed in increments of 0.1 mm across the shear layer. The jet exhibits an approximately tophat velocity profile shown for $y/D =$ [0 to 0.75] in the top plot. The bottom plot shows a zoomed view of the region $y/D =$ [0.45 to 0.55] which corresponds to the shear layer. The momentum thickness θ is computed by

$$\theta = \int_0^\infty \frac{\bar{u}}{\bar{u}_0}\left(1 - \frac{\bar{u}}{\bar{u}_0}\right) \mathrm{d}y, \tag{3.1}$$

and gives a value $\theta/D = 0.012$, which corresponds to approximately 1 % of the nozzle diameter.

Beyond $x/D > 10$, the unforced jet starts to exhibit self-similar behaviour (Wygnanski & Fiedler 1969; Panchapakesan & Lumley 1993; Hussein *et al.* 1994; Pope 2001). Figure 4(*b*,*c*) shows the normalized profiles and the centreline decay of streamwise velocity. The profiles in figure 4(*b*) collapse on the self-similar Gaussian profile

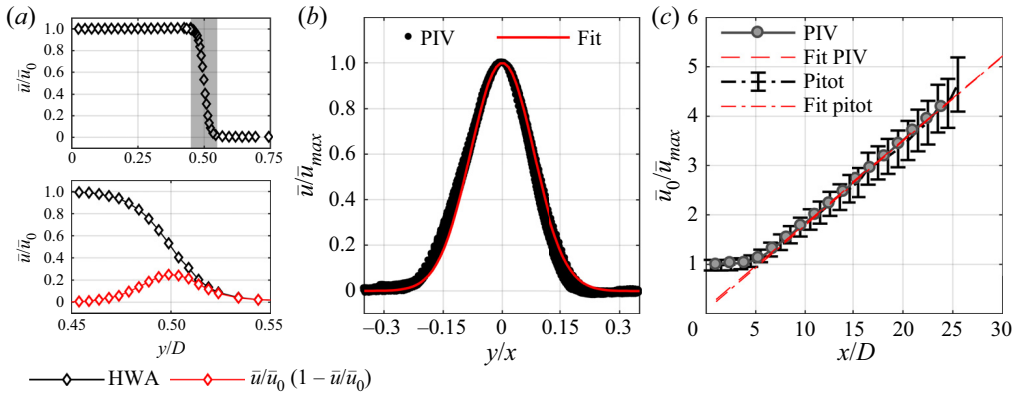

Figure 4. Measurements of the unforced jet providing characteristics summarized in table 1. (*a*) Jet exit profile measured at $x/D \approx 0$. The lower panel shows a zoomed view of the shear layer indicated by the shaded region in the upper panel. (*b*) Profiles of $\bar{u}$ plotted against y/x in the far field, $x/D > 10$, normalized by the centreline velocity $\bar{u}_{max}$. (*c*) Centreline decay of velocity measured by PIV and the Pitot probe.

	W & F	P & L	H	Present
Re_D	$\sim 10^5$	$\sim 10^4$	$\sim 10^5$	$\sim 10^4$
θ/D	—	—	∼0.03	0.012
y_0	0.086	0.096	0.094	0.094
B	5.4	6.1	5.9	6.0
M/M_0	0.62	1.00	1.05	0.93

Table 1. Summary and comparison of jet parameters with Wygnanski & Fiedler (1969) Panchapakesan & Lumley (1993) and Hussein *et al.* (1994).

given by

$$\bar{u}/\bar{u}_{max} = \exp\left(\ln(0.5)\left(\frac{y}{xy_0}\right)^2\right), \tag{3.2}$$

where y_0 is the jet half-width and $\bar{u}_{max}$ is the centreline velocity. The fitted value $y_0 = 0.095 \pm 0.002$ is consistent with previous measurements (see table 1 for a comparison).

Figure 4(*c*) shows the decay of the centreline velocity measured by PIV and a Pitot probe. The two measurements are in good agreement and show that the potential core with constant velocity extends to $x/D \approx 5$ before the velocity starts to decay exponentially as indicated by the self-similar linear decay rate. The decay rate is given by

$$\bar{u}_0/\bar{u}_{max} = \frac{1}{B}\left(\frac{x - x_0}{D}\right), \tag{3.3}$$

where B is the velocity decay rate and x_0 is the virtual origin. The fitted values of PIV and the Pitot probe give $B = 5.98 \pm 0.01$ and $B = 6.04 \pm 0.02$, respectively, which are similar to previous measurements (see table 1). The ratio M/M_0 is the momentum in the jet relative to that at the nozzle exit. Inserting the fitted values for B and y_0 gives $M/M_0 = 2.89 y_0^2 B^2 = 0.93 \pm 0.01$ demonstrating momentum conservation and self-similarity within the measurement domain (up to $25D$).

4. Acoustic characterization

The experimental apparatus described in § 2 provides a novel way to simultaneously excite the symmetric and anti-symmetric modes. In this section, a thorough characterization of the forcing method is presented together with some comments on how the different nozzle locations correspond to, or differ from, conditions previously reported.

The pressure time series p_{5-6} are used to reconstruct the acoustic mode in the pipe using the multiple microphone method (MMM) (Seybert & Ross 1977). Assuming one-dimensional acoustic waves and a negligible influence by the mean flow, the acoustic mode is given by

$$\hat{p}_l(x) = A^+ \mathrm{e}^{-jkx} + A^- \mathrm{e}^{jkx}, \quad \hat{u}(x)\rho c = A^+ \mathrm{e}^{-jkx} - A^- \mathrm{e}^{jkx}, \tag{4.1a,b}$$

where $\hat{p}_l$ are the acoustic pressure and $\hat{u}$ the longitudinal acoustic velocity fluctuations. The circumflex (^) denotes complex amplitudes and is reserved for acoustic quantities. The complex-valued variables A^+ and A^-, estimated using the MMM, give the amplitude and phase of the upstream and the downstream propagating acoustic waves, $k = 2\pi f/c$ is the wavenumber and ρ is the density. Similarly, using the pressure time series p_{1-4} the acoustic mode in the box is reconstructed. For this case in (4.1*a*,*b*) the x coordinate is substituted by y, the wavenumber $k = 2\pi n_y/L_y$ and $\hat{v}$ and $\hat{p}_t$ are used instead of $\hat{u}$ and $\hat{p}_l$ to represent the transverse velocity and pressure fluctuations. With both modes reconstructed, the values of the longitudinal and transverse velocity fluctuations at the nozzle exit ($x/D = 0$, $y/D = 0$) together with the maximum pressure in the box, $\hat{p}_T = \max(|\hat{p}_t|)$, and the maximum pressure in the pipe, $\hat{p}_L = \max(|\hat{p}_l|)$, can be evaluated.

For calibration, the HWA is placed at the nozzle exit while longitudinal forcing is applied by the horn drivers in the upstream plenum at a range of Strouhal numbers $St =$ [0.27 to 0.54] with a constant peak-to-peak voltage of 2 V. Figure 5(*a*) shows the magnitude and phase of $\hat{u}$ measured by the MMM and HWA which are in excellent agreement. Two resonances of the jet plenum are observed at $St = 0.37$ and $St = 0.43$ corresponding to $f = 550$ Hz and $f = 640$ Hz, respectively. These frequencies are avoided to obtain transverse and longitudinal oscillations of the same order of magnitude simultaneously.

To verify that similar pressure levels $\hat{p}_T$ and $\hat{p}_L$ are obtained simultaneously in the box and in the pipe, transverse forcing is applied by the horn drivers in the box at the same range of frequencies with constant voltage. Figure 5(*b*) shows $\hat{p}_T$ and $\hat{p}_L$ normalized by the maximum pressure observed at $St = 0.32$. Hence the plot shows the relative pressure level in the box and pipe. The two peaks at $St = 0.32$ and $St = 0.47$ correspond to the fourth and sixth transverse modes of the box shown in figure 2. At these Strouhal numbers, the pressure level in the pipe is also amplified and the relative magnitudes between $\hat{p}_T$ and $\hat{p}_L$ are similar.

To characterize the levels of $\hat{v}$ and $\hat{u}$ at the nozzle exit and how they change relative to the standing wave, the nozzle is first placed at the centre of the box corresponding to the velocity node at $Y = 0$. The pressure level $\hat{p}_T$ is then tuned such that three forcing levels defined as $A = |\hat{u}|/\bar{u}_0 = [0.05, 0.15, 0.25]$ are achieved. The pressure level in the box $\hat{p}_T$ is then kept approximately constant and the nozzle is moved to seven locations, $Y = [-1, -0.5, 0, 0.25, 0.5, 0.75, 1]$, when $St = 0.32$ and five locations, $Y =$ [0, 0.25, 0.5, 0.75, 1], when $St = 0.47$. At these locations the velocity field $\boldsymbol{u}$ is measured, in the x–y plane by PIV, simultaneously with the acoustic pressure. The MMM is then used to obtain $\hat{u}$ and $\hat{v}$ at the nozzle. These are presented next.

Figure 6 shows the magnitude of $\hat{u}$, $\hat{v}$ and the phase $\Delta\varphi/\pi = \angle(\hat{u}/\hat{v})/\pi$ at the different values of Y, A and St. In figure 6(*a*,*c*) $\hat{u}$ is indicated by the solid lines and $\hat{v}$ by the dashed lines. In figure 6(*b*,*d*) all the measurements are normalized by $\hat{p}_T$. Normalizing by $\hat{p}_T$

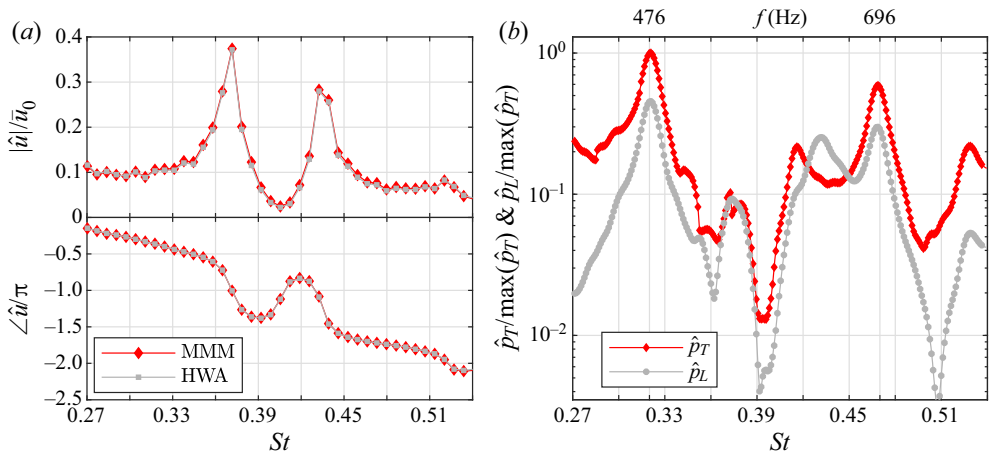

Figure 5. Acoustic characterization of the rig for Strouhal numbers corresponding to $f = [400 \text{ to } 800]$ Hz. (*a*) Measurements of $\hat{u}$ using the MMM and HWA at the nozzle exit subject to longitudinal forcing with constant voltage applied to the speakers in the plenum. (*b*) Measurements of $\hat{p}_T$ and $\hat{p}_L$ using the MMM subject to transverse forcing with constant voltage applied to the speakers in the box.

collapses all the data into the standing wave pattern where the magnitude of $\hat{u}$ and $\hat{v}$ follows the modulus of pressure and velocity in the transverse standing acoustic wave, respectively:

$$\left|\hat{u}\right| \propto \left|\hat{p}_t\right| \propto \left|\cos\left(\pi/2Y\right)\right|, \quad \left|\hat{v}\right| \propto \left|\sin\left(\pi/2Y\right)\right|. \tag{4.2a,b}$$

The relative phase $\Delta\varphi/\pi$ also follows the standing wave solution where $\Delta\varphi/\pi$ changes by half a cycle on each side of $Y = 0$. At all intermediate positions the two fluctuations are in anti-phase where $\Delta\varphi/\pi = 1$ if $Y > 0$ and in phase where $\Delta\varphi/\pi = 0$ if $Y < 0$. The level of $\hat{u}$ is proportional to the pressure level $|\hat{p}_t|$ at the nozzle. As indicated by the solid lines in figure 6(*b*,*d*), $\hat{u}$ is 3.5 times larger than $\hat{v}$ at $St = 0.32$ and 4.3 times larger at $St = 0.47$. These different ratios lead to $\approx 20\,\%$ larger values of $\hat{u}$ relative to $\hat{v}$ for $St = 0.47$ as compared to $St = 0.32$. This difference is an acoustic feature of the set-up and needs to be distinguished from the differences in the maximum response due to the 'preferred' mode of the jet (Crow & Champagne 1971; Bechert & Pfizenmaier 1975; Moore 1977; Hussain & Zaman 1981; Gutmark & Ho 1983).

Having characterized the acoustic velocities, we briefly discuss their effects in terms of body forces acting on the jet column. An acoustic field produces a body force proportional to the acoustic pressure gradient. In the streamwise direction we find the equivalent body force is proportional to $\partial\hat{p}_l/\partial x$. This body force is composed only of the $m = 0$ mode, and its strength depends on Y. In the experiment, at $Y = 0$, $\partial\hat{p}_l/\partial x$ reaches its maximum, and at $Y = 1$, $\partial\hat{p}_l/\partial x$ is almost zero. Similarly, the transverse wave produces a body force proportional to $\partial\hat{p}_t/\partial y$. As shown in O'Connor *et al.* (2015) and in Appendix A, a transformation of this body force into a cylindrical coordinate system fixed at the jet centre shows that its components vary with Y. At $Y = 0$ the force has contributions of the $m = 0$ mode and, with a smaller amplitude, the $m = \pm 2$ mode, while the $m = 1$ mode is negligible. As one moves towards $Y = 0.5$ the mode $m = \pm 1$ gains strength and dominates over the other modes. Finally at $Y = 1$ the force is composed mainly of the $m = \pm 1$ mode, with the others being negligible. This decomposition explains the dominant response observed in the experiments.

In what follows, the forcing conditions at the various nozzle positions are compared and contrasted against available studies in the literature. At the velocity node, $Y = 0$, $\hat{u}$ is at a

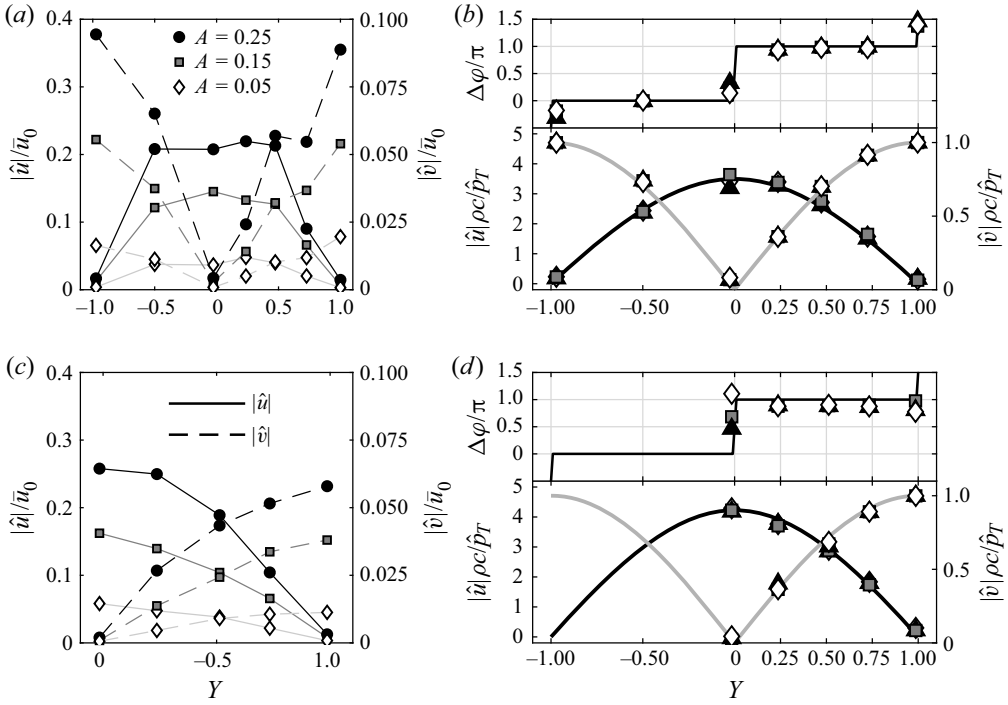

Figure 6. Longitudinal and transverse acoustic fluctuations ($\hat{u}$ and $\hat{v}$) measured using the MMM at the nozzle exit at different locations relative to the standing wave. Measurements (*a*,*b*) at $St = 0.32$ and (*c*,*d*) at $St = 0.47$. (*a*,*c*) The magnitude of the velocity fluctuations normalized by $\bar{u}_0$ and (*b*,*d*) the same but normalized by $\hat{p}_T$ making the data collapse to the standing wave solution indicated by the solid lines ($|\hat{u}|$ (black solid line) and $|\hat{v}|$ (grey solid line)) as described in (4.2*a*,*b*).

local maximum and $\hat{v}$ is approximately zero. This condition corresponds to axisymmetric forcing similar to what is used in Crow & Champagne (1971), exciting the axisymmetric ($m = 0$) mode of the jet column. At this location, the jet can be considered to be submitted to longitudinal perturbations and experiences maximum pressure fluctuations at the nozzle exit. As the nozzle is moved towards either pressure node $|Y| = 1$, $\hat{v}$ increases and $\hat{u}$ decreases. At the intermediate locations the jet is forced by a combination of symmetric ($\hat{u}$) and anti-symmetric ($\hat{v}$) excitation with the same frequency. To the best of the authors' knowledge this type of combined forcing at $r_f = 1$ has only been studied numerically by Tyliszczak & Geurts (2014), where the mixed mode is shown for a couple of cases. Parekh *et al.* (1987) also used speakers to generate simultaneous transverse and longitudinal forcing. However, in this particular study $r_f = 2$ and the transverse acoustic wave is not characterized. Later in this paper it is shown that forcing both $m = 0$ and $m = \pm 1$ at the same frequency, i.e. $r_f = 1$, leads to significantly different dynamics. At the two pressure nodes ($|Y| = 1$) $\hat{v}$ reaches a local maximum while $\hat{u}$ is approximately zero. Hence, the jet is submitted to pure anti-symmetric fluctuations corresponding to a flapping mode excitation similar to what is reported in Danaila & Boersma (2000), da Silva & Métais (2002), Gohil & Saha (2019), Suzuki *et al.* (2004) and Worth *et al.* (2020).

As mentioned in the introduction, $r_f = 1$ is a particularly relevant condition for a variety of flows immersed in cavities that are in resonance, such as those that occur during combustion instabilities in annular geometries. The response of an axisymmetric jet at $Y = 0$ and $|Y| = 1$ for $r_f = 1$ has been, at least partially, explored whereas the coupled

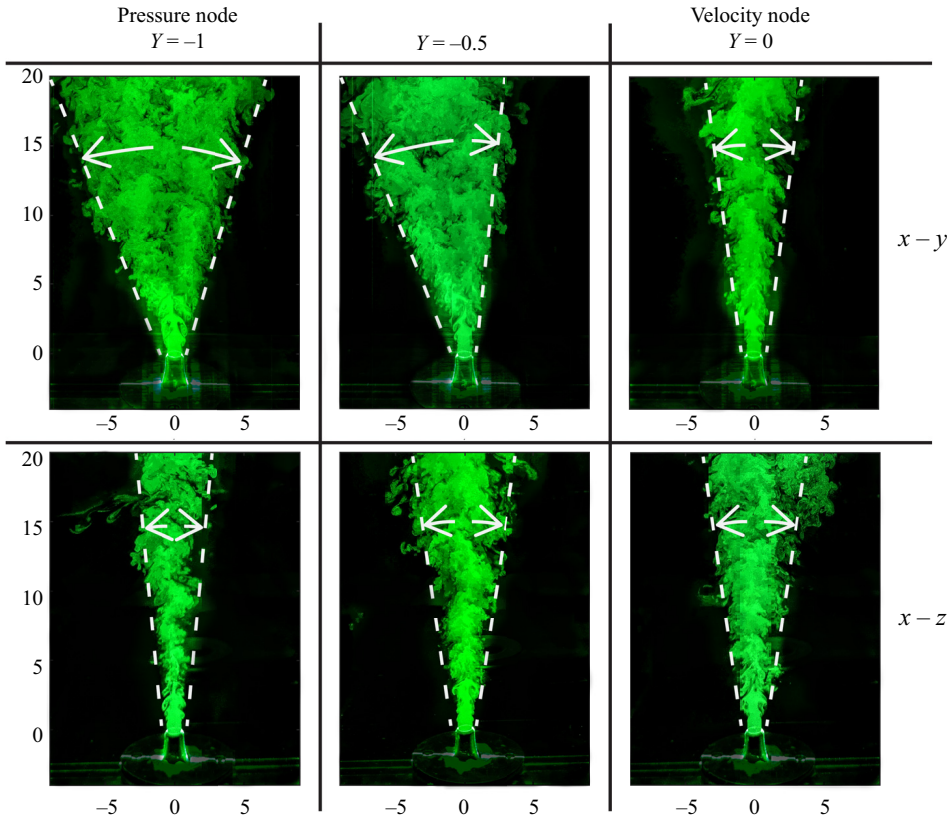

Figure 7. Mie scattering visualization of the forced jets at three different positions relative to the standing wave, illustrating the modified jet shapes due to acoustic forcing. The dashed lines indicate the jet boundary and all coordinates are normalized showing x/D, y/D and z/D.

mode forcing of the jet that occurs between the nodal and anti-nodal positions has not been investigated.

5. Flow visualization of the forced jet

In the previous section, the coupled longitudinal and transverse acoustic fluctuations at the nozzle exit due to transverse forcing of the box modes were characterized. To show the effect of forcing on the jet structure, Mie scattering images were taken to visualize the flow in the x–y and x–z planes.

Figure 7 shows single snapshots of the flow taken at $Y = -1$, $Y = 0$ and $Y = -0.5$ at $St = 0.32$. As discussed in the previous section these locations correspond to symmetric forcing at $Y = 0$, anti-symmetric forcing at $Y = -1$ and a combination of the two at $Y = -0.5$. The top row shows the flow in the transverse plane (x–y) and the bottom row the cross-plane (x–z). The white lines indicate the approximate border of the jet and the curved arrows indicate the deflection from the nozzle centreline.

At $Y = 0$ the jet structure is symmetric in both planes corresponding to an axisymmetric response. As the nozzle is moved away from the velocity node, $|Y| > 0$, asymmetry is observed between the two planes. The x–y plane remains symmetric but the x–z plane shows an increased asymmetric spreading rate to one side of the jet and is indicative of the separation into more than one momentum stream. At the pressure node ($Y = -1$) the

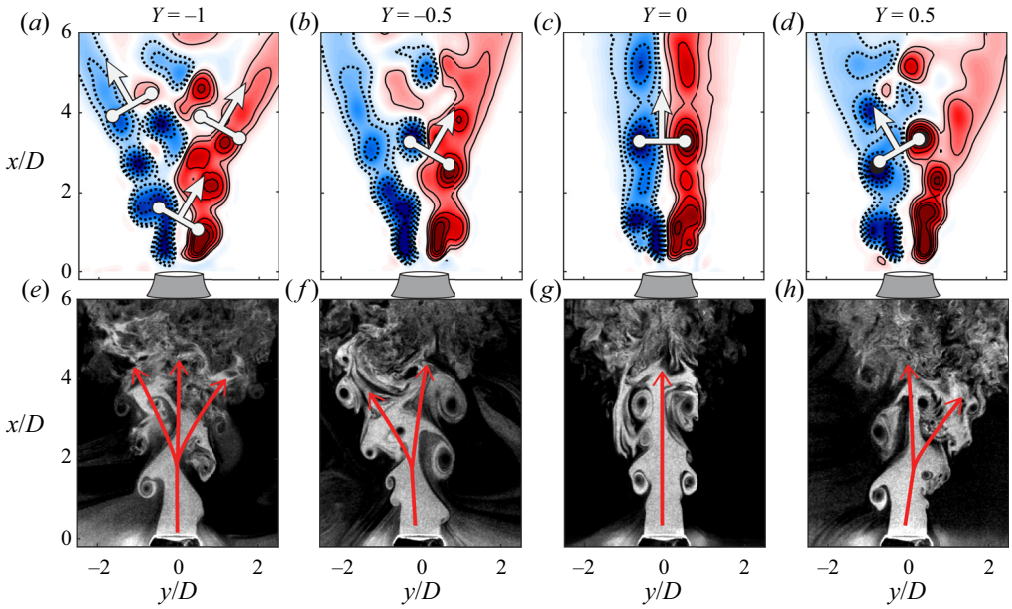

Figure 8. Phase-averaged vorticity ($\langle\omega_z\rangle_b$) (*a–d*) and Mie scattering visualization (*e–h*) illustrating the vortex dynamics in the near field of the jet at different positions of the nozzle relative to the standing wave for $St = 0.32$ at $A = 0.15$.

spreading rate increases symmetrically in the x–y plane. In the x–z plane, the jet spreads less than at $Y = 0$. At $Y = 0$ and $Y = 1$ the jet is excited by a single acoustic component, i.e. either $\hat{u}$ or $\hat{v}$ is negligible, leading to plane symmetry across the nozzle centreline in both planes.

The effect of simultaneous forcing is shown at $Y = -0.5$. Here, the increased spreading rate in the x–y plane is asymmetric across the nozzle centreline where the mean jet structure tilts towards $Y = -1$. This asymmetry is due to the simultaneous fluctuations of $\hat{u}$ and $\hat{v}$ where $\Delta\varphi/\pi = 0$ inducing a preferred direction for the coherent structures. To the best of the authors' knowledge this asymmetry has only been reported numerically in Tyliszczak & Geurts (2014) and experimentally in Longmire & Duong (1996) and is a feature of an asymmetry introduced by the active or passive forcing, respectively.

6. Vortex dynamics in the near field

In this section, the dynamics of the coherent structures, formed as a result of the forcing, are investigated in the near field of the jet. The different behaviours are then linked to the dynamics previously reported in the literature.

Figure 8 shows contours of normalized vorticity $\langle\omega_z\rangle_b D/\bar{u}_0$ and the corresponding snapshots of the instantaneous Mie scattering images for the same positions shown in figure 7. To show that the asymmetry is induced by $\Delta\varphi/\pi$, the response is also shown at $Y = 0.5$. These correspond to planar cuts of a vortex ring wrapped around the nozzle (see Worth *et al.* (2020) or Gohil & Saha (2019) for three-dimensional views). The trajectory of the vortices is indicated schematically by the red arrows in the particle images. At all nozzle positions, coherent structures form along the shear layer close to the nozzle exit. The images show how the forcing conditions imposed by $\hat{u}$ and $\hat{v}$ induce different patterns in which the coherent structures roll up and propagate downstream.

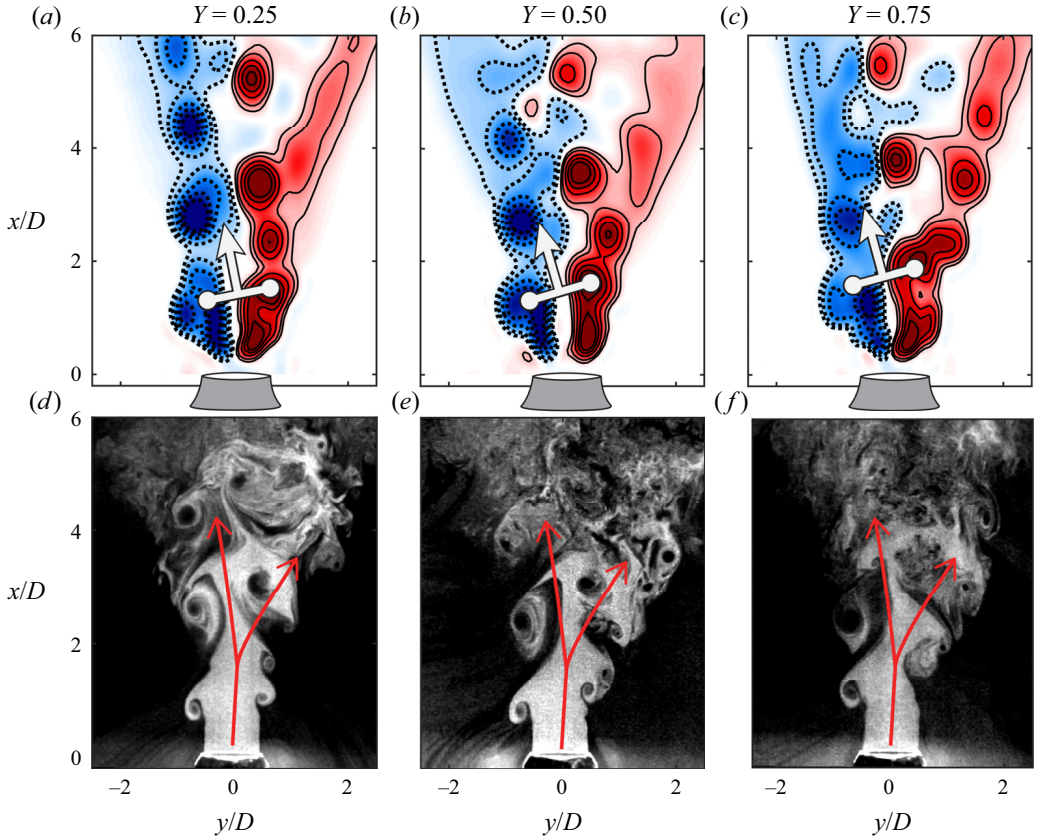

Figure 9. Phase-averaged vorticity ($\langle\omega_z\rangle_b$) (*a–c*) and Mie scattering visualization (*d–f*) illustrating the vortex dynamics in the near field of the jet at different positions between the pressure and velocity nodes for $St = 0.32$ at $A = 0.15$.

At $Y = 0$ an axisymmetric vortex ring, seen as a pair in two dimensions, forms once every forcing cycle at the nozzle exit which grows and breaks down into turbulence at the end of the potential core (Crow & Champagne 1971). As shown in figure 7 (and, for example, by Crow & Champagne (1971) and Hussain & Zaman (1981)), this type of axisymmetric roll-up process does not lead to the separation of the jet into more than one momentum stream.

At $Y = -1$, where the spreading rate is preferentially increased in the x–y plane, vortex structures roll up in an alternating pattern once every cycle. Worth *et al.* (2020) showed that the three-dimensional structure provides tilted interconnected vortex rings that resemble inverted-hairpin/horseshoe vortices. However, their data only covered a small field of view ($x/D = [0 \text{ to } 4]$). Here, it is shown that at $x/D \approx 3$, the structure breaks into two smaller structures each convected along different streams towards the far field as indicated by the arrows. This leads to the separation of the jet into three momentum streams in the transverse plane similar to the structures shown by Danaila & Boersma (2000), Tyliszczak & Geurts (2014) and Gohil & Saha (2019).

At $Y = \pm 0.5$, where the mean jet structure is asymmetric in the x–y plane, the vortex dynamics result from a superposition of the response observed at $Y = -1$ and $Y = 0$. The axisymmetric response induced by $\hat{u}$ generates a 'train' of symmetric vortex rings formed once every cycle. Simultaneously, the anti-symmetric response induced by $\hat{v}$ generates

an alternating vortex pattern. Since both oscillations occur at the same frequency and $\Delta\varphi/\pi = 1$ for $Y > 0$ and $\Delta\varphi/\pi = 0$ for $Y < 0$, they are superimposed and the transverse component induces the preferred direction for the axisymmetric vortex ring. This becomes evident from the vortex pattern observed at $Y = -0.5$ which is a mirror of that at $Y = 0.5$. At $Y = -0.5$, $\Delta\varphi/\pi = 0$, which means that $\hat{u}$ and $\hat{v}$ are in phase and thus the vortex ring has a preferred direction, propagating towards $Y = 0$. At $Y = 0.5$, $\Delta\varphi/\pi = 1$, which reverses the preferred direction towards $Y = 0$ on the other side of the nozzle. This is the main difference from the study of Parekh *et al.* (1987) who force the jet longitudinally twice every transverse cycle, leading to the formation of two pairs of axisymmetric vortex rings for every transverse cycle resulting in a symmetric jet splitting into two separate momentum streams. Here, an asymmetric splitting is observed as a result of the acoustic mode.

The jet response to further combinations of $|\hat{u}|$ and $|\hat{v}|$ is shown in figure 9 at $Y = 0.25$, $Y = 0.5$ and $Y = 0.75$. At these positions the preferred direction induced by $\Delta\varphi/\pi$ results in a tilted jet where the vortex ring moves towards $Y = 0$. However, as the nozzle is moved closer to the velocity node at $Y = 0.25$ the asymmetry reduces and the vortex dynamics become more axisymmetric. As the nozzle is moved closer to the pressure node at $Y = 0.75$ the vortex dynamics are dominated by the anti-symmetric response as demonstrated by the alternating vortex pattern. This indicates that the response at intermediate nozzle positions can be approximated as a superposition of the symmetric and the anti-symmetric modes, depending on the position of the jet relative to $Y = 0$ and $|Y| = 1$.

7. Fourier modes and modification of the base flow

To further characterize the modes excited by the acoustic fluctuations $\hat{u}$ and $\hat{v}$ the Fourier modes $\tilde{u}$ and $\tilde{v}$ were computed using (2.1). Figure 10 shows the magnitude and phase of the modes. The top and bottom rows correspond to $\tilde{u}$ and $\tilde{v}$, respectively. The data for the modes are only shown inside the jet, where $\bar{u}/\bar{u}_0 > 0.025$, and the region outside is shaded in grey. The first two columns correspond to the symmetric mode at $Y = 0$, the second to the mixed mode at $Y = 0.5$ and the third to the anti-symmetric mode at $Y = 1$. The phase contours indicate the patterns of convective propagation where a quantity, e.g. $\tilde{u}$, is convected along the gradient of the phase map. The symmetric mode at $Y = 0$ is characterized by an anti-symmetric pattern of the phase $\angle(\tilde{v})$ and a symmetric pattern of $\angle(\tilde{u})$ with respect to the nozzle centreline. This is a feature of the propagation of the axisymmetric vortex rings shown in the previous section. The anti-symmetric mode at $Y = 1$ is characterized by a symmetric pattern of $\angle(\tilde{v})$ and an anti-symmetric pattern of $\angle(\tilde{u})$. This is indicative of the alternating vortex pattern shown in the previous section. At the mixed position $Y = 0.5$ the structures of $\tilde{u}$ and $\tilde{v}$ contain features of both the symmetric and anti-symmetric modes which are utilized next.

The transverse acoustic velocity $|\hat{v}|$ is estimated by averaging $|\tilde{v}|$ in the region $x/D =$ [10 to 14] and $y/D = [-1$ to $1]$. The normalized velocity $|\hat{v}|\rho c/\hat{p}_T$ from the MMM and PIV was shown to be in good agreement in figure 2 for all values of A, Y and St, showing that for $x/D > 10$, $\tilde{v}$ is reduced to the transverse acoustic velocity $\hat{v}$. However, in the near field $\tilde{v}$ differs significantly from the one-dimensional acoustic mode shape given by (4.1*a*,*b*). Next, it is demonstrated that the manipulated boundary conditions, i.e. the jet exit profiles at $x/D = 1$ of $\tilde{u}$ and $\tilde{v}$, at mixed positions are linear combinations of the symmetric and anti-symmetric boundary conditions measured at $Y = 0$ and $Y = 1$.

The jet exit boundary conditions at $x/D = 1$ are shown in terms of the r.m.s. (u_{rms} and v_{rms}) and Fourier mode profiles ($|\tilde{u}|$ and $|\tilde{v}|$) in figure 11 for $St = 0.32$ at all

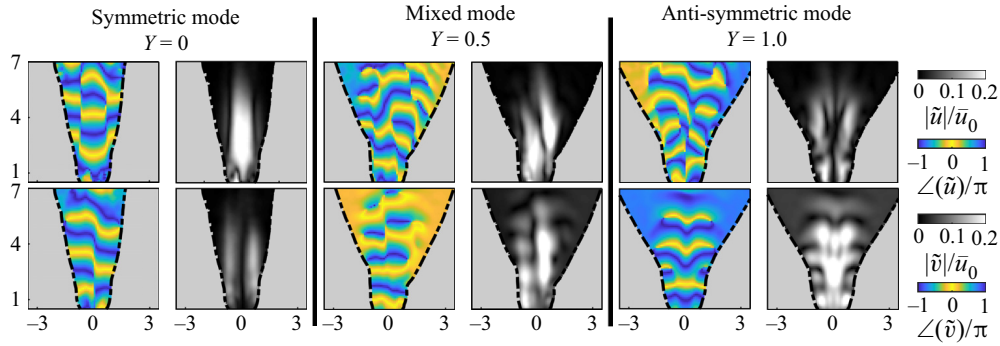

Figure 10. Fourier modes $\tilde{u}$ and $\tilde{v}$ for $St = 0.32$ at $A = 0.15$ showing the symmetric mode at $Y = 0$, a mixed mode at $Y = 0.5$ and the anti-symmetric mode at $Y = 1$. The black dashed lines indicate the jet boundary where $\bar{u}/\bar{u}_0 = 0.025$. All images are shown in the region $x/D =$ [0.5 to 7] and $y/D =$ [−3.5 to 3.5].

nozzle locations for $A = 0.15$. Figure 11(*a*,*e*,*i*,*m*) shows the profiles at $Y = 0$ and $Y = 1$ corresponding to boundary conditions for the symmetric and anti-symmetric modes. As a reference, the r.m.s. profiles are shown for the unforced case. All r.m.s. values are multiplied by a factor $\sqrt{2}$ to compare with the harmonic amplitudes of the modes. The magnitude of all Fourier mode profiles are similar to the r.m.s. profiles indicating that most of the energy and thus most of the flow dynamics are captured by the modes. The discrepancies between the Fourier modes and r.m.s. are mainly observed in the shear layer and are of the same order of magnitude as the r.m.s. measured in the unforced case. As mentioned before, at $Y = 0$ a symmetric pattern is observed for $\tilde{u}$ and an anti-symmetric pattern is observed for $\tilde{v}$, whereas the opposite is seen at $Y = 1$. This symmetry and anti-symmetry in the boundary conditions is not visible in the profiles, since it is contained in the phase distribution of the modes as shown in figure 10. At $Y = 0$, $|\tilde{u}|$ is increased at the jet centreline proportional to $\hat{u}$ measured by the MMM where $\sqrt{2}u_{rms}/\bar{u}_0 \approx |\tilde{u}|/\bar{u}_0 \approx A \approx 0.15$. At $Y = 1$, $|\tilde{u}|$ is similar to the unforced profile and $|\tilde{v}|$ is increased significantly across the jet. Note that the magnitude of $|\tilde{v}|/\bar{u}_0$ is significantly larger than the magnitude of the transverse acoustic velocity $|\hat{v}|$. These two sets of boundary conditions induce different motions of the potential core which are discussed in the last part of this section.

At the intermediate locations all profiles are skewed with respect to the nozzle centreline where $|\tilde{u}|$ and $|\tilde{v}|$ are significantly increased in the direction $y/D < 0$ for $Y > 0$. This is due to a superposition of the boundary conditions at $Y = 0$ and $Y = 1$ leading to an asymmetric profile. This asymmetry is symmetric with respect to the velocity node, and is shown in figure 11(*c*,*g*,*k*,*o*) with the profiles for both $Y = -0.5$ and $Y = 0.5$. At $Y = -0.5$ the skewed profiles show increased fluctuations at $y/D > 0$ caused by a change of the phase $\Delta\varphi/\pi$ by half a cycle.

We now consider whether the boundary conditions at $0 < Y < 1$ and $-1 < Y < 0$ can be well approximated by linear combinations of the symmetric and anti-symmetric boundary conditions at $Y = 0$ and $|Y| = 1$. In figure 6 it is shown that the amplitude and phase of the acoustic fluctuations $\hat{u}$ and $\hat{v}$ at a given Y position change as a function of the pressure and velocity in a standing wave. Hence, the proportionalities in (4.2*a*,*b*) can be utilized as weighting functions where the profiles $\tilde{u}_p^Y(y)$ and $\tilde{v}_p^Y(y)$ at an intermediate position Y can be approximated by

$$\tilde{u}_p^Y(y) = \tilde{u}^{Y_0}(y)\cos(\pi/2Y)\frac{\hat{p}_T^Y}{\hat{p}_T^{Y_0}} + \tilde{u}^{Y_1}(y)\sin(\pi/2Y)\frac{\hat{p}_T^Y}{\hat{p}_T^{Y_1}}, \tag{7.1}$$

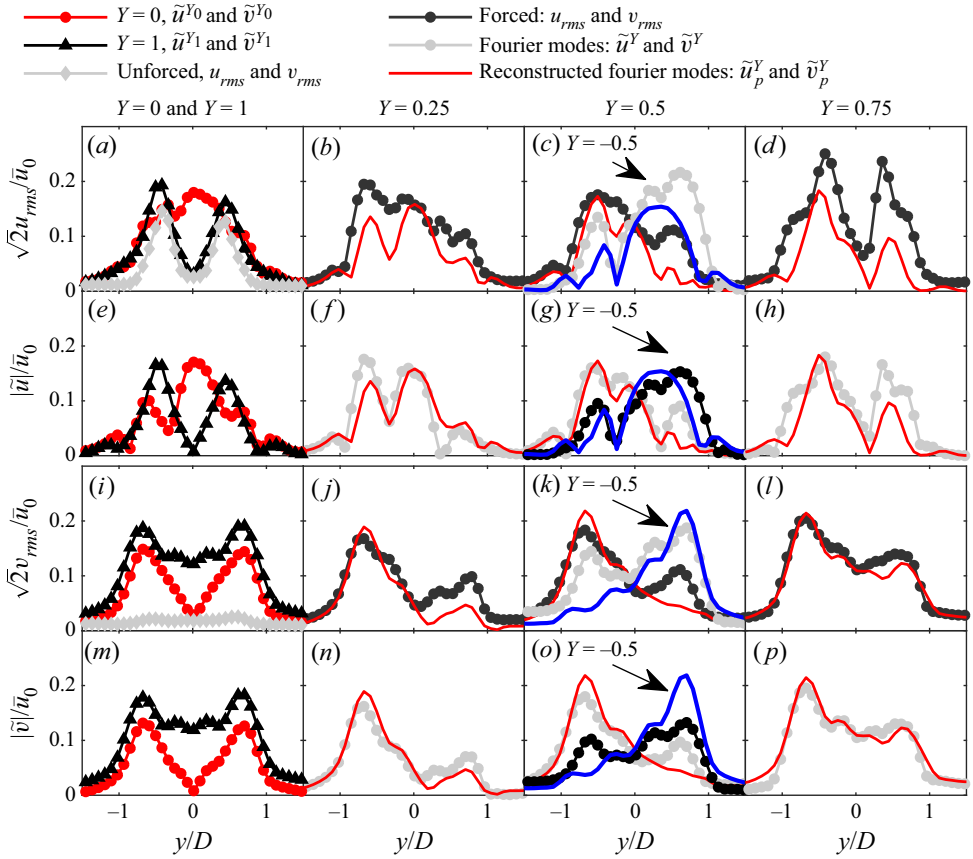

Figure 11. Jet exit boundary conditions in terms of root mean square (r.m.s.) fluctuations (*a–d,i–l*) and Fourier mode profiles (*e–h,m–p*) shown at $x/D = 1$ for $A = 0.15$ at $St = 0.32$. (*a,e,i,m*) Boundary conditions for the symmetric ($Y = 0$) and anti-symmetric ($Y = 1$) modes, and for the unforced jet. (*b,f,j,n,c,g,k,o,d,h,l,p*) Boundary conditions measured at the intermediate positions and the solid lines show reconstructed mixed modes from superposition of the symmetric and anti-symmetric profiles. All the measured profiles contain uncertainties of $\Delta/\bar{u}_0 \approx \pm 0.02$, and the reconstructed profiles contain $\Delta/\bar{u}_0 \approx \pm 0.04$.

$$\tilde{v}_p^Y(y) = \tilde{v}^{Y_0}(y)\cos(\pi/2Y)\frac{\hat{p}_T^Y}{\hat{p}_T^{Y_0}} + \tilde{v}^{Y_1}(y)\sin(\pi/2Y)\frac{\hat{p}_T^Y}{\hat{p}_T^{Y_1}}, \tag{7.2}$$

where $\tilde{u}^{Y_0}(y)$, $\tilde{u}^{Y_1}(y)$, $\tilde{v}^{Y_0}(y)$ and $\tilde{v}^{Y_1}(y)$ are jet exit profiles of the Fourier modes $\tilde{u}$ and $\tilde{v}$ measured at $Y = 0$ and $Y = 1$. From these profiles the harmonic time evolution can be obtained from (2.1). The profiles used for the reconstructions here are the ones shown at $x/D = 1$ in figure 11(*a,e,i,m*). The pressure ratios, $\hat{p}_T^Y/\hat{p}_T^{Y_0} \approx 1$ and $\hat{p}_T^Y/\hat{p}_T^{Y_1} \approx 1$, account for the differences in the maximum pressure level in the box between measurements. Ideally these two ratios are one and are only added to the equation to account for experimental differences in A between the measurements. The weights $\cos(\pi/2Y)$ and $\sin(\pi/2Y)$ are proportional to the acoustic fluctuations $\hat{u}$ and $\hat{v}$ in the standing wave. At $Y = 0$, $\tilde{u}_p^Y$ becomes $\tilde{u}^{Y_0}$, at $Y = 1$, $\tilde{u}_p^Y$ becomes $\tilde{u}^{Y_1}$, and at $0 < Y < 1$ and $-1 < Y < 0$, $\tilde{u}_p^Y$ becomes a superposition of the two whose weights depend on the position in the standing wave. The magnitudes of the reconstructed boundary conditions $|\tilde{u}_p^Y|$ and $|\tilde{v}_p^Y|$ are overlaid at all intermediate locations in figure 11 as red lines and show good agreement

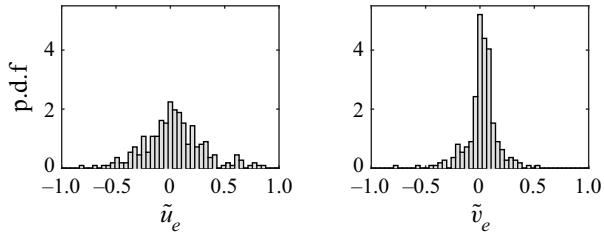

Figure 12. Histograms of relative errors $\tilde{u}_e$ and $\tilde{v}_e$ for all jet exit profiles computed across the nozzle $y/D = [-0.5 \text{ to } 0.5]$ at $x/D = 1$. The mean error and standard deviation are 3 % and 27 % for $\tilde{u}_e$ and 1 % and 14 % for $\tilde{v}_e$ respectively.

with the measured ones, $|\tilde{u}|$ and $|\tilde{v}|$. This shows that the jet exit boundary conditions at $0 < Y < 1$ and $-1 < Y < 0$ are well approximated as a linear combination of the boundary conditions of the symmetric and anti-symmetric modes measured at $Y = 0$ and $Y = 1$. This also indicates that the acoustic forcing is an inviscid effect primarily altering the jet exit boundary conditions, which leads to linear amplification of convective modes. It also shows that when superimposing $m = 0$ and $m = \pm 1$ forcing at $r_f = 1$ the result is an asymmetry in the base flow that develops into the asymmetric dynamics presented in the previous section.

The reconstructions in figure 11 are only shown for $St = 0.32$ and $A = 0.15$. To quantify errors of the reconstruction and to demonstrate that it works for all values of St, A and Y, we compute relative errors, using

$$\tilde{u}_e = \frac{|\tilde{u}| - \left|\tilde{u}_p^Y\right|}{|\tilde{u}| + \left|\tilde{u}_p^Y\right|}, \quad \tilde{v}_e = \frac{|\tilde{v}| - \left|\tilde{v}_p^Y\right|}{|\tilde{v}| + \left|\tilde{v}_p^Y\right|}, \tag{7.3a,b}$$

for all measurements. The relative errors are computed across the nozzle, i.e. $y/D = [-0.5 \text{ to } 0.5]$, and are shown as histograms in figure 12. The average errors are 2 % and 1 % and the standard deviations are 27 % and 14 % for $\tilde{u}_p^Y$ and $\tilde{v}_p^Y$ respectively. The errors are slightly larger for $\tilde{u}_p^Y$ due to the influence of the shear layer. However, the procedure works reasonably well at all operating points and the skewness of the profiles is well captured.

The asymmetric forcing observed at $0 < Y < 1$ and $-1 < Y < 0$ has the effect of deflecting the jet away from its geometric centre as shown in figures 7, 8 and 9. This can also be captured by reconstructing the time series of vorticity and velocity using (2.2), as shown in figure 13. Contours of the velocity magnitude $|\langle \boldsymbol{u} \rangle_F| = \sqrt{\langle u \rangle_F^2 + \langle v \rangle_F^2}$ indicating the potential core (grey) and vorticity $|\langle \omega_z \rangle_F| D/\bar{u}_0 > 1$ (red and blue) show the evolution of the coherent structures.

At $Y = 0$ the axisymmetric mode, $m = 0$, occurs with the potential core deforming into regions of high and low velocity accompanied by the axisymmetric roll-up of coherent structures. At $Y = 1$ the potential core is periodically deflected generating a sinuous shape resulting in an alternating pattern of vortices. These vortices continue to propagate towards the far field significantly increasing the jet spreading rate which is quantified in the next sections. As the nozzle is moved from $Y = 0$ towards $Y = 1$, the jet transitions from the symmetric to anti-symmetric modes, $m = 0$ to $m = \pm 1$. At $Y = 0.25$ significant asymmetry in the vorticity fields is evident and when placed at $Y = 0.75$ show a clear bifurcation. The effect is mirrored if the jet is traversed in the $-Y$ direction as shown at $Y = -0.5$ due to the change of $\Delta\varphi/\pi$ by half a cycle between $\hat{u}$ and $\hat{v}$.

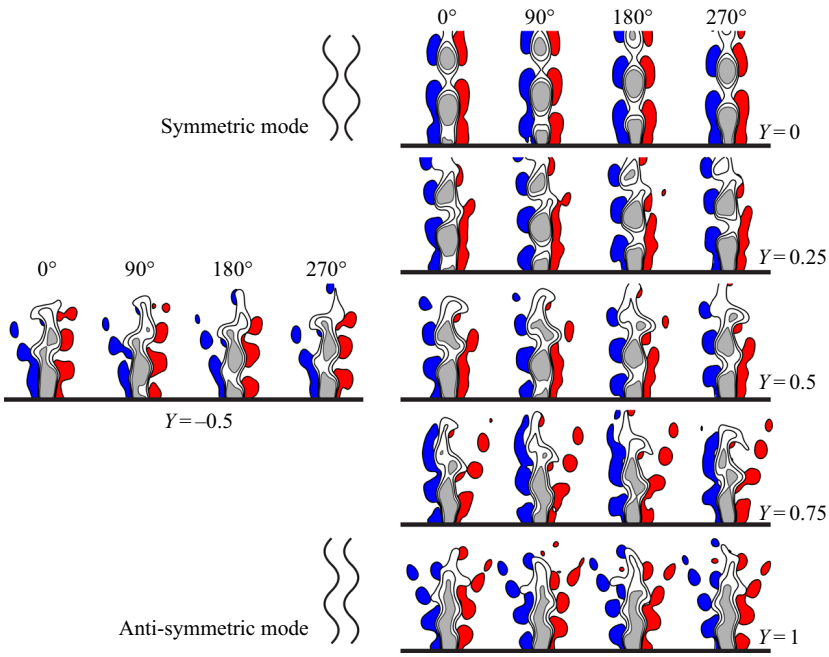

Figure 13. Time series reconstructed from the Fourier modes using (2.2) for $St = 0.32$ at all nozzle locations indicating the dynamics of the potential core and the induced vortex dynamics. The black and grey contours indicate $|\langle \boldsymbol{u} \rangle_F|/\bar{u}_0 > 0.8$. The red and blue contours indicate $|\langle \omega_z \rangle_F| D/\bar{u}_0 > 1$. The data are shown for $A = 0.15$ but the dynamics are similar at all A and for both St.

The effect of St is depicted in figure 14 with Mie scattering images, and $|\langle \boldsymbol{u} \rangle_F|$ and $|\langle \omega_z \rangle_F|$ reconstructed from the Fourier modes for both $St = 0.32$ and $St = 0.47$. Contours are added at $\bar{u}/\bar{u}_0 = 0.025$ to indicate the jet boundary and the streamwise velocity profiles are included at $x/D = 8$. The two images in figure 14(*a*,*b*) have been processed to highlight the edges of the potential core in order to show the jet boundary, growth and relative positioning of the coherent structures. The spreading rate is significantly greater for $St = 0.32$ compared with $St = 0.47$ consistent with the observations by Gohil & Saha (2019). Increasing spreading rates occur closer to the preferred mode where the forcing is most amplified. This leads to an optimal spacing between coherent structures. Compared with $St = 0.32$, the separation between coherent structures is smaller at $St = 0.47$ due to the higher frequency shown by labels A and C. Location A shows where the primary structure breaks into two smaller structures and C indicates their downstream trajectories. For $St = 0.32$, the same event is labelled B and D, respectively, where the coherent structures split into two smaller structures that propagate downstream in different directions. These effects are captured by the reconstructed time series in figure 14(*c*). The difference in separation and direction leads to significantly different profiles shown by the velocity profiles at $x/D = 8$. At 0° the events A–D are also labelled showing that the wider profile is a direct result of the increased angle of the separated structure as it propagates towards the far field when $St = 0.32$.

8. Time-averaged jet development

In the previous sections, it was shown that the dynamics in the near field of the jet depends on the position of the nozzle with respect to the standing wave. Furthermore, the boundary

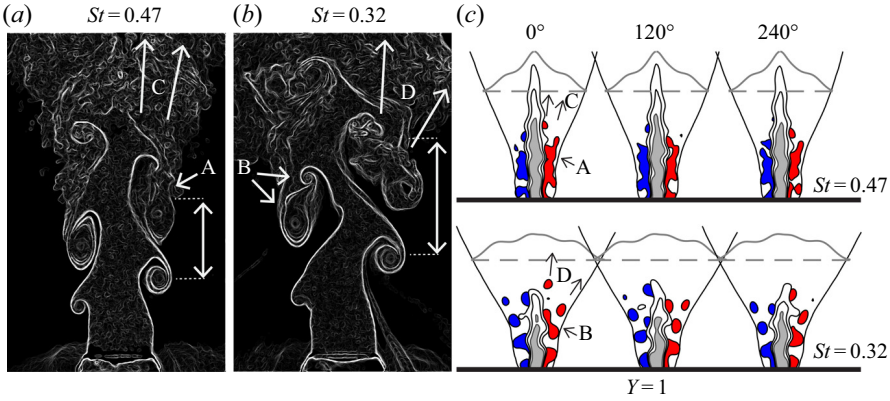

Figure 14. Influence of increased forcing frequency at $Y = 1$ for $A = 0.15$. (*a*,*b*) Processed Mie scattering images illustrate the separation and growth of coherent structures and indicate the boundary of the potential core. (*c*) Contours for $|\langle \boldsymbol{u} \rangle_F|$ and $|\langle \omega_z \rangle_F| D/\bar{u}_0 > 1$ similar to what is shown in figure 13. Contours of $\bar{u}/\bar{u}_0 = 0.025$ (black solid line) are added to indicate the spreading rate and the streamwise velocity profile $\bar{u}/\bar{u}_0$ (grey solid line) is shown at $x/D = 6$.

conditions leading to the mixed modes are well approximated by a linear combination of the boundary conditions for the symmetric and anti-symmetric modes. In this section the time-averaged flow fields $\bar{u}$, $\bar{v}$ and $\bar{\omega}_z$ are presented to show their influence on the developing region of the jet.

Figure 15 shows the time-averaged flow fields for all positions and forcing levels at $St = 0.32$ in the range $x/D = [0 \text{ to } 20]$. Normalized vorticity $\bar{\omega}_z D/\bar{u}_0$ is given by the colour map and the contours of constant streamwise velocity $\bar{u}/\bar{u}_0$ show how the jet develops downstream.

At $Y = 0$ the jet is similar to the unforced case. As the forcing level is increased the mean shape and structure of the jet remain approximately axisymmetric. The differences observed at $A = 0.25$ are due to a small but increasing value of $|\hat{v}|$ due to imperfect alignment of the nodal line with the centre of the nozzle. This shows that the jet is very sensitive to transverse oscillations.

The sensitivity to $\hat{v}$ becomes evident when $Y > 0$. Already at $Y = 0.25$ a significant increase in the spreading rate is observed. The asymmetric dynamics shown in the previous sections leads to preferential spreading of the jet towards $|Y| = 1$ whilst the jet centreline is deflected in the opposite direction towards $Y = 0$. The same behaviour is observed for all intermediate positions where the jet centreline is tilted left for $Y > 0$ and right for $Y < 0$. Although the forcing conditions and dynamics at $Y = 0.25$ and $Y = 0.75$ are different, the time-averaged structure of the jets appears similar at the same forcing level. As the jet is moved towards $|Y| = 1$ the profiles of $\bar{u}/\bar{u}_0 = 0.3$ show reduced skewness becoming symmetric at $|Y| = 1$. As A is increased the profiles of $\bar{u}/\bar{u}_0 = 0.5$ split into two or more streams indicative of a 'bifurcated' jet (Reynolds *et al.* 2003). This separation into two streams is stronger at $St = 0.32$ compared to $St = 0.47$ which is not shown here for brevity.

At $|Y| = 1$ the spreading rate is significantly increased and is symmetric across the jet centreline. As A is increased the jet splits into three momentum streams similar to the 'Ψ' jet observed in Danaila & Boersma (2000) and Gohil & Saha (2019). We can also obtain the bifurcation angles $\Delta\beta$ at $Y = 1$ to compare with the numerical simulation of Gohil & Saha (2019). Using their methodology, we track the jet boundary corresponding to isocontours of $\bar{u}/\bar{u}_0 = 0.1$ of the mean fields shown in figure 15 which results in 'bifurcation angles' of $\Delta\beta \approx 65^\circ$ for $St = 0.32$ and $\Delta\beta \approx 35^\circ$ for $St = 0.47$ which are

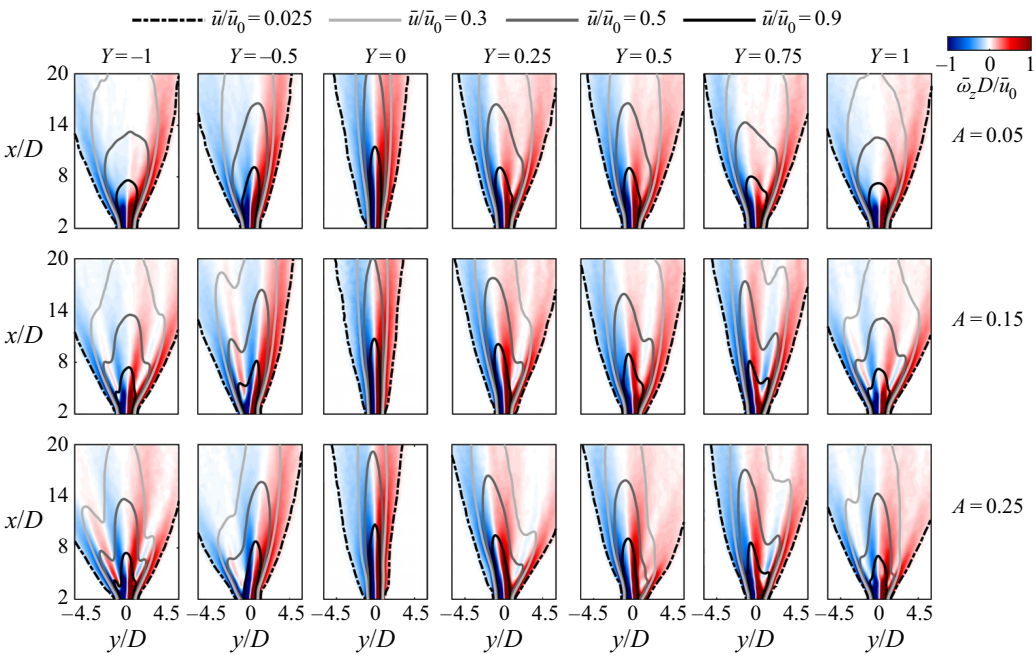

Figure 15. Time-averaged flow fields showing the average jet structure at all operating conditions for $St = 0.32$. The colour map shows normalized vorticity $\bar{\omega}_z D/\bar{u}_0$ indicating the shear layers. The contours correspond to regions of constant streamwise velocity $\bar{u}/\bar{u}_0$ indicating the outer boundary of the jet (black dashed line) and the development of the potential core (black solid line) towards the far field.

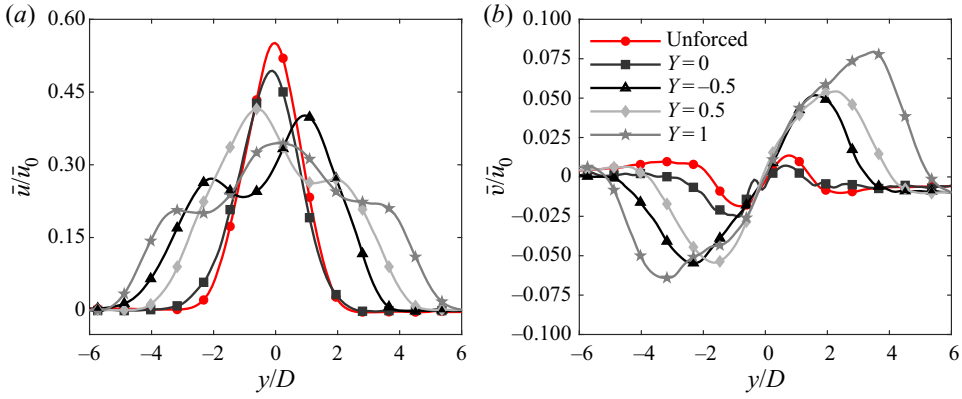

Figure 16. Velocity profiles at $x/D = 10$ for $St = 0.32$ at $A = 0.15$. (a) Streamwise velocity $\bar{u}/\bar{u}_0$. (b) Transverse velocity $\bar{v}/\bar{u}_0$. The wider profiles indicate an increased spreading rate.

in excellent agreement with the results of Gohil & Saha (2019). However, the use of $\Delta\beta$ to characterize the spreading rate is not suitable for asymmetric velocity profiles as shown in figure 16 and in numerous previous studies (e.g. da Silva & Métais 2002; Tyliszczak 2015; Gohil & Saha 2019) and we therefore propose an alternative approach based on a statistical analysis of the streamwise momentum presented in the next section.

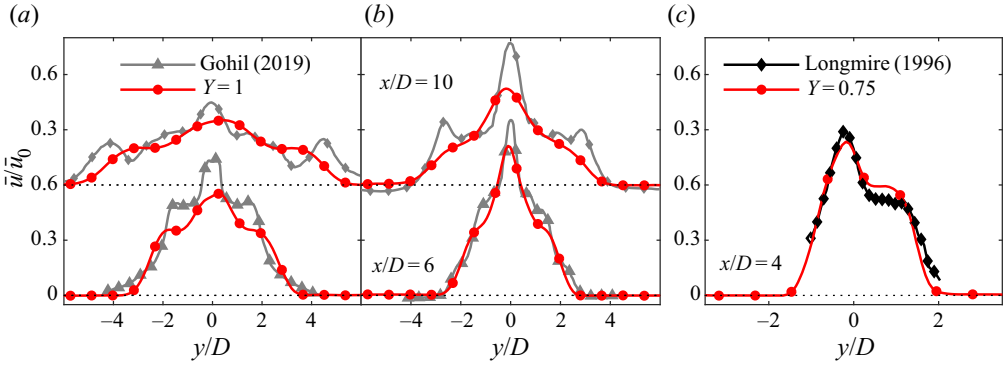

Figure 17. Comparison of velocity profiles $\bar{u}/\bar{u}_0$ against those reported in Gohil & Saha (2019) and Longmire *et al.* (1992) for similar conditions. (*a*,*b*) Profiles for $x/D = [6, 10]$ at $Y = 1$ for $A = 0.15$: (*a*) $St = 0.32$ compared against $St = 0.3$ and (*b*) $St = 0.47$ compared against $St = 0.5$. (*c*) Profile for $x/D = 4$ for $A = 0.15$ at $Y = 0.75$ compared against the profile produced by the forced step nozzle in Longmire & Duong (1996).

As shown for $Y = 1$ in figure 14, the structure of the jet is similar for similar positions at both St. However, the spreading rate and strength of the jet splitting is significantly lower for $St = 0.47$ for all positions and forcing levels as they are away from the preferred mode.

To highlight bifurcation or splitting of the jet from a single momentum stream, the mean streamwise and transverse velocity profiles are shown in figure 16 for $A = 0.15$ at $x/D = 10$. For brevity profiles are only shown for $St = 0.32$ noting that similar profiles were observed for $St = 0.47$ but with a reduced spreading rate. Figure 16(*a*) shows profiles of $\bar{u}/\bar{u}_0$. Figure 16(*b*) shows profiles of $\bar{v}/\bar{u}_0$. At $Y = 0$ profiles of $\bar{u}/\overline{u_0}$ and $\bar{v}/\overline{u_0}$ are similar to the unforced case. At $Y = 1$ the $\bar{u}/\overline{u_0}$ profile shows a symmetric distribution characterized by three peaks with maximum velocity at the nozzle centreline. The corresponding profile $\bar{v}/\overline{u_0}$ shows that both sides contain a significant $\bar{v}$ component. This indicates that the jet has separated into three separate momentum streams and is very similar to the 'Ψ' jet in Gohil & Saha (2019).

Figure 17 compares the response at $Y = 1$ with Gohil & Saha (2019) and $Y = 0.75$ with Longmire & Duong (1996). Figure 17(*a*,*b*) plots velocity profiles at various downstream locations and Strouhal numbers for the $Y = 1$ case. Overall, good agreement for both Strouhal numbers is found indicating the jet response is similar in both instances. Excellent agreement at $Y = 0.75$ with Longmire & Duong (1996) is also found in figure 17(*c*).

Finally, we consider the effect of the jet position and forcing amplitude on the relative change to the normalized momentum thickness θ/θ_0 as plotted in figure 18. These were evaluated from the PIV data at $x/D = 1$ as hot wire measurements were not conducted for all operating conditions investigated. Figure 18(*a*) shows that the spreading rate increases with $A^* = A\,\hat{p}_T^{Y}/\hat{p}_T^{Y_0}$ due to the formation of larger structures. Figure 18(*b*) shows the effect of amplitude and jet position on θ/θ_0. Increasing A results in an approximately linear increase in θ/θ_0 up to approximately $A^* = 0.25$. At $Y > 0$ it appears that the response becomes nonlinear at lower amplitudes.

Overall, the results and comparisons in this section illustrate that transverse acoustic forcing leads to a family of 'bifurcated' jets in the transverse plane. This planar splitting of the jet is very similar to previous 'bifurcated' jets produced by active or passive forcing but with some important differences. The forcing is monochromatic, $r_f = 1$, and the forcing components are varied by the jet's relative location within the standing wave which has not been explored before to the best of the authors' knowledge.

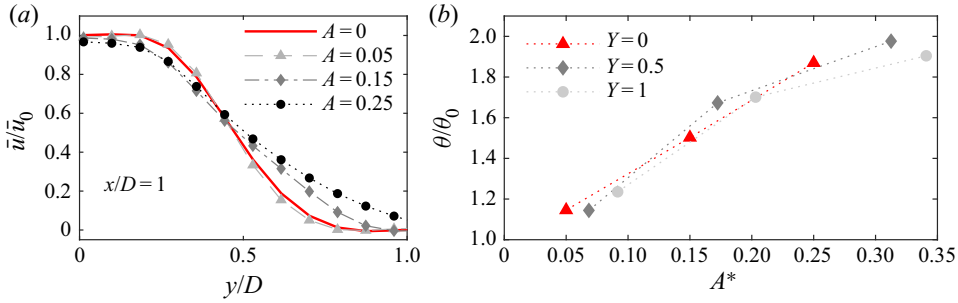

Figure 18. Effect of forcing on the momentum thickness θ computed at $x/D = 1$. (*a*) The velocity profile at $Y = 0$ against A. (*b*) The momentum thickness θ/θ_0 relative to the unforced case against the pressure-corrected forcing amplitude $A^* = A\,\hat{p}_T^Y/\hat{p}_T^{Y_0}$.

9. Statistical analysis of the streamwise momentum

In the following sections, two new methods to characterize the degree of bifurcation are presented. First, the jet is characterized based on the development of the statistical behaviour of the streamwise momentum downstream. Then, in the next section, a model is proposed to identify the number of individual momentum streams.

To characterize the modified behaviour of the forced jets statistically, p.d.f.s of streamwise momentum f_M are constructed from profiles of the streamwise velocity field, where

$$f_M = \frac{\rho\bar{u}(x,y)^2}{\rho\displaystyle\int_{-\infty}^{\infty}\bar{u}(x,y)^2\,\mathrm{d}y}. \tag{9.1}$$

The $n^{(\mathrm{th})}$ statistical moment μ_n of f_M was computed using

$$\mu_n = \int_{-\infty}^{\infty}(y - C_M)^n f_M\,\mathrm{d}y, \tag{9.2}$$

where $n = 1$ gives the centre of momentum, C_M, $n = 2$ gives the variance, $V_M = \sigma_M^2$, indicating the spreading rate, and $n = 3$ gives the skewness, S_M, indicating departure from symmetry. Figure 19 shows f_M at $x/D = 10$ for $Y = [-1, -0.5, 0]$ for $A = 0.15$ at $St = 0.32$. The insets show an image of $f_M(x, y)$ which appears as a collection of p.d.f.s in the region $y/D = [-7$ to $7]$ and $x/D = [1$ to $24]$. In the image of $f_M(x, y)$ all p.d.f.s are normalized by the maximum value $\max_x(f_M)$ to highlight the trajectories of momentum. In the main figures the profiles of f_M are shown at $x/D = 10$ corresponding to the red lines in the insets. The dashed lines indicate the centre of momentum, C_M, and $C_M \pm 3\sigma_M$.

At $Y = 0$ the shape of f_M is approximately Gaussian, characterized by $S_M \approx 0$ and a 95 % confidence interval of $6\sigma_M$. At $Y = -1$ and $Y = -0.5$, f_M is clearly not well represented by a single Gaussian distribution. At $Y = -1$, f_M contains three distinct peaks and is approximately symmetric ($S_M \approx 0$) with respect to C_M. At $Y = -0.5$ the distribution is asymmetric ($S_M < 0$) and f_M contains two peaks. The asymmetry is also shown by the different lengths between $C_M \pm 3\sigma_M$ and the tails of f_M on each side.

The moments C_M, σ_M and S_M are computed in the region $x/D = [1$ to $24]$ which are plotted in figure 20. The figure shows the downstream development of the moments for $St = 0.32$ and $A = 0.05$ at different positions Y. The red lines show the unforced case which is added for reference.

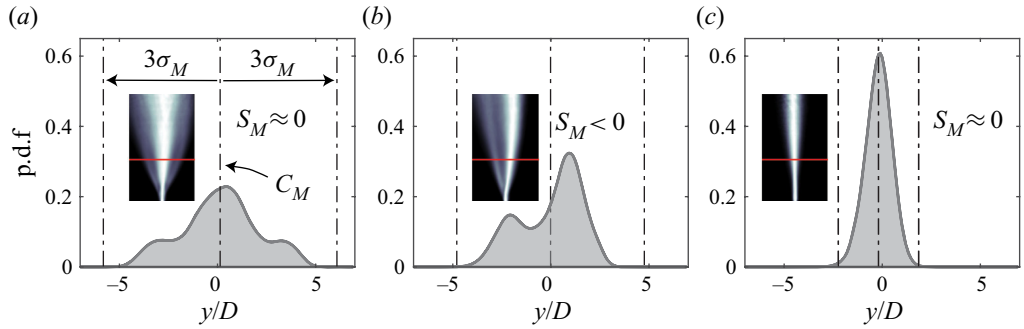

Figure 19. The p.d.f.s of streamwise momentum f_M shown at $x/D = 10$ (red solid line) for $A = 0.15$ and $St = 0.32$. The dot-dashed lines indicate the location of C_M and $C_M \pm 3\sigma_M$. The insets show $f_M(x, y)/\max_x(f_M)$ coloured by magnitude in the region $y/D = [-7$ to $7]$ and $x/D = [1$ to $24]$ where each p.d.f. is normalized by the maximum value $\max_x(f_M)$. (*a*) Pressure node ($Y = -1$) characterized by a symmetric distribution containing three peaks. (*b*) Intermediate position ($Y = -0.5$) characterized by an asymmetric distribution containing two peaks. (*c*) Velocity node ($Y = 0$) characterized by a symmetric distribution containing a single peak.

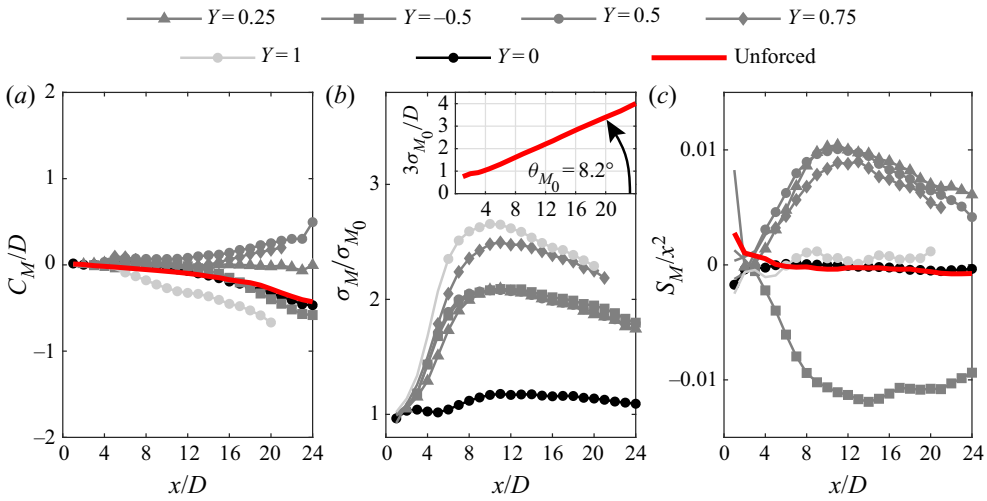

Figure 20. Development of statistical moments for $St = 0.32$ and $A = 0.05$: (*a*) C_M, (*b*) σ_M/σ_{M_0} and (*c*) S_M. The inset in (*b*) shows $3\sigma_{M_0}/D$ for the unforced jet which has an average spreading angle $\theta_{M_0} = 8.2°$. Moment S_M is normalized by x^2 to account for the linear spreading rate.

Figure 20(*a*) shows that $|C_M/D| < 1$ for all positions. This result indicates that the centre of momentum is located along the nozzle centreline and shows that introducing transverse forcing does not alter the location of the average streamwise momentum. The same observation is made for the other values of A and St, which are not shown for brevity.

Figure 20(*b*) shows σ_M normalized by σ_{M_0} which is computed for the unforced jet. Here σ_{M_0} develops linearly as shown in the inset and the average spreading angle of momentum is $\theta_{M_0} = 8.2°$. In § 3 it was verified that the unforced jet is self-similar with a half-width $y_0 = 0.095$. In this way, the lines in figure 20(*b*) show the spreading rate of momentum relative to the unforced case. At $Y = 0$ the jet develops similarly to the unforced case. For all cases where $|\hat{v}| > 0$, σ_M/σ_{M_0} increases rapidly in the region $x/D = [2$ to $8]$ before it levels off and starts to decrease slowly. This indicates that the spreading of momentum

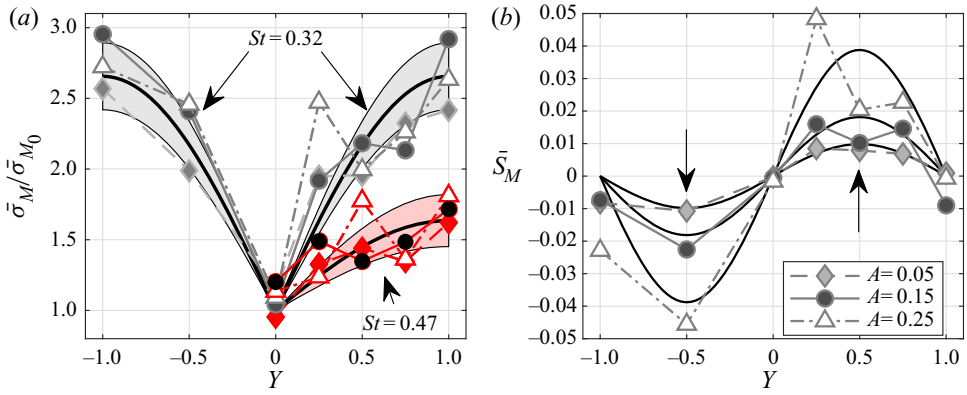

Figure 21. (*a*) Average relative momentum spreading rate $\bar{\sigma}_M/\bar{\sigma}_{M_0}$ and (*b*) average symmetry $\bar{S}_M$ in the far field $x/D > 10$ at different nozzle positions. In (*a*), the black solid lines indicate fits of $\bar{\sigma}_M/\bar{\sigma}_{M_0}$ to (4.2*a*,*b*) which is proportional to $|\hat{v}|$. The scatter is indicated by the coloured regions. The variation of $\bar{\sigma}_M/\bar{\sigma}_{M_0}$ due to the change in A is significantly smaller than the variation due to the change of St. In (*b*), the black solid lines indicate fits of $\bar{S}_M$ to the product $\hat{u}\hat{v} \propto \sin(\pi/2Y)\cos(\pi/2Y)$. The asymmetry increases with A and is proportional to the product of $\hat{u}$ and $\hat{v}$ where $\bar{S}_M < 0$ for $Y < 0$ and $\bar{S}_M > 0$ for $Y > 0$.

increases linearly with x albeit at a significantly larger rate than the unforced case. This rapid increase of the spreading rate for $x/D > 2$ is consistent with the 'bifurcation point' usually reported in the range $x/D =$ [2 to 4], e.g. as reported in Suzuki *et al.* (2004). The slow decrease of σ_M/σ_{M_0} at $x/D > 10$ indicates that after the jet splits, the centreline of each momentum stream slowly restores itself towards a more streamwise orientation as it develops. This slow change in orientation is captured by the method proposed in the next section.

For comparison, the average relative spreading rate $\bar{\sigma}_M/\bar{\sigma}_{M_0}$ is computed at $x/D > 10$. Figure 21(*a*) shows $\bar{\sigma}_M/\bar{\sigma}_{M_0}$ at different Y, A, and St. The variation of $\bar{\sigma}_M/\bar{\sigma}_{M_0}$ with Y closely follows the variation of $|\hat{v}|$. Therefore $\bar{\sigma}_M/\bar{\sigma}_{M_0}$ can also be fitted to (4.2*a*,*b*) for each St and is shown in black lines. The amplitudes of the black lines are obtained by fitting $\bar{\sigma}_M/\bar{\sigma}_{M_0}$ to (4.2*a*,*b*) for each St separately which includes the variation due to different forcing levels. The coloured regions indicate 95 % confidence intervals. The fits give $\bar{\sigma}_M/\bar{\sigma}_{M_0} \approx 2.7 \pm 0.2$ for $St = 0.32$ and $\bar{\sigma}_M/\bar{\sigma}_{M_0} \approx 1.8 \pm 0.1$ for $St = 0.47$. These show that there is a significant difference between the two frequencies even after including the variation in forcing amplitude. Furthermore, the increased spreading rate is found to be more sensitive to the forcing frequency than to the forcing level as would be expected when the jet is forced closer to the preferred mode. For instance, the spreading rate is larger for $St = 0.32$ at $A = 0.05$ compared with $St = 0.47$ at $A = 0.25$ even though the latter is forced with a magnitude five times larger. Hence, the difference is unlikely to be due to the 20 % difference in the ratio between $|\hat{u}|$ and $|\hat{v}|$, which was shown in § 4 to be an acoustic feature of the rig.

The skewness S_M is shown in figure 20(*c*) normalized by x^2 to compensate for the linear spreading rate. It is evident that $S_M/x^2 > 0$ for $Y > 0$ and $S_M/x^2 < 0$ for $Y < 0$. The initial development is similar to σ_M/σ_{M_0} where S_M/x^2 increases rapidly in the region $x/D =$ [2 to 8] before it levels off and slowly decreases. At $Y = 1$ and $Y = 0$, $S_M/x^2 \approx 0$ and hence the jet develops symmetrically. This shows that the asymmetry at the intermediate locations is caused by the asymmetry in forcing across the jet nozzle.

To compare the symmetry for different forcing levels and positions $\bar{S}_M$ is computed similarly to $\bar{\sigma}_M/\bar{\sigma}_{M_0}$ by taking the average at $x/D > 10$. Figure 21(*b*) shows $\bar{S}_M$ at different Y and A. For brevity data are only shown for $St = 0.32$. The variation of $\bar{S}_M$ with Y is similar to the product of $\hat{u}\hat{v}$ given by $\sin(\pi/2Y)\cos(\pi/2Y)$ which is fitted to the data at each value of A and are shown by the solid lines. At $|Y| = 1$ and $Y = 0$, $\bar{S}_M \approx 0$ for most operating points. However, at this location a significant value of $\bar{S}_M$ is observed at high forcing levels, e.g. at $Y = -1$ for $A = 0.25$. This is believed to be due to imperfect alignment with the nodal line and the jet centreline resulting in small asymmetries due to the absence of both $\hat{u}$ and $\hat{v}$. However, the fits provide amplitudes $\bar{S}_M = [0.020 \pm 0.004, 0.036 \pm 0.016, 0.077 \pm 0.047]$. Dividing the fitted amplitudes by A yields $\bar{S}_M/A = [0.39 \pm 0.08, 0.25 \pm 0.11, 0.31 \pm 0.19]$ showing that the symmetry is proportional to A.

In this section the jets are characterized by the development of statistical moments of the streamwise momentum in terms of the centre of momentum, the spreading rate and the symmetry. This method provides an alternative way to characterize the jets rather than labelling the jets based on the number of 'branches'. However, an interesting question still remains. The velocity profiles downstream clearly indicate a 'bifurcation', i.e. separation into separate momentum streams. If the jet 'bifurcates', do each of these streams behave like a self-similar jet in the far field? In the next section this question is investigated by proposing a method to isolate each momentum stream from the measurements. Then each branch is analysed individually using a similar approach to that taken when studying the unforced case.

10. Number of momentum streams and self-similarity

To decompose the jet into separate momentum streams, profiles of the streamwise velocity $\bar{u}$ are fitted to a sum of Gaussian profiles given by

$$\bar{u}_t(x, y) = \sum_{i=1}^{n_g} \bar{u}_i = \sum_{i=1}^{n_g} a_i(x) \exp\left(\ln(0.5)\left(\frac{y - b_i(x)}{c_i(x)}\right)^2\right). \tag{10.1}$$

Here $\bar{u}_t$ is a slice of the total streamwise velocity represented as a sum of $n_g = 1$, $n_g = 2$ or $n_g = 3$ velocity profiles. Each profile represents a momentum stream and is described by $\bar{u}_i$. The parameters $a_i(x)$ and $c_i(x)$ are similar to $\bar{u}_{\max}$ and y_0 in (3.2), respectively, and $b_i(x)$ is the centreline position of the profile. Therefore, $b_i(x)$ accounts for the separation between the nozzle centreline $y/D = 0$ and the jet centreline of each momentum stream $\bar{u}_i$. Equation (10.1) is fitted to $\bar{u}$ in the range $x/D = [4 \text{ to } 24]$; hence $\bar{u}_t(x, y)$ is the reconstructed velocity field in terms of Gaussian profiles.

The result of the method is depicted in figure 22. This corresponds to the jet located at $Y = 0.75$, $St = 0.32$ and $A = 0.15$ corresponding to a condition where the jet clearly splits into two momentum streams; hence $n_g = 2$ is chosen. Figure 22(*a–c*) shows contours of constant streamwise velocity described by $\bar{u}_1$, $\bar{u}_2$ and their sum $\bar{u}_t$, respectively. Figure 22(*d*) shows the jet centrelines $b_1(x)$ and $b_2(x)$ for both momentum streams where the dashed line indicates the nozzle centreline. Figure 22(*e*) shows the profiles along the lines $x/D = 10$ in figure 22(*a–c*), and the PIV measurements $\bar{u}$ are shown in red circles. There is an excellent agreement between the fit and the measurements indicating that the model captures the velocity field. Notice that $|b_2(x)| > |b_1(x)|$ and $a_1(x) > a_2(x)$. The trajectories of $b_1(x)$ and $b_2(x)$ shown in figure 22(*d*) also indicate that the jet centrelines are starting to restore towards a more streamwise orientation for $x/D > 10$. This explains the

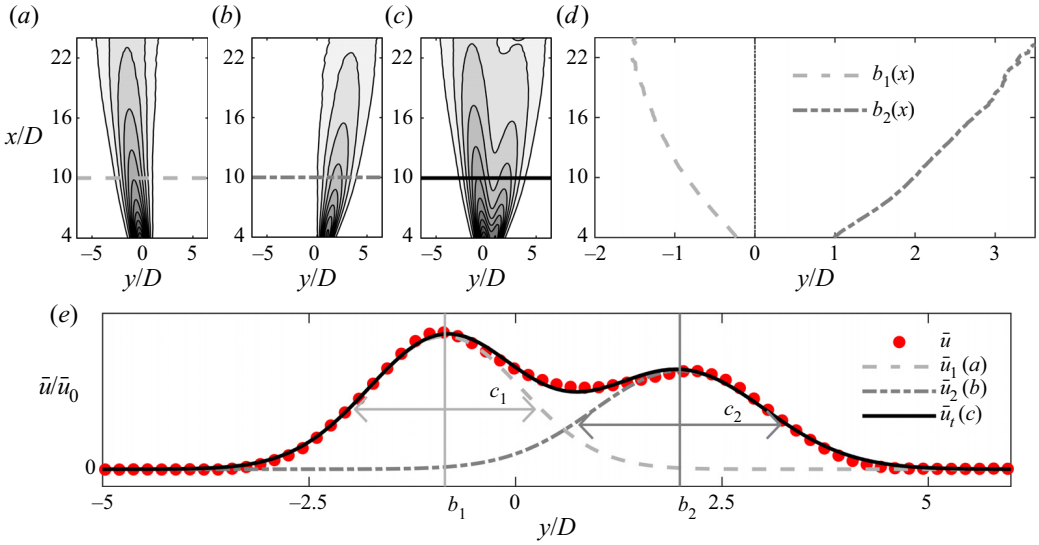

Figure 22. Reconstruction of $\bar{u}$ at $Y = 0.75$ and $A = 0.15$ by superposition of $n_g = 2$ Gaussian profiles. Contours of constant streamwise velocity for (*a*) the left-hand momentum stream $\bar{u}_1/\bar{u}_0$, (*b*) the right-hand momentum stream $\bar{u}_2/\bar{u}_0$ and (*c*) the sum of both streams $\bar{u}_t/\bar{u}_0$. (*d*) Streamwise trajectories of the jet centrelines $b_1(x)$ and $b_2(x)$ for the two momentum streams. (*e*) Profiles of streamwise velocity at $x/D = 10$. The profiles are shown along the lines indicated in (*a–c*).

slowly reducing trends of the momentum spreading rate σ_M/σ_{M_0} shown in figure 20. The left-hand stream contains a higher centreline velocity when compared with the right-hand stream which is a result of the preferred direction induced by the acoustic fluctuations. Their sum results in an asymmetric bifurcation.

The excellent agreement of the expression given by (10.1) with the measurements provides an alternative method to classify a number of separated momentum streams which is shown next. The method is used to classify if the jet consists of one, two or three momentum streams. First, relative errors $\bar{u}_e$ are computed between the model and the measurements:

$$\bar{u}_e = \frac{\bar{u}_t - \bar{u}}{\bar{u}_{max}}. \tag{10.2}$$

The normalization by $\bar{u}_{max}$ is used to avoid amplified errors due to low velocities outside of the jet where $\bar{u}/\bar{u}_0$ approaches zero. In this way, lower values of $\bar{u}_e$ indicate better fits. The reconstruction of $\bar{u}$ shown in figure 22 was computed using $n_g = 2$ and provided excellent agreement with the measurements. To demonstrate the improvement of using $n_g = 2$ as compared with $n_g = 1$ for a jet consisting of two momentum streams, $\bar{u}_e$ is computed for both cases. Histograms of $\bar{u}_e$ are shown for both profiles $n_g = 1$ and $n_g = 2$ in figure 23(*a*). The insets show the spatial distribution of $\bar{u}_e$ in the region $x/D = [4 \text{ to } 24]$ and $y/D = [-7 \text{ to } 7]$. The mean value μ_e gives the average error and σ_e gives the standard deviation indicating the scatter of $\bar{u}_e$. It is evident that using $n_g = 2$, compared with $n_g = 1$, reduces the errors by an order of magnitude for the 'bifurcated' jet. To show that this is only the case when the jet consists of more than a single momentum stream, figure 23(*b*) shows $\bar{u}_e$ for the unforced jet. The unforced jet consists of a single momentum stream which is well approximated by a single Gaussian as was shown in § 3. This is shown by the similar histograms between $n_g = 1$ in figure 23(*b*) and $n_g = 2$ in figure 23(*a*). Furthermore, introducing a second profile, i.e. $n_g = 2$, does not reduce significantly

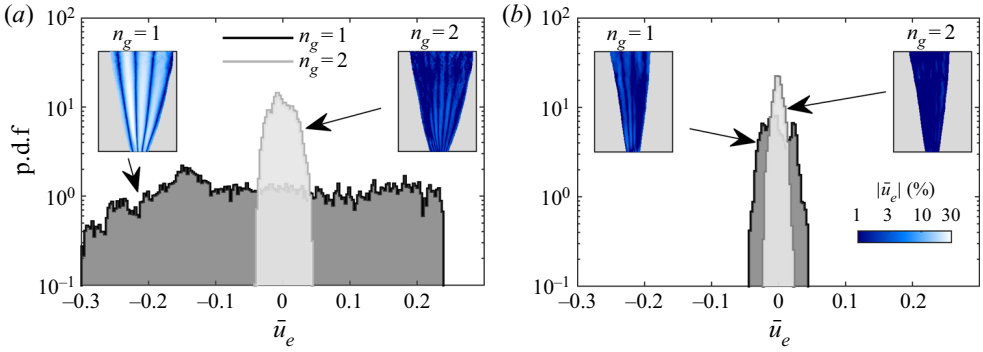

Figure 23. Histograms of relative errors $\bar{u}_e$ using $n_g = 1$ and $n_g = 2$. The insets show the spatial variation of $\bar{u}_e$. (*a*) At $Y = 0.75$ with $A = 0.15$ where the jet contains two momentum streams. Using $n_g = 2$ reduces the error by an order of magnitude when compared with using $n_g = 1$. (*b*) The unforced jet containing a single momentum stream. Excellent agreement is obtained with $n_g = 1$; using $n_g = 2$ does not reduce the errors significantly.

the errors. In other words, based on the reduction of fitting errors, the model is able to distinguish between a jet consisting of a single or several separated momentum streams. A similar conclusion is made for the jets at $|Y| = 1$ where $n_g = 3$ is required to reduce the errors to a sufficient level, which is discussed next.

The method just described can be used to classify the number of momentum streams, based on the following steps. (i) First $\bar{u}$ is fitted to (10.1) with $n_g = 1$, $n_g = 2$ and $n_g = 3$. (ii) Then $\bar{u}_e$ is computed using (10.2), and the mean μ_e and standard deviation σ_e of the errors are computed. (iii) Finally μ_e and σ_e are then plotted against n_g and two threshold values $\text{tol}_1 = 0.004$ and $\text{tol}_2 = 0.02$ are obtained from the unforced case using $n_g = 1$. The value of n_g that leads to $|\mu_e| < \text{tol}_1$ and $|\sigma_e| < \text{tol}_2$ determines the number of individual streams.

Figure 24 plots μ_e and σ_e for all operating points including the unforced jet which is used as the benchmark for a single momentum stream. Grey shaded regions indicate the threshold values $\text{tol}_1 = 0.004$ and $\text{tol}_2 = 0.02$ obtained from the unforced case fitted to $n_g = 1$. To show how the different combinations of forcing generate different jet structures figure 24 shows groups of cases at $Y = 0$, intermediate positions and $|Y| = 1$. The insets show $|\bar{\boldsymbol{u}}|$ for the unforced jet, and at $Y = 0.75$ and $Y = 1$ for $A = 0.15$, where the jet shows clear characteristics of one, two or three momentum streams. Here μ_e and σ_e corresponding to the insets are highlighted by red lines and circles and their trends are discussed next.

For the unforced jet using $n_g = 1$ already provides an excellent fit with the measurements where the values of μ_e and σ_e define the thresholds tol_1 and tol_2. Adding additional profiles ($n_g = [2, 3]$) does not decrease the errors significantly. For the jet at $Y = 0.75$, μ_e and σ_e are above the threshold when $n_g = 1$. Setting $n_g = 2$ reduces the errors by an order of magnitude and thus brings μ_e and σ_e below the threshold. Hence, the number of individual momentum streams can be classified as two. Using $n_g = 3$ does not significantly decrease the errors further. At $Y = 1$ the errors are above the threshold for $n_g = 1$, although the errors are significantly lower when compared with $n_g = 1$ at $Y = 0.75$. This shows that a symmetric distribution with three peaks is better captured by a single Gaussian compared to a skewed distribution containing two peaks. Using $n_g = 2$ reduces the errors, although the reduction is not as large when compared with the reduction at $Y = 0.75$. The errors are still above the threshold for σ_e and thus using $n_g = 3$ is required

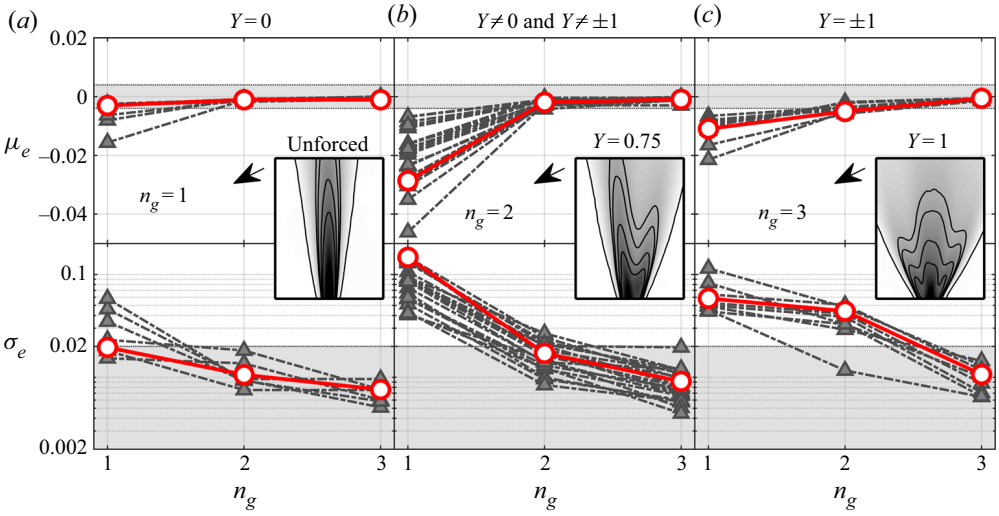

Figure 24. Mean μ_e and standard deviation σ_e of the fitting errors $\bar{u}_e$ plotted against n_g. The grey regions are separated by the thresholds $\text{tol}_1 = \mu_e$ and $\text{tol}_2 = \sigma_e$ computed for the unforced jet using $n_g = 1$. The insets show the PIV measurements of $|\bar{\boldsymbol{u}}|$ corresponding to the red lines with circle markers. The highlighted cases shown in the insets indicate cases that are characterized by one, two and three individual momentum streams. (*a*) All cases at the velocity node ($Y = 0$) and the unforced jet. (*b*) All cases at the intermediate locations. (*c*) All cases at the pressure nodes ($|Y| = 1$).

to reduce the errors below the limit. Note that the reduction of σ_e is significantly larger from $n_g = 2$ to $n_g = 3$ than the reduction from $n_g = 1$ to $n_g = 2$. This result shows that the method is able predict the correct amount of momentum streams by using the correct amount of profiles, making it a robust method to classify the number of streams. In this case $n_g = 3$ is required to get a satisfactory representation of the jet at $Y = 1$ for $A = 0.15$.

The dependence of μ_e and σ_e with respect to n_g for the other cases shows very similar patterns to the ones discussed. It is evident that most cases at the velocity node, $Y = 0$, consist of a single momentum stream, most cases at intermediate positions consist of two and most cases at the pressure nodes $|Y| = 1$ consist of three. This result shows that forcing the symmetric and anti-symmetric modes simultaneously leads to skewed jets separating into two individual momentum streams. At the pressure nodes, $|Y| = 1$, strong anti-symmetric forcing leads to three momentum streams. At the velocity node, the jet remains a single momentum stream. However, there are three cases that need $n_g = 2$: $A = [0.15, 0.25]$ for $St = 0.47$ and $A = 0.25$ for $St = 0.32$. As discussed before, this is caused by a small but non-negligible component of $|\hat{v}|$ due to imperfect alignment between the nozzle centreline and the velocity node, showing that the jet is very sensitive to transverse forcing. It should be emphasized that this way of classifying the number of streams is dependent on the threshold level obtained from the unforced jet which ultimately depends on the accuracy of the measurements. However, it has been shown multiple times in the literature that the unforced jet is well characterized by the self-similar profile and thus using the fitting errors tol_1 and tol_2 as a baseline provides a way of quantifying the reasonable level of accuracy that the model needs.

The fitted profiles shown in figure 22 are not constrained to behave in a self-similar manner. However, as shown in figure 25(*a*,*b*), the normalized velocity profiles of each individual stream still behave in a self-similar manner beyond $x/D > 10$. To separate the streams $\bar{u}_i$ is subtracted from $\bar{u}$ and the remainder is normalized by a_i. The data are then

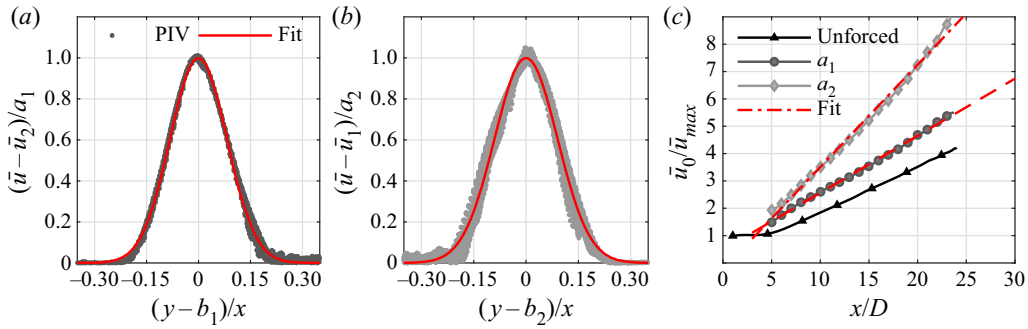

Figure 25. Self-similarity of the bifurcated jet at $Y = 0.75$ and at $A = 0.15$. (*a*,*b*) The normalized streamwise velocity profiles $\bar{u} - \bar{u}_2$ and $\bar{u} - \bar{u}_1$ shifted by $b_1(x)$ and $b_2(x)$ and normalized by $a_1(x)$ and $a_2(x)$ in the region $x/D > 10$. Both profiles are fitted to (3.2) to obtain the jet half-width y_0. (*c*) Centreline decay of streamwise velocity. The velocity in both streams decays linearly indicated by the dashed lines which show fits of (3.3).

plotted against the shifted coordinate $((y - b_i)/x)$. Both streams approximately collapse on the self-similar profile given by (3.2). This indicates that the half-width of both streams increases linearly with x following classical scaling. The small discrepancies might occur due to the streams being at an angle with respect to the nozzle centreline. Hence, fitting the profiles normal to the y–z plane instead of the plane normal to the jet centreline of each stream is only a good representation for small angles. This explains the large scatter for the right-hand stream which is more angled when compared with the left-hand stream. The jet half-width y_0 is obtained by fitting the data to (3.2) and shown in the red lines. For the left-hand stream the half-width is $y_0 = 0.096 \pm 0.000$ and for the right-hand stream the half-width is $y_0 = 0.106 \pm 0.001$. Both streams have similar half-widths to the unforced case, $y_0 = 0.095$.

The centreline decay of streamwise velocity, represented by $\bar{u}_0/a_i$, is shown for both streams in figure 25(*c*). As a reference, the data for the unforced jet are also shown. The decay rate is linear for all cases. However, the forced jet splits into two streams each containing a portion of the total streamwise momentum. Thus, the velocity of each stream decays more rapidly than in the unforced jet. The decay rate B is obtained for both streams of the forced jet by fitting the data to (3.3). The left-hand stream gives $B = 4.8 \pm 0.1$ and the right-hand stream gives $B = 2.7 \pm 0.1$, both of which are significantly lower than the unforced case, $B = 6.04 \pm 0.01$, as expected.

Having characterized the half-width and decay rate of each branch we test if the momentum of both streams adds up to the total momentum of the unforced case ($M/M_0 = 0.93 \pm 0.01$). Substituting the values gives $M_1/M_0 = 0.62 \pm 0.02$ and $M_2/M_0 = 0.23 \pm 0.02$. Adding the contributions of the two streams yields $M_1/M_0 + M_2/M_0 = 0.85 \pm 0.04$, which is reasonably close to the total momentum of the unforced jet. This result indicates that, as the jet splits into two streams, each stream behaves in a self-similar manner.

11. Conclusions

The hydrodynamic response of an axisymmetric turbulent jet subjected to transverse downstream forcing has been investigated in detail. Downstream forcing was achieved by placing the jet inside a long rectangular box of adjustable length that used speakers to generate plane acoustic waves that were oriented normal to the streamwise direction of the jet. The jet was acoustically forced at different Strouhal numbers to measure its

response when placed at different positions between the pressure anti-node to the pressure node in a standing wave. When located at the pressure anti-node and pressure node, respectively, the $m = 0$ and $m = \pm 1$ modes of the jet were excited. This leads to dynamics similar to that previously reported in the literature, where the $m = 0$ or preferred mode results in the axisymmetric formation of coherent structures formed close to the nozzle exit, whereas the $m = \pm 1$ mode results in anti-symmetric vortex patterns that lead to bifurcation downstream of the potential core.

However, when the jet was placed at any other position in between the pressure node and anti-node, both the $m = 0$ and $m = \pm 1$ modes of the jet were excited at the same frequency which amplified both the streamwise and transverse fluctuating components with differing magnitudes. This leads to distinct asymmetric vortex patterns and bifurcation patterns which depend on the location of the jet within the standing wave. The observed responses show important differences from previous bifurcating jet studies where optimal jet spreading was achieved by simultaneous forcing at different frequencies as summarized by Reynolds *et al.* (2003), but show some similar features to the asymmetric mixed patterns observed in the large-eddy simulations of Tyliszczak & Geurts (2014) and the experiments of Longmire & Duong (1996).

Furthermore, despite the fact that the jet is acoustically compact ($D \ll \lambda_y$) transverse forcing was observed to have a significant effect on the jet boundary conditions resulting in asymmetric profiles of the component velocity fluctuations at the jet exit. This was caused by the relative phase $\Delta\varphi/\pi$ between the acoustic fluctuations $\hat{u}$ and $\hat{v}$ leading to the observed asymmetric formation patterns of the coherent structures and preferential increase in the spreading rate of the jet on the side closest to the pressure node. The modified jet exit boundary conditions were shown to be linear combinations of the symmetric and anti-symmetric boundary conditions measured at the pressure and velocity nodes of the jet.

The effect of anti-symmetric forcing leads to a significant increase of the spreading rate of the jet in the transverse plane. At sufficient forcing amplitudes the jet 'bifurcates' and separates into several momentum streams. At the pressure nodes the 'Ψ' jet reported numerically by Danaila & Boersma (2000) and Gohil & Saha (2019) is observed. Away from the nodal positions the jet splits into two streams which are asymmetric with respect to the nozzle centreline due to combined longitudinal and transverse forcing at the same frequency ($r_f = 1$). Again, this is the major difference compared with the measurements performed by Parekh *et al.* (1987) where a symmetric 'bifurcation' is observed when the symmetric mode is forced at twice the frequency of the anti-symmetric mode ($r_f = 2$).

A statistical method was proposed to quantify the modified time-averaged jet behaviour by considering the statistical moments of p.d.f.s of streamwise momentum quantifying the centre of momentum, spreading rate and symmetry. It is shown that the spreading rate is proportional to $|\hat{v}|$ and the skewness giving the symmetry is proportional to the product $\hat{u}\hat{v}$. The increase in spreading rate showed a clear dependence on Strouhal number. Compared with the unforced jet, the spreading rate at pressure node is approximately 3 times larger when $St = 0.32$ and 1.6 times larger when $St = 0.47$.

Finally a method was proposed to reconstruct the streamwise velocity field of the forced jets as a sum of Gaussian profiles. The method is used to determine the number of individual momentum streams which are analysed independently. At the velocity node the jet contains a single stream, whereas at the pressure node the jet splits into three streams. Away from the nodal locations, the jet splits into two asymmetric streams due to combined forcing, breaking the plane symmetry. It was also shown that each momentum stream is self-similar.

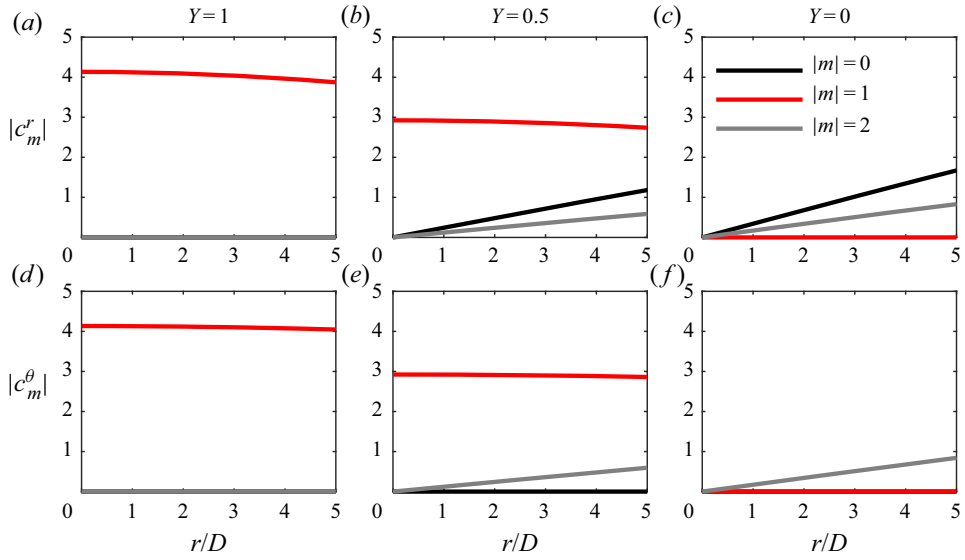

Figure 26. Coefficients of the Fourier series, with $A_y = 1$, $k_y = 4\pi/L$.

Acknowledgements. The authors would like to thank Thomas Indlekofer for invaluable help with the experiments.

Funding. The authors acknowledge support from the NCCS Centre, funded under the Norwegian research programme Centres for Environment-friendly Energy Research (FME), grant no. 257579/E20.

Declaration of interests. The authors report no conflict of interest.

Author ORCIDs.
Eirik Æsøy https://orcid.org/0000-0001-6185-5633;
José G. Aguilar https://orcid.org/0000-0002-6923-6527;
Nicholas A. Worth https://orcid.org/0000-0002-7084-9304;
James R. Dawson https://orcid.org/0000-0002-3069-6948.

Appendix A. Transverse and longitudinal forcing in a cylindrical coordinate system

In this appendix the azimuthal modes excited by an acoustic field composed of a transverse pressure wave are discussed. The development is similar to the one found in O'Connor *et al.* (2015, § 4.2), and it is only included here for completeness.

The transverse acoustic pressure fluctuations in the box, p_y, are assumed to be given by

$$p_y = A_y \sin(k_y y + \phi_y)\sin(\omega t), \quad \text{for } -L/2 \le y \le L/2. \tag{A1}$$

The body force in the transverse direction is given by $f_y = \partial p_y/\partial y$. Converting it to a cylindrical coordinate system yields

$$\left[f_r, f_\theta, f_z\right] = \left[f_y \sin(\theta), f_y \cos(\theta), 0\right], \tag{A2}$$

with $y = r\sin(\theta)$. Here f_r and f_θ are functions of r and θ. Decomposing the spatial component of each of the forces into complex Fourier series in θ gives

$$f_i = \sum_{m=-M}^{M} c_m^{(i)}(k_y r)\exp(\mathrm{i}m\theta). \tag{A3}$$

In figure 26 we plot the coefficients $c_m^{(i)}$ for each forcing component at three different positions in the standing wave and a fixed value of k_y which emulates similar conditions as in the experimental set-up.

Figures 26(*a–c*) and 26(*d–f*) show the coefficients of the transverse force in terms of its radial and azimuthal components, respectively. When $Y = 1$ (pressure node) the $|m| = 1$ component is the dominant one, and it loses its strength as one moves towards $Y = 0$ (velocity node). At $Y = 0$ we observe a small contribution of the $m = 0$ mode and an even smaller contribution of the $m = 2$ mode, which lose their strength as one moves towards $Y = 1$. The rest of the modes only become relevant far away from the jet centre.

It is evident that within the potential core of the jet, a transverse wave is composed mainly of the $m = \pm 1$ modes, except at the velocity node where the $m = 0$ mode has the largest amplitude.

References

Batchelor, G.K. & Gill, A.E. 1962 Analysis of the stability of axisymmetric jets. *J. Fluid Mech.* **14** (04), 529–551.

Bechert, D. & Pfizenmaier, E. 1975 On the amplification of broad band jet noise by a pure tone excitation. *J. Sound Vib.* **43** (3), 581–587.

Becker, H.A. & Massaro, T.A. 1968 Vortex evolution in a round jet. *J. Fluid Mech.* **31** (3), 435–448.

Bourgouin, J.-F., Durox, D., Moeck, J., Schuller, T. & Candel, S. 2013 Self-sustained instabilities in an annular combustor coupled by azimuthal and longitudinal acoustic modes. *Proceedings of the ASME Turbo Expo 2013: Turbine Technical Conference and Exposition, vol. 1B: Combustion, Fuels and Emissions. San Antonio, Texas, USA. June 3–7, 2013. V01BT04A007*. ASME.

Brown, G.L. & Roshko, A. 1974 On density effects and large structure in turbulent mixing layers. *J. Fluid Mech.* **64** (4), 775–816.

Cohen, J. & Wygnanski, I. 1987 The evolution of instabilities in the axisymmetric jet. Part 1. The linear growth of disturbances near the nozzle. *J. Fluid Mech.* **176**, 191–219.

Corke, T.C. & Kusek, S.M. 1993 Resonance in axisymmetric jets with controlled helical-mode input. *J. Fluid Mech.* **249**, 307–336.

Crow, S.C. & Champagne, F.H. 1971 Orderly structure in jet turbulence. *J. Fluid Mech.* **48** (03), 547–591.

Danaila, I. & Boersma, B.J. 2000 Direct numerical simulation of bifurcating jets. *Phys. Fluids* **12** (5), 1255–1257.

Dawson, J.R. & Worth, N.A. 2014 Flame dynamics and unsteady heat release rate of self-excited azimuthal modes in an annular combustor. *Combust. Flame* **161** (10), 2565–2578.

Gohil, T.B. & Saha, A.K. 2019 Numerical simulation of forced circular jets: effect of flapping perturbation. *Phys. Fluids* **31** (8), 083602.

Gohil, T.B., Saha, A.K. & Muralidhar, K. 2015 Simulation of the blooming phenomenon in forced circular jets. *J. Fluid Mech.* **783**, 567–604.

Gutmark, E. & Ho, C.-M. 1983 Preferred modes and the spreading rates of jets. *Phys. Fluids* **26** (10), 2932–2938.

Ho, C.M. & Huerre, P. 1984 Perturbed free shear layers. *Annu. Rev. Fluid Mech.* **16** (1), 365–422.

Hussain, A.K.M.F. & Zaman, K.B.M.Q. 1981 The 'preferred mode' of the axisymmetric jet. *J. Fluid Mech.* **110**, 39–71.

Hussain, F. & Husain, H.S. 1989 Elliptic jets. Part 1. Characteristics of unexcited and excited jets. *J. Fluid Mech.* **208** (−1), 257–320.

Hussein, H.J., Capp, S.P. & George, W.K. 1994 Velocity measurements in a high-Reynolds-number, momentum-conserving, axisymmetric, turbulent jet. *J. Fluid Mech.* **258**, 31–75.

Kasagi, N. 2006 Toward smart control of turbulent jet mixing and combustion. *JSME Intl J.* B **49** (4), 941–950.

Kusek, S.M., Corke, T.C. & Reisenthel, P. 1990 Seeding of helical modes in the initial region of an axisymmetric jet. *Exp. Fluids* **10** (2), 116–124.

Lee, M. & Reynolds, W.C. 1985 Bifurcating and blooming jets. Report TF-22, Thermosciences Division, Department of Mechanical Engineering, Stanford University.

Longmire, E.K. & Duong, L.H. 1996 Bifurcating jets generated with stepped and sawtooth nozzles. *Phys. Fluids* **8** (4), 978–992.

LONGMIRE, E.K., EATON, J.K. & ELKINS, C.J. 1992 Control of jet structure by crown-shaped nozzles. *AIAA J.* **30** (2), 505–512.

MICHALKE, A. & HERMANN, G. 1982 On the inviscid instability of a circular jet with external flow. *J. Fluid Mech.* **114**, 343–359.

MOORE, C.J. 1977 The role of shear-layer instability waves in jet exhaust noise. *J. Fluid Mech.* **80** (2), 321–367.

O'CONNOR, J., ACHARYA, V. & LIEUWEN, T. 2015 Transverse combustion instabilities: Acoustic, fluid mechanic, and flame processes. *Prog. Energy Combust. Sci.* **49**, 1–39.

PANCHAPAKESAN, N.R. & LUMLEY, J.L. 1993 Turbulence measurements in axisymmetric jets of air and helium. Part 1. Air jet. *J. Fluid Mech.* **246**, 197–223.

PAREKH, D., REYNOLDS, W.C. & MUNGAL, M.G. 1987 Bifurcation of round air jets by dual-mode acoustic excitation. *AIAA Paper* 87-0164.

PAREKH, E., LEONARD, A. & REYNOLDS, W.C. 1988 Bifurcating jets at high Reynolds numbers. Dep. Mech. Eng. Thermosci. Div. Rep. p. 263.

POPE, S.B. 2001 Turbulent flows. *Meas. Sci. Technol.* **12** (11), 2020–2021.

REYNOLDS, W.C., PAREKH, D.E., JUVET, P.J.D. & LEE, M.J.D. 2003 Bifurcating and blooming jets. *Annu. Rev. Fluid Mech.* **35** (1), 295–315.

SEYBERT, A.F. & ROSS, D.F. 1977 Experimental determination of acoustic properties using a two-microphone random-excitation technique. *J. Acoust. Soc. Am.* **61** (5), 1362–1370.

DA SILVA, C.B. & MÉTAIS, O. 2002 Vortex control of bifurcating jets: a numerical study. *Phys. Fluids* **14** (11), 3798–3819.

STAFFELBACH, G., GICQUEL, L.Y.M., BOUDIER, G. & POINSOT, T. 2009 Large Eddy Simulation of self excited azimuthal modes in annular combustors. *Proc. Combust. Inst.* **32** (2), 2909–2916.

SUZUKI, H., KASAGI, N. & SUZUKI, Y. 2004 Active control of an axisymmetric jet with distributed electromagnetic flap actuators. *Exp. Fluids* **36** (3), 498–509.

TYLISZCZAK, A. 2015 Multi-armed jets: a subset of the blooming jets. *Phys. Fluids* **27** (4), 041703.

TYLISZCZAK, A. & GEURTS, B.J. 2014 Parametric analysis of excited round jets – numerical study. *Flow Turbul. Combust.* **93** (2), 221–247.

URBIN, G. & MÉTAIS, O. 1997 Large-eddy simulations of three-dimensional spatially-developing round jets. In *Direct and Large-Eddy Simulation II* (ed. J.-P. Chollet, P.R. Voke & L. Kleiser), pp. 35–46. Springer.

WIENEKE, B. 2015 PIV uncertainty quantification from correlation statistics. *Meas. Sci. Technol.* **26** (7), 074002.

WINANT, C.D. & BROWAND, F.K. 1974 Vortex pairing: the mechanism of turbulent mixing-layer growth at moderate Reynolds number. *J. Fluid Mech.* **63** (2), 237–255.

WORTH, N.A. & DAWSON, J.R. 2013 Modal dynamics of self-excited azimuthal instabilities in an annular combustion chamber. *Combust. Flame* **160** (11), 2476–2489.

WORTH, N.A., MISTRY, D., BERK, T. & DAWSON, J.R. 2020 Vortex dynamics of a jet at the pressure node in a standing wave. *J. Fluid Mech.* **882**, A22.

WYGNANSKI, I. & FIEDLER, H. 1969 Some measurements in the self-preserving jet. *J. Fluid Mech.* **38** (3), 577–612.